

BRUNEL UNIVERSITY, LONDON



Optically Transparent UWB Antenna for Wireless Application & Energy Harvesting

A thesis submitted in partial fulfilment of the requirements for the degree of Doctor of
Philosophy (Ph.D.) to:
Electronic and Computer Engineering
School of Engineering and Design
Brunel University
United Kingdom.

by:
Thomas Peter

August 2012

Supervised By:
Dr Rajagopal Nilavalan

Abstract

Transparent UWB antennas have been the focus of this PhD research. The use of transparent UWB antennas for stealth and energy harvesting has been the underlying applications that have given impetus to this research. Such transparent antennas being built on materials that are discreet, flexible, conformal, conductive and having the ability to provide good antenna performance on glass to serve as the 'last mile' link in subsequent generation communications after 4G have been the basis for this contention. UWB in this regard is able to provide the transmission and reception of high data rates and fast video transmission that is an elementary demand of even a 4G wireless communications system. The integration of UWB antennas with photovoltaic to provide integral energy harvesting solutions that will further enhance the value of the UWB system in terms of cost effectiveness and performance are thus the basis of this work.

This work hence starts with the study of a transparent conductive oxide polymer, AgHT and its properties, and culminates in the development of a transparent UWB antenna, which can be integrated with photovoltaic for window glass applications on homes and buildings. Other applications such transparent antennas can find use for like on-body wireless communications in healthcare monitoring was also analysed and presented. The radar absorbing material (RAM) property of the AgHT was investigated and highlighted using CST simulation software, as no measurement facilities were available. The transparent UWB antenna in lieu of the inherent absorbent property of the AgHT material is thus able to exhibit stealth characteristics, a feature that would be much desired in military communications.

Introduction of a novel method of connecting the co-axial connector to the feed of the antenna to improve gain and efficiency of transparent polymer based antennas and the development of a UWB antenna that maintains its Omni-directional characteristic instead of becoming directional on an amorphous silicon solar cell are presented as some of the contributions for this research work. Some preliminary analysis on the impact of glass on UWB antennas for video transmission and how to improve transmission is presented. The ability of the conductive part of the antenna radiator to be used as a RF and microwave harvester and how it can further add value to a transparent UWB antenna is presented by way of experimental data.

Finally yet importantly, this thesis presents some insight into how transparent antennas may be used in Green Technology Buildings to provide an integrated solution for both wireless communications and energy harvesting as part of the future work. Improvement to the aesthetics of the external appearance of residential buildings through the integration of transparent satellite dish onto solar panels on rooftops is also discussed and illustrated as part of this future work.

Acknowledgments

I am grateful to the Yahweh and Yeshua through whom, by whom and for whom all things were created, and who gladly laid down his life at the cross that we can have eternal life. Without his blessing and divine guidance in my research, this thesis would not have been possible.

I owe my deepest gratitude to my wife and children without whom I would not have made it through my PhD degree. Their tremendous understanding and prayers showed me the way and helped me persevere to complete this thesis.

It is my pleasure at the same time, to thank all those who made this thesis possible. I am heartily thankful to my supervisor, Dr R. Nilavalan as well as Dr S.W. Cheung of Hong Kong University whose encouragement, guidance and support from the initial to the final level enabled me to develop an understanding of this work. I appreciate all their help and support. I too, am indebted to my many of my colleagues at WNCC and friends at Brunel University. I would like to show my gratitude to all staff at Brunel University. I would like to thank them for their encouragement and supportive attitude. I would also like to take this opportunity to thank the administrative staff of Hong Kong University and the academic staff of Queen Mary University of London for all help rendered to enable me to use their test and measurement facilities for this thesis work.

I would like to express gratitude to those who helped me to finalize my thesis; without them, I could not have written this thesis.

Lastly, I offer my regards to all of those who supported me in any respect during the completion of the project.

Table of Contents

Chapter 1: Introduction.....	1
1.1 Motivations	1
1.1.1 Stealth	4
1.1.2 Energy Harvesting	4
1.2 Aim and Objectives.....	6
1.3 Contribution to Knowledge.....	6
1.4 Thesis Structure	8
1.5 References.....	10
Chapter 2: Transparent Antenas: A Literature Review, Material Development and Properties of Transparent Conductive Oxides.....	11
2.1 Introduction.....	11
2.2 Literature Review.....	11
2.3 Transparent Conductive Materials – Development Review	20
2.4 Properties of Transparent Conductive Oxides (TCOs).....	22
2.4.1 Characterisits, Properties & Applications of TCOs	22
2.4.2 Other Properties	25
2.4.2.1 Transparency	25
2.4.2.2 Electrical Conductivity.....	27
2.4.2.3 Plasma Frequency	28

Table of Contents

2.4.2.4	Deposition Temperature	29
2.4.2.5	TCOs on Soda Lime Glass	30
2.4.2.6	Durability and Etching Patterns on TCOs.....	31
2.4.2.7	Hardness of TCOs	33
2.4.2.8	Sun Shileding and Low Emissivity	33
2.4.2.9	Electromagnetic Shielding	34
2.4.2.10	Integration of TCOs with Solar Cells.....	34
2.4.2.11	TCO Coated PET as Radar Absorption Material.....	35
2.5	Summary	36
2.6	References.....	38
 Chapter 3: UWB Antennas.....		41
3.1	Introduction.....	41
3.2	Requirements for UWB Antennas	42
3.2.1	Other Requirements	44
3.3	Planar UWB Antennas.....	44
3.4	CPW Feed.....	45
3.4.1	Circular Disc Monopole.....	45
3.4.2	Rectangular Patch LCP Monopole.....	46
3.4.3	T-Shaped Monopole.....	47
3.4.4	Elliptical Monopole	48
3.5	Leakage Currents in CPW Feed.....	48
3.6	Extensions to the CPW Feed.....	49
3.6.1	Microstrip to CPW Transition	50
3.7	Negating Unwanted Frequency Bands.....	55
3.8	Summary	57

Table of Contents

3.9	References.....	58
Chapter 4: Transparent UWB Antennas		62
4.1	Introduction.....	62
4.2	Modelling and Design of Transparent UWB Antennas.....	63
4.3	The Mushroom Top UWB Antenna	70
4.3.1	Parametric Study-Impedance Matching Through Resonators	71
4.3.2	Conformability and Flexibility of the Antenna.....	71
4.2.3	Single Layered Mushroom Top Antenna.....	75
4.4	A Method to Improve the SMA to Antenna Connection.....	79
4.5	Band Notch to Negate Unwanted Bands inTransparent UWB Antennas.....	79
4.6	Analysis of Coupling, Proximity Sensitiveness and Radar Cross Section Characteristics of Transparent Antennas	82
4.6.1	Analysis of Mutual Coupling in Arrays.....	82
4.6.2	Insensitiveness to Proximity Interference	85
4.6.3	Analysis of RAM Properties of AgHT based TransparentAntenna using RCS.....	86
4.7	Summary	90
4.8	References:.....	91
Chapter 5: Analysis of Transparent UWB Antennas for Body Centric Applications		93
5.1	Introduction.....	93
5.2	A Compact Transparent UWB Antenna for Wireless Body-Centric Applications .	94
5.3	Transparent UWB Antennas for Wearable Applications.....	106
5.4	Summary	106

Table of Contents

5.5	References.....	107
-----	-----------------	-----

Chapter 6: Analysis of Transparent UWB Antennas On-Glass Structures.....109

6.1	Introduction.....	109
6.2	Dielectric of the Glass.....	109
6.2.1	Experimental Determination of Glass Dielectric	110
6.3	Antennas with Glass Substrate.....	112
6.3.1	UWB Transmission Test.....	120
6.4	Antennas with Glass Superstrate	128
6.4.1	Feed Connection for Superstrate Configuration	129
6.5	Antennas Sandwiched Between Glass	130
6.6	Summary	135
6.7	References.....	137

Chapter 7: Development of a Novel Antenna for Integration of Solar Panels and RF Energy Harvesting139

7.1	Introduction.....	139
7.2	Non-Optically Transparent Green Antennas	141
7.2.1	Solar Ray Collector Green Antenna	141
7.2.2	Solar-cell Integrated Antennas.....	141
7.2.3	Antenna Incorporated Onto Solar Cells/Panels	143
7.2.4	Rectennas	144
7.2.4.1	Narrowband Rectenna	145
7.2.4.2	Ultra Wideband Rectenna	146

Table of Contents

7.2.4.3	Integrated Rectenna.....	147
7.2.5	Power Saving Antennas	148
7.3	Transparent Green UWB Antennas	149
7.3.1	Transparent CTSA for Solar Energy Harvesting	150
7.3.1.1	Simulated and Measured Results for the CTSA in Free Space.....	151
7.3.1.2	Simulated and Measured Results for the CTSA on Solar Panel	154
7.3.1.3	Simulated and Measured Results for the CTSA on Solar Panel with a 2mm Glass Superstrate.....	155
7.3.2	Transparent CTSA Rectenna for RF/Microwave Harvesting.....	159
7.3.2.1	Rectenna in Free Space	160
7.3.2.1.1	Rectenna Measurement Set-up	163
7.3.2.1.2	Rectenna Efficiency	163
7.3.2.1	Rectenna on Glass	166
7.4	Summary.....	170
7.5	References.....	172
Chapter 8: Conclusions and Future Work.....		175
8.1	Conclusions.....	175
8.1.1	Characteristics and Properties of AgHT	175
8.1.2	Development of Transparent AgHT UWB Antennas and Its Features.....	176
8.1.3	Transparent Green UWB Antennas for Energy Harvesting	176
8.2	Future Work.....	177
8.2.1	Energy Saver for Green Technology Building in Wireless Communication System.....	177
8.2.2	Satellite Dish Integrated Solar Energy Harvester.....	179

Table of Contents

Appendix:

Appendix A.1	UWB Spectrum for EU	180
Appendix A.2	UWB Spectrum for EU (continued).....	181
Appendix B.1	Properties of PET	182
Appendix B.2	Tan δ and Q Factor	183
Appendix B.3	Malaysian Flagship Project	184
Appendix B.3	Malaysian Flagship Project (continued).....	185
Appendix C.1	How PET is Made	186
Appendix C.2	Barrier Film for PET	187
Appendix C.3	Eccosorb FGMU-125	188
Appendix C.3	Eccosorb FGMU-125 (continued).....	189

List of Papers

1. **T. Peter** and R. Nilavalan, "Study on the performance deterioration of flexible UWB antennas," *Antennas and Propagation Conference Loughborough (LAPC'09)*, pp. 669-672, 2009.
2. **T. Peter**, R. Nilavalan, H.F. AbuTarboush and S.W. Cheung, "A non-thermal soldering technique to improve polymer based antenna performance," *European Microwave Conference (EuMC)*, 2010, pp.1476-1479, Sept. 28-30, 2010.
3. **T. Peter**, R. Nilavalan, H.F. AbuTarboush and S.W. Cheung, "A Novel Technique and Soldering Method to Improve Performance of Transparent Polymer Antennas," *IEEE Antennas and Wireless Propagation Letters*, vol.9, pp.918-921, 2010.
4. **T. Peter**, R. Nilavalan, H.F. AbuTarboush, S.W. Cheung and Y.F. Weng, "Investigative Study on the Development of a Green UWB Antenna", International Symposium on Antennas and Propagation in 2010 (ISAP 2010).
5. **T. Peter**, Y.Y. Sun, T.I. Yuk, H.F. AbuTarboush, R. Nilavalan and S.W. Cheung, "Miniature transparent UWB antenna with tunable notch for green wireless applications," *International Workshop on Antenna Technology (iWAT)*, 2011, pp.259-262, 7-9 March 2011.
6. **T. Peter**, R. Nilavalan and S.W. Cheung, "A Novel Transparent TSA for Laptop and UWB Applications", *PIERS Proceedings*, Kuala Lumpur, MALAYSIA, March 27-30, 2012.
7. **T. Peter**, R. Nilavalan, R. DiBari, A. Alomainy, S.W. Cheung and A.R. Tharek, "Analysis of Transparent UWB Antennas for Body-Centric Applications" *Piers*, submitted for publication.
8. **T. Peter**, R. Nilavalan, S.W. Cheung and H.F. AbuTarboush, "Analysis of Transparent UWB Antenna on Glass Structures," *IEEE Transaction on Antennas and Propagation*, submitted for publication.
9. **T. Peter**, S. Reza, R. Nilavalan, S.W. Cheung, A. Vilches and H.F. AbuTarboush, "A Novel Transparent UWB Antenna for Energy Harvesting," *IEEE Transaction on Antennas and Propagation*, submitted for publication.

10. H.F. AbuTarboush, R. Nilavalan, **T. Peter** and S.W. Cheung, "Multiband Inverted-F Antenna with Independent Bands for Small and Slim Cellular Mobile Handsets," *IEEE Transactions on Antennas and Propagation*, vol.59, no.7, pp.2636-2645, July 2011.
11. H.F. Abutarboush, R. Nilavalan, S.W. Cheung, K.M. Nasr, **T. Peter**, D. Budimir and H. Al-Raweshidy, "A Reconfigurable Wideband and Multiband Antenna Using Dual-Patch Elements for Compact Wireless Devices," *IEEE Transactions on Antennas and Propagation*, vol.60, no.1, pp.36-43, Jan. 2012.

List of Figures

Figure 1.1	Comparison between FCC and European Commission Regulations for UWB.....	2
Figure 1.2	Compressing the Omni-directional radiation pattern as in (b) will increase the gain laterally thus allowing a reduction in power.....	3
Figure 1.3	Basic schematic of a rectifier.....	5
Figure 2.1	Schematic illustrating the construction of the optically transparent patch antenna. (a) Microstrip line feed, a=53 mm, b=37 mm, d=8 mm, w=2 mm. (b) Probe feed, a=9 mm, b=7 mm.....	12
Figure 2.2	Geometry of the microstrip dipole antenna.....	13
Figure 2.3	Photo of fabricated multilayer patch antenna.....	14
Figure 2.4	Comparison of measured and simulated return loss for multilayer patch antennas	14
Figure 2.5	Multilayer patch antenna and its assembly sequence. (a) Exploded 3D view showing the individual layers of the antenna. (b) Partially assembled antenna (without directors). (c) Complete assembled antenna (substrate and directors).....	14
Figure 2.6	A Tranztenna installed on the window pane of a military vehicle.....	15
Figure 2.7	Semi-transparent broadband antenna developed by NICT: (a) antenna with the ultra-fine elements of various lengths (b) antenna with ultra-fine elements of uniform lengths but with set breakpoints.....	16
Figure 2.8	(a) PIFA (b) Monopole antenna (c) Transparent radiator of the monopole antenna.....	17
Figure 2.9	Radiation efficiency for varied sheet resistivity.....	17
Figure 2.10	(a) The transparent uwb antenna (b) return loss measurements of the antenna.....	18
Figure 2.11	(a) RFID $\frac{1}{2}$ dipole antenna (b) RFID meandering dipole antenna.....	18
Figure 2.12	The copper trace mesh antenna fed through coupling.....	19
Figure 2.13	Transparent conductive oxide films used for sun shielding from harmful UV rays.....	22

Figure 2.14	The basic composition of a Dye Sensitive Solar Cell (DSSC) – Courtesy of Solar Print.....	23
Figure 2.15	Transparent antenna for installation on the inside of a car windshield...24	
Figure 2.16	Basic properties of AgHT.....	25
Figure 2.17	The Tranzenna mounted on the side window of a military jeep.....	26
Figure 2.18	Composite structure of the AgHT.....	33
Figure 2.19	Composite structure of a transparent electromagnetic absorber from TDK.....	36
Figure 3.1	A log periodic antenna (left) has a dispersive waveform (right).....	42
Figure 3.2	(a) Log Spiral Conical antennas (b) transmitted (left) and received (right) voltage waveform from a pair of conical log spiral antennas.....	43
Figure 3.3	An elliptical dipole (left) has a non-dispersive waveform (right).....	43
Figure 3.4	Geometry of the CPW-fed circular disc monopole.....	45
Figure 3.5	Overlapping of the multiple resonance modes.....	46
Figure 3.6	Planar type flexible antenna.....	47
Figure 3.7	Broadband T-shaped antenna.....	47
Figure 3.8	CPW-fed elliptical monopole UWB antenna.....	48
Figure 3.9	CPW-fed printed dipole UWB antenna with a SMA connector attachment showing the leakage blocking slots and the leakage currents.....	49
Figure 3.10	Transition from coplanar line to microstrip line.....	50
Figure 3.11	(a) Microstrip to CPW on GaAs chip substrate (b) Microstrip to CPW on opposite sides of a common substrate.....	51
Figure 3.11	(c) Microstrip to CPW transition on superposition of two different substrates.....	51
Figure 3.11	(d) Microstrip to CPW transition through electromagnetic coupling.....	52
Figure 3.11	(e) Microstrip to CPW transition through gradual transformation.....	52
Figure 3.11	(f) Microstrip to CPW transition through electromagnetic coupling.....	52

Figure 3.11	(g) Microstrip to CPW transition through electromagnetic coupling using radial stubs.....	53
Figure 3.11	(h) Microstrip to CPW transition through electromagnetic coupling using folded baluns.....	53
Figure 3.12	(a) Attachment of a radiating stub to implement a band notch.....	55
Figure 3.12	(b) A tuning stub approach to effect a band notch.....	55
Figure 3.12	(c) Use of filter to give a band notch.....	56
Figure 3.12	(d) Band notch through inclusion of parasitic patches.....	56
Figure 3.12	(e) Meandered lines being used to create band notches for the unwanted frequencies.....	56
Figure 3.12	(f) Use of grounded stubs to achieve a band notch.....	57
Figure 4.1	Selection of the project template for creating the MTA design project..	63
Figure 4.2	Creating the AgHT-8 conducting material.....	64
Figure 4.3	Creating the PET material.....	64
Figure 4.4	Loss tangent dispersion list to reflect the losses in the PET.....	65
Figure 4.5	The created MTA design using the new material properties that were uploaded.....	65
Figure 4.6	(a) Creation of waveguide port (b) Activating monitors to show farfield results.....	66
Figure 4.7	Activating postprocessing steps to tabulate into graphs.....	67
Figure 4.8	Final design of the MTA to be simulated using the transient solver.....	67
Figure 4.9	Geometry of the designed MTA illustrating the various parts of the antenna.....	68
Figure 4.10	Geometry of the optimized MTA design with inset showing the resonators for impedance matching.....	68
Figure 4.11	Simulated results for the MTA: (a) return loss (b) gain (c) efficiency; 3-D radiation patterns at (d) 5 GHz (e) 7 GHz.....	69
Figure 4.12	3D Layout showing the two-layered structure of the antenna.....	70
Figure 4.13	(a) Layout of the two-layered antenna (b) prototype of the antenna.....	70

Figure 4.14	Resonator dimensions.....	71
Figure 4.15	Maximum bend angle recommended for antennas smaller than 30 mm.....	72
Figure 4.16	(a) AgHT antenna being flexed through the various radius of curvatures (b) return loss of the antenna for the various radius of curvatures.....	72
Figure 4.17	(a) Copper film antenna being flexed through the various radius of curvatures (b) return loss of the antenna for the various radius of curvatures.....	74
Figure 4.18	Geometry of antenna directly inscribed onto the AgHT film.....	75
Figure 4.19	(Left) Antenna with the coating removed. (Right) Antenna after application of the conductive silver paint.....	75
Figure 4.20	Measured gain of the new silver base technique in comparison to three other soldering techniques.....	77
Figure 4.21	Measured efficiency of new silver base technique in comparison to three other soldering techniques.....	77
Figure 4.22	The Star Lab antenna measurement equipment at HKU, Hong Kong....	78
Figure 4.23	MTA undergoing measurement on the Star Lab.....	78
Figure 4.24	Dimensions of the modified KHA.....	79
Figure 4.25	(a) Layout (b) prototype of transparent UWB antenna with slots for notch tuning.....	79
Figure 4.26	Simulated and measured reflection coefficients of the antenna with slots for notch tuning tuned at 5 GHz. The measured return loss without notch is given for comparison.....	80
Figure 4.27	Simulated and measured gain.....	81
Figure 4.28	Simulated and measured efficiency.....	81
Figure 4.29	Measured 3-D radiation patterns of antenna: (a) 3 GHz (b) 5 GHz (c) 7 GHz (d) 9 GHz.....	82
Figure 4.30	H and E plane arrangements of the antennas.....	83
Figure 4.31	Simulated and measured S ₂₁ of a 2x1 CTSA array placed a) face to face b) face to side c) side to side orientation at 150mm spacing.....	84

Figure 4.32	Simulation measurement set-up. Plane polarization set by setting the E-theta or E-phi component in the monostatic RCS calculation dialog box.....	88
Figure 4.33	Simulated Antenna Mode RCS of the mushroom top antenna for plane wave polarization in E-theta plane.....	88
Figure 4.34	Simulated Structural Mode RCS of the mushroom top antenna for plane wave polarization in E-theta plane.....	89
Figure 5.1	Dimension, geometry and prototype of the transparent TSA.....	94
Figure 5.2	Measurement set-up in the anechoic chamber for the heart (a), chest (b), and belly (c) on-body area tests.....	95
Figure 5.3	Simulated and measured return loss of the antennas in free space.....	95
Figure 5.4	On-body measured reflection coefficient of the TRTSA and TSA on heart (a), chest (b) and belly (c).....	96
Figure 5.5	Measured gain of the antenna in free space and on-body (chest location) in the X-Y plane at QMUL. This is not the maximum gain but the highest measured gain along the X-Y plane.....	97
Figure 5.6	Simulated and measured free space radiation patterns in the X-Y plane: simulated (a) – (b) and measured (c) – (d).....	98
Figure 5.7	Simulated and measured radiation patterns on-body (chest location) in the X-Y plane: simulated (a) – (b) and measured (c) – (d).....	99
Figure 5.8	The time domain signal synthesized from the frequency domain.....	100
Figure 5.9	Received time-domain signals for a pair of transparent UWB tapered slot antennas in different configurations on the body.....	103
Figure 5.10	Fidelity factor for the antennas on-body.....	104
Figure 5.11	Fidelity factor for the antennas in free space in the FF, FS and SS configurations.....	105
Figure 5.12	Fidelity factor in the SS configuration at 11 cm spacing on-body compared to that of free space.....	105
Figure 5.13	(a) Transparent UWB MTA tested on a military outfit (b) measured return loss of the antenna on military attire compared to free space.....	106
Figure 6.1	Microstrip patch antenna calculator from emtalk.com.....	110

Figure 6.2	(a) Patch antenna after being tuned with feed insets for impedance match and (b) return loss of the patch resonating at 2.4 GHz.....	111
Figure 6.3	Measured value of the fabricated patch on the 2mm glass for the dielectric value of 5.9.....	112
Figure 6.4	(a) Scale down of antenna dimensions to compensate for increase in dielectric of glass from 3.228 to 5.7 and (b) parametric study to obtain the optimized dimensions.....	114
Figure 6.5	(a) Isometric view of the quick end launchers and (b) illustration of the snap on clip that provides tension to hold the connector to a pcb (c) demonstration of ease of mounting onto a pcb.....	115
Figure 6.6	Simulated and measured return loss of the TRTSA on a 2 mm glass substrate.....	116
Figure 6.7	Measured gain of the TRTSA on 2 mm glass substrate.....	117
Figure 6.8	Measured efficiency of the TRTSA on 2 mm glass substrate.....	117
Figure 6.9	Simulated and measured return loss of the antenna on a 4 mm glass substrate.....	118
Figure 6.10	Measured gain of the antenna on 4 mm glass substrate using Star Lab.....	118
Figure 6.11	Measured efficiency of the antenna on 4 mm glass substrate using Star Lab.....	118
Figure 6.12	Comparison of the measured TRTSA gain: on-glass (substrate) vs free space.....	119
Figure 6.13	Comparison of the measured TRTSA efficiency: on-glass substrate vs free space.....	119
Figure 6.14	Measurement set-up for the UWB video transmission test.....	121
Figure 6.15	(a) Direction of the maximum and minimum transmission ranges of the antennas on the 2 mm and 4 mm glass substrate (b) simulated farfield power pattern showing energy refocused to behind glass at 7 GHz.....	122
Figure 6.16	3-D Farfield radiation plot at 7 Ghz (linear scaling) showing radiation intensity behind glass is greater than in front.....	123
Figure 6.17	Comparison of return loss at 7 GHz.....	123
Figure 6.18	Comparison of gain at 7 GHz.....	124
Figure 6.19	Comparison of energy patterns at 7 GHz.....	124

Figure 6.20	Optimizing return loss at 7 GHz through descaling antenna structure by 60% in x-axis and 70% in y-axis in CST.....	125
Figure 6.21	Tuning of antenna for optimum return loss response through scaling and descaling of antenna structure in x and y axis.....	125
Figure 6.22	Gain optimized for 7 GHz using CTSA geometry (grid lines included for clarity) on 2mm glass substrate.....	126
Figure 6.23	(a) The CTSA mounted on 2 mm glass substrate and connected to the A/V Link Extender's transmitter (b) measurement set-up for the wireless transmission using the CTSA on the 2 mm glass substrate.....	127
Figure 6.24	Non-conducting AgHT border to suppress surface waves.....	128
Figure 6.25	Ribbon feed contact for antenna on glass superstrate.....	129
Figure 6.26	Simulated return loss of the TRTSA on a 2 mm glass substrate with a 2 mm glass superstrate.....	130
Figure 6.27	Simulated gain of the TRTSA sandwiched between 2 mm glass superstrate and substrate compared to the TRTSA in free space and on a 2 mm glass substrate.....	131
Figure 6.28	Simulated efficiency of the TRTSA sandwiched between 2 mm glass superstrate and substrate compared to the TRTSA in free space and on a 2 mm glass substrate.....	131
Figure 6.29	Simulated radiation power patterns (linear scaling) of the antennas for 3 GHz, 5 GHz, 7 GHz and 10 GHz.....	134
Figure 6.30	Simulated refraction of microwaves through the 2 mm glass substrate of the TRTSA.....	135
Figure 7.1	The TG35 self-powered radio antenna uses a solar pack to harvest energy to power it.....	140
Figure 7.2	The solar ray collector.....	141
Figure 7.3	Prototype and layout of the aperture coupled antenna with solar cell..	142
Figure 7.4	(a) Basic working principle of the solar antenna (b) the antenna design layout	143
Figure 7.5	Layout of the solar antenna geometry.....	143
Figure 7.6	Isometric view of a small satellite with mesh antennas integrated onto solar panels.....	144

Figure 7.7	The 900 MHz E-pHEMT rectenna.....	146
Figure 7.8	Frequency independent spiral rectenna prototype.....	147
Figure 7.9	Geometry of the integrated rectenna with a broadband stub band-pass filter.....	148
Figure 7.10	Simulated gain of SP73 antenna with different dielectrics in emboss vs P73.....	149
Figure 7.11	(a) Ground plane-SP73 (b) Embossed antenna-SP73 (c) Planar antenna-P73.....	149
Figure 7.12	Layered structure of the amorphous solar cell.....	150
Figure 7.13	Prototype, geometry and dimensions of the CTSA in free space.....	151
Figure 7.14	Simulated and measured return loss of the AgHT-4 CTSA in free space.....	151
Figure 7.15	Simulated and measured gain of the CTSA in free space.....	152
Figure 7.16	Measured radiation pattern of the CTSA in free space.....	152
Figure 7.17	(a) CST model of the a-Si solar cell (b) exploded view of the structure of the CTSA place between a glass superstrate and an a-Si solar panel.....	153
Figure 7.18	Simulated and measured return loss of the CTSA on the a-Si solar panel without a superstrate.....	154
Figure 7.19	Simulated and measured gain of the CTSA on the a-Si solar panel without a superstrate. Free space results included for comparison.....	154
Figure 7.20	Measured radiation pattern of the CTSA on the a-Si solar panel substrate.....	155
Figure 7.21	The CTSA with a 2 mm glass superstrate on an a-Si solar panel in the Star Lab antenna measurement chamber.....	156
Figure 7.22	Simulated and measured return loss of the CTSA on the a-Si solar panel with a 2 mm glass superstrate. Free space and without glass superstrate results given for comparison.....	157
Figure 7.23	Simulated and measured gain of the CTSA on the a-Si solar panel with a 2mm glass superstrate. Free space and without glass superstrate results given for comparison.....	157
Figure 7.24	Simulated 3-D radiation patterns for the CTSA on a-Si solar panel with a 2 mm glass superstrate.....	158

Figure 7.25 Measured radiation patterns for the CTSA on a-Si solar panel with a 2 mm glass superstrate. Free space and without glass superstrate results given for comparison.....	158
Figure 7.26 (a) The 2.55 GHz rectenna (b) rectenna components (CTSA + rectifier) (c) equivalent circuit of rectifier.....	160
Figure 7.27 Peak return loss response of the rectifier circuit.....	161
Figure 7.28 Comparison of output voltage with different loads at 2.53 GHz and 2.51 GHz operating frequency for input power of 10 dBm for the rectenna in free space..	162
Figure 7.29 Measurement set-up for the CTSA rectenna (left) with diagrammatic representation (right).....	163
Figure 7.30 Output power of CTSA rectenna versus input power on a 50 Ω and 100 Ω load at 2.51 GHz and 2.53 GHz.....	165
Figure 7.31 Rectenna system efficiency at 2.51 GHz and 2.53 GHz at 50 Ω and 100 Ω load.....	165
Figure 7.32 Prototype of CTSA on a 2 mm glass substrate with geometry and dimensions.....	166
Figure 7.33 Simulated and measured return loss of the CTSA on a 2 mm glass substrate with the measured free space return loss given for comparison	167
Figure 7.34 Measured gain of the CTSA antenna on a 2 mm glass with inset showing a close-up view from 2.4 GHz to 2.6 GHz. The measured free space gain given for comparison.....	167
Figure 7.35 Output voltage optimum at 2.57 GHz for both 50 Ω and 100 Ω load at 10 dBm on the 2 mm glass substrate (b) the output voltage for the rectenna in free space shown in comparison.....	168
Figure 7.36 Output voltage versus distance for a 10 dBm signal input on a 2 mm glass substrate (b) the free space output voltage versus distance shown in comparison.....	169
Figure 8.1 Putting solar energy to use: Drive communications system & harvest energy to power building.....	177
Figure 8.2 (a) SkyTech Flat KU Dish Antenna (b) Picture of a solar panel and the proposed flat dish integrated solar panel for future work.....	178

List of Tables

Table 1-1 Restrictions to EC Ultra-Wide Band Spectrum Allocation.....	2
Table 2-1 Order of Conductivity (electron concentration) and Transparency of TCOs.....	28
Table 2-2 Deposition Temperature of TCOs.....	30
Table 2-3 Etchants for TCOs.....	32
Table 6-1 Measured video transmission range on AV Link Transmitter.....	122
Table 7-1 Dimensions of the antenna	151
Table 7-2 Output voltage of rectifier versus frequency for -30 dBm.....	161
Table 7-3 Output voltage of rectenna system versus frequency for -30 dBm input power	162
Table 7-4 Dimensions of the antenna geometry on a 2mm glass with $\epsilon_r = 5.7$	166

Abbreviations

Ag	silver
Al	aluminium
AP	access point
a-Si	amorphous silicon
Au	gold
AWGN	additive white gaussian noise
BW	bandwidth
Cu	copper
CPW	coplanar waveguide
CTSA	cone top tapered slot antenna
DOE	design of experiment
DSSC	dye sensitive solar cell
DSRC	dedicated short range communication
EC	European Commission
EIRP	equivalent isotropically radiated power
EL	electroluminescence
EM	electromagnetic
EMC	electromagnetic compatibility
ETC	electronic toll collection
FCC	Federal Communications Commission
FDTD	finite-difference time-domain
FPD	flat panel display
GPS	global positioning system

GT	gain of transmitter
HKU	Hong Kong University
KHA	knight helm antenna
LCP	liquid crystal polymer
IR	impulse radio
ISM	industrial, scientific and medical
ITO	indium tin oxide
MB-OFDM	multi-band orthogonal frequency division multiplexing
MHz	mega hertz
MIMO	multi-input multi-output
MoM	method of moments
MTA	mushroom top antenna
NASA	national aeronautics and space agency
OFDM	orthogonal frequency division multiplexing
PA	power amplifier
PCB	printed circuit board
PET	polyethylene terephthalate
PT	power transmitted
QEL	quick end launchers
QMUL	Queen Mary University of London
QPSK	quadrature phase shift keying
RAM	radar absorbing material
RCS	radar cross-section scattering
RF	radio frequency
RFI	radio frequency interference

RFID	radio frequency identification
SMA	submissive version A
SNR	signal to noise ratio
SRR	split ring resonator
TCO	transparent conductive oxide
TE	transverse electric
TEM	transverse electromagnetic
TM	transverse magnetic
TRTSA	transparent tapered slot antenna
TSA	tapered slot antenna
UOF	UWB over fibre
UTM	University Technology Malaysia
UWB	ultra-wideband
VNA	vector network analyser
VLТ	visible light transmission
Wi-Fi	wireless fidelity
WLAN	wireless area network
WPANs	wireless personal area network

Author's Declaration

The work described in this thesis has not been previously submitted for a degree in this or any other university and unless otherwise referenced it is the author's own work.

Statement of Copyright

The copyright of this thesis rests with the author. No quotation from it should be published without his prior written consent and information derived from it should be acknowledged.

CHAPTER 1

Introduction

1.1 Motivations

Ultra-Wideband (UWB) is a new technology from a commercial or civilian viewpoint. In actual it is an old technology with a new lease of life. Long used by the U.S. military, in February 2002 the FCC approved the commercial implementation of UWB, within limits [1]. However, UWB was only legalised in the European Union at the start of 2007.

The European Commission (EC) detailed the licensing regulations for ultra-wideband networking in Europe, albeit some restrictions that were lifted in early 2008. The EC had chosen to make use of only part of the spectrum that was approved for use in the US in 2002. The equivalent isotropic radiated power (EIRP) value of -41.3 dBm/MHz which was denoted as the ‘magic figure’ was to be applied over the 6.0 to 8.5-GHz frequency range whereas in the United States the FCC applied this over a broader spectrum from a much lower frequency. The same power was also to be applied provisionally until the end of 2010 in the 4.2 to 4.8-GHz range. In the other bands there were to be more restrictive limits (see Table 1-1 [2-3] and Figure 1.1).

These power limits were essentially compromises, an agreement struck between those who wanted UWB to be introduced with characteristics rather closer to the US regulations and those that felt other radio users needed greater protection. In essence, it was essentially an annex in the EC decision providing a compromise which was believed to be sufficient to trigger a market in the European Union for UWB at the beginning.

Table 1-1 Restrictions to EC Ultra-Wide Band Spectrum Allocation

Restrictions apply to EC ultra-wide band spectrum allocation The isotropic radiated power (EIRP) of UWB devices are strictly regulated		
Frequency range (GHz)	Maximum mean EIRP density (dBm/MHz)	Maximum peak EIRP density (dBm/50 MHz)
Below 1,6	-90,0	-50,0
1,6 to 3,4	-85,0	-45,0
3,4 to 3,8	-85,0	-45,0
3,8 to 4,2	-70,0	-30,0
4,2 to 4,8	-11,3 (until December 31, 2010)	0,0 (until December 31, 2010)
	-70,0 (beyond December 31, 2010)	-30,0 (beyond December 31, 2010)
4,8 to 6,0	-70,0	-30,0
6,0 to 8,5	-41,3	0,0
8,5 to 10,6	-65,0	-25,0
Above 10,6	-85,0	-45,0

Source: European Commission, Radio Spectrum Policy Unit

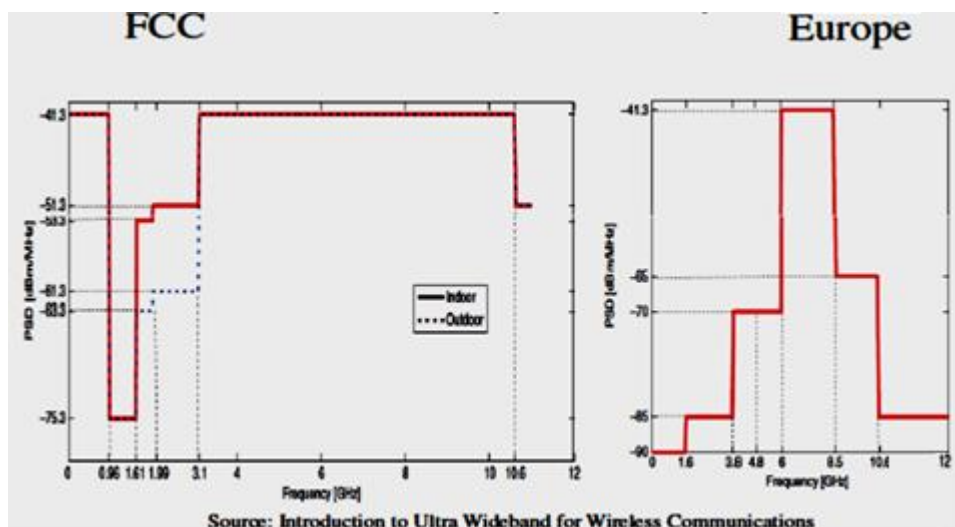


Figure 1.1 Comparison between FCC and European Commission Regulations for UWB.

UWB has three basic areas of applications which are communication, positioning and imaging. The main commercial application will be for communication since it has very high data transfer rate for short distance currently. Research is however, on-going to further the distance to diversify its range of applications. The maximum achievable data rate or capacity for the ideal band-limited additive white Gaussian noise (AWGN) channel is related to the

bandwidth and signal-to-noise ratio (SNR) by Shannon-Nyquist criterion [4-5] as shown in Equation 1.1.

$$C = B \log_2 (1 + SNR) \quad \text{Eqn (1.1)}$$

where C denotes the maximum transmit data rate, B stands for the channel bandwidth.

Equation 1.1 indicates that the transmit data rate can be increased by increasing the bandwidth occupation, transmission power or reducing the SNR as much as possible. However, the transmission power cannot be readily increased because many portable devices are battery powered and the potential difference should be avoided. Thus a large frequency bandwidth will be one of the solutions to achieve high data rate. Research on reducing the SNR is being actively pursued by those involved in channel capacity and range improvement. In regard to channel capacity, Multiband Orthogonal Frequency Division Multiplexing (MB-OFDM) seems to be the key area of interest. In recent times, active research on range improvement applying green approaches like improving the gain of the UWB antenna to improve range with power consumption kept constant or further reducing the power consumed with a compromise on the range improved is seriously being pursued using innovative UWB antenna designs. However, due to the fact that UWB regulations stipulate EIRP should not exceed the regulated levels and EIRP is $P_T G_T$ i.e. power transmitted (P_T) x gain of transmitter (G_T), increasing the gain while keeping the power constant will increase EIRP and hence would violate the regulation. As such the research in this area has been confined to the latter that is, improving the gain with an aim to reduce power to go green [6]. One way to do that would be to laterally compress the Omni-directional radiation pattern as shown in Figure 1.2. This would increase the gain laterally while allowing the power to be reduced to maintain EIRP at the regulated levels (Figure 1.1)

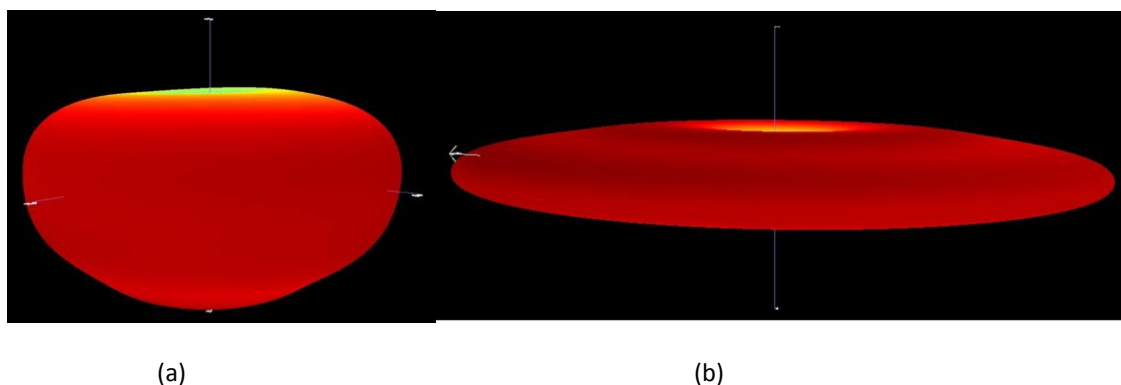


Figure 1.2 Compressing the omni-directional radiation pattern laterally as in (b) will increase the gain laterally thus allowing a reduction in power.

Besides communication, it can also be used for indoor and outdoor 3-D positioning. Another important application is imaging like microwave remote sensing. A UWB sensor can pass through doors and walls and hence detect the objects inside the room.

The research presented in this thesis, however, is motivated by the introduction of another area of recent research focus which also opens up a new avenue for UWB application namely, stealth and energy harvesting.

1.1.1 Stealth:

The National Aeronautics and Space Agency (NASA) first experimented on transparent antennas to look into applications for covert and discreet applications in the late nineties [7]. There has been a wide gap in time since then, when researchers finally took the challenge to make them available for UWB technology with the lifting of the restrictions for UWB networking in Europe in 2008. One of the first material used for this research by NASA is the patented AgHT-8 [7], the first of the two variants of the AgHT performance film trademark which is essentially a transparent electrically conductive film made of silver sandwiched between two layers of tin oxide. Since then, others have used semiconducting oxides of indium, zinc and cadmium and metals such as gold and titanium nitride. A figure of merit for these transparent conductors is the ratio of the electrical conductivity to the optical absorption coefficient of the film [8]. The lower the resistivity, higher the conductivity of the film must be but with a compromise on transparency. Antennas developed so far have shown to have improved gain by virtue of having a glass substrate or superstrate as an RF lens. However, for a film antenna in cellular, wearable and other non-glass applications where discreteness is warranted, a single transparent antenna with improved gain and efficiency is needed.

1.1.2 Energy Harvesting:

Energy harvesting is made possible through the development and use of the optical transparency and as well as the gain of the conductive layer of the flexible polymer antennas. Transparent antennas that allow a high transmittance of visible light both ambient and solar have become good candidates for integration onto solar cells for energy generation and

harvesting. Previously, the solar cells were mounted onto the top of a typical antenna patch or array but with the advent of transparent antennas, the solar cells or films are being integrated behind the see-through antenna [9]. Current research focus in the solar fraternity is to develop transparent solar films. As for now, only New Energy Technologies [10] has succeeded in developing a workable prototype through collaboration with the University of South Florida. This advanced Dye Sensitive Solar Cell (DSSC) prototype was demonstrated in February of 2011 over the web. Solutia, a key developer and producer of performance films is teaming up with Brunel University in collaboration with the University of Hong Kong and the University Technology Malaysia with the prospect of a similar transparent solar film. Such films can be applied as an additional film layer laminate on the back of the transparent antennas as an integrated wireless-cum-energy harvesting solution in homes, office and industrial buildings. With such intense focus to develop such solutions as part of the green technology revolution, the need for high gain and efficient transparent antennas both for narrowband and wideband application is in ever more urgent demand. Improvement of the gain also improves reception which then could aid the antenna to be used as rectennas in harvesting free energy through converting the electromagnetic energy received and rectifying them from ac to dc [10-12] for domestic and industrial use to complement the already harvested solar energy. As glass space in homes and buildings are ample, multiple antennas or arrays could be implemented to increase the harvest through consolidation of the electromagnetic energy. Figure 1.3 shows a generic circuit schematic of a rectenna which is basically a rectifier circuit connected to an antenna.

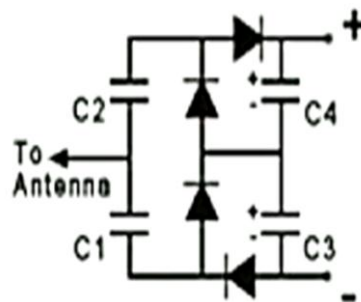


Figure 1.3 Basic schematic of a rectifier.

1.2 Aim and Objectives

The aim of the research presented in this thesis was to develop optically transparent UWB antennas for wireless applications and energy harvesting.

The objectives are:

- study the characteristics of the commercially available transparent conductive polymers such as AgHT from Solutia Inc. and how to apply the knowledge in transparent antenna design.
- develop a transparent UWB antenna with good gain and efficiency for UWB wireless applications through different geometries and improved feed connection.
- integration of transparent UWB antennas with solar panels for solar energy harvesting, and with rectifiers as a rectenna to harvest RF energy.

1.3 Contribution to Knowledge

The various chapters of the thesis aim to highlight the five contributions made towards the advancement and development of the transparent UWB antennas for their application in the area of stealth and energy harvesting.

The key contributions are summarized as follows:

- A method to improve the SMA to antenna connection [12].*

A method was introduced to improve the SMA to antenna connection. Improvement was demonstrated through enhancement of gain and efficiency. The proposed method also reinforced the colder solder bond connecting the SMA and antenna.

ii. Analysis of coupling, sensitiveness to proximity and radar cross section characteristics of transparent antennas.

- Insentiveness due to proximity interference was analysed and found to be due to the low conductivity of the AgHT material.
- Coupling – UWB antennas made from different materials of AgHT, Copper on a PET (CuPET) substrate and Copper on a Rogers substrate were compared. The coupling was quantified through simulation and experiment. The results showed antennas made from AgHT and a mixed array of AgHT and CuPET/Rogers demonstrated low coupling.
- RCS – The RCS of AgHT, CuPET and Rogers UWB antennas were compared and their response quantified.

iii. Analysis of transparent antennas for body centric applications [13].

The performance of a transparent UWB antenna made from AgHT was compared against that of an antenna made from copper on a Duroid substrate on body. The analysis showed that the AgHT antenna's gain on body did not vary much compared to its free space gain which was not the case for the Duroid antenna. The AgHT antenna also demonstrated better coverage than its comparison.

iv. Analysis of transparent antennas on glass structures.

Analysis of a transparent UWB antenna on glass in the substrate, and in the superstrate/substrate sandwich configuration was carried out. It was observed that the gain of the antenna improved for some frequencies by redirecting the radiated power.

v. Development of a novel antenna for integration of solar panels and RF energy harvesting [11].

A transparent UWB antenna was developed on AgHT for integration to solar panels and for RF energy harvesting as a rectenna. The integration was achieved by placing the antenna on a amorphous silicon solar panel with a glass superstrate. The integrated antenna demonstrated that is was able to maintain an omni-directional pattern. The

antenna when connected to a rectifier was able to harvest RF energy and output it as dc voltage.

1.4 Thesis Structure

The thesis spans eight chapters and covers the research works carried out in achieving the aim and objectives spelled out earlier in section 1.2.

Chapter 1, as just seen gives a brief introduction into the motivations, aim and objectives behind this PhD research work. It also briefly highlights the contributions made to the development of transparent UWB antennas for wireless communication and energy harvesting.

Chapter 2 presents the literature review followed by a development review of transparent conductive oxides and their characteristic properties. Why ITO is not available on polymer at such low resistivity as that of AgHT on polymer is also highlighted and explained.

Chapter 3 meanwhile gives a background on the characteristics of non-transparent UWB antennas from which the knowledge base to design the transparent UWB antennas was attained and built upon.

Chapter 4 covers the transparent UWB antennas developed in the course of writing this thesis. The various antennas designed and published are discussed in depth in regard to the simulation and experimental challenges that were encountered and overcome as well as the contributions. The contribution on gain and efficiency improvement of transparent antennas built from transparent conductive oxides and analysis on the coupling, sensitivity to proximity and radar absorbing material (RAM) properties of the AgHT antennas are presented in this chapter.

Chapter 5 is a short chapter that introduces the analysis done using the transparent tapered slot antenna for body-centric applications. Signal fidelity of the transmitted and received signal in the time domain is also analysed and presented. Experimental measurements done on a human subject is also presented.

Chapter 6 gives an insight into the practical application of the transparent polymer UWB antenna when it is actually mounted on to glass, as well as the resulting effects of the glass on the performance of the antenna. The use of the antenna and the modifications required for its application on a glass substrate or in a superstrate/substrate sandwich configuration is discussed and presented.

Chapter 7 introduces the use of the transparent UWB antenna in green applications where it is incorporated in between glass and solar cells to provide a 3-in-1 solution for buildings and home applications. The development of a novel transparent UWB antenna for integration onto amorphous silicon solar panels, and also as a rectenna to harvest ambient RF energy is presented.

Finally, Chapter 8 summarizes and concludes the research work and provides insight into future development by modifying the existing antennas for use in Green Technology Buildings to harvest energy besides providing wireless communication.

1.5 References:

- 1) FCC, First Report and Order 02-48, February 2002.
- 2) Europe approves UWB regulations. [Online]. Available: <http://eetimes.eu/197800214>.
- 3) Europe finally homing in on Ultra Wideband. [Online]. Available: <http://eetimes.eu/197008300>.
- 4) J.G. Proakis, "Digital Communications", New York: McGraw-Hill, 1989.
- 5) C.E. Shannon, "A Mathematical Theory of Communication", *Bell Syst. Tech. J.*, vol.27, pp. 379-423, 623-656, July & October 1948.
- 6) T. Peter, R. Nilavalan, H.F. AbuTarboush, S.W. Cheung and Y.F. Weng, "Investigative Study on the Development of a Green UWB Antenna", International Symposium on Antennas and Propagation in 2010 (ISAP 2010).
- 7) R.N. Simons and R.Q. Lee, "Feasibility Study of Optically Transparent Microstrip Patch Antenna" International Symposium and Radio Science Meeting cosponsored by IEEE, AP-S, and U.R.S.I., Montreal, Canada, July 13-18, 1997.
- 8) R. G. Gordon, "Criteria for Choosing Transparent Conductors," *MRS Bulletin*, vol. 25, pp. 52-57, August 2000.
- 9) T. Peter, Y.Y. Sun, T.I. Yuk, H.F. AbuTarboush, R. Nilavalan and S.W. Cheung, "Miniature transparent UWB antenna with tunable notch for green wireless applications," International Workshop on Antenna Technology (iWAT), 2011, pp.259-262, 7-9 March 2011.
- 10) Transparent Solar Window. [Online]. Available: www.newenergytechnologiesinc.com
- 11) T. Peter, S. Reza, R. Nilavalan, S.W. Cheung and A. Vilches, "A Novel Transparent UWB Antenna for Energy Harvesting," *IEEE Transaction on Antennas and Propagation*, submitted for publication.
- 12) T. Peter, R. Nilavalan, H.F. AbuTarboush and S.W. Cheung, "A Novel Technique and Soldering Method to Improve Performance of Transparent Polymer Antennas," *IEEE Antennas and Wireless Propagation Letters*, vol.9, pp.918-921, 2010.
- 13) T. Peter, R. Nilavalan, R. DiBari, A. Alomainy, S.W. Cheung and A.R. Tharek, "Analysis of Transparent UWB Antennas for Body-Centric Applications", *Piers*, submitted for publication.

Chapter 2

Transparent Antennas: A Literature Review, Material Development and Properties of Transparent Conductive Oxides

2.1 Introduction

With the search for discreetness and covertness in the field of wireless communications, transparent antennas have been researched on since 1997 [1]. The next section provides a literature review in the form of a chronological review of the research, related issues and progress that has taken place since then till today. This is then followed by a material development review and a detailed analysis of the characteristics and properties of transparent conductive oxides.

2.2 Literature Review

The first study on transparent antenna was presented by the National Aeronautics and Space Agency (NASA) in 1997 when its researchers, Simmons and Lee demonstrated the use of AgHT-8 to produce single patch antennas to operate at 2.3 GHz and 9.5 GHz [1]. Figure 2.1 shows the two antennas that they presented. The structures had Plexiglass as a support for the microstrip feed antenna and an aluminium plate for the probe feed antenna. Both these antennas had a high profile and were not structurally rigid on their own. As they were

designed for narrow band frequencies, the ground for both antennas was provided through an additional layer of AgHT-8.

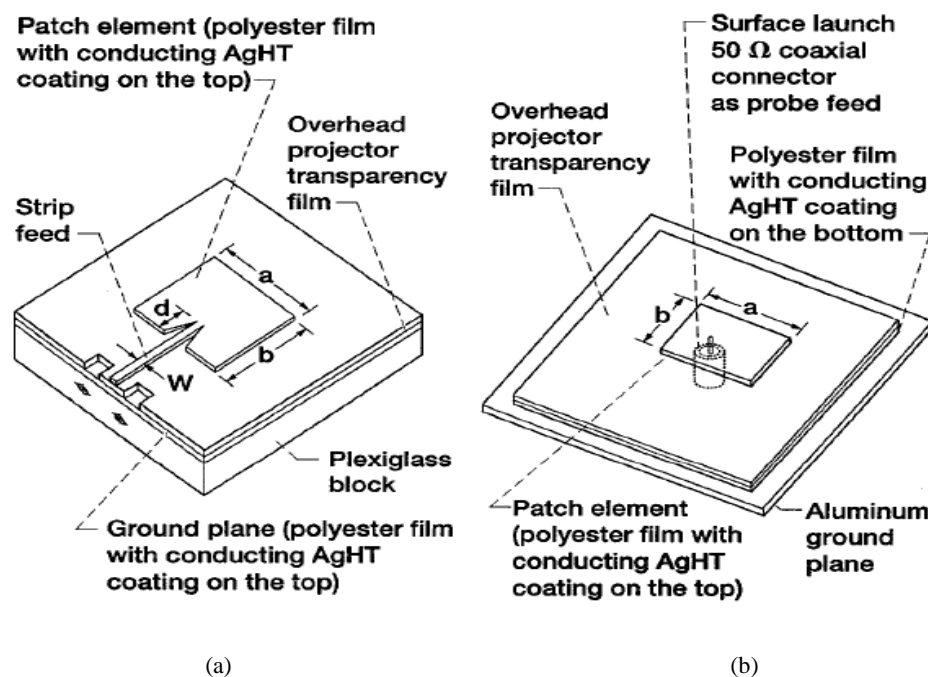


Figure 2.1 Schematic illustrating the construction of the optically transparent patch antenna (a) Microstrip line feed, $a=53$ mm, $b=37$ mm, $d=8$ mm, $w=2$ mm (b) Probe feed, $a=9$ mm, $b=7$ mm [1].

Since then, others followed suit by using AgHT-8 or its variant AgHT-4, and also other materials like Indium Tin Oxide (ITO) and Aluminium doped Zinc Oxide to name a few, to design and produce workable antennas. Except for those produced using ITO or AgHT, most of the so-called transparent antennas are simply antennas constructed by coating transparent polymer substrates with non-transparent conductive traces of silver or other conductive ink. Such kind of transparent antennas cannot be really categorized as fully transparent antennas since the traces are visible to the naked eye. What are construed as transparent antennas in this thesis are those that are fully transparent, in other words, even the conductive traces are transparent and discreet to the naked eye.

However, for the purpose of recording down the chronological development of these transparent antennas be it fully or partially transparent as part of this literature review, both are listed and the works done or published are highlighted as comparison to the research undertaken in this thesis study.

Work on transparent antennas again resurfaced in 2000 when Mias et al [2] published their paper on “Optically Transparent Microstrip Antennas”. Basically, it was a feasibility study on the performance of antennas made from different transparent conductors. The performance of a dipole antenna as shown in Fig. 2.2 was compared using different materials like aluminium (Al), copper (Cu), silver (Ag), gold (Au) and ITO. The study was to compare how good the ITO trace performed against the other conductive traces that made up the dipole on a transparent glass substrate. The designed transparent antennas were compared to conventional copper-based antennas and an antenna made from non-transparent thin film aluminium. How transparent the coatings of the conductive traces were, depended on its thickness. The dipole antennas were situated on a glass substrate of thickness, $t = 0.7$ mm and a relative permittivity and loss tangent at 1MHz of 5.84 and 0.001 respectively. Deposition, cut and paste and etching techniques were used to fabricate the various antennas in their paper. Their study concluded that transparent coatings of especially, gold and silver have the potential to be is used in antenna production.

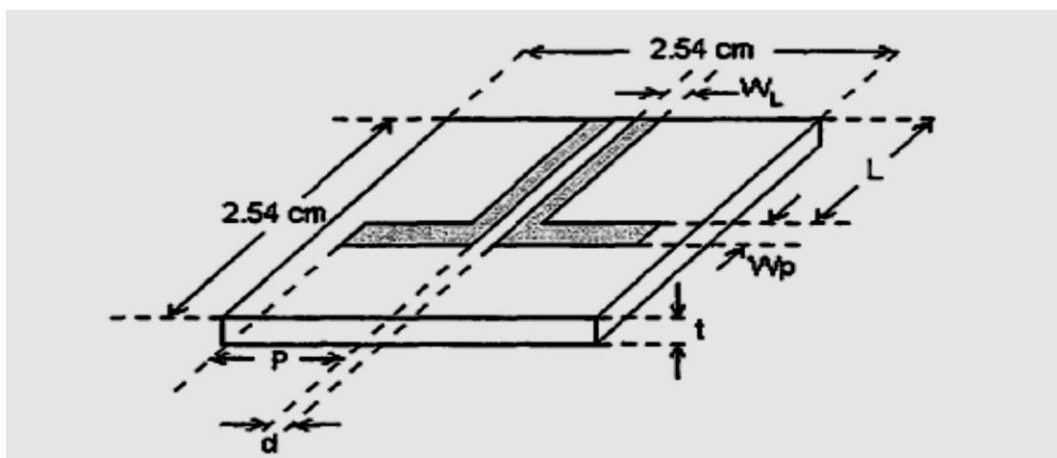
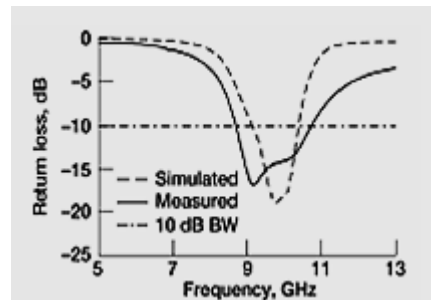
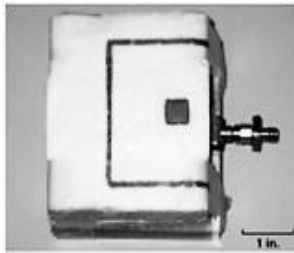


Figure. 2.2 Geometry of the microstrip dipole antenna [2].

In 2005, after a lapse of eight years, NASA engineers Nessel et al [3] demonstrated a transparent “X-band Multi-Layer Yagi like Microstrip Antenna with High Directivity and Large Bandwidth” using AgHT-8. Figures. 2.3 to 2.5 summarizes their work. Jessel et al basically pointed out although patch antennas are low profile and low cost with ease of solid state integration, they are limited by their inherently narrow bandwidths and low directivity.



Figure\ 2.3 Photo of fabricated multilayer patch antenna [3]. Figure 2.4 Comparison of measured and simulated return loss for multilayer patch antennas [3].

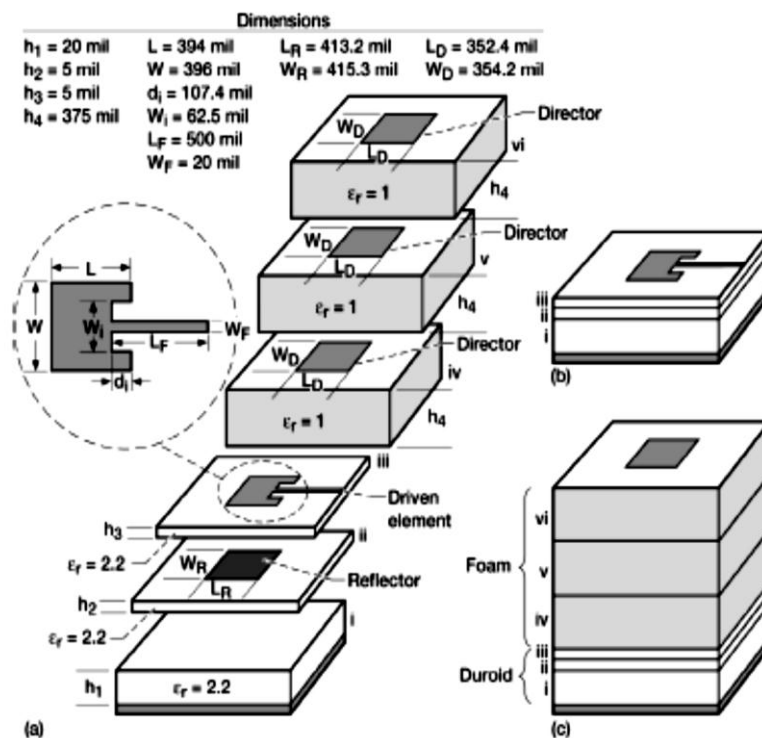


Figure 2.5 Multiplayer patch antenna and its assembly sequence. (a) Exploded 3D view showing the individual layers of the antenna (b) partially assembled antenna (without directors) (c) complete assembled antenna (substrate and directors) [3].

Although there were attempts by earlier researchers to overcome these deficiencies through shorting walls, shaped slots, and electromagnetically coupled patches to achieve a larger bandwidth; and higher directivities with parasitic patches or high permittivity substrates, the attempts were focused on either the bandwidth or the directivity that is, only one aspect was focused on at a time. The NASA engineers in this paper, attempted to demonstrate an improvement in both parameters simultaneously to increase the versatility of the patch

antenna. These antennas were developed basically for satellite and space exploration in mind and not for compact and versatile terrestrial application devices where a low and slim profile would be much preferred.

Subsequently, the following year Dr Cohen's team from Fractal Antenna Systems, Inc. produced a commercially viable multiband transparent antenna, Tranztenna (TM) shown in Figure 2.6, which incorporated their company's patented fractal antenna technology in an optically transparent film that can be placed on a building or a vehicle [4]. The antenna performs over a wide frequency range and provides excellent gain. The manufacturer claimed that a single Tranztenna can replace multiple traditional antennas because of its wide frequency range, and also that it uses a transparent film substrate that is superior to that of ITO. The antenna is also compact and flexible to be easily transported and deployed in field and military operations. However, its frequency range is limited between 9 GHz to 11 GHz which leaves most of the other current wireless applications out of its range of operations.



Figure 2.6 A Tranztenna installed on the window panel of a military vehicle [4].

Hitachi Cable Ltd and Communications Technology (NICT) of Japan prototyped a semi-transparent sheet antenna (Figure 2.7 (a)) handling a wide range of frequencies in February of 2007 [5]. However, this antenna was designed for a frequency range from 470 MHz to 770 MHz and also the 2 GHz band mobile telephony and 5 GHz WLAN application.

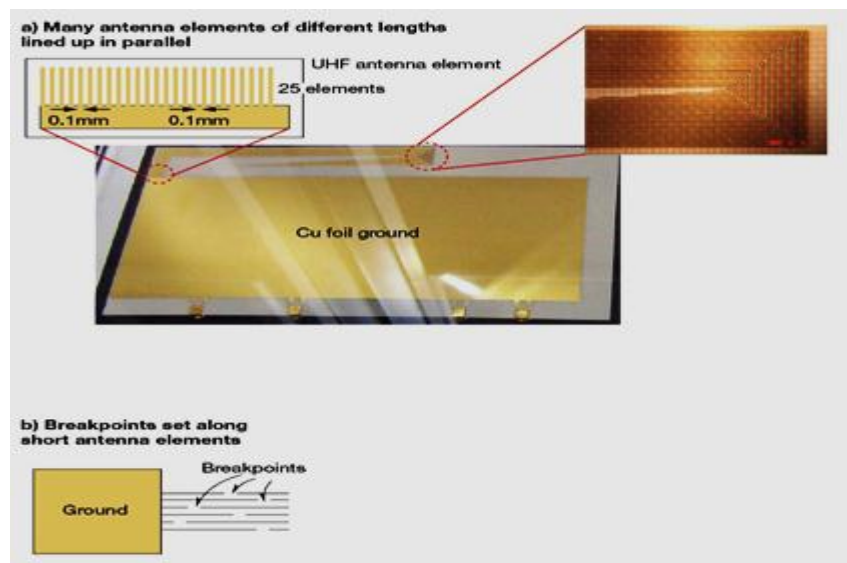
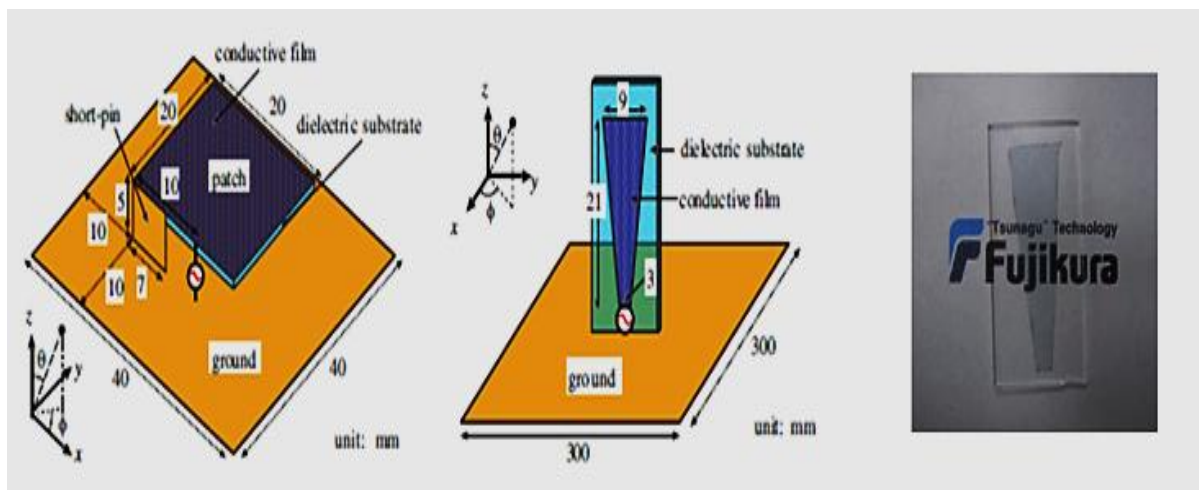


Figure 2.7 Semi-transparent broadband antenna developed by NICT: (a) antenna with the ultra-fine elements of various lengths (b) antenna with ultra-fine elements of uniform lengths but with set breakpoints [5].

The prototype was a partially transparent antenna using a transparent film substrate with copper radiators and ground. NICT successfully demonstrated bandwidth expansion through the use of multiple ultra-fine elements. The antenna for terrestrial digital broadcasting consisted of 25 ultra-fine elements which were only 0.1 mm in width and of various lengths aligned in parallel. An alternate version as shown in Figure 2.7 (b) had uniform length but with breakpoints set in each element to handle a wide bandwidth. Both designs could handle frequencies from 470 MHz to 770 MHz. However, although the radiator was small and narrow in size, the antenna required a large surface area for the ground.

In 2008, Guan et al, in their paper titled “Antenna Made of Transparent Conductive Films” [6], demonstrated a narrowband PIFA and monopole designed to work at 2.4 GHz. The performances of the antennas were compared with each other on several films with different sheet resistivity (Figure 2.9). However, both type of antennas had a copper ground leaving only the patch as transparent. The monopole antenna was essentially a high profile antenna as can be seen in Figure 2.8 (b).



(a) (b) (c)

Figure 2.8 (a) PIFA (b) Monopole antenna (c) Transparent radiator of the monopole antenna [6].

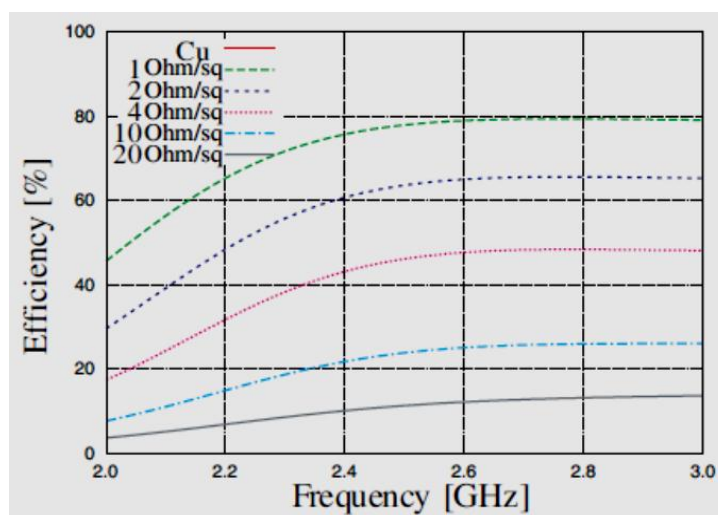
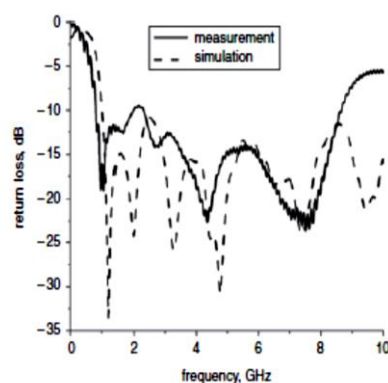


Figure 2.9 Radiation efficiency for varied sheet resistivity [6].

There was a spurge of research activity in 2009 on transparent antennas. Katsouraros et al [7] from Queen Mary University, UK published a paper on a novel optically transparent UWB antenna using AgHT-4. The antenna was fed by coplanar waveguide (CPW) and had an operational bandwidth from 1 to 8.5 GHz. However, the transparent antenna was sandwiched between a glass substrate and a Perspex superstrate which helped improve the antenna gain (Figure 2.10). Also, the radiator was fed using an aluminium strip and as such was not wholly transparent.



(a)



Measured and simulated return loss of transparent UWB antenna

(b)

Figure 2.10 (a) The transparent UWB antenna (b) return loss measurements of the antenna [7].

This was later followed by Drexel University’s team from Philadelphia, USA which demonstrated an “Optically Meandering Dipole Antenna” [8] as shown in Figure 2.11. The designed antenna was an optically transparent antenna for radio frequency identification systems. Drexel’s engineers are currently working on commercializing the technology for industrial use that can be customized for printing onto fabrics, automobiles and military vehicles. The antennas are created using an inkjet printer technique that coats conductive ink onto flexible materials. To maintain high conductivity, there was a compromise on transparency and as such the traces of the meandering dipole can be easily noticed on the transparent polymer.



a)



b)

Figure 2.11 (a) RFID 1/2 dipole antenna (b) RFID meandering dipole antenna [8].

An interesting thesis [9] on an optically transparent antenna operating at 2.4 GHz for small satellites was presented in 2010. However, the transparency of the antenna was achieved through the gaps in a copper trace mesh as shown in Figure 2.12. The empty portions (voids or gaps) of the copper mesh expose the polymer substrate which was to be used to harness solar energy through integration of solar panels underneath the antenna to power the satellite.

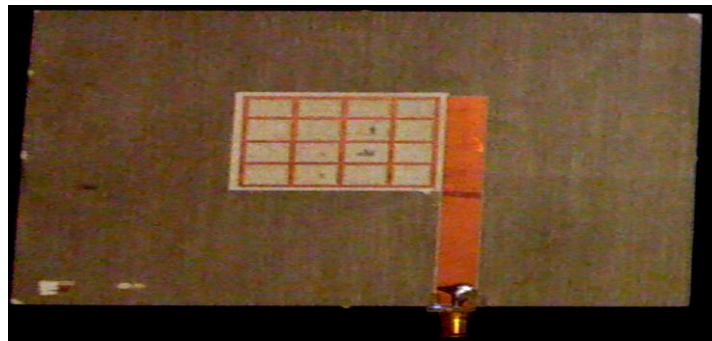


Figure 2.12 The copper trace mesh antenna fed through coupling [9].

The thesis also demonstrated some work on optically transparent antennas using ITO. In this study, the author presented the effect of the deposition thickness of the ITO on efficiency and surface resistance. However, no design of the experimental antenna was published. One interesting fact that was presented, however, was the effect of placing a material with higher conductivity like copper around areas of the antenna where the current density is high to improve the efficiency of the transparent antenna. This was used as the basis to develop the meshed copper antenna in Figure 2.12.

This concludes the literature review of the work so far done with regard to transparent antennas. An additional section (section 2.3) on transparent conductive materials is provided as extension to this literature review to show how material development has played a part in the direction and focus of this PhD research work. A further section on transparent conductive oxides (TCOs) then follows giving an in-depth analysis on the characteristics and properties of the material especially in regard to AgHT.

2.3 Transparent Conductive Materials – Development Review

They say necessity is the “Mother of Inventions”. Perhaps it may be true and may be one of the reasons for so much work being carried out by scientists and researchers in the field of material science to develop conductive materials that are transparent. The technology behind transparent conductive film has been around since the 1950s. Over the last decade however, the applications for transparent conductive films has sky-rocketed. Some of the products include display electrodes for paper-thin LCD, plasma, and organic electroluminescence (EL) televisions, touch screen monitors on ATMS, ticket vending machines, handheld game consoles and mobile phones. Transparent conductive films are also very commonly used for electrodes in solar cells which are poised to sweep the market in the near future. Materials research on TCO started out based on metallic films that are based on conductivity specific to metals such as gold and its property of visible transmission. However, it was later discovered that oxide thin films demonstrated much more stable characteristics for electrical conductivity and electrical transmissions. As such research focus has been in this direction for the last two decades. TCO films are essential to electrical products that require thin film materials with superior optical and electrical properties or essentially good transmission qualities. Besides this, the resistivities of TCOs have to be as low as possible in order to conserve energy, power and resources. With these in mind, much focus has been put by researchers on ITO which is a tin doped indium oxide (Sn-doped In_2O_3) and is now the most widely used transparent conductive film material. Although the ITO market has since expanded rapidly with the development of products like flat panel display (FPD) televisions, their market share has been hovering around 10% of the global market so far.

Also, with the Indium rare metal facing the risk of depletion, there is a concern that there may be a disruption in the supply for the production of ITO [10]. With time running out, focus has been on Tin Oxide (SnO_2) and Zinc Oxide [11]. Aluminium doped zinc oxide has been in the lime light since then but is still in the development phase for commercial use as a replacement for ITO. Tin Oxide however, has found its use in AgHT. AgHT is a 3-layered film made of a Silver (Ag) layer sandwiched between two-layers of tin oxide. It is a highly conductive coated film developed for use in EMI/RFI shielding and infrared heat

rejection applications. Compared to ITO which can only be made available at a resistivity of not less than 50 $\Omega\text{-m}$ on a polymer, AgHT is readily available at a resistivity as low as 4 $\Omega\text{-m}$. This is because the conductive layer for ITO is easily breakable at such a low resistivity; AgHT has managed to overcome this through its patented design structure. ITO is thus only available at 4 $\Omega\text{-m}$ on a glass substrate through deposition techniques, thus giving an edge to AgHT which is available at 4 and 8 $\Omega\text{-m}$ resistivity on flexible polymer substrates. The polymer substrate gives AgHT the advantage of being conformable, lightweight and easily replaceable on window glass thus providing easy maintenance at a lower cost.

AgHT's unique combination of high visible light transmittance, nearly neutral colour and low electrical resistance makes it ideal as an EMI shield for electronic displays and membrane switches. It is also outstanding in its ability to transmit visible light while rejecting infrared heat making it popular for use commercially as projector lamp shields, theatrical lighting filters and for window shielding in buildings [11]. However, with the publications of its potential suitability as an antenna material by Simmons et al [1], research has been ongoing to improve its efficiency which has been a major non-plus point in it being a contender to copper or other metallic based antennas. Although, the author has managed to increase its efficiency up to 20% [12], there is still much to do in term of its efficiency to make it a strong contender for antennas made out of TCOs in the wake of depleting Indium for ITO, and Aluminium Zinc Oxide being still in the development phase. However, antennas made out of AgHT could make a dual impact as a solar module integrated antenna for green technology and provide a 3-in-1 solution of sun shielding, wireless communication, and solar energy harvesting for energy provision and storage [13]. A further impact that it could make is its potential use as rectennas especially on glass windows and panels where there is no constraint on the size of the antenna design or use of large scale antenna arrays. Large transparent rectennas whether narrow band, multiband, wideband or ultra widebands, or combinations of these, or arrays of any of these could use the limitless glass area to harvest radio or microwaves from miles away across a wide range of frequencies and convert them to useful DC current to be used in building or homes.

2.4 Properties of Transparent Conductive Oxides (TCOs)

Transparent conductive oxide films can be prepared from a variety of materials including semiconducting oxides of tin, zinc, indium, gold, silver and titanium [14]. A review of the physical properties of these materials is introduced in this section and compared, to gain an insight into understanding how it would affect the performance of an antenna made from that material.

A *figure of merit* for a transparent conductor may be effectively defined as the ratio of its electrical conductivity to the optical absorption coefficient of the film. Besides the figure of merit, conductivity; physical, chemical, thermal durability; etch-ability; work function, plasma wavelength; deposition temperature; toxicity; uniformity; and cost are other factors that may influence the selection of a particular transparent conducting material for an antenna [15].

2.4.1 Characteristics, Properties & Applications of TCOs

Transparent conductive oxides have a variety of uses. One common use is its ability to reflect thermal infrared heat. This feature is exploited to make energy-conserving windows. An example of which is AgHT, which is effectively a sun-shielding film manufactured by Solutia Inc. This low-emissivity window application (Figure 2.13) is currently the largest area of use for TCOs.

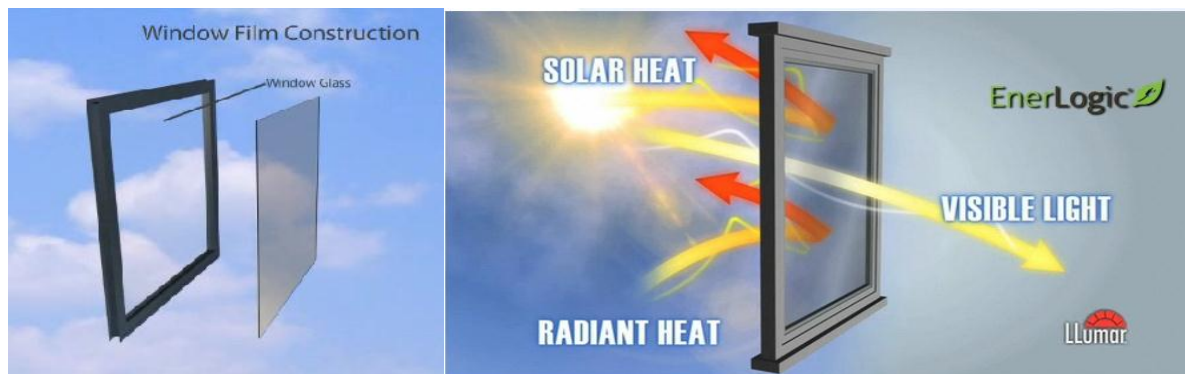


Figure 2.13 Transparent conductive oxide films used for sun shielding from harmful UV rays [16].

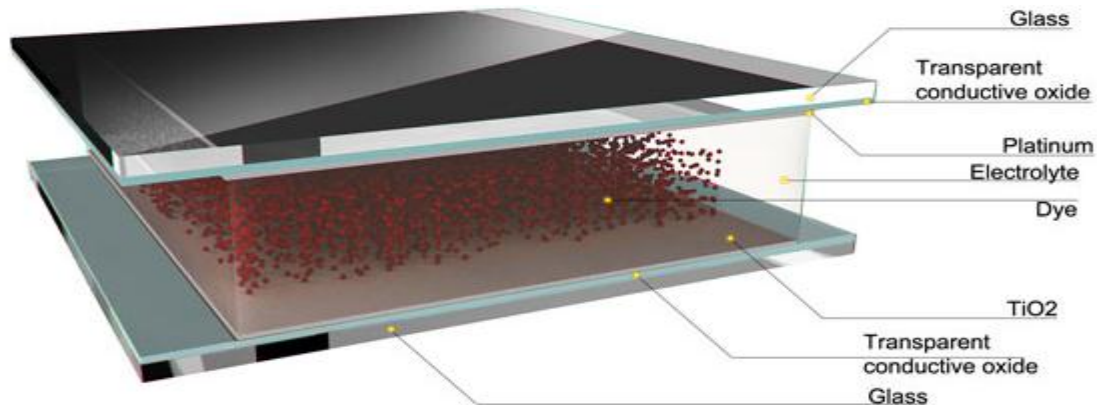


Figure 2.14 The basic composition of a Dye Sensitive Solar Cell (DSSC) [17].

Ovens are other applications in which TCOs are also used. Oven windows employ TCOs to conserve energy and to maintain an outside temperature that makes them safe to touch. The electrical conductivity of these TCOs is exploited widely in flat panel displays as well as in the front-surface electrodes for solar cells. The use of TCOs in Dye Sensitive Solar Cells (DSSC) is shown in Figure 2.14.

Transparent conductive oxides are also used in rear view mirrors of automotive that can be automatically dimmed and in electrically controlled smart windows; here an electrochromic material is sandwiched between a pair of TCO films. Defrosting windows in vehicles is made possible by passing electric current through TCOs.

Another very common use of TCOs is the touch screen panels of ATMs and PC monitors. TCOs can be also made into magnetic shields, invisible and discreet security circuits on windows. Since the last two decades, TCOs have been used to build transparent radio antennas that can be mounted or built into automobile windows or windscreens. Figure 2.15 shows one such example from Laser Antennas, Australia [18].

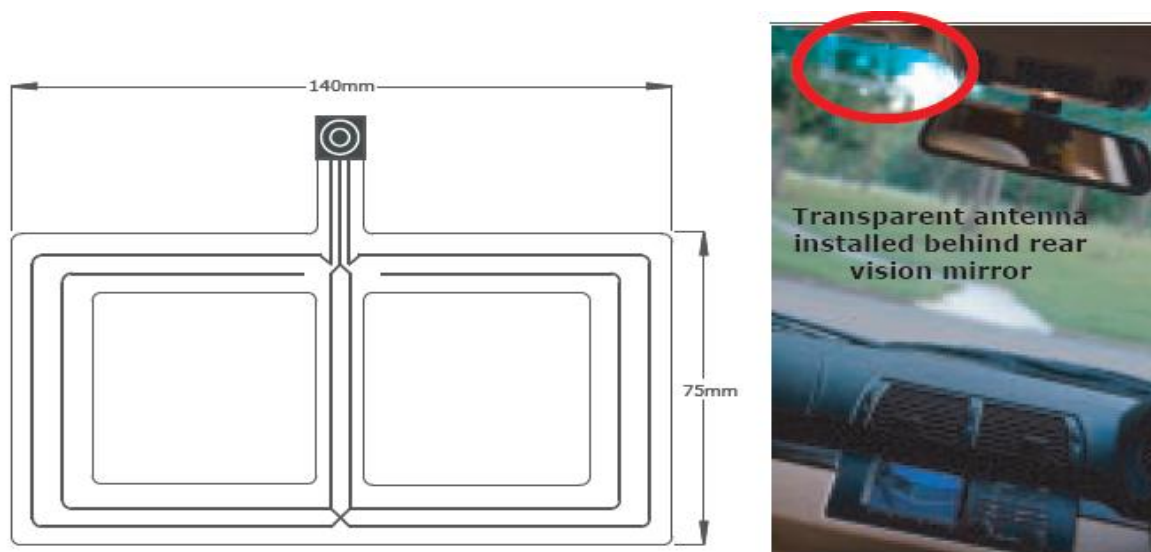


Figure 2.15 Transparent antenna for installation on the inside of a car windshield [18].

However, the use of TCOs for ultra wideband antennas other than narrow band applications like in the automobile radio antennas above, is still in the research stage basically because of the roller-coaster nature of the regulatory support UWB technology had received in the past and which has since seen change with the commissioning bodies of Europe taking a more positive stand. With the first UWB antenna being demonstrated by Katsouraros et al [7], more research is being done to improve the capability and performance of TCO based UWBs.

AgHT was the TCO used to demonstrate the feasibility of the first transparent narrowband antenna in 1997 [1]. Ironically, AgHT was also the TCO used to demonstrate the first UWB antenna [7].

In this thesis, the characteristics of AgHT have been noted through experimental, visual and documented publications.

AgHT-8 has been notably used for EMI/RFI shielding and infrared reflection applications in buildings, cars and other applications. It is produced by a subsidiary of Solutia Inc., CPFilms (formerly known as Courtaulds Performance Films). The company produces the two trademark variants of the AgHT, i.e. AgHT-4 and AgHT-8 for the world market. AgHT-4 has a surface resistance of 4 Ω -m while AgHT-8, a surface resistance of 8 Ω -m basically, the number designation being an indicator of the product's approximate

surface resistance. $4 \Omega\text{-m}$ is equivalent to a conductivity of 250,000 S/m and $8 \Omega\text{-m}$ to a conductivity of 125,000 S/m since conductivity is the inverse of resistivity. Figure 2.16 provides details of AgHT’s light transmittance properties which were extracted from CPFilms’ AgHT datasheet.

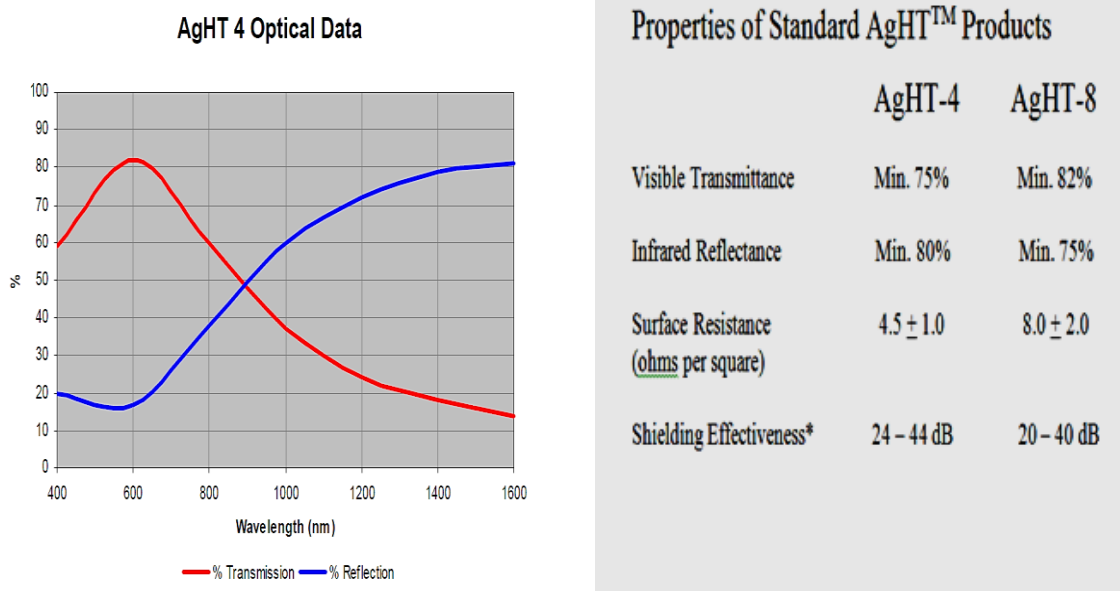


Figure 2.16 Basic properties of AgHT [16].

As can be seen, AgHT has a Visible Light Transmittance (VBLT) of between 75 – 82% which makes it quite suitable for use in conjunction with DSSC for solar energy harvesting in green technology applications [19].

2.4.2 Other Properties

Properties other than those reflected in Figure 2.16 have been observed through experimental data and observations in relation to its use as antenna material.

2.4.2.1 Transparency

As described earlier, AgHT became a potential candidate as an antenna material when engineers at NASA successfully demonstrated a patch antenna radiating at 2.3 GHz and 9.5

GHz in 1997 [1]. AgHT is made of a 3-layered conductive coating on a polymer base. This 3-layered coating on a transparent polyethylene terephthalate (PET) or polymer, comprises of a silver layer sandwiched between 2 layers of tin oxide. The coating is electrically conductive and transparent with a VBLT of 75-82%. The AgHT film has an approximate thickness of 0.175mm. About 40% of this thickness is the coating and the balance PET. The film was made through a process as described in Appendix 4.1.

The AgHT film is strong enough to stand alone to give support to a miniature antenna designed on it upto a size of 50 x 50 mm. Above 50 x 50 mm, some additional support is needed. A raw PET without coating can effectively be added via transparent adhesive to provide additional support above the 50 x 50 mm guideline and still maintain its VBLT. The supported structure can still be conformal. Above 100 x 100 mm, the antenna needs a more solid support like glass or other transparent material to be effectively transparent.

The transparent features of the AgHT provides the antenna with excellent discreetness for use in stealth and covert operations similar to Fractal Antenna System's "Tranzenna" as shown in Figure 2.17 [4].



Figure 2.17 The Tranzenna mounted on the side window of a military jeep [4].

The optical transparency of a TCO is inversely related to its electrical conductivity which in turn depends on the mobility of free electrons in the material. In order to improve the optical transparency of the AgHT, the conductive coating in this case silver, has to be as thin as possible. Consequently, the number of free electrons is also decreased thus decreasing the conductivity of the material. Alternatively, it can be said that the resistivity of the AgHT increases as the free electron mobility decreases with the thinning of the silver layer.

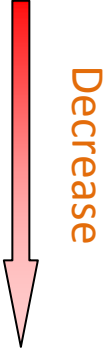

2.4.2.2 Electrical Conductivity

The electrical properties of TCOs are determined by their sheet resistance and this in turn is related to the specific resistivity, ρ and the film thickness, d that is, sheet resistance = ρ/d . Electrical conductivity is the inverse of the resistivity of the TCO material. And as earlier stated, the electrical conductivity of AgHT-4 and AgHT-8 are 250,000 S/m and 125,000 S/m respectively. In this section, it will be seen how conductivity is dependent on material properties and for which reason the silver based AgHT is a very suitable candidate for antenna material.

For current modern day applications like touch screen and high resolution displays, it is critical for the TCO to be as thin as possible. This is because if the film is thick, the etched patterns for the displays in the TCOs could create height variations in the device. Hence, the topography has to be as thin as possible which is only possible with a thin as possible TCO. The AgHT's conductive layer for example, is as thin as 0.0525 mm. However, the thinness comes with a price namely, a reduction in conductivity. As mentioned earlier in section 2.4.2.1, conductivity depends on the free electrons available in the conductive layer of the TCO. The conductivity, σ increases with the products of the concentration of free electrons and the mobility. For the metallic layer of silver in AgHT, the free electron concentration is fixed by the structure and electronic properties of the metal. In semi-conductors however, the free electron concentration is determined by the maximum number of electronically active dopant atoms in the lattice structure. Hence, a logical approach would be to increase the conductivity by the increasing the number of dopant atoms; however, such attempts to place a large number of dopant atoms into the lattice produces a neutral defect that adversely affects or decreases the mobility and consequently the conductivity [15].

Table 2-1 attempts to summarize the order of electron concentration in terms of conductivity as they are generally found in TCOs. As the conductivity or electron concentration is reduced through the thinning of the material, transparency increases. The table attempts to reflect this also.

Table 2-1 Order of Conductivity (electron concentration) and Transparency of TCOs

TCO Type	Conductivity	Transparency
Ag based		
TiN		
In ₂ O ₃ :Sn		
ZnO:Al		
SnO ₂ :F		
ZnO:F		

2.4.2.3 Plasma Frequency

The plasma frequency for the conduction electrons in a TCO can be considered as the dividing line or plasma edge for optical properties.

This dividing line can be explained using the classical Drude free electron theory. The Drude model indicates that transmittance drops in the near infra-red region associated with plasma frequency, ω_p . At longer wavelengths (i.e lower frequencies), reflection occurs because of the plasma edge, and light cannot be transmitted due to this phenomenon.

The plasma frequency is obtained from the plasma wavelength, λ_p which can be obtained from equation 2.1 [22]:

$$\lambda_p = \left(\frac{\epsilon_1}{\epsilon_1 - 1} \right)^{1/2} \lambda_o \quad \dots \text{Eqn (2.1)}$$

where λ_o , is the wavelength at which reflectance reaches a minimum and ϵ_1 is the relative electric permittivity determined from the measurement of the refractive index (η) in the visible region [23-24].

The plasma frequency is directly related or controlled by the free carrier density (n) via equation (2.2) [22]:

$$\omega_p = \left(\frac{ne^2}{\epsilon_0 \epsilon_1 m^*} \right)^{1/2} \quad \dots \text{Eqn (2.2)}$$

where ϵ_0 is the permittivity of free space, (m^*) the effective mass and (e) the conduction electron.

As such, at frequencies higher than the plasma frequency, the electrons cannot respond, and the TCO behaves as a dielectric. At frequencies below the plasma frequency, the TCO is characterized by high reflectance and functions as a screen of incident electromagnetic waves [22]. For most TCOs, the plasma frequency is around the near-infrared part of the spectrum. As such, in this region there is high reflectance, a feature which is used in AgHT to provide infra-red screening in window applications. The visible or transmittance region in contrast is in the higher frequency range of the spectrum.

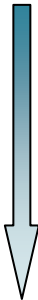
As can be seen from equation (2.2), the plasma frequency increases approximately with the square root of the conduction-electron concentration. The maximum obtainable electron concentration and plasma frequency of TCOs in general increase in the same order as resistivity. In essence, as the plasma wavelength decreases, the resistivity decreases resulting in an increasing conductivity.

2.4.2.4 Deposition Temperature

This section explains why ITO and silver based AgHT are the common commercially found polymer TCOs. In the manufacturing process of TCOs, a sufficiently high temperature needs to be maintained in order to develop the required properties in the TCOs. The list in Table 2-2, gives the order in which the temperature usually increase with some TCOs. The list is given in descending order that is, from the highest temperature required to that of the lowest.

As such it can be seen why silver or ITO is preferred for deposition on thermally sensitive substrates like polymer plastics. Cadmium Stannate (Cd_2SnO_4) because of its highest temperature requirement may require very refractory substrates to develop its best properties [15].

Table 2-2 Deposition Temperature of TCOs

TCO Type	Deposition Temperature
Cd_2SnO_4	 <p>Highest</p> <p>Lowest</p>
SnO_2	
ZnO	
ITO	
Ag	

Also, it is found that, ITO is commercially available on polymer plastics like PET only at a resistivity of between 40-60 $\Omega \cdot m$ and above. This is the lowest available in the market unlike AgHT which is available at 4 $\Omega \cdot m$. ITO becomes too brittle and is susceptible to electrical discontinuity on polymers if subject to bending during handling or otherwise. As such, ITO at 4 $\Omega \cdot m$ can only be found on rigid bases with glass being the most common.

On the other hand, the silver based AgHT, through a patented manufacturing process and design is able to overcome this and maintain its electrical conductivity when flexed or bent but however, with some limits. This thus makes AgHT material the better choice for the design and manufacture of flexible and conformal antennas compared to ITO.

2.4.2.5 TCOs on Soda Lime Glass

Sodium in sodium containing glass like soda-lime glass can be an issue for TCOs. When TCOs are deposited on soda-lime glass, there is a possibility of the sodium diffusing into the TCO and increasing its resistance thus reducing its conductivity. Tin oxide is

particularly affected in this regard. Sodium diffuses rapidly at the high substrate temperature (usually $>550\text{ }^{\circ}\text{C}$) used for the tin oxide deposition. As such, it is common to deposit a barrier layer on the glass prior to the deposition of tin oxide. When laminating AgHT on soda-lime glass which is the most commonly used glass material in homes and buildings, a barrier film is recommended to be used as a protective layer. However, this is not because of diffusion as there is no heating or temperature required during the lamination process but more for prevention of moisture creeping in between the glass layer and the top tin oxide layer of the AgHT film. The barrier layer is also available from Solutia.

Even though, silicon may not be particularly effective in blocking the sodium diffusion, it is however, the most commonly used barrier material. Silica also serves a second purpose, it is able to eliminate the interference colours that would otherwise be shown by the TCO film [25]. To provide a much more complete barrier against the sodium diffusion, alumina is recommended [26].

2.4.2.6 Durability and Etching Patterns on TCOs

Durability in TCO environment is its ability to withstand corrosive chemical environment which is inversely related to its ease of etching. Tin oxide is the most resistant and as such its application in AgHT. Silver is easily tarnished by air and the moisture in the air. Hence when handling AgHT film, it is advised to use vinyl gloves to avoid sweat from the palms and fingers getting onto the surface of the AgHT film. The film normally comes with a layer of barrier film and it is best to leave the barrier film intact on the surface of the film if the geometry of the antenna is to be manually inscribed with a scalpel.

If etching method is to be used like for display, heaters or even antennas, parts that need to be removed are done so using etchants, a list of which [15] is shown in Table 2-3. From the Table, which is listed with materials in the order of the highest ease of etching at the top, it is noticed that Zinc Oxide is the easiest and tin oxide the most difficult.

As it is not possible to carry out etching on an already manufactured AgHT film and moreover as mentioned earlier, tin oxide is quite resistant to etching, alternative approaches have been used to fabricate AgHT antennas. Antenna geometry using AgHT is normally ‘cut-

out’ in papers published by other researchers. However, the author has introduced an inscribing method in his later papers to minimize the difficulty of attaining narrow feed gaps. It is also possible to develop an ‘imprint-cut technology’ to imprint the geometry of the antenna through very sharp edged dies onto the surface of the AgHT polymer as an improvement of this approach to attain a precise and repeatable prototype.

Table 2-3 Etchants for TCOs

TCO Type	Etchants
ZnO	Dilute acids
ZnO	Ammonium Chloride
TiN	H ₂ O + NH ₃
In ₂ O ₃	HCl + HNO ₃ or FeCl ₃
SnO ₂	Zn + HCl
SnO ₂	CrCl ₂

AgHT as mentioned earlier is comprised of a thin layer of silver sandwiched between two layers of tin oxide coated on to a film of PET. A milling method that will not damage the coating surface can be implemented. For this method, a high precision milling machine will be required especially one that is capable of milling slots of 0.05 to 0.1 mm in width. Laser cutting is not suitable as the heat generated at the cutting point causes discolouration along the edges of the geometry that is traced or cut-off as well as damage to the conductive material along those edges. This will greatly affect the performance of the antenna that is made in this way.

2.4.2.7 Hardness of TCOs

The mechanical durability of TCOs is related to the hardness of the crystals from which they are formed [15]. Hardness values are usually given in Mohs where higher values indicate harder materials.

Tin oxide is known to be even harder than glass and hence its popularity in the manufacture of TCOs especially in applications which are exposed to contact. Zinc oxide is one of the easiest to be scratched. Thin silver films are very fragile and need to be coated with protective layers just like in AgHT where the protection as shown in Figure 2.18 is provided by the tin oxide.

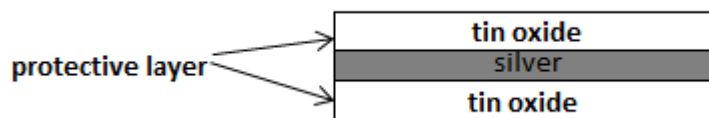


Figure 2.18 Composite structure of the AgHT

2.4.2.8 Sun Shielding and Low Emissivity

As already shown in Figure 2.13, one of the most common use of TCO is as sun screens or low emissivity films on window glass. AgHT is primarily used for this application. Integrating antennas onto TCO films is merely taking advantage of its conductive properties to provide multiple applications using a single material.

AgHT or TCOs in general when applied on glass windows, improve the energy efficiency of the windows because free electrons reflect infrared radiation for wavelengths longer than the plasma wavelength. During winter or in cold climates, the plasma wavelength should be fairly long about $2 \mu\text{m}$ so that most of the solar spectrum is transmitted into heat inside the building [15]. For hot climates, conversely a short plasma wavelength, $\leq 1 \mu\text{m}$ is desirable so that the near infra-red portion of the incident light can be reflected out of the building.

Metals such as silver have short plasma wavelength and hence its use in AgHT for low emissivity windows. Normally, the silver layer because of its poor durability is sealed inside double glazed panes for protection from air and moisture. This protection is already provided in AgHT as the silver layer is sandwiched as shown earlier in Figure 2.18 between two layers of durable tin oxide.

2.4.2.9 Electromagnetic Shielding

A very interesting property of TCOs is its ability to block strong signals. Silver and ITO are the best materials for this purpose. As such applying such TCOs on windows will make it possible to prevent eavesdropping on computers and communications by detecting electromagnetic signals passing through windows [15].

2.4.2.10 Integration of TCOs with Solar Cells

Transparent conductive oxides make up an important part of solar cells. They normally serve as the front contact in thin film silicon solar cells with a reflective material as the back contact. The front surfaces of solar cells are usually transparent electrodes. This has to be, otherwise light would not be able to transmit through to fall on to the solar cells. The optical qualities of the transmitting layer affect the silicon absorber layer in terms of providing the optimal irradiation [27]. Amorphous silicon cells can be grown on plastic substrates. In such cases, the top TCO needs to be deposited at low temperatures on thermally sensitive cells. Silver, ITO and ZnO have low deposition temperatures and hence are suitable candidates for this. So it is no wonder, that ITO and ZnO are generally chosen for this purpose.

Much research, indeed has to be done to see how AgHT can be used for this purpose to be incorporated as front electrodes for solar cells. However, this is beyond the scope of this thesis. What will be demonstrated and briefed is how AgHT can be incorporated onto amorphous solar cells to provide integrated wireless and energy harvesting solutions using UWB antennas. This is described in more detail in Chapter 7 under sub-section 7.3.

2.4.2.11 TCO Coated PET as Radar Absorption Material

Thin conductive metallic films have been researched on and also used in industry as radar absorption material (RAM). Some of these conductive materials include aluminium, titanium and indium. In the case of indium it is used as ITO coated on PET for use as transparent electromagnetic or radio wave absorbers [28]. Figure 2.19 shows the structure of a transparent electromagnetic absorber developed by TDK, Japan [28]. The electromagnetic absorber uses a transparent conductive film and is designed for $\lambda/4$ electromagnetic absorbers. The reflection layer (ITB010) is an ITO film formed on a PET base and having a surface resistivity of $10 \Omega \cdot m$; the designation “010” meaning $10 \Omega \cdot m$. Similarly, the absorption layer (ITB390) is also an ITO film on a PET base but with a higher resistivity of $390 \Omega \cdot m$. ITB010 is designed to reflect radio waves while ITB390 is designed to absorb radio waves. The transparent electromagnetic absorber has an optical transparency or visible ray transmission of 70%.

A recent paper by V.L. Soethe et al [29], presented thin films of titanium with nanometer thickness on PET as having radar absorption properties. The researchers observed that a thin titanium film-polymer substrate composite attenuated incident electromagnetic wave in the frequency range of 8 to 12 GHz making it suitable for use as radar absorbing material that can be employed in automobile, telecommunication, aerospace, medical and electronic areas. Reflectivity results from this paper tend to show that the attenuation depended on the thin film thickness as a determining factor. Thin films with 25 to 100 nm thickness showed attenuation of electromagnetic wave energy from 20 to 50%.

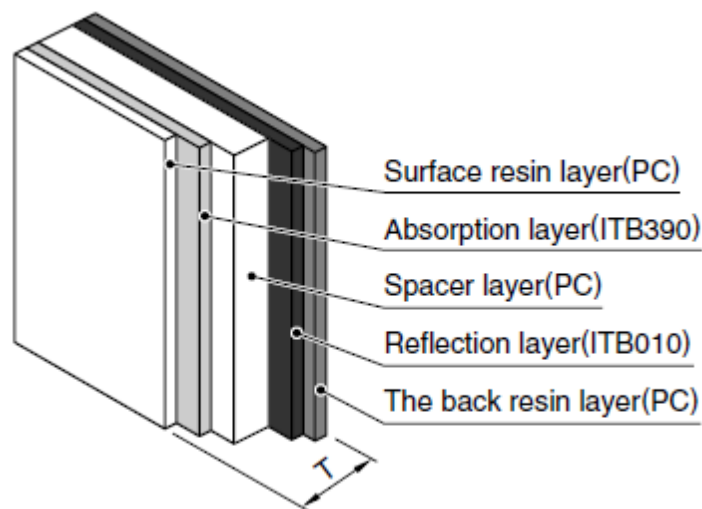


Figure 2.19 Composite structure of a transparent electromagnetic absorber from TDK [28].

From TDK's datasheet and V.L. Soethe et al's findings, there is a possibility that AgHT could in a similar way exhibit RAM property. This was thus investigated in simulation for the Mushroom Top UWB antenna. Experimental measurements were not able to be done due to lack of facilities and security restrictions imposed by antenna measurement companies in regard to RCS measurements. The simulated findings are presented in Chapter 4.

2.5 Summary

A brief literature review on transparent antennas was presented in the beginning of this chapter to highlight the research and progress in this area. This was followed by a short note on the development and current status of transparent conductive materials which are essential in the manufacture and development of transparent antennas. A detailed analysis of the main characteristic properties of TCOs and in particular, AgHT was then given. Hence by understanding the physics and physical processes that make possible the co-existence of optical transparency and electrical conductivity, we are able to appreciate how such knowledge has aided the advancement of research and development of TCOs in the recent decades in particular that of AgHT. Solutia Inc. a leading provider of performance films in

the world market has besides AgHT, done appreciable research and developed many other custom tailored TCOs for a variety of applications. One such material is PDP2P which has a very low resistivity of $2 \Omega \cdot \text{m}$ and hence a conductivity of $500,000 \text{ S/m}$. However, this material has a bluish tint due to its higher absorption of light. Nevertheless, such a material can find its use for stand-alone antennas where high transparency is not critical.

2.6 References:

- 1) R.N. Simons and R.Q. Lee, “Feasibility Study of Optically Transparent Microstrip Patch Antenna” International Symposium and Radio Science Meeting cosponsored by IEEE, AP-S, and U.R.S.I., Montreal, Canada, July 13-18, 1997.
- 2) C. Mias, C. Tsakonas, N. Prountzos, D.C. Koutsogeorgis, S.C. Liew, C. Oswald, R. Ranson, W.M. Cranton and C.B. Thomas, "Optically transparent microstrip antennas," *IEEE Colloquium on Antennas for Automotives* (Ref. No. 2000/002), pp.8/1-8/6, 2000.
- 3) J.A. Nessel, A. Zaman, R.Q. Lee and K. Lambert, “Demonstration of an X-Band Multilayer Yagi-Like Microstrip Patch Antenna With High Directivity and Large Bandwidth” *IEEE Antennas and Propagation Society Symposium*, vol. 1B, 227 – 230, 2005.
- 4) Fractal Antenna Systems. Available: <http://www.fractenna.com/whats/060228.html>.
- 5) “Antenna Technologies Advance for MIMO Era”, *Nikkei Electronics Asia*, p. 4, September, 2008.
- 6) N. Guan, H. Furuya, D. Delaune and K.Ito, “Antennas Made of Transparent Conductive Films”, *PIERS proceedings*, China, p. 720, March, 2008.
- 7) A. Katsounaros, Y. Hao, N. Collings and W.A. Crossland, "Optically transparent ultra-wideband antenna," *Electronics Letters* , vol.45, no.14, pp.722 -723, July 2, 2009.
- 8) N.J. Kirsch, N.A. Vacirca, E.E. Plowman, T.P. Kurzweg, A.K. Fontecchio and K.R. Dandekar, "Optically transparent conductive polymer RFID meandering dipole antenna," *IEEE International Conference on RFID*, 2009, pp.278-282, April 27-28, 2009.
- 9) J. Saberlin, “Optically Transparent Antennas for Small Satellites”, M.S. thesis, ECE Dept., UoU, Salt Lake City, UT, 2010.
- 10) M. Bradel and S. Conover, “Transparent Conductors and the Need to Replace ITO”, Eleventh Annual Freshman Conference, Swanson School of Engineering, April 9, 2011.
- 11) ULVAC Corporate Center. [Online]. Available: http://www.ulvac-uc.co.jp/pdf/prm_arc/056e/No56E-04.pdf

- 12) T. Peter, R. Nilavalan, H.F. AbuTarboush and S.W. Cheung, "A Novel Technique and Soldering Method to Improve Performance of Transparent Polymer Antennas," *IEEE Antennas and Wireless Propagation Letters*, vol.9, pp. 918-921, 2010.
- 13) T. Peter, Y.Y. Sun, T.I. Yuk, H.F. AbuTarboush, R. Nilavalan and S.W. Cheung, "Miniature transparent UWB antenna with tunable notch for green wireless applications," *International Workshop on Antenna Technology (iWAT)*, 2011, pp.259-262, March 7-9, 2011.
- 14) R.G. Gordon, *Thin Films for Photovoltaic and Related Device Applications*, edited by D. Ginley, A. Catalano, H.W. Schock, C. Eberspacher, T.M. Peterson and T. Wada, (Mater. Res. Soc. Symp. Proc. 426, Pittsburgh, 1996) p.419.
- 15) R. G. Gordon, "Criteria for Choosing Transparent Conductors," *MRS Bulletin*, vol. 25, pp. 52-57, August 2000.
- 16) Solutia Inc. [Online]. Available: <http://www.solutia.com/en/SolutiaCPFilmsVideo.aspx>
- 17) DSSC. [Online]. Available: <http://www.solarprint.ie>
- 18) Laser Clear Antennas. [Online]. Available: http://www.laser-antenna.com/latest_innovation.php
- 19) The Malaysian Flagship Grant Project: Energy Saver for Green Technology Building in Wireless Communication System (Appendix B.3).
- 20) S. Assia, O. Ratiba, M. El-Mahdi and K. Mohamed, "Optical Reflectance of Pure and Doped Tin Oxide: From Thin Films to Poly-Crystalline Silicon/Thin Film Device" *International Journal of Chemical and Biological Engineering*, 2:1, 2009.
- 21) R.P. Howson, M. Ridge and A. Bishop, "Production of transparent electrically conducting films ion plating," *Thin Solid Films*, vol. 80, issue 1-3, pp. 137-142.
- 22) H. Gueddaoui, S. Maabed, G. Schmerber, M. Guemmaz and J. C. Parlebas, "Structural and optical properties of vanadium and hafnium nitride nanoscale films: effect of stoichiometry," *Eur. Phys. J., B.* 60, pp. 305-312 (2007).
- 23) R.G. Gordon, US patent No. 4,187,336 (1980); U.S. Patent No. 4,419,386 (1983).
- 24) J.D. Chapple-Sokol, PhD thesis, Harvard University, 1988.

- 25) A. V. Shah, H. Schade, M. Vanecek, J. Meier, E. Vallat-Sauvain, N. Wyrsh, U. Kroll, C. Droz, and J. Bailat, “Thin-film silicon solar cell technology” *Prog. Photovolt. Res. Appl.*, vol. 12, Issue 2-3, pp. 113–142, March - May 2004.
- 26) TDK RF Solutions. [Online]. Available: http://www.tdk.co.jp/tefe02/e9e_bdj_003.pdf
- 27) V.L. Soethe, E.L. Nohara, L.C. Fontana and M.C. Rezende, “Radar absorbing materials based on titanium thin film obtained by sputtering technique”, *Journal of Aerospace and Technology Management*, vol. 3, issue 3, pp. 279-286, 2011.

CHAPTER 3

UWB Antennas

3.1 Introduction

Transparent UWB antennas basically evolved from non-transparent ones on which a lot has been researched. As such it would be more appropriate here to give some relevant background on the characteristics of the non-transparent UWB antennas as it is from this knowledge base that the transparent UWB antenna is characterized and developed. UWB antennas in the early days have been typically “multi-narrowband” antennas instead of antennas optimized to receive a single coherent signal across their entire operating bandwidth. Antenna variations may be tolerated in some modulation schemes but not all. A good example of the positive case is the multiband or OFDM modulation scheme. This modulation approach may be less vulnerable to dispersion or other variations across an antenna’s operational bandwidth. Desirably, a UWB antenna should allow a stable pattern control as well as stable matching across the entire band. In essence, it can be said that a UWB system requires an antenna that is capable of receiving on all operational frequencies at the same time. Hence, a UWB antenna’s behaviour must be predictable and consistent across its operating band.

3.2 Requirements for UWB Antennas

A UWB antenna should preferentially be non-dispersive and having a fixed phase center. A change in phase center may cause distortion on the transmitted pulse and worsen the performance at the receiver. If waveform dispersion occurs in a predictable fashion, it may be possible to compensate for it. However, it is desirable to have similar radiating waveforms in all directions. The log periodic antenna shown in Figure 3.1, is an example of a dispersive antenna. This antenna comprises of large scale elements as well as small scale elements. The large scale elements radiate low frequency components while the small scale elements, high frequency components resulting in a chirp-like, dispersive waveform and will vary at different azimuth angles around the antenna [1].

Another example of a dispersive antenna, is the conical log spiral antenna which is fed from the tip on which it has a smaller scale spiral. From this tip, higher frequency components must propagate to the lower frequency components that is, the larger scale structure at the base of the antenna before they radiate. Figure 3.2 shows the result of this physical structure on a received signal. The transmit antenna accepts a transmitted impulse voltage signal (left) at its terminals. A receive antenna subsequently yields a received impulse voltage signal (right) at its terminals. The dispersion of the log spiral antennas used for both transmit and receive results in a dispersed receive signal. This dispersion is clearly manifested in two respects. First, the received signal has a temporal extent over twice as long as the transmit signal. Second, the received signal shows a distinct “chirp.” The earlier portion of this signal exhibits relatively high frequency content with a shorter time duration between zero as can be seen in Figure 3.2 (b) [2].

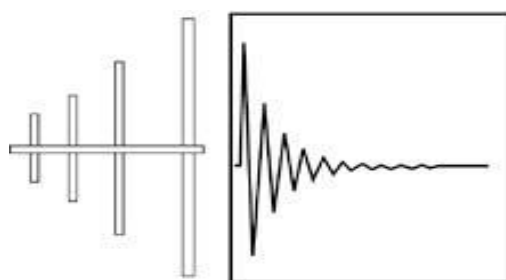


Figure 3.1 (a) A log-periodic antenna (*left*) has a dispersive waveform (*right*) [1].

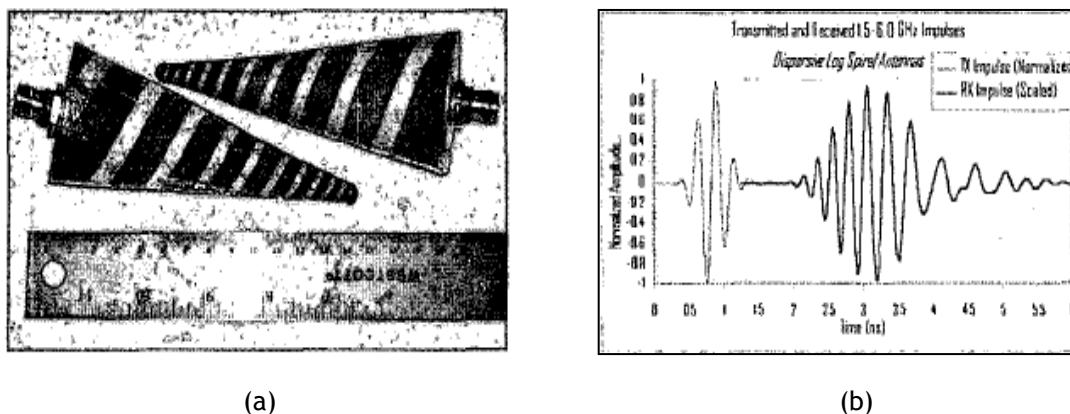


Figure 3.2 (a) Log Spiral Conical antennas (b) transmitted (left) and received (right) voltage waveform from a pair of conical log spiral antennas [2].

In contrast a small-element antenna such as a planar elliptical dipole antenna radiates a compact non-dispersive waveform similar to a “Gaussian W”. This is shown in Figure 3.3.

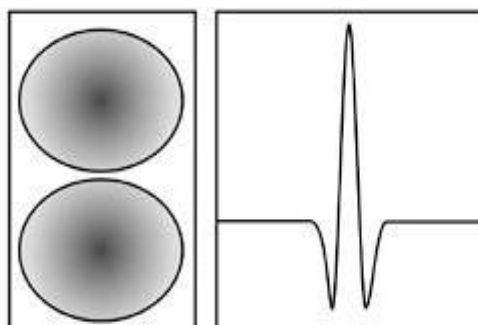


Figure 3.3 An elliptical dipole (left) has a non-dispersive waveform (right) [2].

With non-dispersive antenna elements, much better system performance can be easier obtained. Hence in recent years, the focus has been on small non-dispersive antennas such as the small UWB antennas due to their many advantages over the conventional wideband antennas. Such small, compact UWB antenna elements have a fixed phase centre and radiate a compact, mostly non-dispersive waveform. Propagation environments that are heavy in multipath with large delay spreads tend to distort waveforms and degrade signals. A non-dispersive UWB antenna will help resolve signals in these type of environments [3].

3.2.1 Other Requirements

Several parameters have been used to assess UWB antennas. Amongst them, the flat impedance characteristics of the UWB antenna to cover the entire UWB frequency band would be deemed one of the most important. Some of the contributions of each portion of the radiator to the impedance characteristics of a UWB antenna can be summarized as follows:

- Lowest portion (closest to the feeding point) portion of the radiating element primarily affects input impedance characteristics in a higher frequency range [4].
- The entire portion (such as the total length) of the radiating element or patch affects the input impedance characteristics at a lower frequency [4].
- The resonant frequency is decided by the distance or gap between the base of the patch and the upper surface of the truncated ground plane.
- The profiles of the lower edge of the patch (which may be altered through a bevel angle) as well as the width of the patch provide optimization of the bandwidth [5].

3.3 Planar UWB Antennas

A planar antenna is those that are usually fed through a microstrip line or coplanar waveguide (CPW). The planar structure enables the radiating element to be on the same dielectric material on which the transmitter and receiver are fabricated. In the next section, the CPW feed type would be introduced and discussed more in detail as this is the most suitable for the transparent antennas on TCOs as the conductive side is only on one side of the surfaces of the TCOs. Nonetheless, monopoles with transparent conductive ground can be designed with TCOs; however, they are much less aesthetically suitable for window glass applications.

3.4 CPW Feed

The CPW configuration facilitates the use of an active device placed near the antenna's radiating surface as well as monolithic integration of circuits.

3.4.1 Circular Disc Monopole

The CPW fed circular disc pole monopole as investigated in [6], in terms of its feed gap, width of the ground plane and dimension of the circular disc is presented here in Figure 3.4 to demonstrate some of the performance characteristics of the CPW configuration.

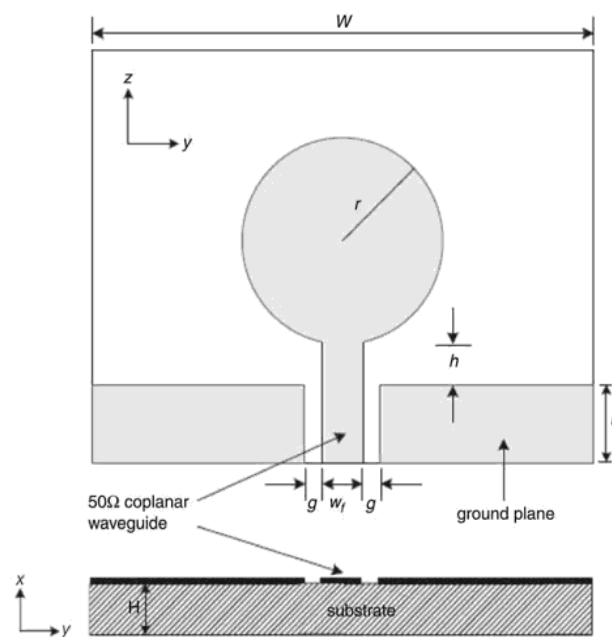


Figure 3.4 Geometry of the CPW-fed circular disc monopole [6].

The dimension of the circular disk, controlled in the geometry by the radius, is shown by Liang et al [6] to be the primary parameter affecting the first resonant frequency. This is because the current is distributed mainly along the edge of the disc. The overlapping of multiple resonant harmonics leads to the UWB characteristic. This is illustrated in Figure 3.5 below which shows the relationship between the disk's diameters and the first resonances.

Diameter r (mm)	First resonance f_1 (GHz)	Wavelength λ at f_1 (mm)	$2r/\lambda$
25	1.52	197.4	0.25
15	2.57	116.7	0.26
12.5	3.01	99.7	0.25
7.5	5.09	58.9	0.25

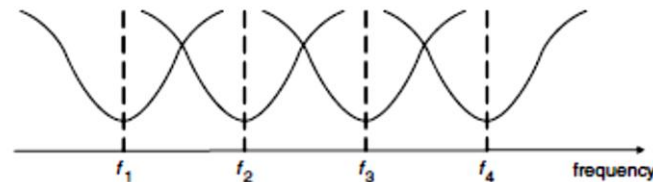


Figure 3.5 Overlapping of the multiple resonance modes [6].

The width of the feed gap was also shown to significantly change the impedance characteristics above 8 GHz. The paper further provided insight as to how the width of the ground plane changes the higher resonating frequencies substantially. In essence, the ground plane serving as an impedance matching circuit, tunes the input impedance and hence the operating bandwidth by changing “h” and “W”.

3.4.2 Rectangular Patch LCP Monopole

The findings in [6] aid in the design of not only a circular disk UWB but also other geometries. Another CPW fed antenna which makes use of a declining shape ground plane plus a stepped feed line is illustrated in Figure 3.6 [7]. The antenna was designed as a flexible planar UWB on a thin sheet of Liquid Crystal Polymer (LCP). The steps in actual fact are incorporated into the ground planes rather than on the feed line of the CPW. Both the decline and steps were essential to provide a wide bandwidth and broadband impedance matching. The bandwidth of the antenna was controlled by adjusting the length TL1 of the stepped CPW line. The inclination angle of the design is used for impedance matching, a concept first introduced by MJ Ammann [8] but on a planar UWB antenna with a perpendicular ground plane.

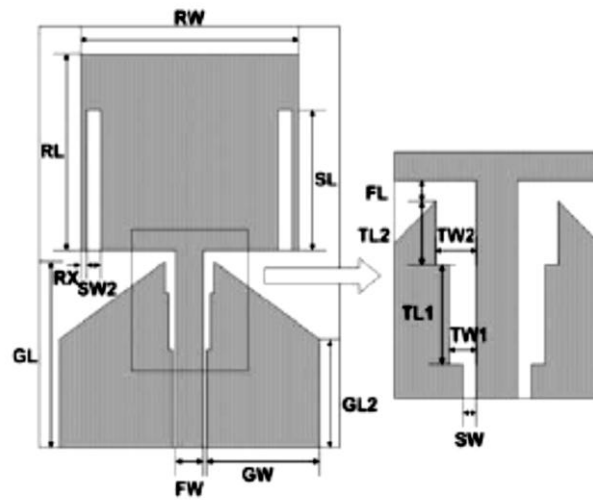


Figure 3.6 Planar type flexible antenna [7].

3.4.3 T-Shaped Monopole

A simple CPW fed geometry is presented by Wang et al [9]. The UWB antenna as presented in Figure 3.7 is made of a rectangular patch with a bevelled ground plane. In this design, the length of the slope-shaped ground plane, L_s determined the low-frequency characteristics. The parameters D_{min} , t , L_m and W_m affect the bandwidth properties and VSWR.

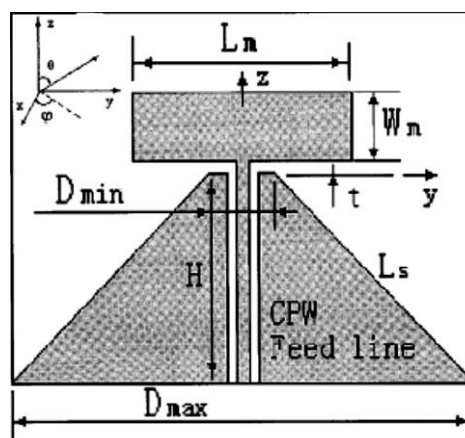


Figure 3.7 Broadband T-shaped antenna [9].

3.4.4 Elliptical Monopole

A CPW fed elliptical monopole UWB antenna was presented by Nikolaou et al [10]. In this design (Figure 3.8), the transition from the feed line to the elliptical radiator patch was via a linearly tapered CPW line. This provided a smooth transition of the energy from the feed to the patch through improved matching thus minimizing loss which would have occurred through abrupt transfers like in the T shape junctions of the earlier two designs. The elliptical shape and the CPW ground in this design provided the bandwidth control.

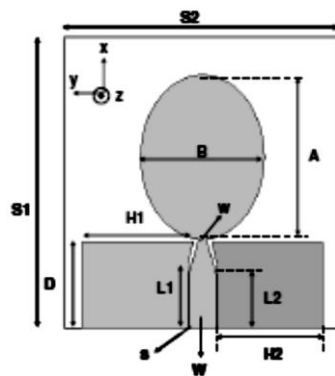


Figure 3.8 CPW-fed elliptical monopole UWB antenna [10].

3.5 Leakage Currents in CPW Feed

Radiation characteristics of an antenna are affected by feeding and cabling configurations. Although many reports present radiation patterns and/or gain profiles of edge-fed dipole antennas [11]–[14], they provide no qualitative or quantitative analysis of the effect of the feeding configurations on the radiation characteristics.

Recently, this problem has been addressed [15], where undesirable cable current effects on radiation patterns have been mitigated by attaching the feeding cable normal to the dipole axis and employing a coplanar waveguide (CPW)-to-coplanar strip transition and balun. However, the azimuth patterns are expected to be distorted due to the presence of the connector and the feeding cable in this case. These adverse effects on radiation pattern

characteristics were mitigated by a simple method presented in [16] by Kwon et al. The suppression of the cable leakage currents were achieved by incorporating leakage blocking slots within radiating elements. The thin slots are positioned and oriented in such a way that it effectively blocks the current component contributing to the leakage current on the outer surface of the feeding co-axial cable. Two types of leakage currents were presented in this paper. The first type was the leakage that occurs at the interface of the CPW and the co-axial cable. The second type comes from the current along the CPW trace but only after it has travelled the surface of the bottom radiator. The thin slots introduced by Kwon et al as shown in Figure 3.9 (b), was effective in blocking the second type of leakage current only.

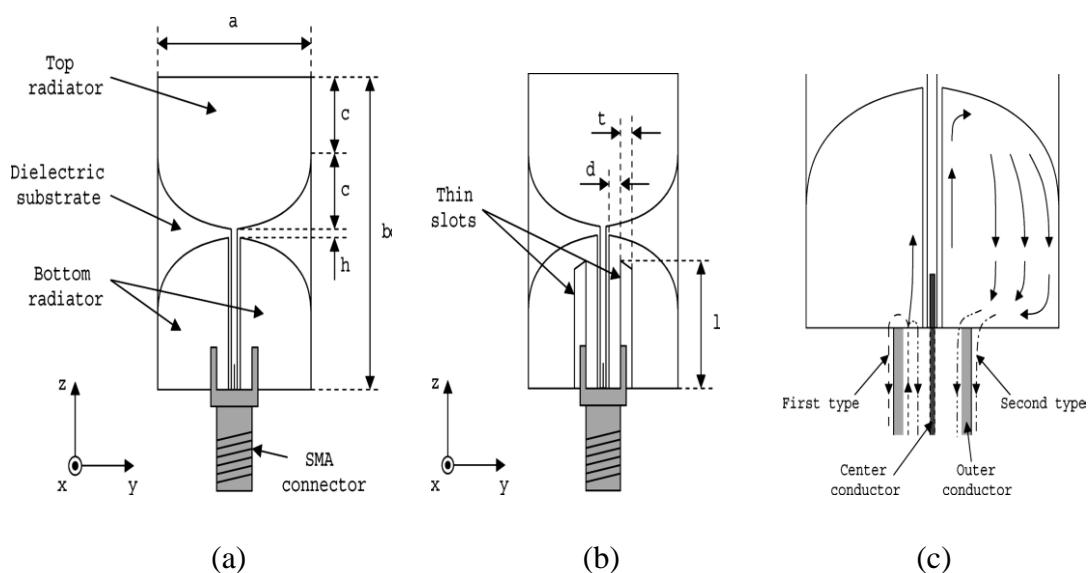


Figure 3.9 CPW-fed printed dipole UWB antenna with a SMA connector attachment showing the leakage blocking slots and the leakage currents [16].

3.6 Extensions to the CPW Feed

At times, due to space restrictions or otherwise, or possibly for aesthetics in the case of window applications for transparent windows, a simple CPW feed approach may not be appropriate, in this case coupling using microstrip transition may prove a better approach. This is especially so to facilitate maintenance of the TCO films when it is affected by wear

and tear or if the design of the antenna needed to be changed to improve the system. A simple CPW to microstrip transition set-up is illustrated below in Figure 3.10 [17].

3.6.1 Microstrip to CPW Transition

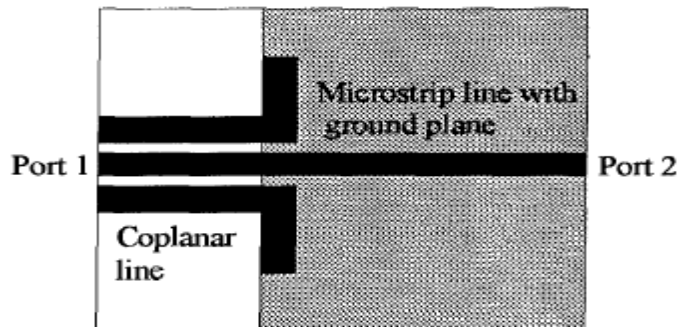


Figure 3.10 Transition from coplanar line to microstrip line [17].

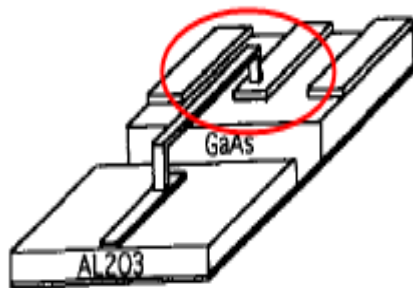
Microstrip to CPW transition is used to avoid the use of via holes and/or air-bridges [18-21] to connect two transmission lines [22]. The continuity of the signal line can be easily achieved even though ground continuity is difficult to obtain because they lie in different layers. Via holes are used for ground contacts in many applications, while electromagnetic coupling without via hole is preferred in ‘on wafer probing’.

The microstrip to CPW transition is essentially an electromagnetic coupling technique. Many types of structures have been used to achieve this, such as straight coupling stubs [23-24], semi-circular stubs [25], coupling radial stubs [26], or 90° open stubs [27]. However, transitions such as coplanar to coax and coplanar to slot line will not be discussed within the scope of this thesis as they are quite impractical to implement on single layer TCO film antennas for glass window applications and as such will be left to future works. In recent years, ground shaping techniques have been further applied to the CPW grounds and/or even the ground planes of the microstrip for bandwidth enhancement [28-30]. The novelty of a single transition was presented in [31] to achieve low profile and minimize cost and space. To achieve field and impedance matching, the use of balun structures from an open-circuited microstrip line and a shorted-circuited CPW have been reported in [32]. Some of these

techniques are briefly illustrated in Figure 3.11 (a) to (h) where the transitions can be summarized to be effected by two methods namely, the electrical contact method and the electromagnetic coupling method.

The air bridge, via hole and ribbon type of transitions fall into the electrical contact category. These are illustrated below in Figure 3.11 (a) to (c). Those effected by electromagnetic coupling are illustrated in Figure 3.11 (d) to (h).

Air bridge



Via hole

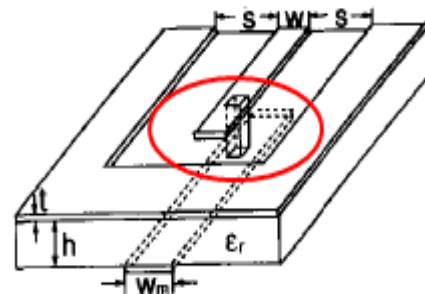


Figure 3.11 (a) Microstrip to CPW on GaAs chip substrate (b) Microstrip to CPW on opposite sides of a common substrate [18].

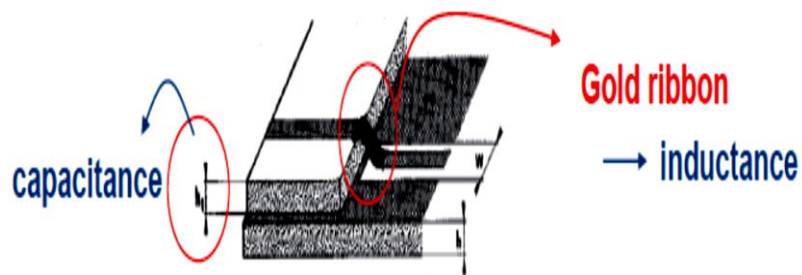


Figure 3.11 (c) Microstrip to CPW transition on superposition of two different substrates [35].

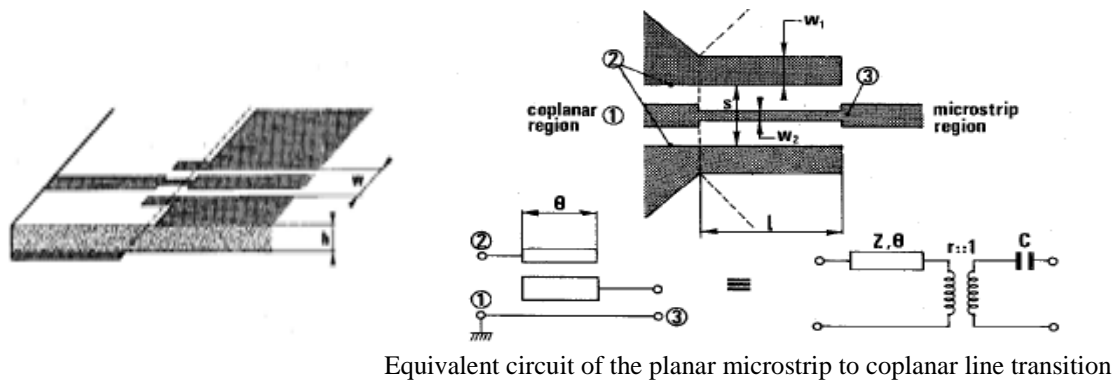


Figure 3.11 (d) Microstrip to CPW transition through electromagnetic coupling [35].

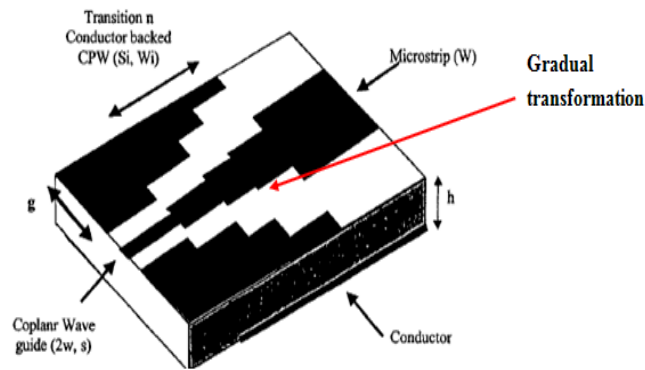


Figure 3.11 (e) Microstrip to CPW transition through gradual transformation [27].

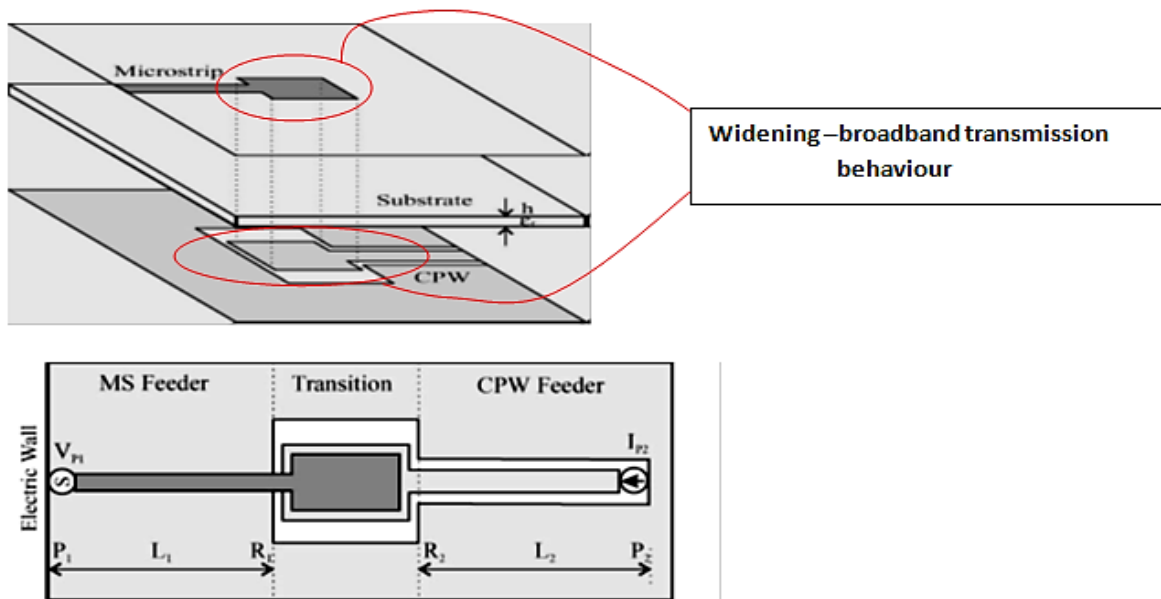


Figure 3.11 (f) Microstrip to CPW transition through electromagnetic coupling [31].

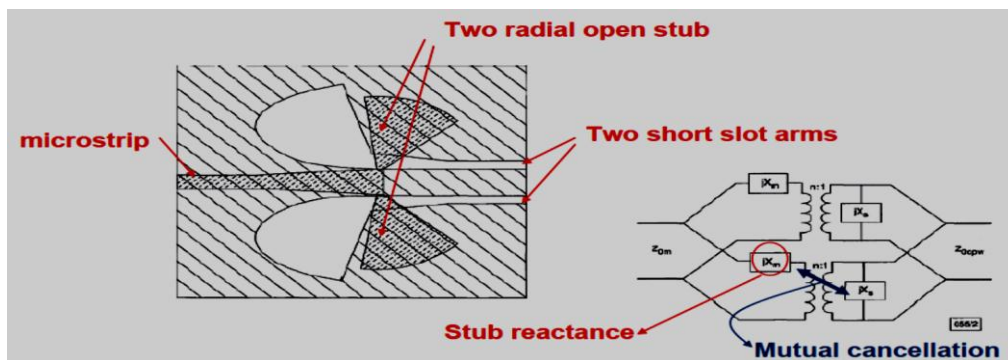


Figure 3.11 (g) Microstrip to CPW transition through electromagnetic coupling using radial stubs [26].

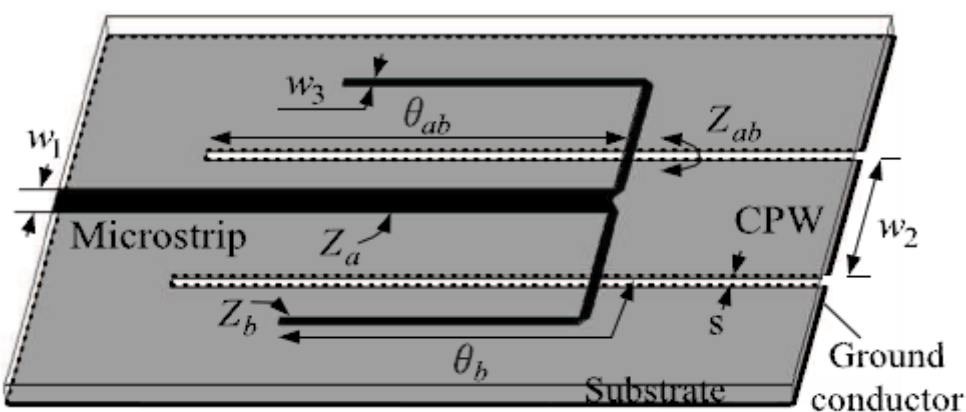


Figure 3.11 (h) Microstrip to CPW transition through electromagnetic coupling using folded baluns [33].

In the ribbon type, the ribbon is applied when the two different layers of substrate are super-positioned.

- the upper substrate works in a microstrip mode
- the lower substrate works in a coplanar mode

In this set-up as shown in Figure 3.11 (c), the continuity of the main line is achieved by a gold ribbon connecting the two photo-etched strips. In order to compensate the discontinuities produced by the open end of the microstrip (capacitance) [34] and by the inductance of the ribbon [35], a small capacitance is introduced at the beginning of the coplanar line making the transition act as a low pass filter whose maximum cut-off frequency is related to the height h_1 of the microstrip substrate.

The Electromagnetic Coupling Method approach uses the coupling between the ground plane of the microstrip and the ground planes of the coplanar line. There are few cases here. However, only five relevant types which have the possibility of being incorporated into the transparent antenna design will be discussed in this section.

An example of the first of these five types and its equivalent circuit is shown in Figure 3.11 (d). The *Planar Microstrip to Coplanar Line Transition* structure can be analyzed as a distributed band-pass filter whose center frequency is determined by the length of the coupling region.

The second type, *Microstrip to CPW Transition through Gradual Transformation* effects transition through gradual transformation of the electric and magnetic fields and constant impedance along the transition between the coplanar waveguide or conductor backed coplanar waveguide on one side and microstrip on the other (Figure 3.11(e)). As the number (n) of conductor backed CPW increases, the return loss, S_{11} decreases. Also, as the length of the transition increases, the bandwidth correspondingly increases.

The third type is the *Single Substrate Transition* illustrated in Figure 3.11 (f). This method effects coupling by enhancing the capacitive coupling in series between the microstrip and CPW stripconductors. An ultra-broad transmission behaviour is achieved by widening the twin slots in the CPW and further expanding the two strip conductors in width.

The fourth type is the *Radial Stub Transition*. The radial shape of the open stub & shorted arm allow wider bandwidth operation. The signal in this transition as shown in Figure 3.11 (g) is effectively transferred though resonant coupling.

The last type in this category is the *Parallel Folded Balun Transition* that uses two parallel folded balun structures as shown in Figure 3.11 (h), to achieve field and impedance matching. The baluns are incorporated into an open-circuited microstrip line which is electromagnetically coupled to a short-circuited CPW structure.

The knowledge obtained from some of the techniques mentioned earlier in this section is applied in the design of the transparent UWB antennas. This will be presented later in the next chapter on “Transparent UWB Antennas”.

3.7 Negating Unwanted Frequency Bands

It is also necessary for UWB to negate unwanted frequency bands to prevent interference and allow electromagnetic compatibility of a UWB system with existing wireless systems. Several methods have been proposed [36-41], to obtain the desired band notch characteristics in the UWB frequency bandwidth. These are basically physical configurations such as introduction of an attached element or removal of a part that provides the band notch characteristics. Attachment of a radiating part as in [36], introduction of a slot in [37], integration of a notch filter in [38], introduction of parasitic patches in [39] meander line filter to ground in [40] and simple grounded stubs in [41] are some of the techniques commonly used in UWB antenna design to block WLANs signals like the 2.4 GHz and the 5 GHz frequency bands. The techniques are summarized in Figure 3.12 (a) to (f).

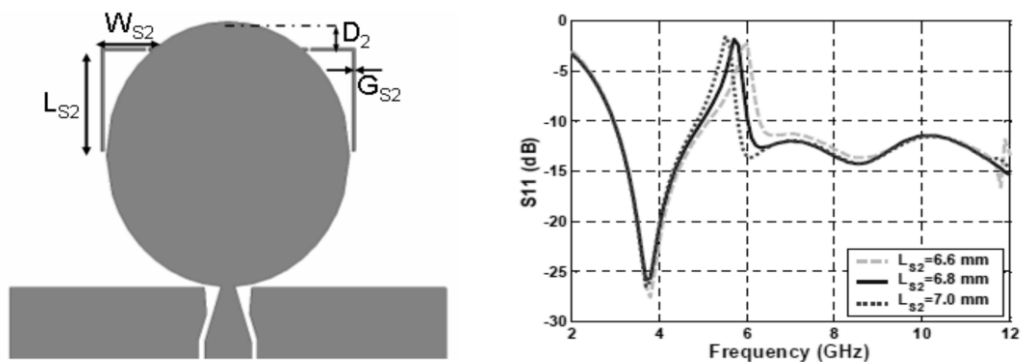


Figure 3.12 (a) Attachment of a radiating stub to implement a band notch [36].

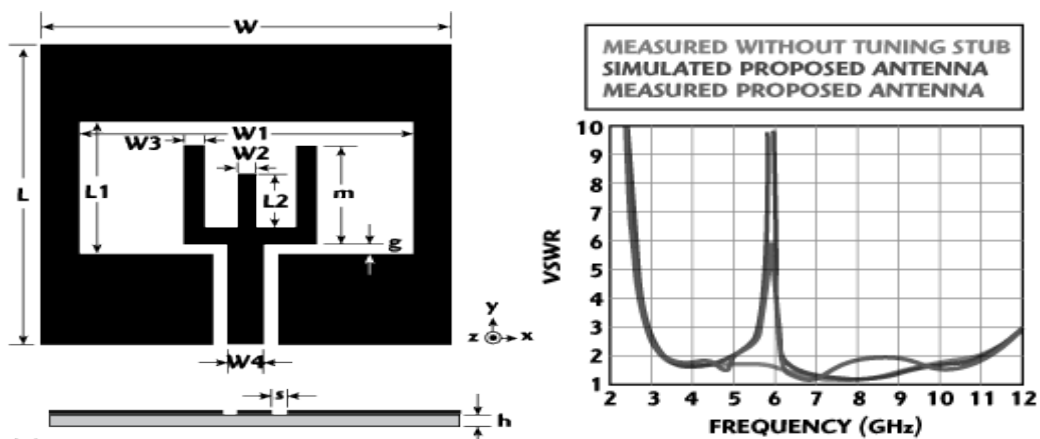


Figure 3.12 (b) A tuning stub approach to effect a band notch [37].

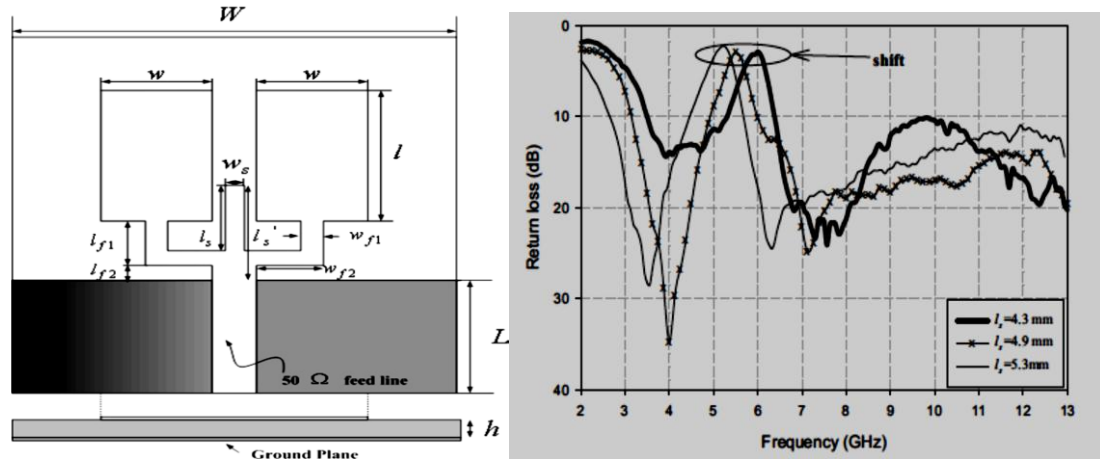


Figure 3.12 (c) Use of filter to give a band notch [38].

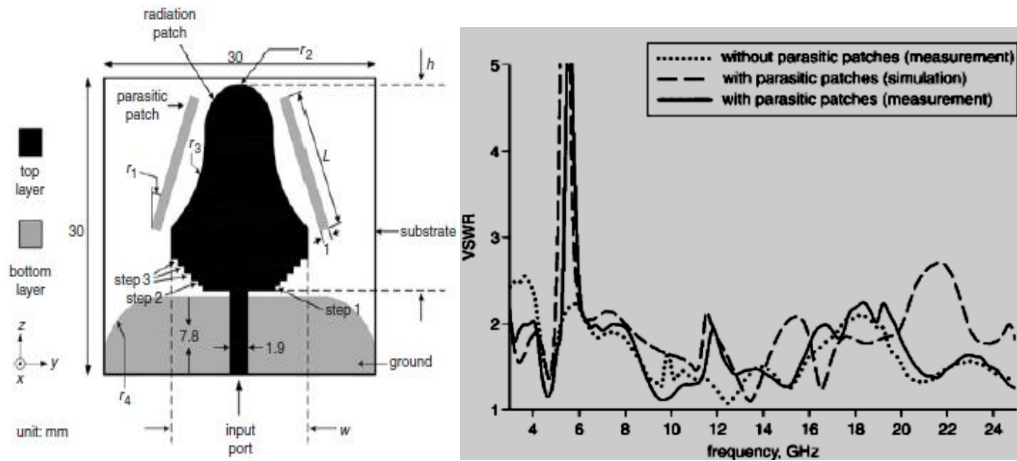


Figure 3.12 (d) Band notch through inclusion of parasitic patches [39].

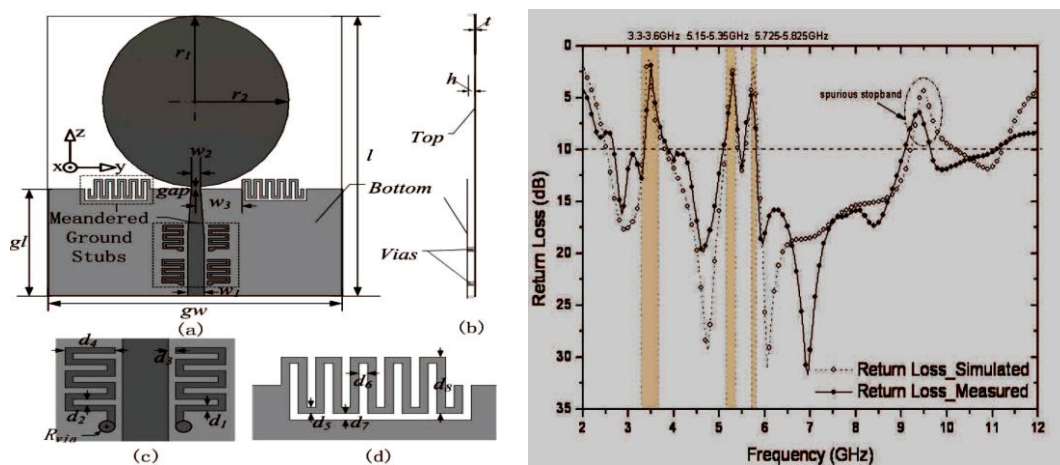


Figure 3.12 (e) Meandered lines being used to create band notches for the unwanted frequencies [40].

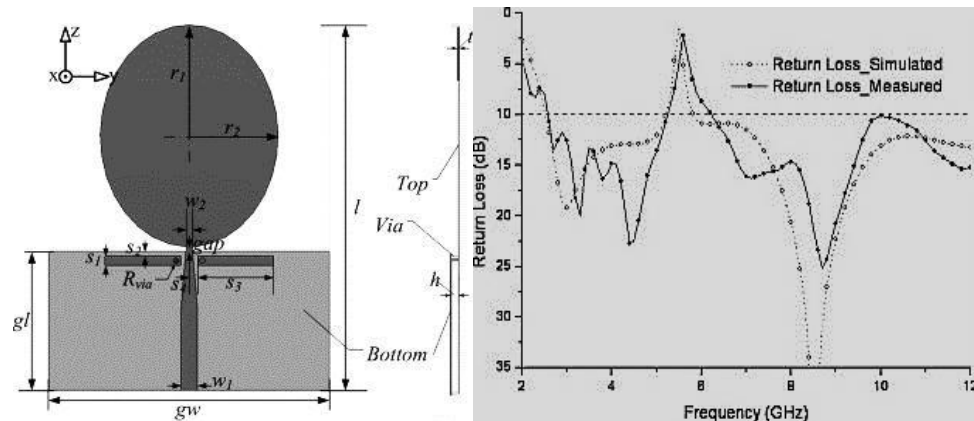


Figure 3.12 (f) Use of grounded stubs to achieve a band notch [41].

3.8 Summary

A quick review of the work done on non-transparent or opaque UWB was presented in this chapter to build the knowledge on which eventually transparent antennas were built. The techniques and approaches greatly aided in the design and fabrication of the transparent antenna although the materials were different and posed great challenges in identifying the characteristics and properties of the AgHT and PET material from scratch at times to build the antennas in order to have simulation results close to actual.

Feed techniques and approaches as how to negate unwanted bands were either utilized directly or modified to suit the transparent antenna design and environment and location where it was designed to be used. For example, the ribbon contact method was eventually modified to provide a contact from the back of the polymer substrate to the CPW feed of the antenna when used in the superstrate configuration when placed on glass. This would make it easy for the transparent antenna to be laminated on glass without the feed connection being a hindrance to connect the transmitter as well as keep the aesthetics of the window glass environment.

3.9 References:

- 1) H.G. Schantz, "Introduction to UWB antennas," *IEEE Conference on Ultra Wideband Systems and Technologies*, Reston, Virginia. pp. 1-9, November 16-19, 2003.
- 2) H.G. Schantz, "Dispersion and UWB Antennas", *Proc. Conf. Ultrawideband Systems and Technologies*, pp. 161-165, May 2004.
- 3) H.G. Schantz, "*The Art and Science of Ultrawideband Antennas*". ArtechHouse, Inc., Norwood, MA, 2005.
- 4) K. Fujimoto, "Mobile Antenna Systems Handbook", Artech House Inc. 2008.
- 5) D. Valderas, J. Legarda, I. Gutierrez and J.I. Sancho, "Design of UWB folded-plate monopole antennas based on TLM," *IEEE Transactions on Antennas and Propagation*, vol. 54, no. 6, pp. 1676-1687, June 2006.
- 6) J. Liang, L. Guo, C.C. Chiau, X. Chen and C.G. Parini, "Study of CPW-fed circular disc monopole antenna for ultrawideband applications," *IEEE Proceedings-Microwaves, Antennas and Propagation*, pp. 520- 526, Dec. 9, 2005.
- 7) S.W. Bae, H.K. Yoon, W.S. Kang, Y.J. Yoon and C.H. Lee, "A Flexible Monopole Antenna with Band-notch Function for UWB Systems," *Asia-Pacific Microwave Conference, APMC 2007*, pp. 1-4, Dec. 11-14, 2007.
- 8) M. J. Ammann, "Control of the Impedance Bandwidth of Wideband Planar Monopole Antennas using a Bevelling Technique." *Microw. Opt. Tech. Letters*, vol. 30 (4), pp. 229-232, July, 2001.
- 9) W. Wang, S.S. Zhong and S.B. Chen, "A novel wideband coplanar-fed monopole antenna," *Microwave Opt. Technol. Lett.*, vol. 43, pp 50–52, 2004.
- 10) S. Nikolaou, D.E. Anagnostou, G.E. Ponchak, M.M. Tentzeris and J. Papapolymerou, "Compact Ultra Wide-Band (UWB) CPW-fed Elliptical Monopole on Liquid Crystal Polymer (LCP)," *IEEE Antennas and Propagation Society International Symposium 2006*, pp.4657-4660, July 9-14, 2006.
- 11) H. G. Schantz, "Bottom fed planar elliptical UWB antennas," in *Proc. IEEE Conf. Ultra Wideband Syst. Technol.*, pp. 219–223, Nov. 2003.
- 12) D.H. Kwon and Y. Kim, "CPW-fed planar ultra-wideband antenna with hexagonal radiating elements," in *Proc. IEEE Antennas Propagat. Soc. Int. Symp.*, vol. 3, Monterey, CA, pp. 2947–2950, June 2004.
- 13) T. Yang and W.A. Davis, "Planar half-disk antenna structures for ultrawideband communications," in *Proc. IEEE Antennas Propagat. Soc. Int. Symp.*, vol. 3, Monterey, CA, Jun. 2004, pp. 2508–2511.

- 14) S.Y. Suh, W. Stutzman, W. Davis, A. Waltho and J. Schiffer, "A novel CPW-fed disc antenna," in *Proc. IEEE Antennas Propagat. Soc. Int. Symp.*, vol. 3, Monterey, CA, pp. 2919–2922, Jun. 2004.
- 15) T.W. Hertel, "Cable-current effects of miniature UWB antennas," in *Proc. IEEE Antennas Propagat. Soc. Int. Symp.*, vol. 3A, Washington, DC, pp. 524–527, Jul. 2005.
- 16) D.H. Kwon and Y. Kim, "Suppression of cable leakage current for edge-fed printed dipole UWB antennas using leakage-blocking slots," *IEEE Antennas and Wireless Propagation Letters*, Vol. 5, 2006.
- 17) G. Strauss, P. Ehret and W. Menzel, "On-wafer measurement of microstrip-based MIMICs without via holes," *IEEE MTT-S International Microwave Symposium Digest*, 1996, vol.3, pp.1399-1402, Jun 17-21, 1996.
- 18) J. Hang, R. Vahldieck, J. Huang and P. Russer, "Rigorous analysis of mixed transmission line interconnects using the frequency-domain TLM method," *IEEE Transactions on Microwave Theory and Techniques*, vol.41, no.12, pp.2248-2255, Dec 1993.
- 19) B. Golja, H. Sequeira, G. Mendenilla and N. Byer, "A coplanar-to-microstrip transition for W-band circuit fabrication with 100-um-thick GaAs wafers," *IEEE Trans. Microwave and Guided Wave Lett.*, pp. 29-31, Feb. 1993.
- 20) J. Izadian and S. Izadian, "*Microwave Transition Design*" Norwood, MA: Artech House, 1988.
- 21) Z. Guizhen, J. Papapolymerou and M.M. Tentzeris, "Wideband coplanar waveguide RF probe pad to microstrip transitions without via holes," *IEEE Microwave and Wireless Components Letters*, vol.13, no.12, pp. 544- 546, Dec. 2003.
- 22) N.I. Dib, R.N. Simons and L.P.B. Katehi, "New uniplanar transitions for circuit and antenna applications," *IEEE Transactions on Microwave Theory and Techniques*, vol.43, no.12, pp.2868-2873, Dec 1995.
- 23) M. Houdart and C. Aury, "Various excitation of coplanar waveguide," *IEEE MTT-S Int. Microwave Symp. Dig.*, vol. 79, no. 1, pp.116-118, 1979.
- 24) T. Chiu, "A building-block design scheme for planar transmission-line transitions," *IEEE Proceedings-Microwaves, Antennas and Propagation*, vol.150, no.6, pp. 405-410, Dec 2003.
- 25) D.F. Williams and T.H. Miers, "A coplanar probe to microstrip transition," *IEEE Trans. on Microwave Theory & Tech.*, vol.36, no.7, pp.1219-1223, 1988.
- 26) T.H. Lin, "Via-free broadband microstrip to CPW transition," *Electronics Letters*, vol.37, no.15, pp.960-961, 19 Jul 2001.

- 27) A. M. E. Safwata, K. A. Zaki, W. Johnson and C. H. Lee, "Novel design for coplanar waveguide to microstrip transition," *IEEE MTT-S Int. Microwave Symp. Dig.*, vol.2, pp.607-610, 2001.
- 28) L. Zhu, K.L. Melde and J.L. Price, "A broadband microstrip-to-CPW vialess transition for on wafer package probing applications," *Proceedings of IEEE 12th Topical Meeting on Electrical Performance of Electronic Packaging, EPEP 2003*, pp.75-78, 2003.
- 29) C. Dengpeng, W. Quanxin and S. Zhongxiang, "A broadband microstrip-to-CPW transition," *Asia-Pacific Microwave Conference Proceedings, 2005. APMC 2005*, vol.2, no., pp. 4 pp., Dec. 4-7, 2005.
- 30) K. Young-Gon, W.K. Kang and C. Young-Ki, "An ultra-wideband microstrip-to-CPW transition," *IEEE MTT-S International Microwave Symposium Digest*, 2008 pp.1079-1082, June 15-20, 2008.
- 31) Z. Lei and W. Menzel, "Broad-band microstrip-to-CPW transition via frequency-dependent electromagnetic coupling," *IEEE Transactions on Microwave Theory and Techniques*, vol.52, no.5, pp. 1517- 1522, May 2004.
- 32) K. Young-Gon, W.K. Kang and C. Young-Ki, "An ultra-wideband microstrip-to-CPW transition," *IEEE MTT-S International Microwave Symposium Digest*, 2008, pp.1079-1082, June 15-20, 2008.
- 33) B. Jung-Woo, L. Tae-Hak and K. Young-Sik, "Novel broadband microstrip-to-CPW transition with easy transmission band control," *IEICE Electronics Express*, Vol.5, No.2, 48-52.
- 34) O.P. Jain, V. Makios and W.J. Chudobiak, "Open-End and Edge Effect in Microstrip Transmission Lines (Short Papers)," *IEEE Transactions on Microwave Theory and Techniques*, vol.20, no.9, pp. 626- 628, Sep 1972.
- 35) M. Houdart, C. Aury and A. Jean-Frederic, "Coplanar Lines : Application to Lumped and Semi-Lumped Microwave Integrated Circuits," *7th European Microwave Conference, 1977*, pp.450-454, Sept. 5-8, 1977.
- 36) N. Symeon, "Design and Implementation of Compact Reconfigurable Antennas for UWB and WLAN Applications", PhD Thesis, Georgia Institute of Technology, Atlanta, Georgia, August 2007.
- 37) C.Y. Liu, Y.S. Li and T. Jang, "Compact CPW-Fed UWB Antenna with a Notched Band Characteristic", *Microwave Journal*, vol. 54, No. 8, Page 104, 2011.
- 38) K. Chung, S. Hong and J. Choi, "Ultrawide-band printed monopole antenna with band-notch filters", *IET Microw. Antennas Propag.*, vol. 1, p.518, 2007.
- 39) K.H. Kim, Y.J. Cho, S.H. Hwang and S.O. Prak, "Band-notched UWB planar monopole antenna with two parasitic patches", *Electronic Letters*, vol. 41, 2005.

- 40) Y.F. Weng, S.W. Cheung and T.I. Yuk, "Triple band-notched UWB antenna using meandered ground stubs," *Antennas and Propagation Conference (LAPC), 2010 Loughborough*, pp.341-344, Nov. 8-9, 2010.
- 41) Y.F. Weng, S.W. Cheung and T.I. Yuk, "Compact ultra-wideband antennas with single band-notched characteristic using simple ground stubs", *Microwave and Optical Technology Letters*, vol. 53, pp. 523–529, 2011.

CHAPTER 4

Transparent UWB Antennas

4.1 Introduction

Basing on the knowledge of the effects of varying the various parameters and dimensions of UWB antennas as presented in Chapter 3, different configurations depending on the applications, such as the transparent mushroom top antenna (MTA), modified version of the Knight's Helm antenna (KHA), TSA antenna and other array configurations were fabricated on AgHT and experimentally verified for use in UWB applications.

A novel technique to improve gain and efficiency [1] as a contribution to the development and improvement of transparent antennas is also presented in this chapter. An analysis is further done to investigate coupling in transparent antennas as well as the phenomena of proximity insensitiveness demonstrated by the fabricated prototypes to see how these features could be used to improve transparent antenna utilization in a practical environment.

PET has also been known to be used as a component in radar absorbent material (RAM) products in anechoic chambers as well as stealth works in the military to disguise a vehicle or structure from radar detection. A Japanese company [2] has also recently developed and exhibited an ITO /PET film absorber for the 5.8 GHz frequency band further affirming the fact that metallized polyesters like PET have good RAM properties. RAM coatings are used in stealth technology to reduce RCS. The RCS property of AgHT is thus also analysed in this chapter to see how it can make AgHT transparent antennas suitable for stealth technology. However, this analysis is only done in simulation due to lack of facilities and restrictions imposed on conducting RCS measurements at test facilities by the defence ministry.

4.2 Modelling and Design of Transparent UWB Antennas

The transparent UWB antennas were designed and modelled using the CST simulation software. The MTA of which more is discussed in section 4.3 is used as an example to demonstrate the modelling process.

First, a project template with the desired units, background material and boundary conditions are chosen. This is done by selecting a ready-made template which is available in the “Create a New Project” dialog box of the software. Here, a planar antenna is selected as shown in Figure 4.1 for designing the MTA.

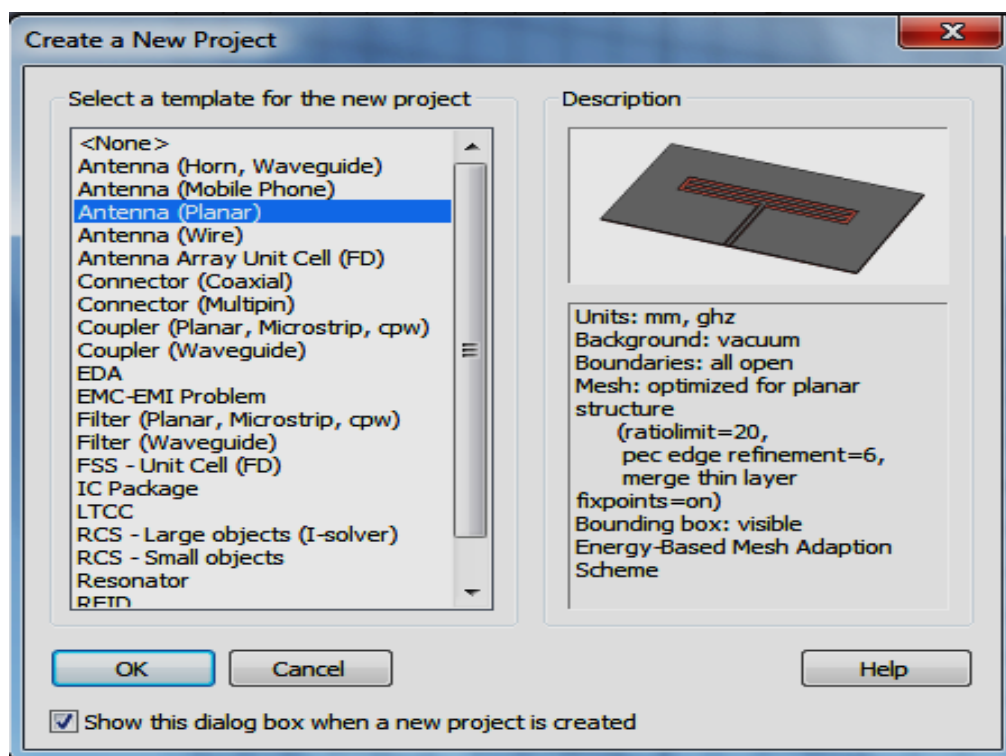


Figure 4.1 Selection of the project template for creating the MTA design project.

Next the materials to be used in the design of the UWB antenna were to be chosen from the material library. However, since the material, AgHT was not available in the material library, this had to be defined and loaded into the library before it could be used to design the antenna. The new material was defined and loaded as shown in the figures that follow. The AgHT was made of a conductive layer coated on a PET base. Although the conductive layer

is a three layered structure of silver oxide sandwiched between two layers of tin oxide, it will be represented as a single layer with the manufacturer's specified conductivity of 125,000 S/m if using AgHT-8 and 250,000 S/m if using AgHT-4. The AgHT-8's Type and conductivity are defined as shown in Figure 4.2 and added to the material library. The PET material is then defined and added similarly as shown in Figure 4.3.

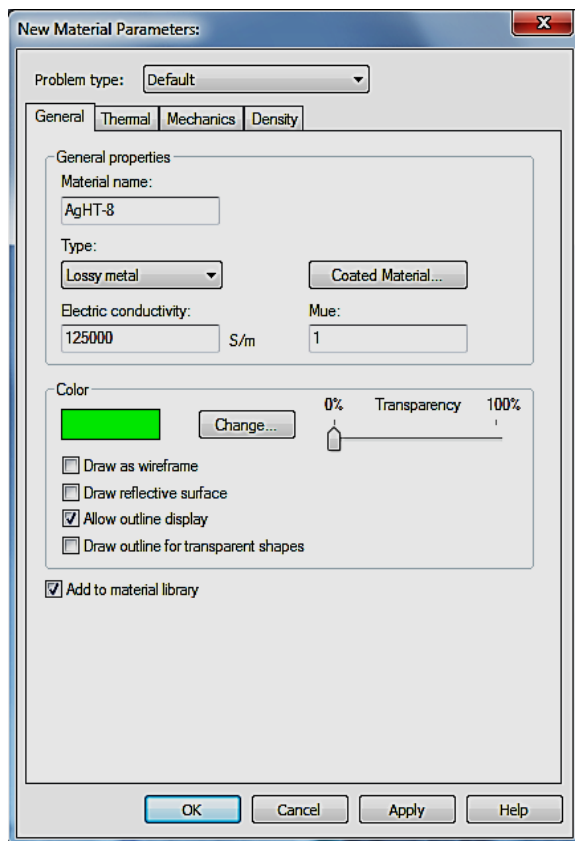


Figure 4.2 Creating the AgHT-8 conducting material.

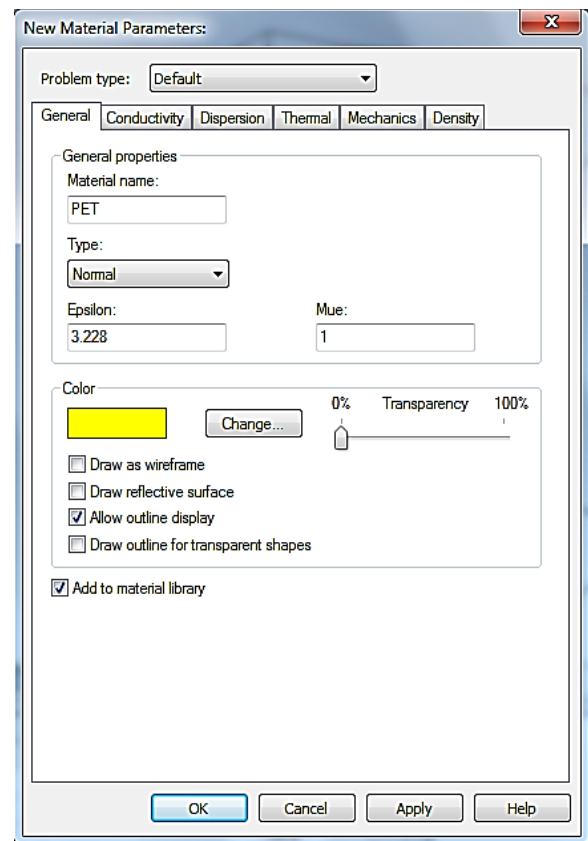


Figure 4.3 Creating the PET material.

For the PET, the permittivity is defined by including a dispersion fit of the loss tangent to describe the losses of the PET material. The dispersion fit was obtained by extrapolation of the measured dielectric values of the PET for 1.8 GHz, 3.9 GHz and 10 GHz. The measurements were done at the National Physics Laboratory (NPL) at Teddington, UK. Fig. 4.4 shows the dispersion list. As the permeability values (Mue) of the PET were not able to be measured and also not available in published documents, it was assumed to be 1. This is reflected in Figure 4.3. The same material settings were used for the rest of the UWB antenna designs presented in the later chapters of this thesis.

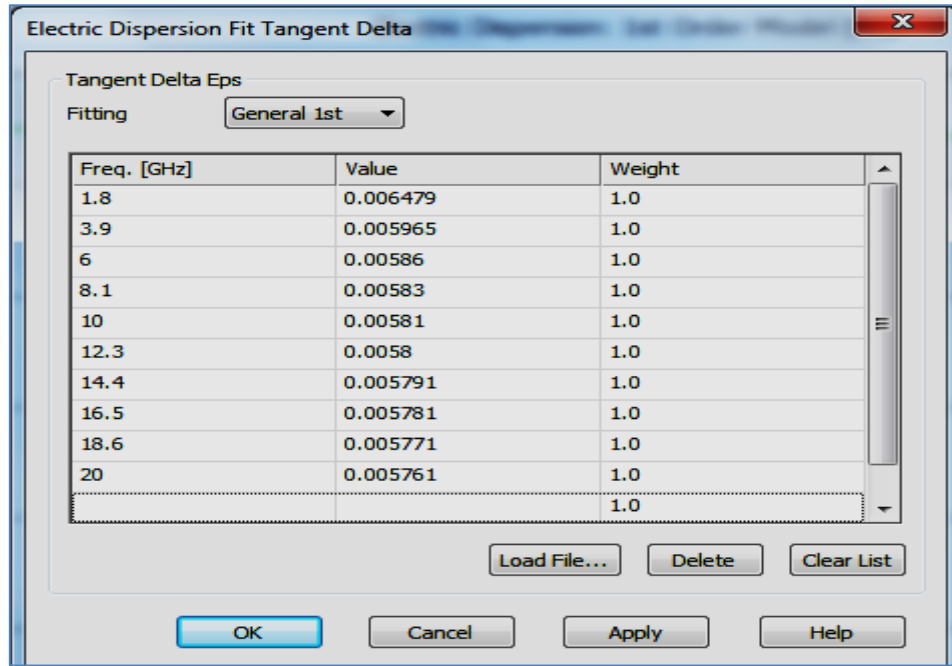


Figure 4.4 Loss tangent dispersion list to reflect the losses in the PET.

Once this was done the desired geometry of the MTA was drawn in CST with the appropriate materials as shown in Figure 4.5.

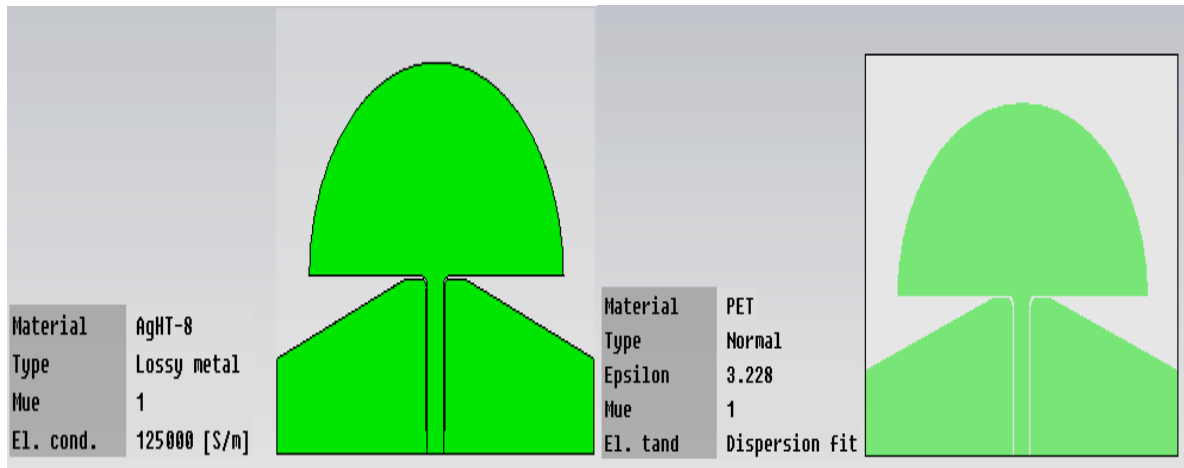
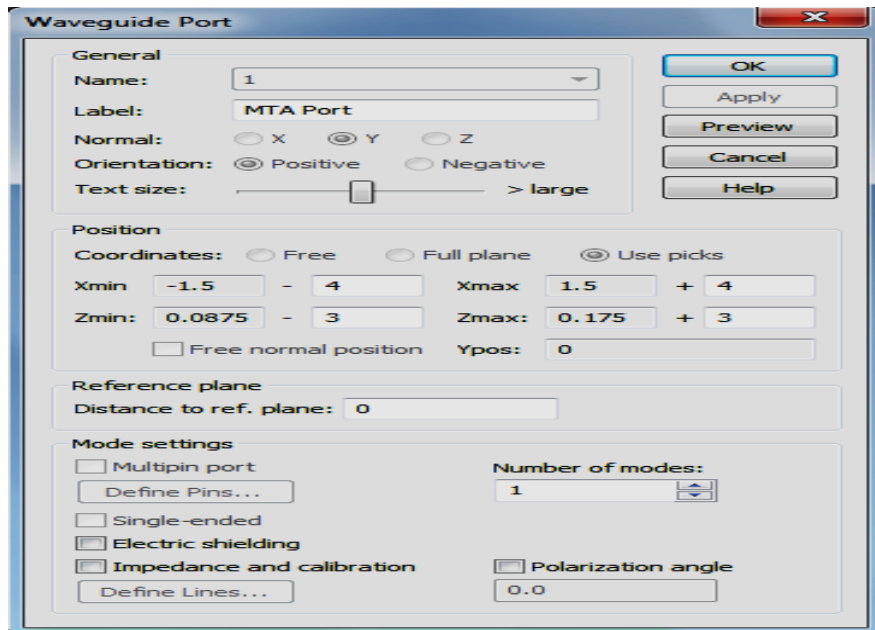
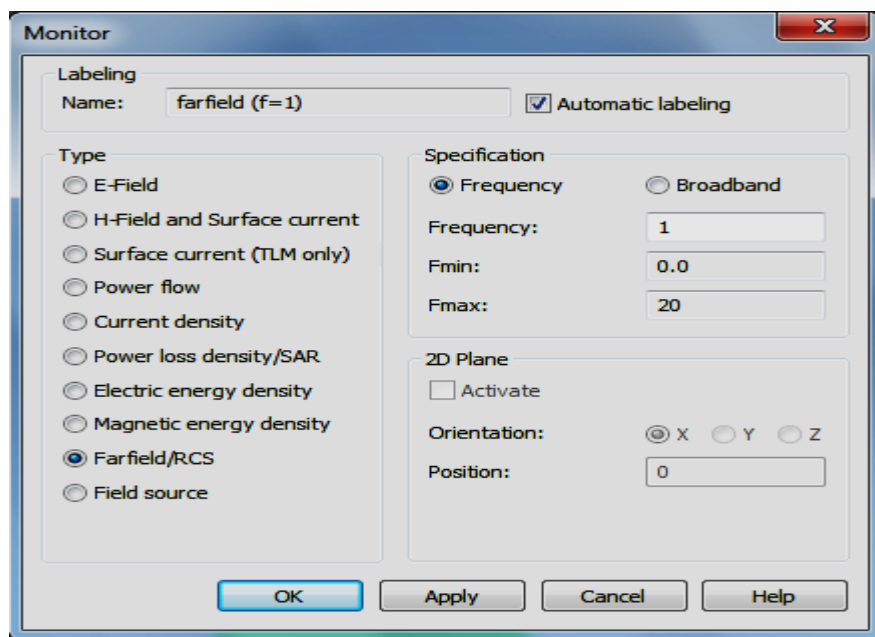


Figure 4.5 The created MTA design using the new material properties that were uploaded.

A waveguide port was then created with the desired frequency range and necessary field monitors to obtain the current and farfield results for the simulation. These are depicted in Figure 4.6.



(a)



(b)

Figure 4.6 (a) Creation of waveguide port (b) Activating monitors to show farfield results.

A post processing template is then activated as in Figure 4.7 with the required macros for S11, gain and efficiency to tabulate into graphs the simulated results for easy interpretation.

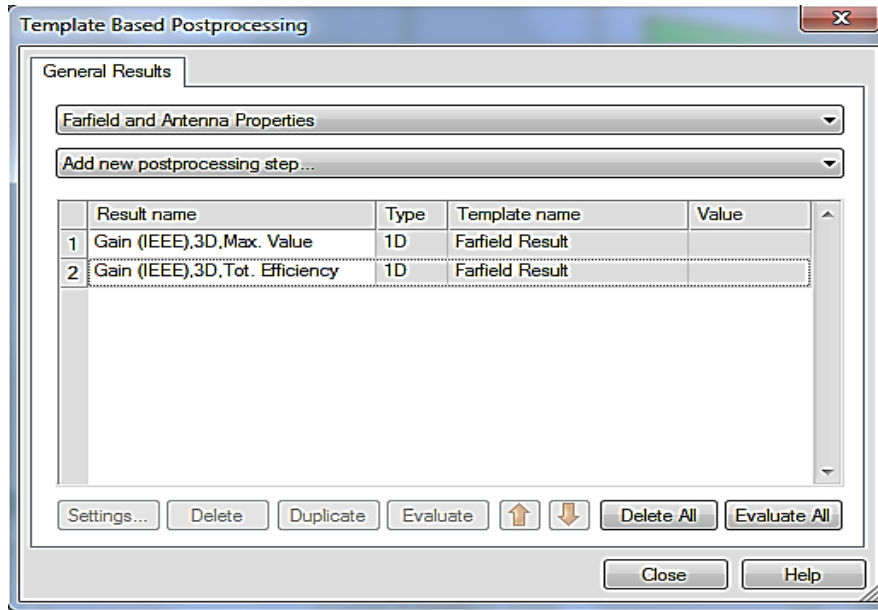


Figure 4.7 Activating postprocessing steps to tabulate into graphs.

The design as shown in Figure 4.8 is then ready for simulation. The transient solver which is a time domain solver is selected for the simulation.

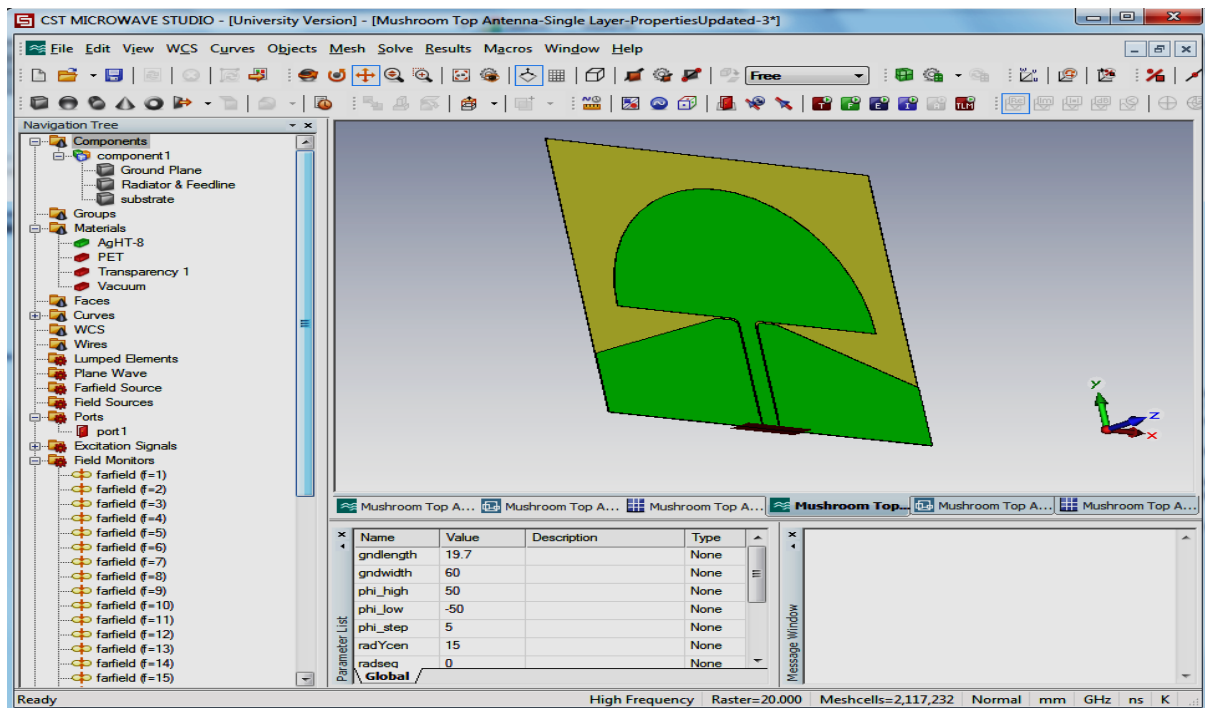


Figure 4.8 Final design of the MTA to be simulated using the transient solver.

The simulated return loss, S11 was optimized to obtain an ultra-wide -10 dB bandwidth. This was done by optimizing the inclines of the bevel edges of the CPW ground plane, the feed gap and the resonators on the internal walls of the CPW ground along the feed gap as shown in Figure 4.9 to obtain a 50 Ohm impedance matching at the port. Figure 4.10 and Table 4-1 give the geometry and optimized dimensions for the designed MTA respectively.

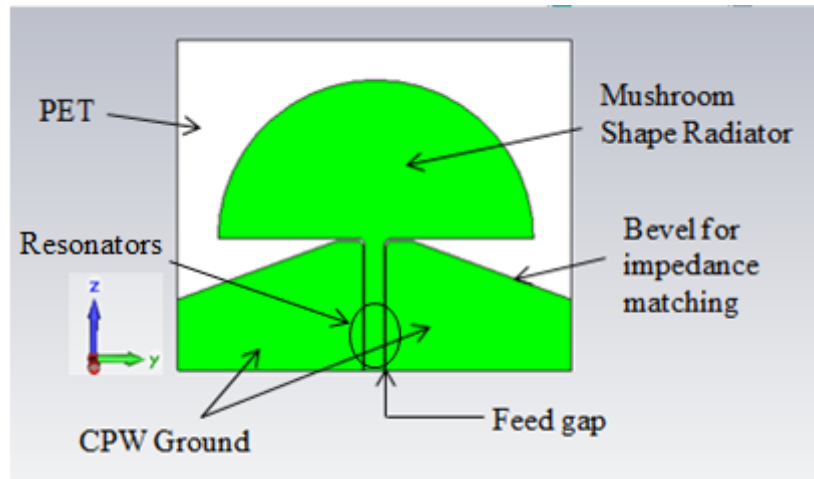


Figure 4.9 Geometry of the designed MTA illustrating the various parts of the antenna.

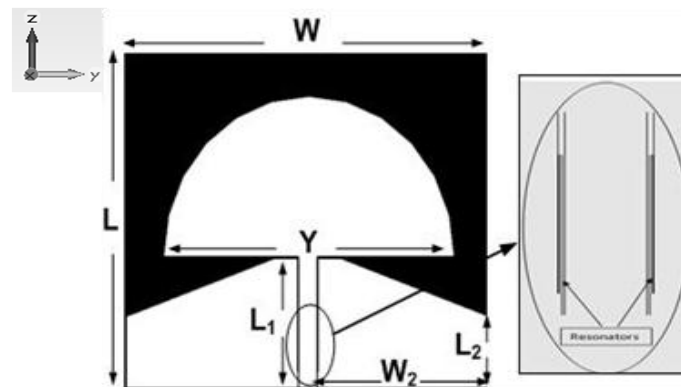
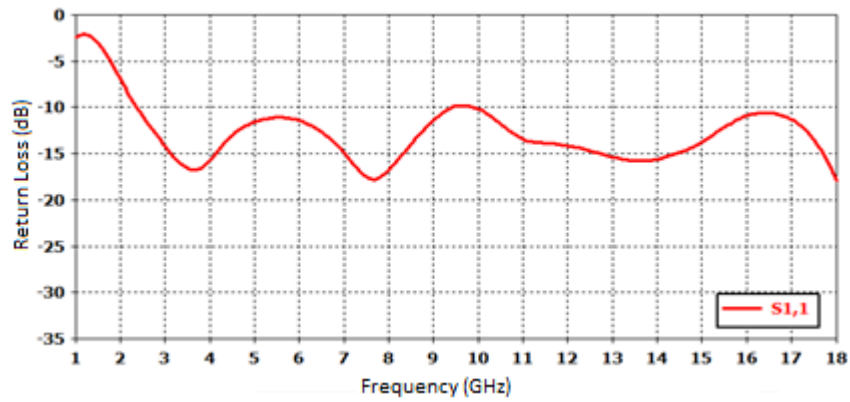


Figure 4.10 Geometry of the optimized MTA design with inset showing the resonators for impedance matching.

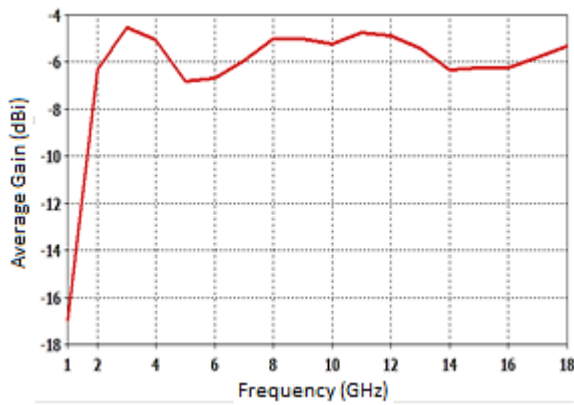
Table 4-1 Dimensions of the antenna structure in Figure 4.10

Parameters	L	W	Y	L ₁	L ₂	W ₂
Size (mm)	50	60	48	20	11	28.4

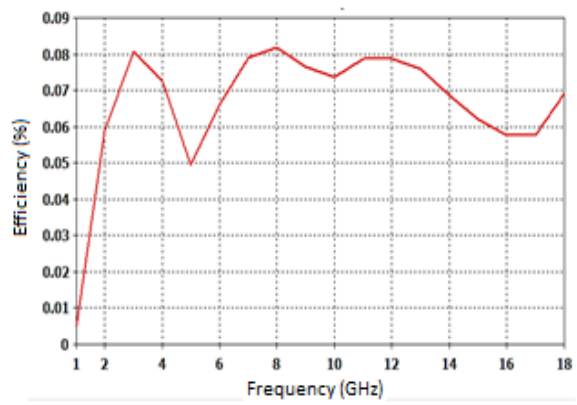
The simulated return loss, gain, efficiency and 3-D radiation far field patterns at 5 GHz and 7 GHz for the MTA are shown in Figure 4.11.



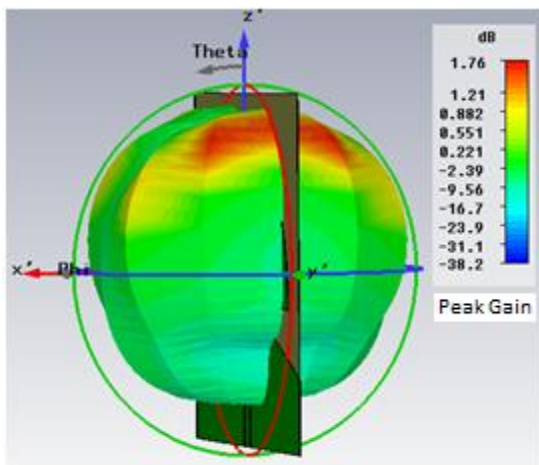
(a)



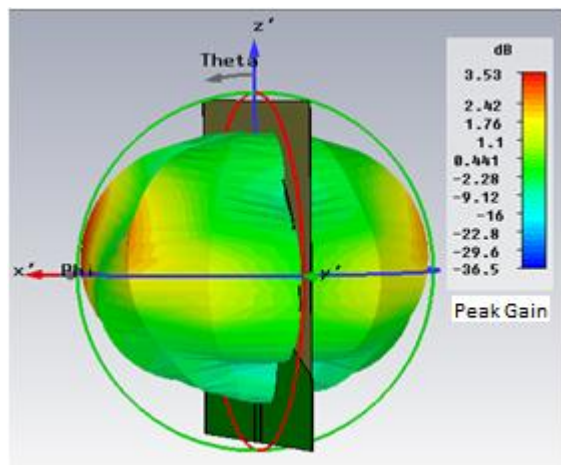
(b)



(c)



(d)



(e)

Figure 4.11 Simulated results for the MTA: (a) return loss (b) average gain (c) efficiency; 3-D radiation patterns showing the peak gain at (d) 5 GHz and (e) 7 GHz.

4.3 The Mushroom Top UWB Antenna

The initial design of the antenna was designed as a two-layered antenna (Figure 4.12 and Figure 4.13 [1]) with the antenna design cut-off and glued using a transparent adhesive onto a sheet of PET substrate.

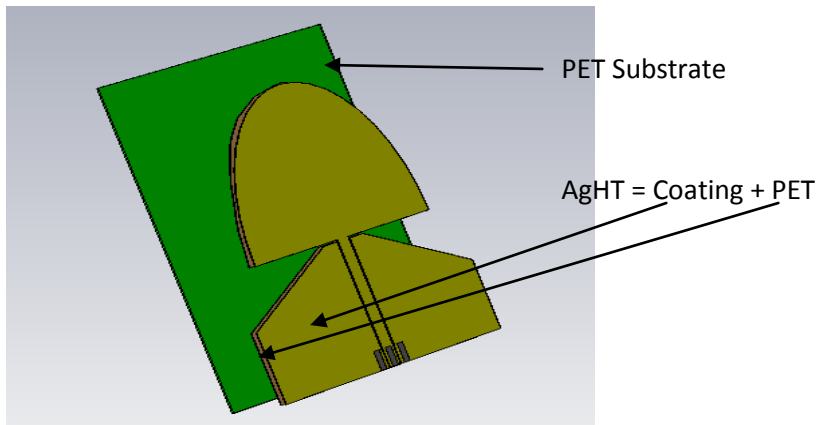


Figure 4.12 3D Layout showing the two-layered structure of the antenna.

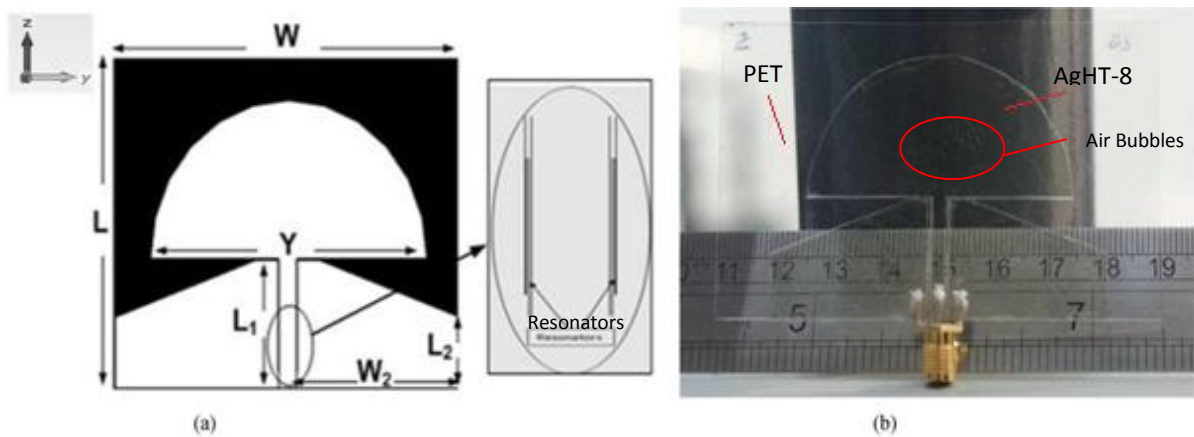


Figure 4.13 (a) Layout of the two-layered antenna (b) prototype of the antenna.

Some effect on the antenna performance was noticed as a result of the adhesive. It was difficult to achieve a uniform spread of the vinyl plastic adhesive (BondLoc) that was used. This caused air bubbles to be trapped in between the AgHT-4 and PET layers. This resulted

in the adhesive becoming a mixture of minute trapped air bubbles and adhesive. As the properties of the adhesive were not known in terms of its dielectric or otherwise, it was difficult to determine or have a quantitative measure of its real impact on the antenna performance. The use of adhesive and its impact on the maximum transfer of electromagnetic energy from a coaxial cable via copper pads glued to the surface of transparent polymer antennas has already been highlighted in [3].

This issue and the difficulty encountered in properly pasting the AgHT profile of the antenna on to the PET, initiated a relook on the design whether it could be done without the PET as the AgHT material itself comprised of a transparent conductive coating on a very thin PET base. A new design approach was taken and a single layered antenna was developed.

4.3.1 Parametric Study - Impedance Matching Through Resonators

However, before the single layer approach is discussed further, the workings of the resonator feature mentioned in the earlier section would be described briefly in regard to its use in impedance matching. Impedance matching through the resonators is achieved by varying their heights. Increasing or reducing the height of the resonators gave the flexibility of tuning the bandwidth to obtain the optimized bandwidth range. A parametric study was done to obtain the optimum height of the resonators; the external height opposite the feed line was 13 mm whilst the shorter internal height of the resonator stub was 10.2 mm for the best impedance match as depicted in Figure 4.14.

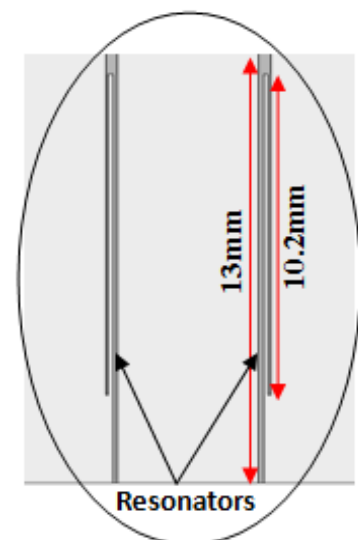


Figure 4.14 Resonator dimensions

4.3.2 Conformability and Flexibility of the Antenna

Another feature that needs to be highlighted is that the AgHT polymer film is flexible. As such can it can be flexed or conformed to the shape of the mount like circular columns or

right angle corners or the edge of a laptop. However, there is a slight limitation to this with regard to the smallest antenna size that can be conformed. Experimentally, it is possible to bend antennas with a width 30 mm and above. Below that because of the ground connection to the connector legs for example, in CPW feeds, makes it difficult to bend. This may be overcome through the use of cable wire connections. Also a 90 degree bending of a small width antenna might introduce a break in the silver layer creating a disconnect in conductivity. In such cases a 120 degree bend angle is the maximum suggested to avoid any disconnect as illustrated in Figure 4.15.

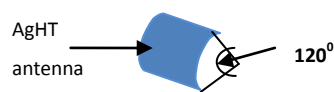
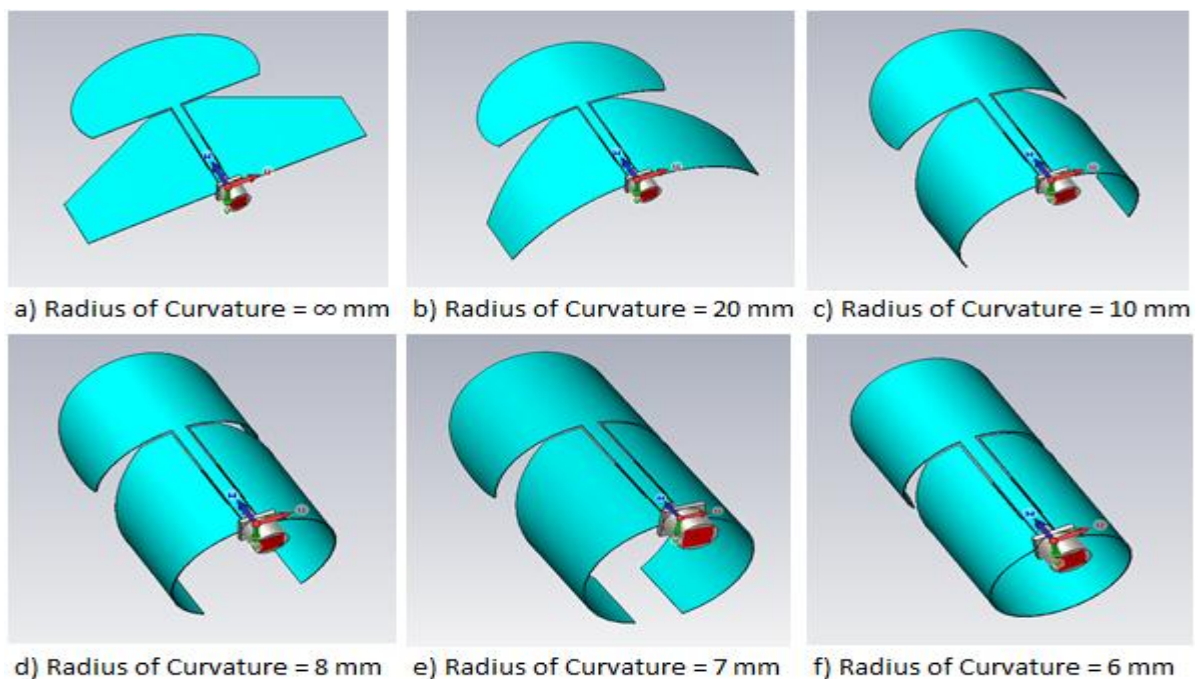
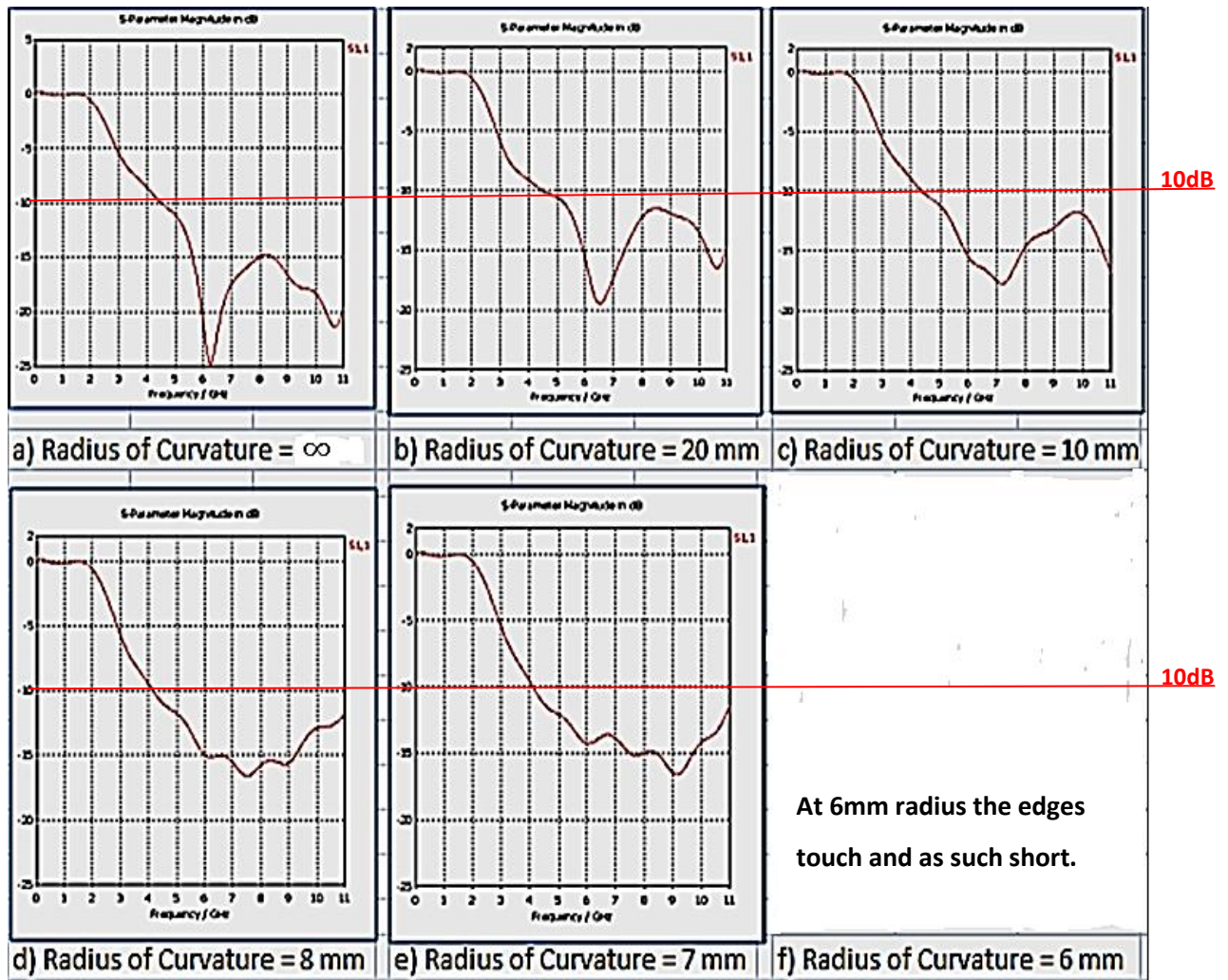


Figure 4.15 Maximum bend angle recommended for antennas smaller than 30 mm in width.

The effect on the performance of the mushroom top antenna during bending or conforming it through various radius of curvature was studied in simulation. The simulated S11 seemed to improve rather than deteriorate as the radius or bend angle gets smaller as depicted in Figure 4.16.



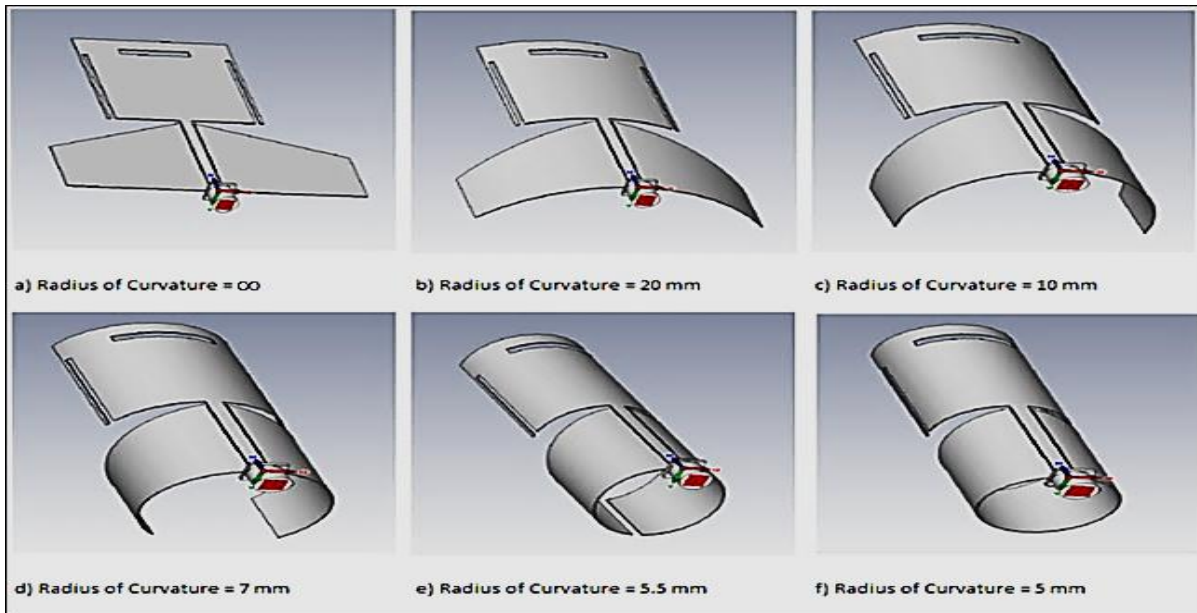
(a)



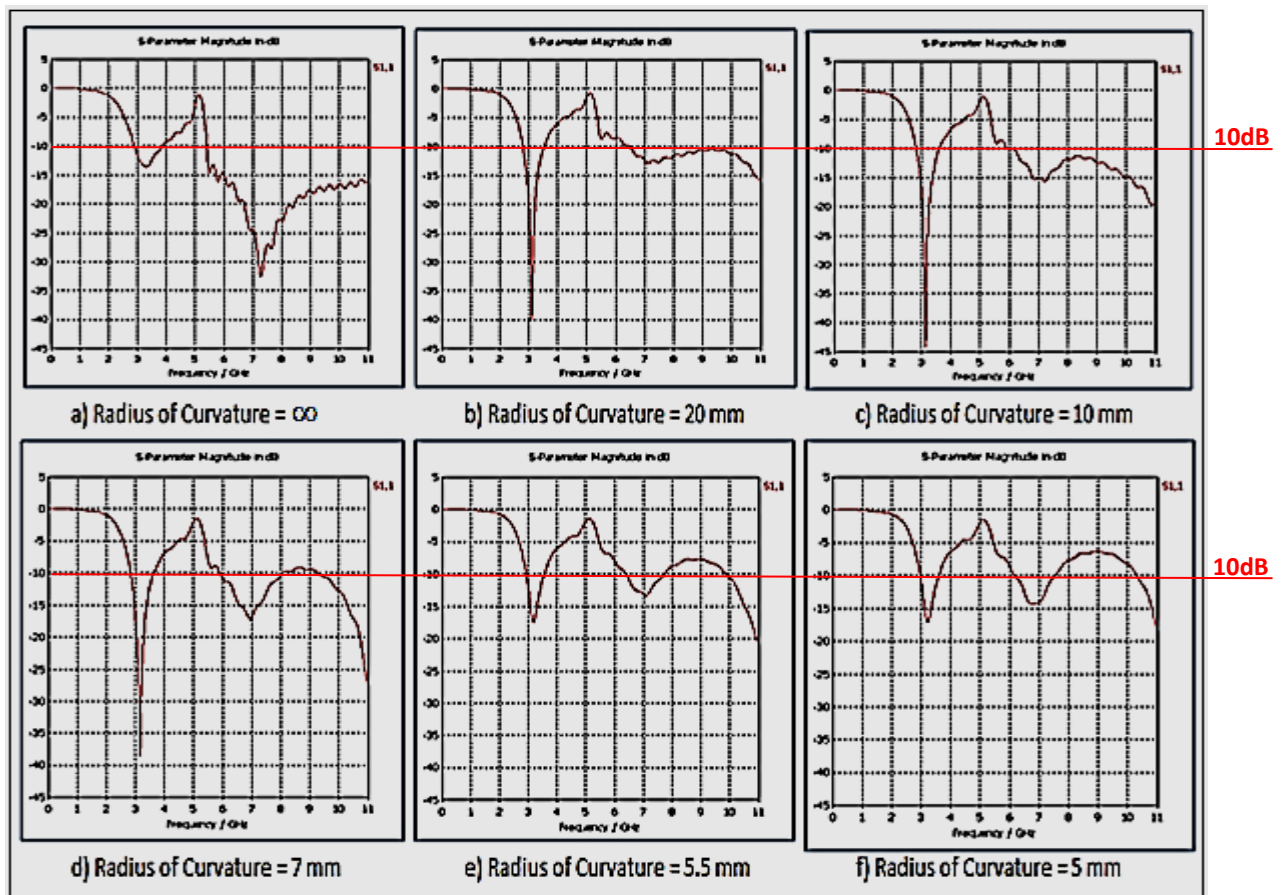
(b)

Figure 4.16 (a) AgHT Antenna being flexed through various radius of curvatures (b) return loss of the antenna for the various radius of curvatures.

A copper antenna was also simulated but its return loss deteriorated the more it was bent or flexed as shown in Figure 4.17. The AgHT-8 antenna as depicted in Figure 4.16 (b) showed a better S-parameter response compared to that of the Copper Film antenna as shown in Figure 4.17 (b) for a planar surface. The AgHT-8 antenna also delivered a stable performance throughout its flexure that is; it was able to maintain its return loss below the 10dB line for the various radius of curvature. This makes it a desirable feature for conformal antennas and highlights the potentials of AgHT-8 being a good candidate for overcoming performance deterioration during bending in body motion for wearable antennas.



(a)



(b)

Figure 4.17 (a) Copper Film Antenna being flexed through various radius of curvatures (b) return loss of the antenna for the various radius of curvatures.

4.3.3 Single Layered Mushroom Top Antenna

The single layer approach was developed by eliminating the additional PET base and directly inscribing the mushroom top geometry on to the AgHT film as shown below in Figure 4.20. This approach removed the use of glue and gave the antenna even more flexibility of bending and conformability besides ease of fabrication.

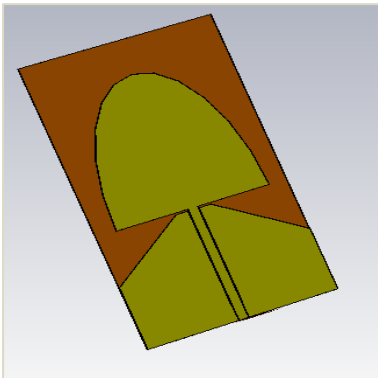


Figure 4.18 Geometry of antenna directly inscribed onto the AgHT film.

4.4 A Method to Improve the SMA to Antenna Connection

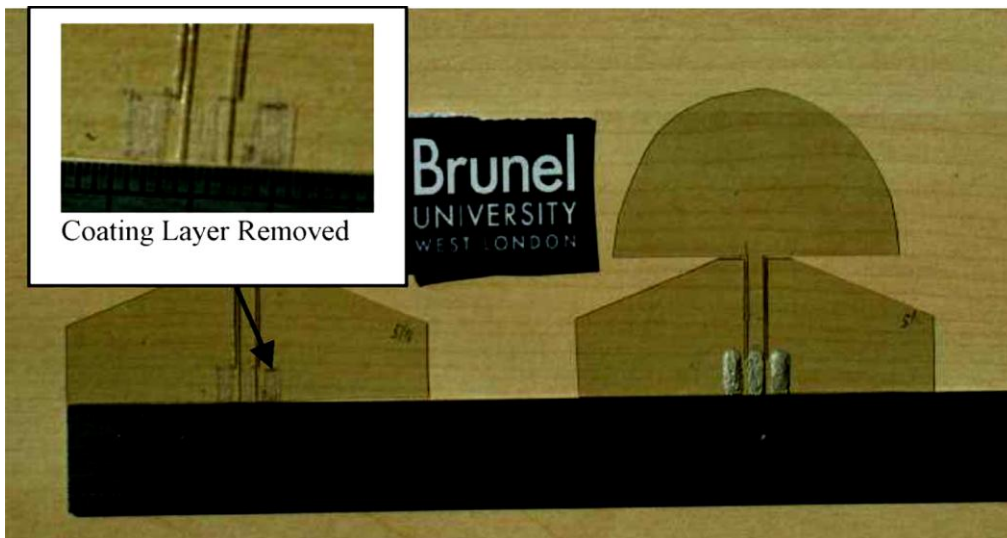


Figure 4.19 (Left) Antenna with the coating removed (Right) antenna after application of the conductive silver paint.

A method to improve the SMA to antenna connection was developed and presented in the course of this PhD research work to improve the gain and efficiency of not only the MTA but also other transparent polymer antennas on transparent conductive oxides for example, ITO. The method involved the removal of the coating layer at areas on the CPW ground and feed line where the connectors of the coaxial feed or legs of the SMA connectors will be attached as shown Figure 4.19 and applying a coat of silver paint on the exposed areas before cold-soldering the coaxial connections or SMA connector legs. Directly cold-soldering the coaxial feeds may result in poor performance. This is because of the fact that the AgHT-8 coating is a three-layered coating made up of a layer of silver sandwiched between two layers of tin oxide. Direct cold soldering will only bring the coaxial feeds in contact with the topmost layer of the coating that is, the tin oxide layer, which has a lower electrical conductivity compared to that of the silver layer. As such, the tin oxide surface would become the main surface along which the electromagnetic waves propagate, resulting in a poorer performance than if the feeds were connected to the silver layer. Additionally, the smooth surface of the AgHT-8 material may also result in a dry joint making the bond weak. The apparent connectivity issues in these two methods prevent maximum power transfer of the electromagnetic energy from the coaxial feeds besides the usual power transfer loss through poor impedance matching, resulting in an overall poor antenna performance.

Figures 4.20 and 4.21 below shows the gain and efficiency improvement that were achieved using the above method compared to 3 other methods namely, i) directly cold soldering the leads on the tin oxide surface, ii) soldering the legs onto copper pads and gluing them onto the tin oxide surface and iii) cold soldering the copper pads instead of gluing them onto the tin oxide surface. The new method gave an average of 3.5 dB gain improvement over the directly cold soldering technique in the FCC's UWB frequency bandwidth. Similarly, the efficiency was shown to improve by an average of 10% from 3 to 8 GHz and 5 % from 8 to 11 GHz.

However, it could be noticed that there is some mismatch between the measured gain in Figure 4.20 and the measured efficiency in Figure 4.21. With the measured gain for the Silver Base antenna as the base for comparison, a maximum variation of 1.3 dB is seen for the Direct Cold Soldered antenna, and 1.4 dB for both the Glued Copper Pad and Cold Soldered Copper Pad antennas. These maximum variations are observed at the higher frequencies. This is typically what would be achieved on a system like "StarLab" on which these measurements

were taken according to its manufacturer, Satimo. The variations seen at the lower frequencies are basically due to cable current leakage and ground plane size issues. Cable current affects the low frequency performance when the antenna is fed by a coaxial line like in the StarLab. For the case of the ground plane, its width affects the efficiency. Studies have shown the measured efficiencies to be lower than the simulated. The discrepancies are larger for small ground planes at the lower frequencies [4-6].

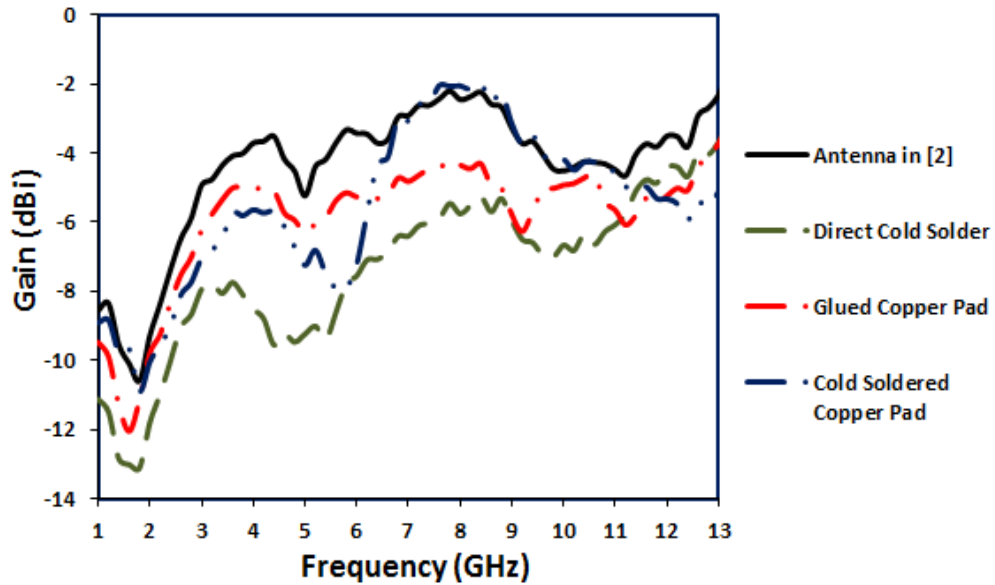


Figure 4.20 Measured gain of the new silver base technique in comparison to three other soldering techniques.

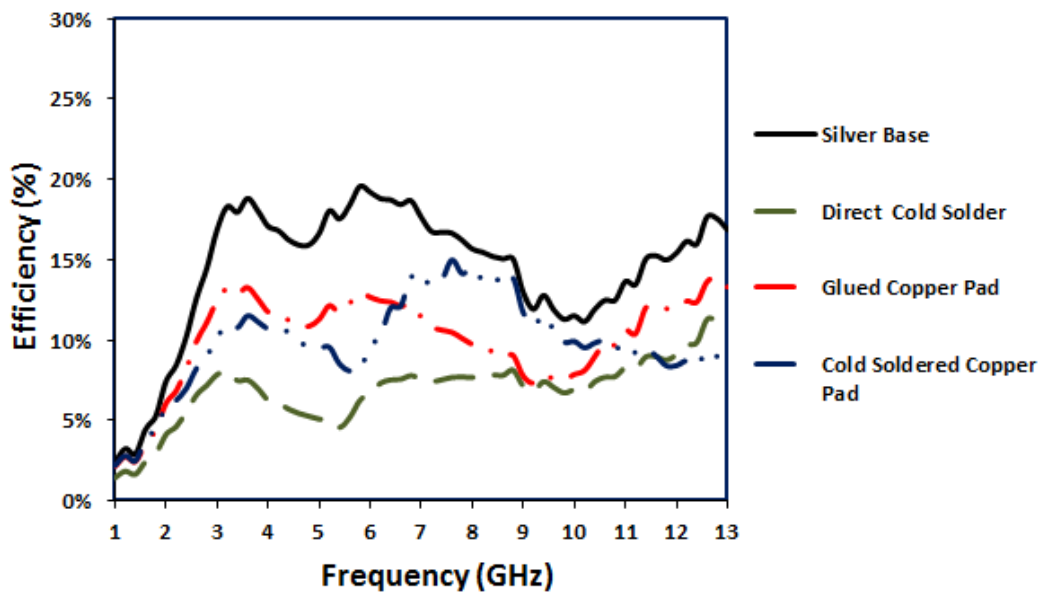


Figure 4.21 Measured efficiency of new silver base technique in comparison to three other soldering techniques.

All S-parameter measurements of the antennas fabricated and presented in this thesis were done on an Agilent Network Analyser (Model N5230A) that was available at Brunel University's laboratory. Radiation pattern, gain and efficiency measurements were carried out at Hong Kong University (HKU)'s antenna measurement facility. The equipment used for the measurement at HKU is Satimo's Star Lab which is shown in Figure 4.22. Figure 4.23 shows the MTA under measurement.

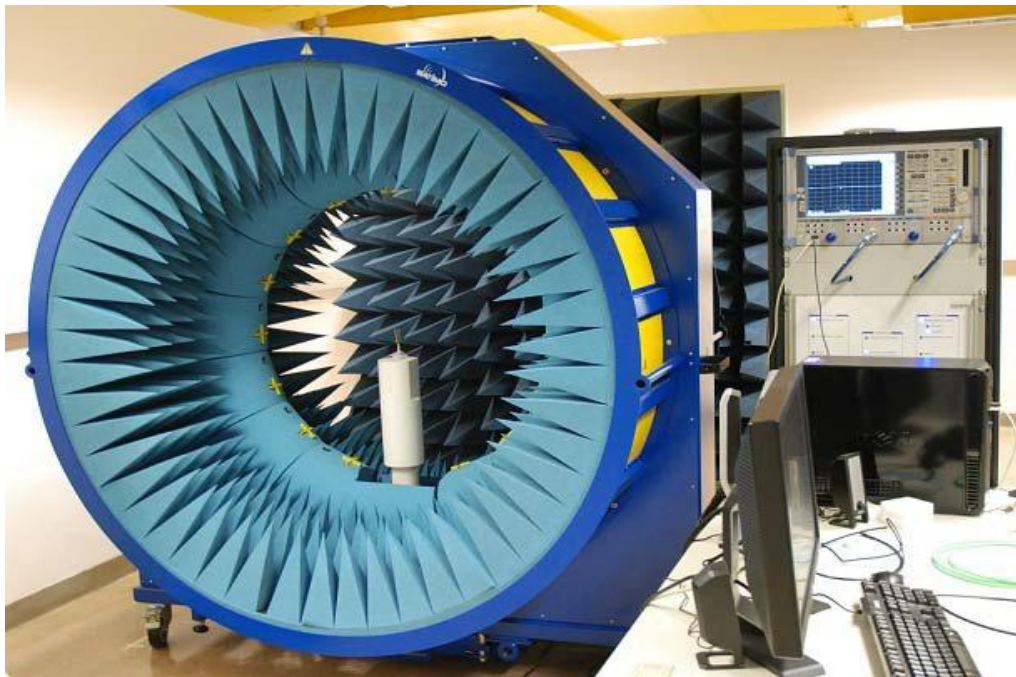


Figure 4.22 The Star Lab antenna measurement equipment at HKU, Hong Kong.

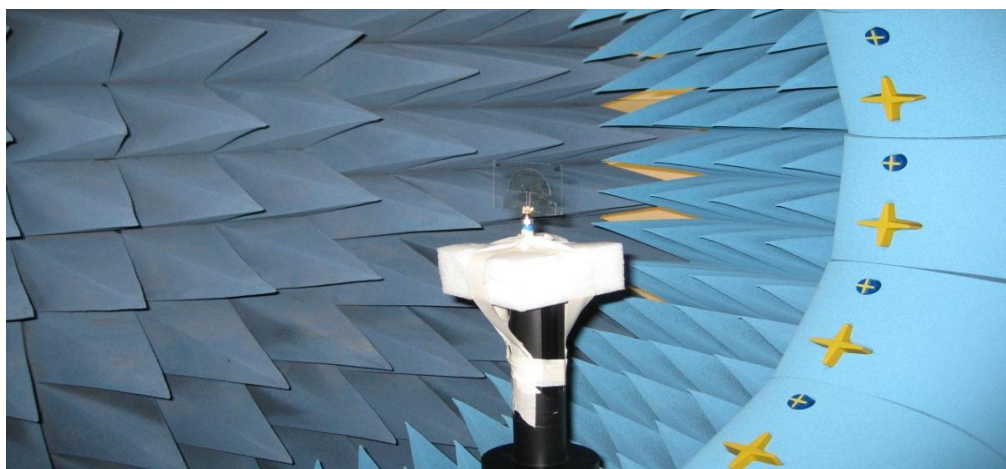


Figure 4.23 MTA undergoing measurement on the Star Lab.

4.5 Band Notch to Negate Unwanted Bands in Transparent UWB Antennas

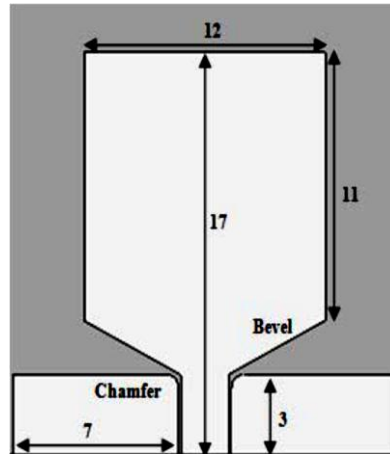


Figure 4.24 Dimensions of the modified KHA.

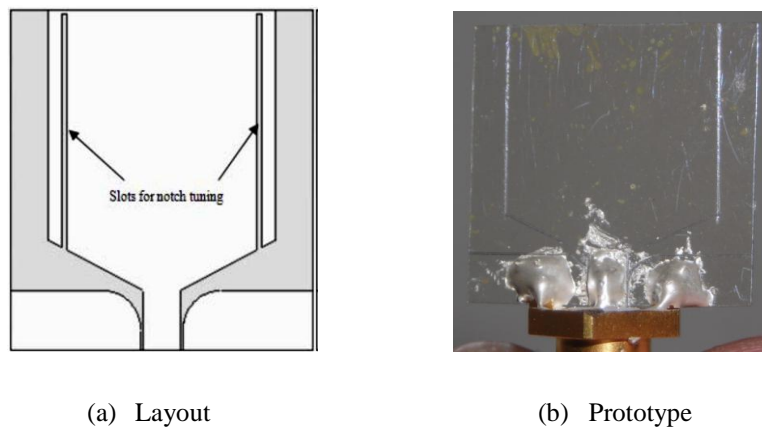


Figure 4.25 (a) Layout (b) prototype of the transparent KHA with slots for notch tuning.

Coming back to the single layered antenna design, a modified version of the knight helm antenna (KHA) as reported in [7] was developed using AgHT-8 in this manner to demonstrate the negation of unwanted bands through band notches. The MTA was not used here due to material constraint. As such an antenna smaller in size which did not exceed the limited material film that was left was designed and developed. The KHA in comparison was approximately one tenth the size of the MTA. The modified KHA's overall size as shown in Figure 4.24 was $16 \text{ mm} \times 17 \text{ mm}^2$ compared to that of the MTA which was $50 \text{ mm} \times 60 \text{ mm}^2$. To date, this is the smallest transparent UWB antenna developed and reported so far. A

layout and prototype of this antenna as presented in [8] is presented in Figure 4.25. The designed antenna geometry was inscribed onto the surface of the conductive layer instead of cutting out the geometry and pasting it onto a separate sheet of PET.

A slot was also introduced to create a notch for band tuning or negate the unwanted frequency band in this case, the 5 GHz band. Figure 4.26 shows the 5 GHz frequency band negated on the measured return loss of the antenna.

As mentioned earlier, the two trademarks of AgHT, AgHT-4 and AgHT-8 is made up of a transparent conductive coating on a thin layer of PET. The conductive layer coating is made of a transparent thin layer of silver sandwiched between two thin layers of tin oxide. The geometry of the antenna is inscribed or cut-out on this coating up to the depth of the coating to fabricate the antenna. The PET is left untouched and acts as the substrate. In this way, the glue process is eliminated and a simple one step fabrication of a transparent antenna is established. The elimination of the extra PET substrate layer did not make much of an impact on bandwidth since it was also very thin with a thickness $t = 175 \mu\text{m}$. Besides the KHA, subsequent UWB antenna unless otherwise required to have an additional PET layer, were designed using the single-layer approach.

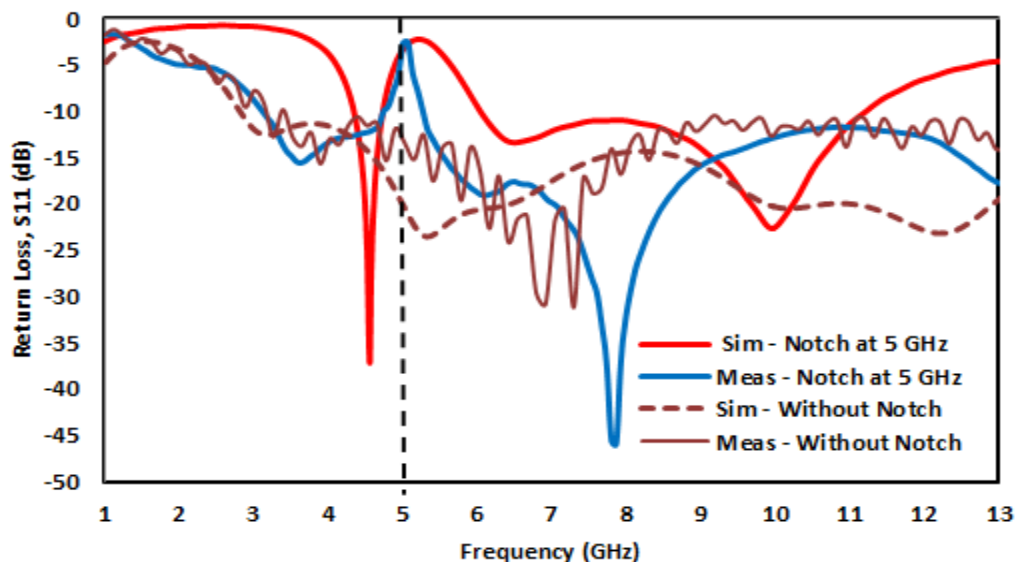


Figure 4.26 Simulated and measured reflection coefficients of the KHA antenna with slots for notch tuning at 5 GHz. The measured return loss without notch is given for comparison.

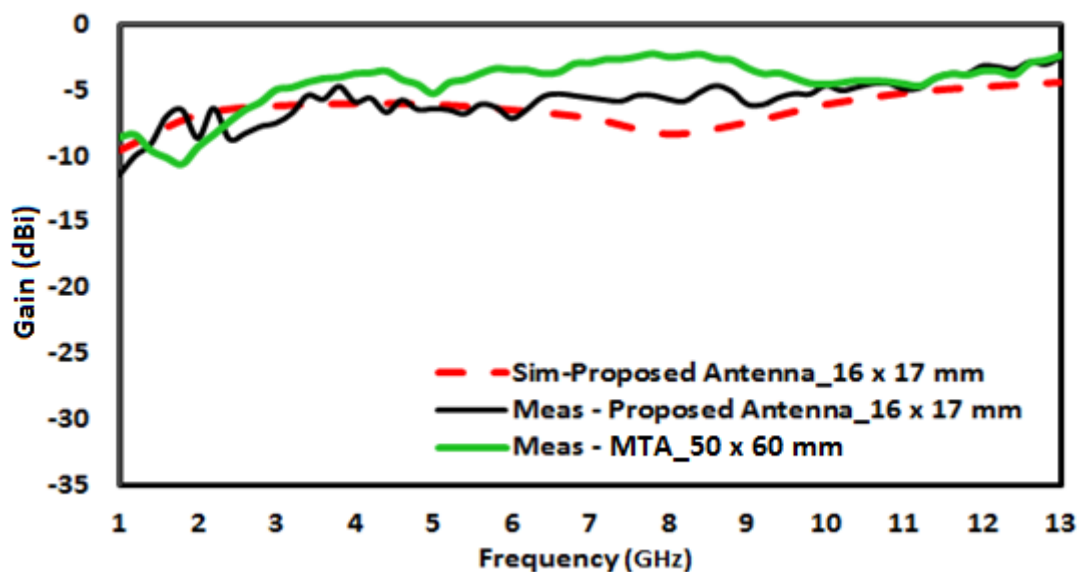


Figure 4.27 Simulated and measured gain.

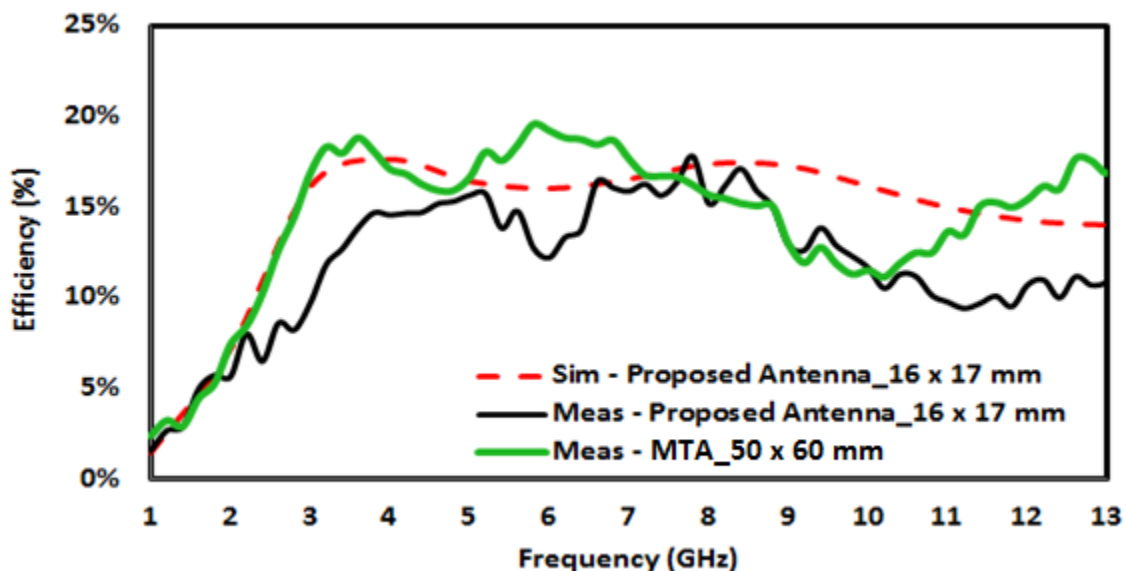


Figure 4.28 Simulated and measured efficiency.

The measured gain of the proposed antenna, KHA as depicted in Figure 4.27 was lesser than that of the MTA by 1dB to 2dB between 3 GHz to 10 GHz. This could be attributed to the smaller size of the modified KHA which is about 90% smaller in comparison to that of the mushroom top antenna in area. The measured gain and efficiency of the KHA are shown in Figures 4.27 and 4.28 respectively. Here again, the variations as pointed out earlier for Figure 4.21 are observed in Figure 4.28. Here the variations due the measurement system are noticed at the higher frequencies between 6 to 9 GHz and 11 GHz and above. At the lower

frequencies below 4 GHz the effect of the ground plane is obvious. The KHA has a much smaller ground plane than that of the MTA.

The measured 3-D radiation patterns show a consistent Omni-directional radiation pattern which is a much desired feature for a UWB antenna's stable performance. This is illustrated in Figure 4.29.

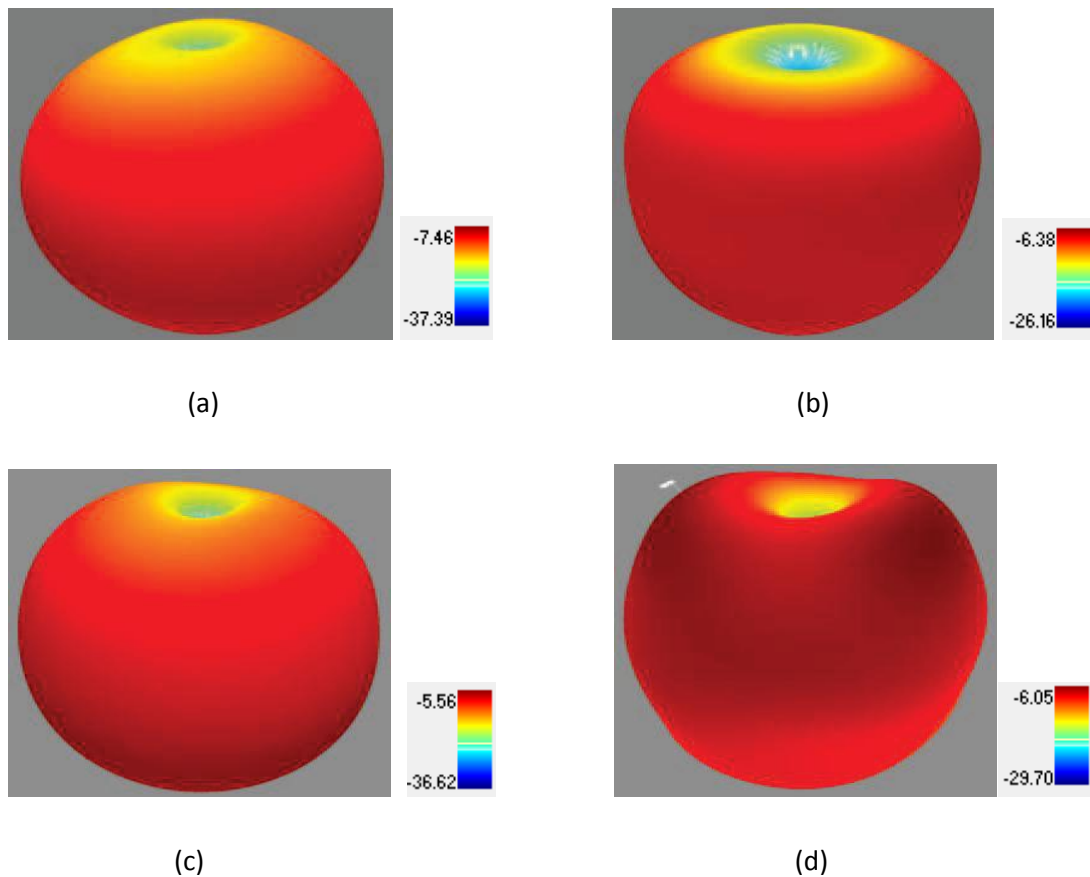


Figure 4.29 Measured 3-D radiation patterns of antenna: (a) 3 GHz (b) 5 GHz (c) 7 GHz and (d) 9 GHz.

4.6 Analysis of Coupling, Proximity Sensitiveness and Radar Cross Section Characteristics of Transparent Antennas

4.6.1 Analysis of Mutual Coupling in Arrays

Mutual coupling happens in any high frequency structures like antennas when they are exposed to each other. The current on one antenna creates an electromagnetic (EM) field or

radiation, and this EM field induces current on another antenna exposed to the field or that is spaced close by. Thus EM energy is transferred from the first antenna to the second antenna. Similarly, the EM energy of the second antenna is also coupled to the first antenna. This mutual coupling could be advantages for example, bandwidth enhancement in arrays [9] as well as disadvantages like ‘blind scan angles’ in beam steered radar arrays [10]. Mutual coupling is a function of the position of an antenna relative to another. The coupling study done on the transparent antennas in this section is in the H-plane as depicted in Figure 4.30 [10] and using a multiport 2x1 array. The study is to show how the low coupling observed in transparent antennas could be utilised to reduce coupling in MIMO applications.

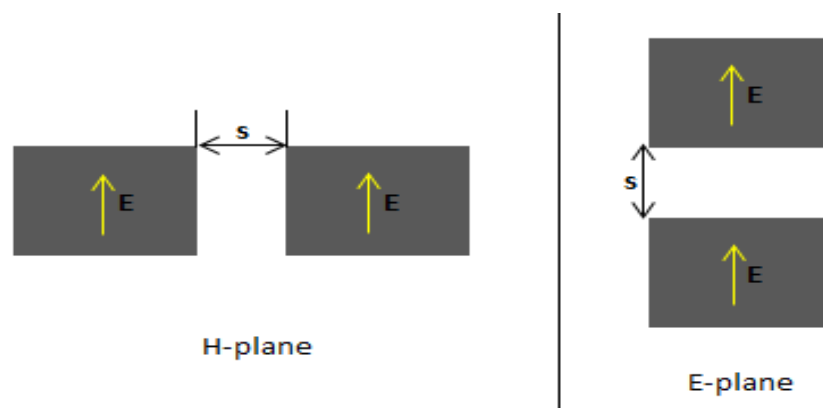


Figure 4.30 H and E plane arrangements of the antennas.

A smaller high gain transparent antenna which was developed for energy harvesting applications was employed for the mutual coupling analysis instead of the larger MTA due to AgHT material constraint. Chapter 7 provides a detailed study on this antenna (CTSA). Mutual coupling in a 2x1 array of the CTSA for three different configurations were studied namely, face to face (FF), face by side (FS) and side by side (SS). The simulated results for the three different configurations at a spacing of $\lambda/2$ (150 mm) for an operation frequency of 1 GHz is shown in Figure 4.31. Additionally, two similar designed antennas on copper cladding, one on a Rogers substrate while the other on a PET substrate were simulated for comparison and included in Figure 4.31. Two prototypes of each of the three types of antennas were fabricated and measured for S21 at the same spacing of 150mm and the three different configurations of FF, FS and SS on the Network Analyser. The measured S21 results are also shown in Figure 4.31.

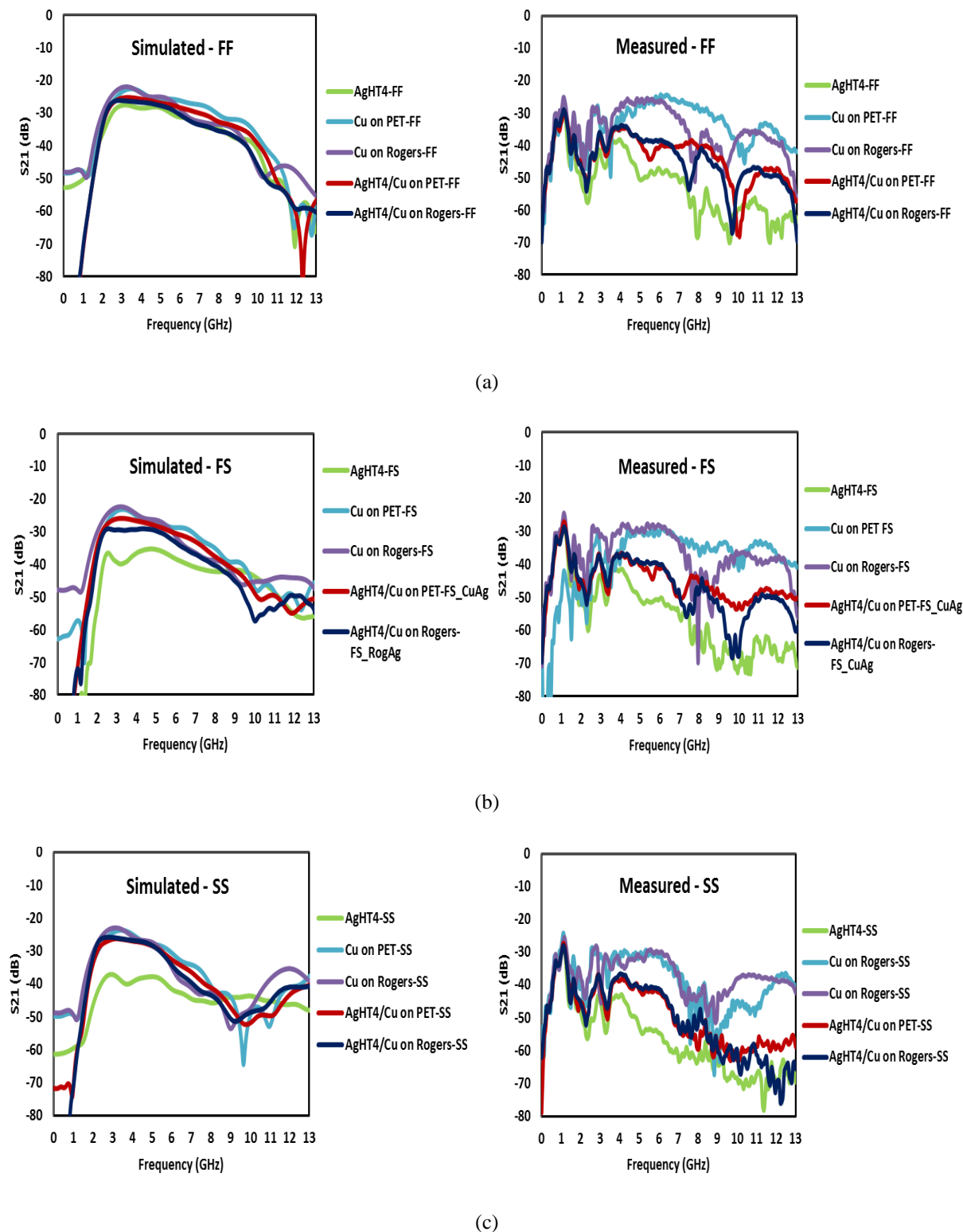


Figure 4.31 Simulated and measured S₂₁ of a 2x1 CTSA array placed (a) face to face (FF) (b) face to side (FS) (c) side to side (SS) orientation at 150mm spacing.

The impact of mutual coupling (S₂₁) for the 2x1 array of the three different antenna types as well as a composite array were observed. The AgHT antennas showed the lowest

mutual coupling in the measured data for the FCC's UWB bandwidth. The mutual coupling between a composite array that is, the S₂₁ of a 2x1 array of an AgHT-4 antenna and a Rogers antenna was the next lowest followed by the AgHT-4 and Copper on PET combination. Taking note of this, we can maintain a high gain and efficiency whilst at the same time reduce mutual coupling by using copper clad antenna arrays intermingled with transparent antennas like those made from AgHT-4 in MIMO applications. The copper on PET antennas can be easily made using deposition techniques [11] in industry to make them cost effective. The AgHT and Copper-PET integrated antennas with reduced coupling can be effectively used for on-body application in Medicare and healthcare industries where such antenna arrays can be wrapped around the arm or leg or body part as the PET polymer on which they are constructed are flexible and conformable. The distance between the antennas on-body would often times be lesser than 150 mm, and in such cases reduced coupling could aid the antenna in delivering better performance.

4.6.2 Insensitiveness to Proximity Interference

During measurement of the return loss with the Network Analyser, it was noticed that the return loss response did not vary on waving the hand or bringing any object within close proximity of the antenna. This was not the case when measurements were done using a copper antenna on a Rogers substrate. Literature review was done to investigate whether this phenomenon of insensitiveness was due to the tin oxide coating on the silver layer of the AgHT. The closest study of depositing tin oxide on a metal was done by Roos et al [12]. As no direct study has been done, efforts to conduct experimental research were taken.

A study to coat samples of the copper patch antennas with tin oxide was undertaken with help from the University of Cambridge. A thin transparent layer of tin oxide was deposited on the copper patch and the performance of the coated antenna studied. As tin oxide is inert, the coating is expected to show a similar type of effect as that of the AgHT material that is, insensitiveness to proximity interference. Also, whether this coating affected the original performance of the antenna was also studied. Besides this, any interaction between the tin oxide coating and the copper surface was monitored to see the reliability of the coating for long periods of time. Results of the tin oxide deposition study showed not

much reduction in sensitiveness to proximity interference or even reduced coupling for a coupling test done between two prototypes of the tin oxide coated copper antenna. This showed that the insensitiveness was due to the low conductivity of the material rather than the tin oxide coating.

4.6.3 Analysis of RAM Properties of AgHT based Transparent Antenna using RCS

Radar cross section (RCS) is a far field parameter that is used to characterize the scattering properties of a radar target [13] or simply, how detectable the target is with a radar. Large RCS means that the target is more easily detectable. Hence for low-profile or stealth, RCS is an essential parameter that needs to be minimized. For a particular target, there is monostatic or backscattering RCS if the transmitter and receiver are placed at the same location and bistatic RCS if they are placed in different locations.

Detectability on radar basically depends on how much energy is reflected by the target. A variety of factors [13] determine how much of the radar's electromagnetic energy returns to it. Some of these are:

- size of the target
- material composition of the target
- relative size of the target (in relation to the wavelength of the radar beam)
- the incident angle (angle at which the radar beam hits a particular portion of the target which depends upon the shape of the target and its orientation to the radar source)
- reflected angle (angle at which the reflected beam leaves the part of the target it hit; this basically depends upon the incident angle)

It should be noted, however, that neither the strength of the emitting radar nor the distance of the target affects the calculation of the RCS as the RCS is dependent upon the target's reflectivity. This reflectivity can be controlled to minimize RCS through shaping and material used [10]. Shaping is used to attempt to direct the scattered energy towards directions other

than the radar, whilst materials are used to trap or absorb the incident energy within the target and to dissipate part of the energy as heat or direct it toward directions other than the radar. One of the ways shaping is utilized to achieve low RCS is to round off corners, avoid flat and concave surfaces, and use material treatment in flare spots [10].

For antennas, the total RCS can be categorized into two separate components namely, Structural Mode RCS (SCS) and Antenna Mode RCS (ACS). The Structural Mode relates to the portion of the electromagnetic signal energy that is back scattered from the surface of the antenna to the space. Antenna Modes RCS is the portion of the absorbed energy that is again scattered back to space due to impedance mismatch. For the RCS study, the SCS properties of a MTA designed on AgHT-8 was compared with that of a Copper-PET and Copper-Rogers version of it in simulation. Experimental verification was not possible due to lack of facilities internally and governmental restriction at antenna measurement houses. The antenna design files for the selected MTAs were run with the RCS macros and other post-processing templates available in CST to calculate the monostatic RCS.

The simulation measurement set-up is as depicted in Figure 4.32. Figure 4.33 shows the RCS simulated for the SCS with the plane wave polarized in the theta direction by setting the E-theta component in the dialog box. The CST macro used to calculate the RCS in the simulation is limited to calculate the monostatic in a single theta = constant plane configuration. The antenna design or target was set in the X-Y plane with the incident plane wave set at theta = 75° for the simulation. Figure 4.34 shows the simulation run for a plane wave set at theta/phi = 0 using a CST post processing template. However, this time the x-axis is orientated to be perpendicular to the front face of the antenna.

Figures 4.33 and 4.34 clearly show that the AgHT antenna exhibits lower RCS than its comparisons. Although polymers are known to be permeable to RF and microwaves and as such would exhibit lower RCS, this study is done to quantify it. In the radar frequency range used for short-range tracking from 8 to 12 GHz, the AgHT antenna exhibits a minimum of 20 mm² and 60 mm² lower RCS than of the CuPET and Rogers respectively. This is shown in Figure 4.34. Moreover, AgHT being a metallized polymer should exhibit even more absorption as RAM materials currently used in military and commercial use are basically metallized polymers that are typically composed of high concentrations of iron powders in a polymer matrix [14].

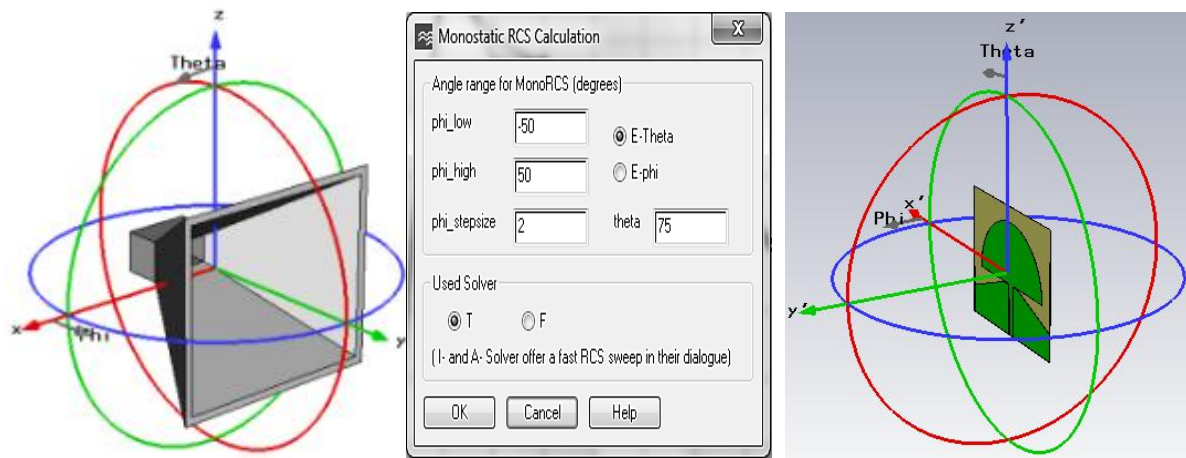


Figure 4.32 Simulation measurement set-up. Plane polarization set by setting the E- θ or E- ϕ component in the monostatic RCS calculation dialog box.

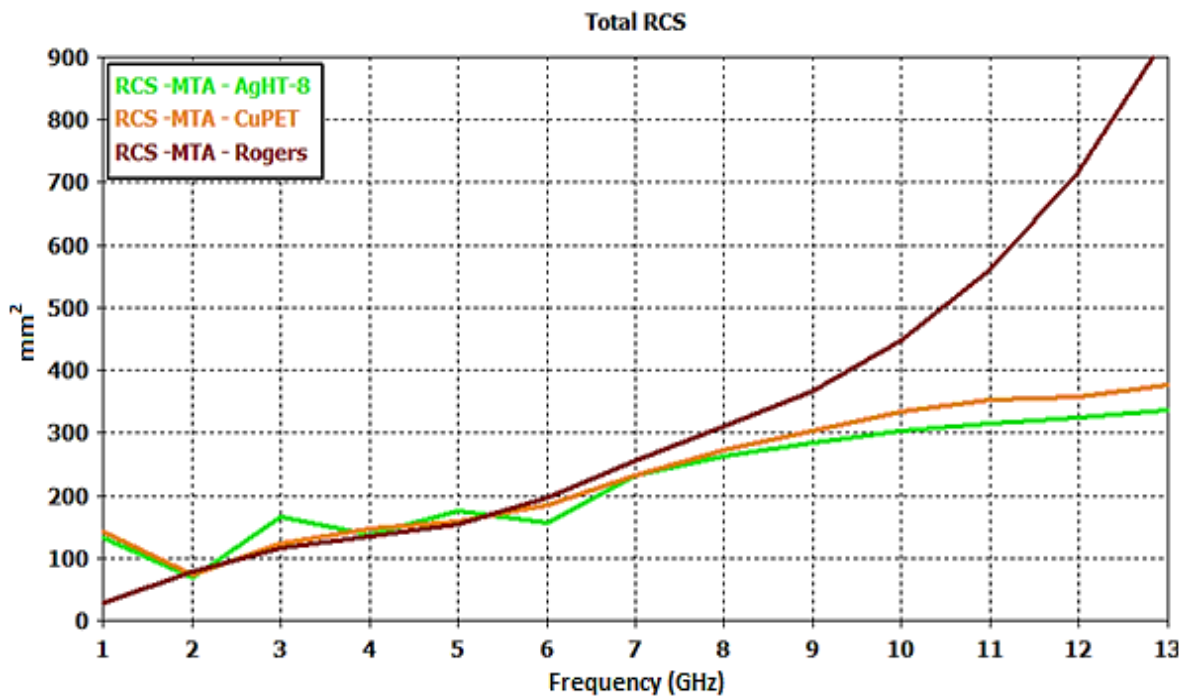


Figure 4.33 Simulated Structural Mode RCS of the mushroom top antenna for plane wave polarization in E- $\theta=75^\circ$.

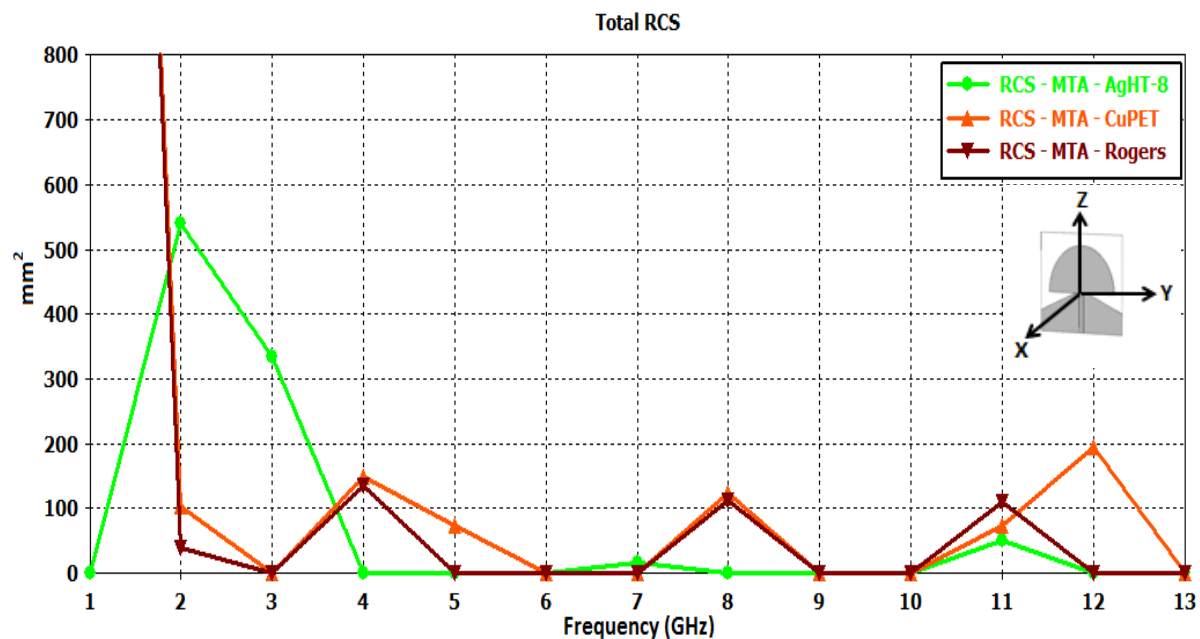


Figure 4.34 Simulated Radar Cross Section of the mushroom top antenna with plane wave at $E-\theta / E-\varphi = 0$.

With the current advancements in detection technology it is quite possible for radar equipment to detect devices mounted with small antennas. AgHT based antennas can thus potentially provide the additional stealth necessary to avoid or minimize radar detection. Clear PET film has been reported in published literature [15] as being RF transparent at 12.5 GHz that is, the signal transmitted at this frequency is returned without loss. As mentioned earlier in section 4.1, TDK a big Japanese firm, has introduced into the market ITO coated PET radio wave absorbers that work in the 5.8 GHz frequency band [2]. These absorbers are made for improving electronic toll collection (ETC) and dedicated short range communication (DSRC) environments. These facts additionally help to confirm that AgHT has radar absorbent properties thus giving the AgHT based UWB transparent antennas stealth properties. As these transparent antennas are mainly suited for use on glass panels of windows of building whether in homes or buildings, the stealth property would indeed give it an additional edge.

4.7 Summary

In this chapter, three different transparent AgHT based UWB antennas that have been developed during the course of this thesis research have been described. These antennas have been developed by building on the knowledge gained from studying the existing non-transparent antennas published in literature. A novel technique to improve gain and efficiency as well as analysis on the mutual coupling, proximity insensitiveness and RAM properties of the AgHT UWB antennas were presented. It has been highlighted how the AgHT transparent antennas can be integrated with Copper-PET antennas to achieve good gain with reduced coupling in applications where conformable antennas are desirable to overcome space constraints or needed to be wrapped around body components like in body centric applications. Although, experimental verification was not possible due to constraints and restriction described earlier in the chapter, the RAM analysis highlights the stealth properties of the AgHT material. This property opens up a whole lot of potential uses for the material not only in antenna applications but also in the semi-conductor industry as well as an absorber material in anechoic chambers.

4.8 References:

- 1) T. Peter, R. Nilavalan, H.F. AbuTarboush and S.W. Cheung, "A Novel Technique and Soldering Method to Improve Performance of Transparent Polymer Antennas," *IEEE Antennas and Wireless Propagation Letters*, vol.9, pp.918-921, 2010.
- 2) TDK RF Solutions. [Online]. Available: http://www.tdk.co.jp/tefe02/e9e_bdj_003.pdf
- 3) T. Peter, R. Nilavalan, H.F. AbuTarboush and S.W. Cheung, "A non-thermal soldering technique to improve polymer based antenna performance," *European Microwave Conference (EuMC)*, 2010, pp.1476-1479, Sept. 28-30, 2010.
- 4) T.W. Hertel, "Cable-current effects of miniature UWB antennas," in *Proc. IEEE Antennas Propagat. Soc. Int. Symp.*, vol. 3A, Washington, DC, pp. 524-527, Jul. 2005.
- 5) Y.F. Weng, S.W. Cheung, T.I. Yuk, 'Effects of ground-plane size on planar UWB monopole antenna', *Proc. TENCON 2010 - 2010 IEEE Region 10 Conf.*, Fukuoka, Japan, pp. 422-425, November 2010.
- 6) Y. Lu, Y. Huang, H.T. Chattha, Y. Shen, "Technique for minimising the effects of ground plane on planar ultra-wideband monopole antennas," *IET Microwaves, Antennas & Propagation*, vol.6, no.5, pp.510-518, April 12 2012.
- 7) Z.N. Low, J.H. Cheong and C.L. Law, "Low-cost PCB antenna for UWB applications," *IEEE Antennas and Wireless Propagation Letters*, vol.4, pp. 237- 239, 2005.
- 8) T. Peter, Y.Y. Sun, T.I. Yuk, H.F. AbuTarboush, R. Nilavalan and S.W. Cheung, "Miniature transparent UWB antenna with tunable notch for green wireless applications," *International Workshop on Antenna Technology (iWAT)*, 2011, pp.259-262, March 7-9, 2011.
- 9) W. Min, W. Wen and S. Zhongxiang, "Bandwidth Enhancement of Antenna Arrays Utilizing Mutual Coupling between Antenna Elements," *International Journal of Antennas and Propagation*, vol. 2010, Article ID 690713, 9 pages, 2010.
- 10) C.A. Balanis, *Antenna Theory Analysis and Design*, 3rd edition: John Wiley & Sons, Inc., 2005.
- 11) S.W. Bae, H.K. Yoon, W.S. Kang, Y.J. Yoon and C.H. Lee, "A Flexible Monopole Antenna with Band-notch Function for UWB Systems," *Asia-Pacific Microwave Conference, APMC 2007*, pp.1-4, Dec. 11-14, 2007.
- 12) A. Roos and M. Georgson, "Tin-oxide-coated anodized aluminium selective absorber surfaces II. Aging and durability," *Solar Energy Materials*, vol. 22, pp. 29-41, 1991.

- 13) RCS. [Online]. Available:
http://en.wikipedia.org/wiki/Radar_cross-section#RCS_of_an_antenna.
- 14) Stealth Materials. [Online]. Available:
<http://www.globalsecurity.org/military/world/stealth-aircraft-material.htm>.
- 15) P. Olla, *Space Technologies for the Benefit of Human Society and Earth*, Springer (Google Ebook), pg 241.

CHAPTER 5

Analysis of Transparent UWB Antennas for Body Centric Applications

5.1 Introduction

Transparent antennas can be effectively used for body-centric applications. AgHT based antennas, besides providing conformability by allowing antenna arrays to be wrapped around the body, also maintain close to free space gain on-body. The latter was the observation made in the collaborative research on transparent antennas for body-centric application carried out with researchers from Department of Electrical and Electronic Engineering, Queen Mary University of London (QMUL) and the Hong Kong University (HKU) [1]. A human subject was used in an anechoic chamber for this study. This study thus provided for the first time actual radiation pattern response of a transparent antenna on a human subject. This study hence initiated a further step forward in the investigation of transparent antennas for body centric applications besides strengthening the potential of use of such polymer based UWB antennas like those made from AgHT for health monitoring applications.

A brief look into the use of transparent UWB antennas for wearable antenna applications is also included in this chapter especially in regard to providing covertness and discreetness in terms of visibility in open grounds especially in the case of military applications. The MTA is demonstrated here in this regard on a military attire.

5.2 A Compact Transparent UWB Antenna for Wireless Body-Centric Applications

For this study, a transparent Tapered Slot Antenna (TRTSA) was designed similar in geometry to the Tapered Slot Antenna (TSA) antenna described in [2] for comparison with published work. The RT/Duroid TSA in [2] had a permittivity of 3 and an overall size of 27x16 mm and a thickness of 1.524 mm. The TRTSA in comparison had a permittivity of 3.228 and a slightly smaller dimension of 23x16 mm with a thickness of 0.175 mm. The feed gap on either side of the feed point is 0.1 mm and it gradually varies giving a tapered waveguide to achieve the impedance transformation required in the design of the UWB [2-4]. The dimension, geometry and a prototype of the TRTSA is shown in Figure 5.1. The TRTSA is fabricated using AgHT-8.

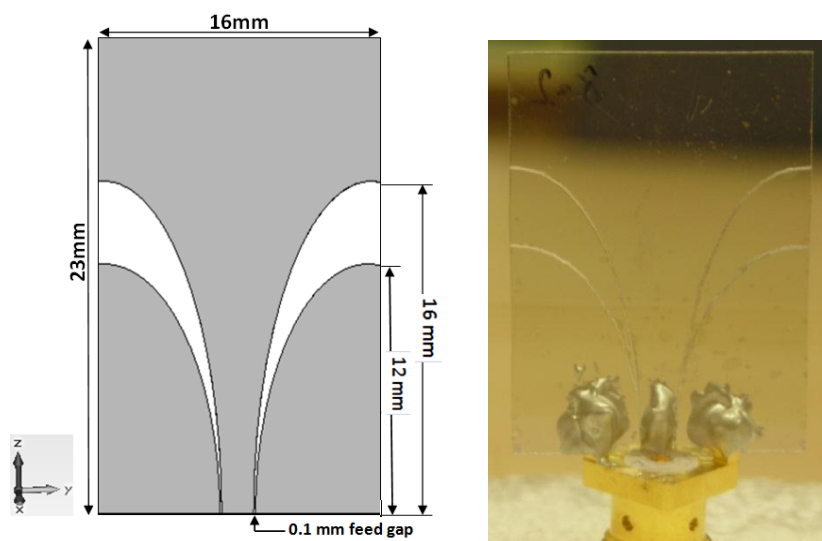


Figure 5.1 Dimension, geometry and prototype of the transparent TSA.

The prototype TRTSA was tested on a human subject in seated posture. Figure 5.2 shows the three different body areas where the return losses were measured with a Vector Network Analyser (VNA). The areas selected have different thicknesses of skin, muscle and fat layers. The test on chest was repeated with a polyester thin layer between the antenna and the skin to mimic clothes on the antenna characteristics. The radiation patterns were taken in an anechoic chamber with the antenna at the chest position with the polyester layer.



Figure 5.2 Measurement set-up in the anechoic chamber for the heart (a), chest (b), and belly (c) on-body area tests.

Figure 5.3 shows the simulated and measured return loss of the TRTSA in free space. The TSA return loss was also included as a baseline. Both the TRTSA and TSA have a 10 dB bandwidth within the 2.3-14.5 GHz range.

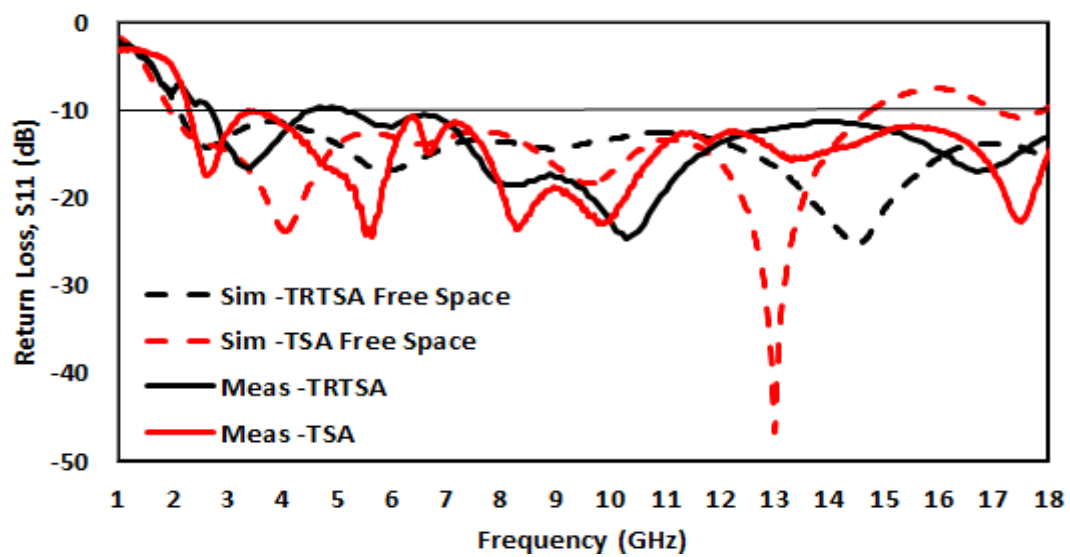


Figure 5.3 Simulated and measured return loss of the antennas in free space.

Figure 5.4 shows the return loss at the heart, chest and belly area. The TSA however, shows a slight detuning from 2.3 to 3.5 GHz for the chest and belly. The detuning was due to the different electrical properties exhibited by the body components. This was verified with numerical simulations. The test with polyester (to mimic a clothing) in between the antenna and different body components did not show any significant difference from that directly done on-body.

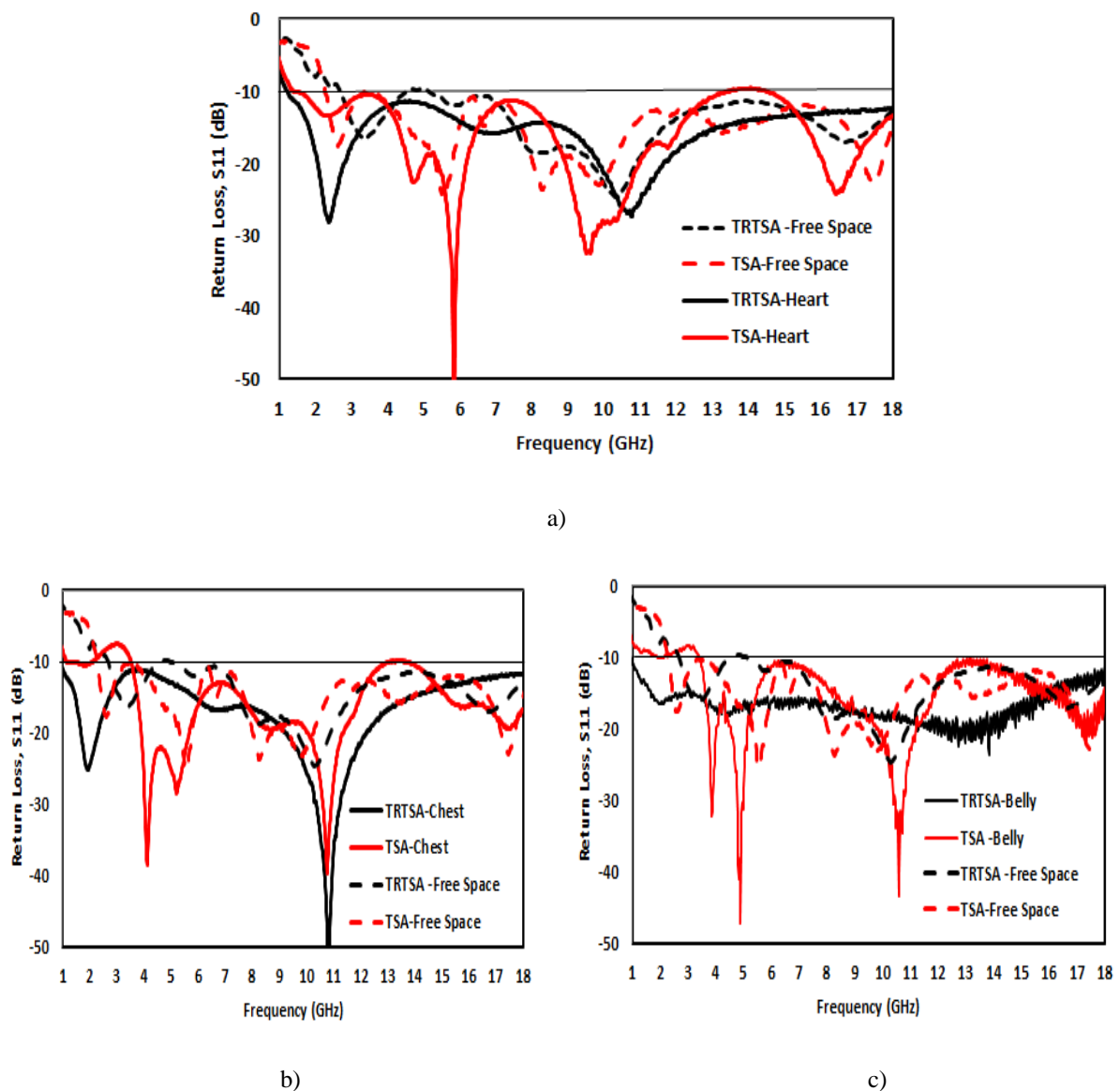


Figure 5.4 On-body measured return loss of the TRTSA and TSA on heart (a), chest (b) and belly(c).

The measured antennas' gain at QMUL is shown in Figure 5.5. The gain measured was in the X-Y plane and as such may not be at its maximum but only the highest along that plane. The TRTSA exhibits a lower gain compared to TSA because of the higher losses of the PET substrate and also because of the lower conductivity of the AgHT-8 material compared to copper [5]. The free space gain of the TRTSA is about 4.2 dB lower at 10 GHz compared to that on-body, but is otherwise comparable.

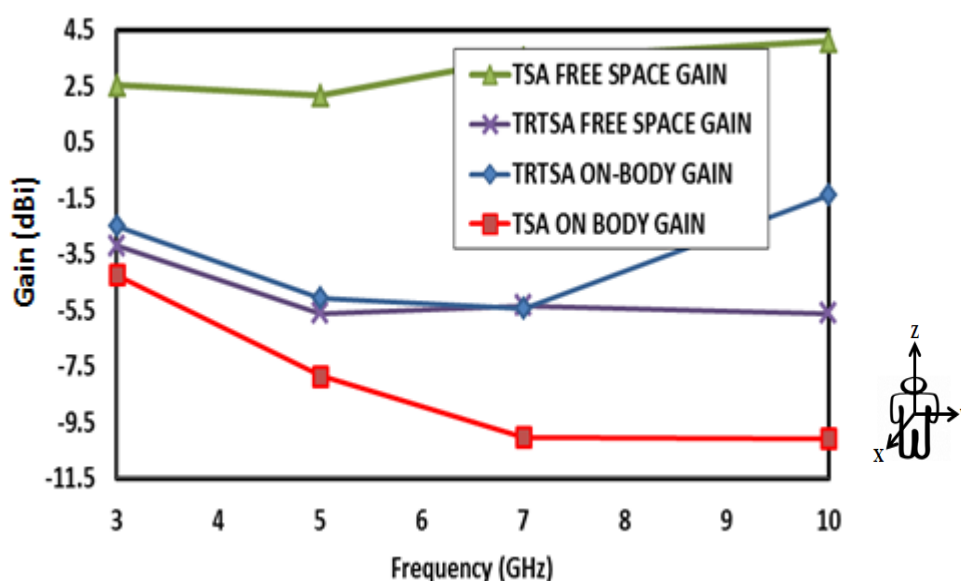
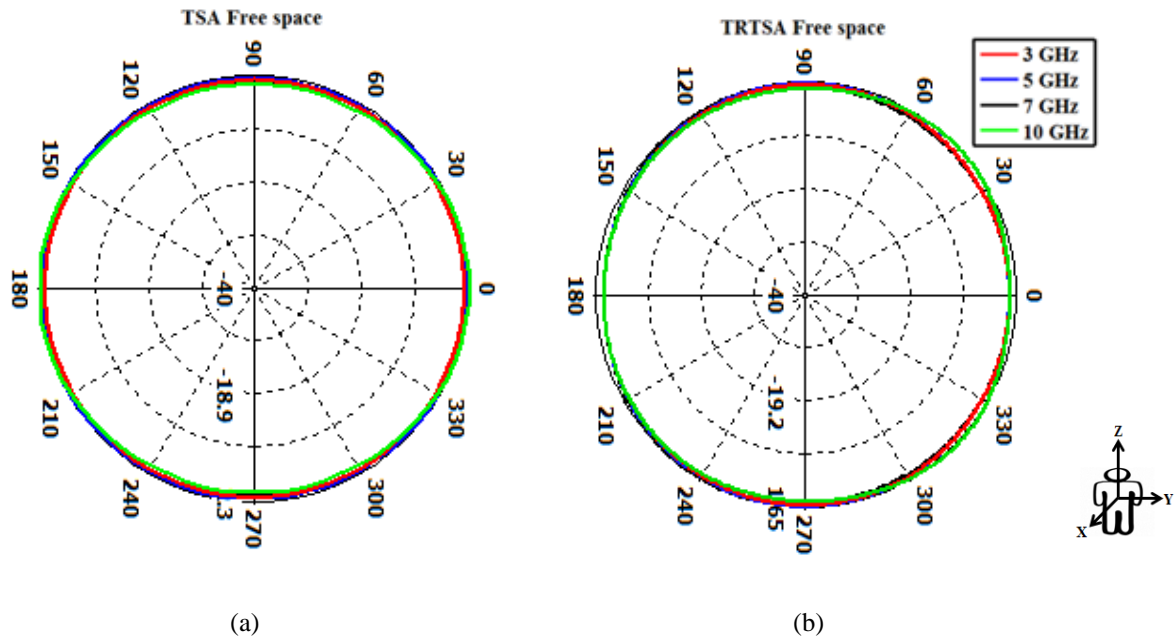


Figure 5.5 Measured gain of the antenna in free space and on-body (chest location) in the X-Y plane at QMUL. This is not the maximum gain but the highest measured gain along the X-Y plane.

The simulated and measured radiation patterns are shown in Figures 5.6 and 5.7. The radiation patterns in free space were comparably similar. For the on-body measurements, both antennas show directional characteristics as well as exhibit backward lobes. However, for the TSA, lesser backward lobes were noticed at 3 and 5 GHz compared to that at 7 and 10 GHz. This indicates that there is more absorption by the body tissues of the radiated waves at the lower frequencies for the TSA. Similar observations have been reported in [6].

Simulated



Measured

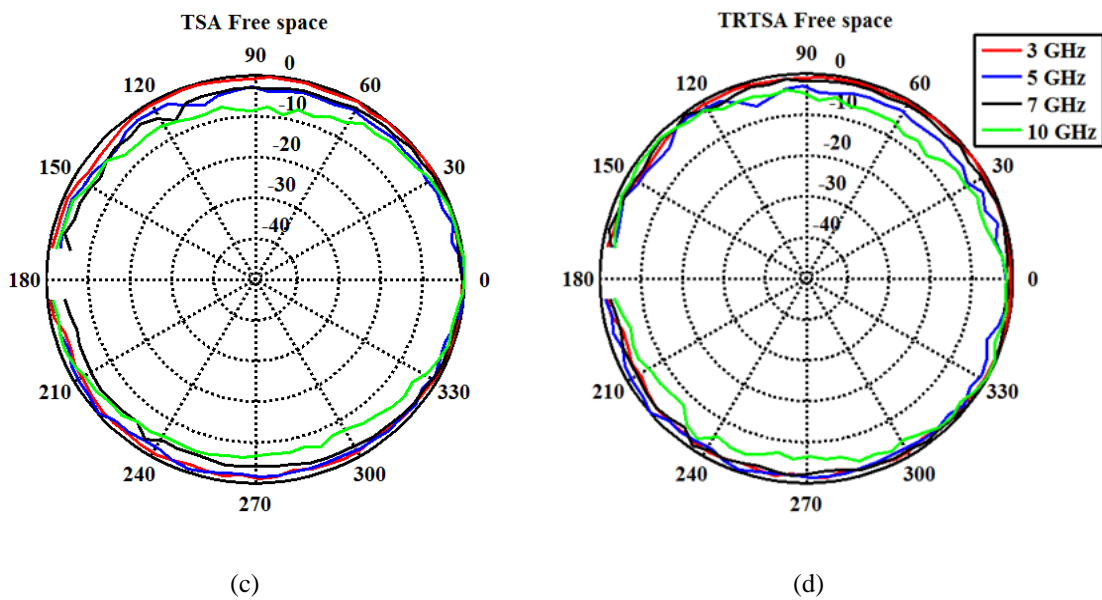
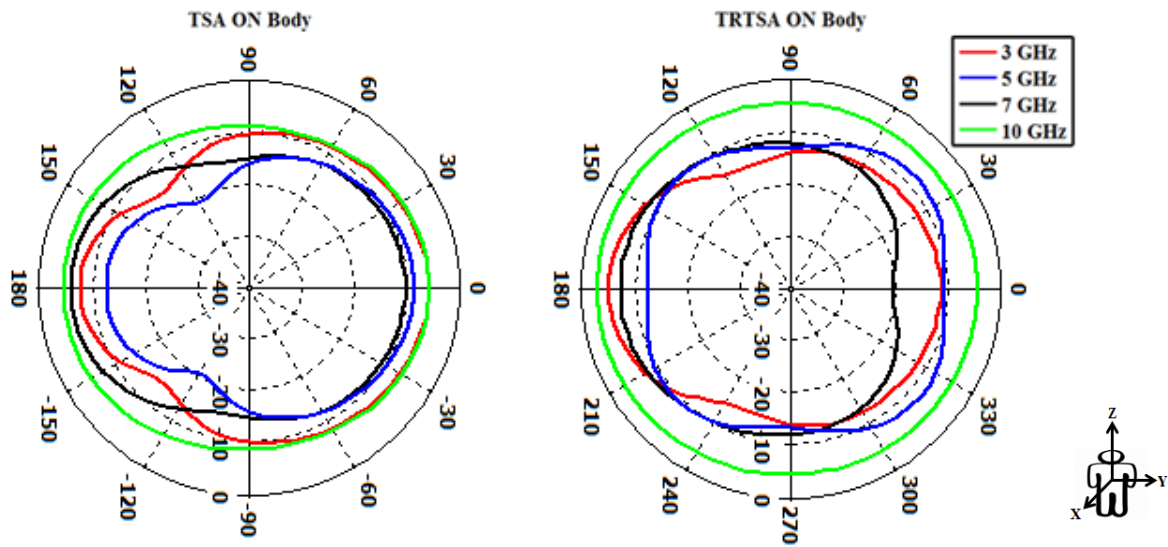
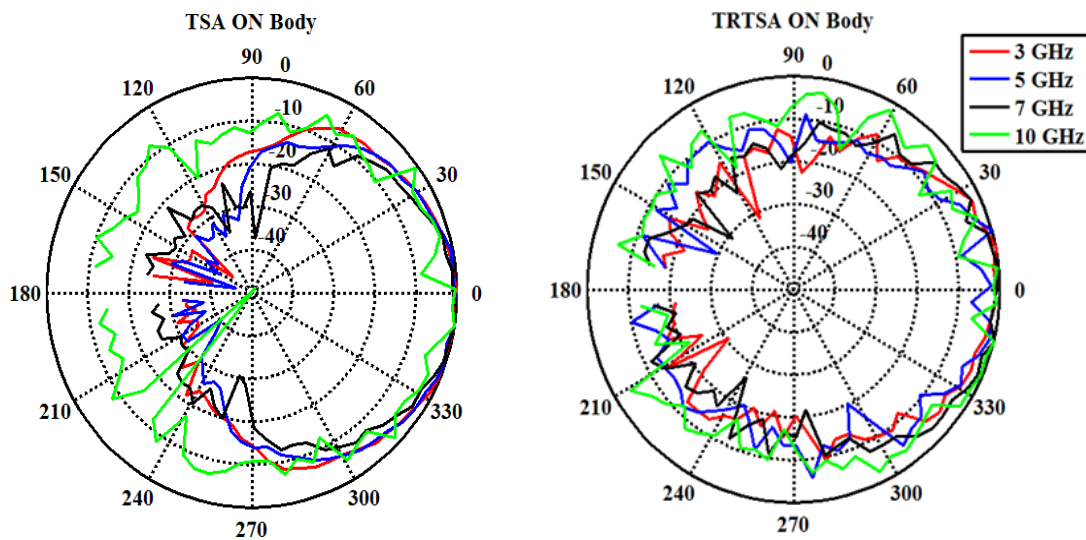


Figure 5.6 Simulated and measured free space radiation patterns in the X-Y plane: simulated (a) – (b) and measured (c) – (d).

Simulated



Measured



(c)

(d)

Figure 5.7 Simulated and measured radiation patterns on-body (chest location) in the X-Y plane: simulated (a) – (b) and measured (c) – (d).

On-body signal fidelity on the TRTSA was done and analysed at HKU's Star Gate Anechoic Chamber as part of the collaborative study. The synthesized time domain transmitted signal from the frequency domain is as shown in Figure 5.8.

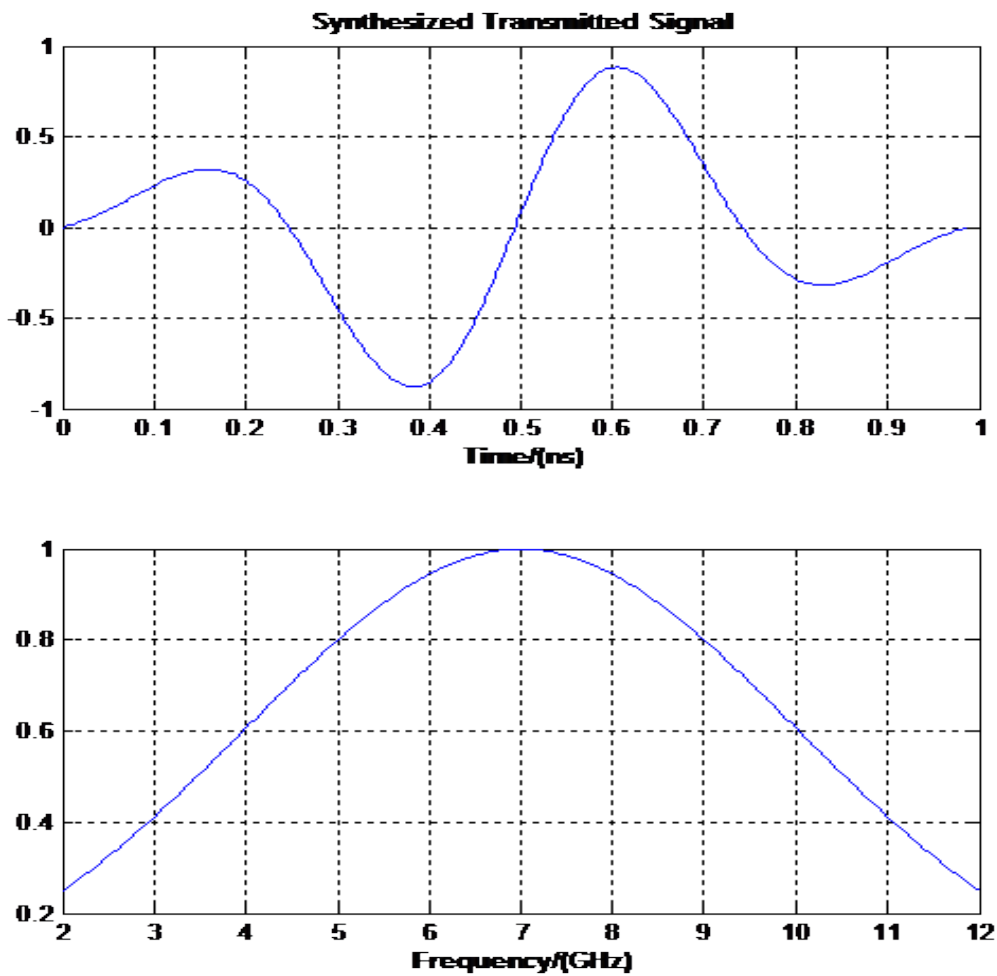
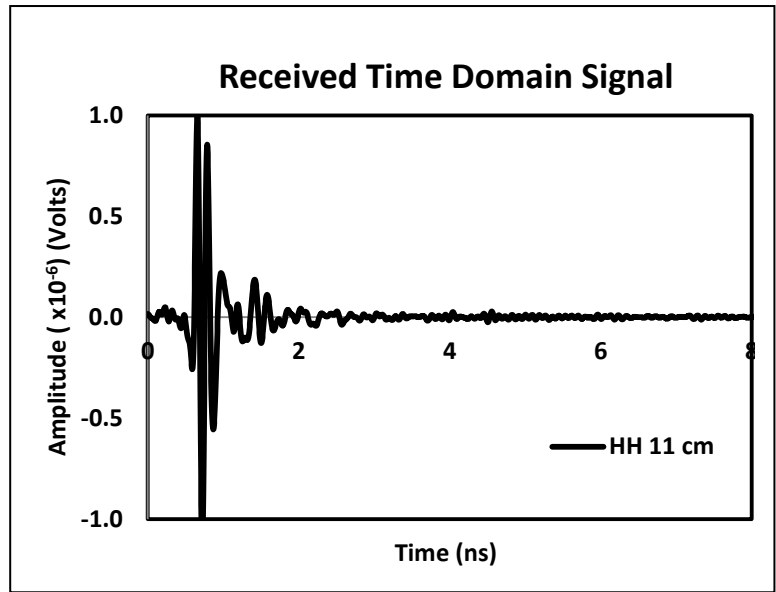
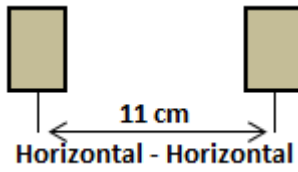
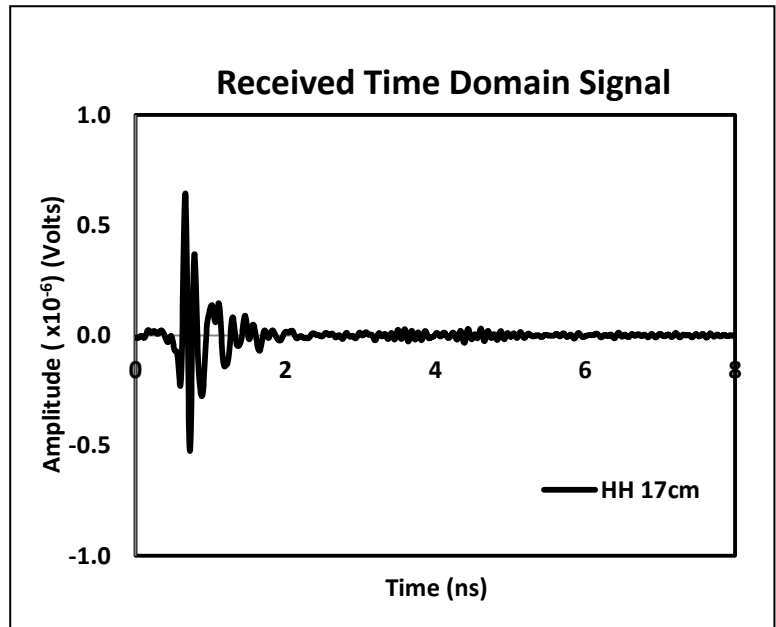
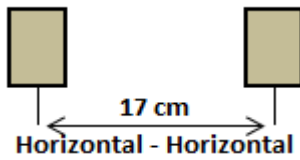
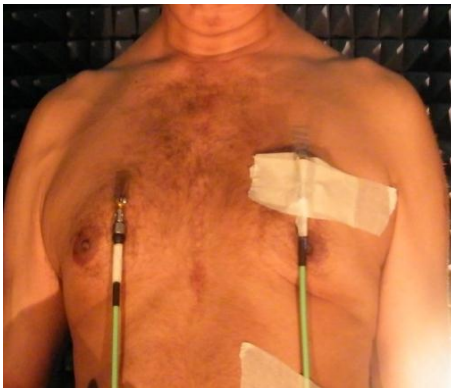


Figure 5.8 The time domain signal synthesized from the frequency domain.

The locations for the various measurement on-body and the received time domain signal are as shown in Figure 5.9 (a) to (e). The transmitting antenna is taped to the body.

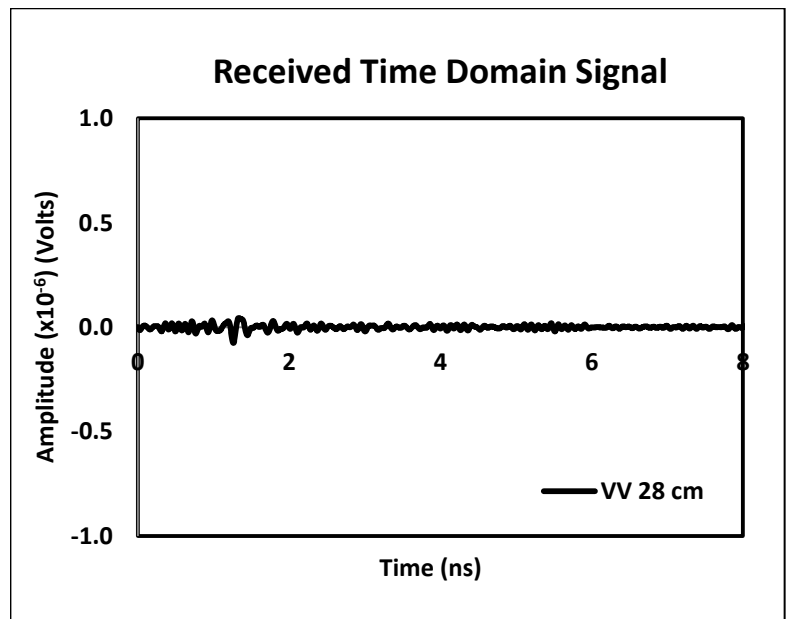
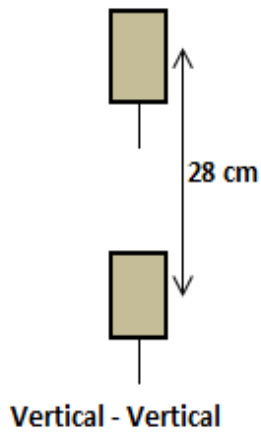


(a)

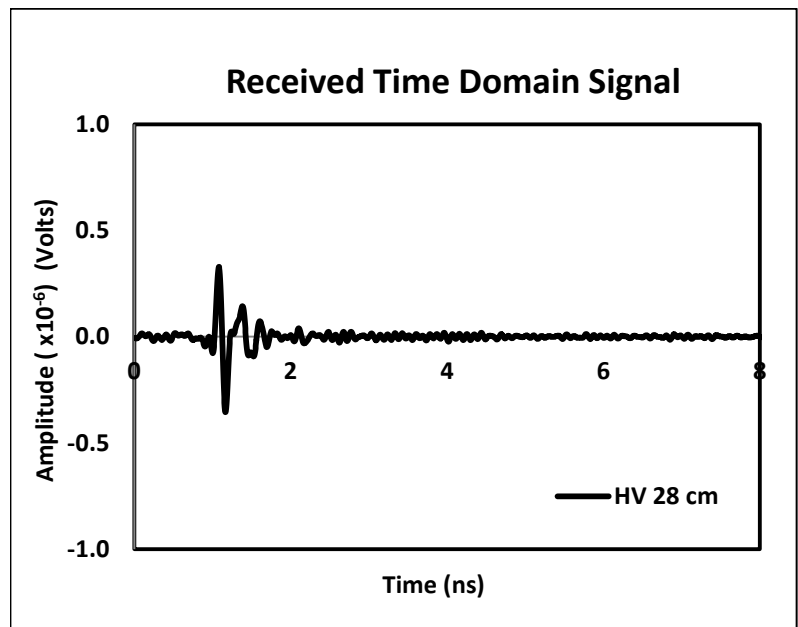
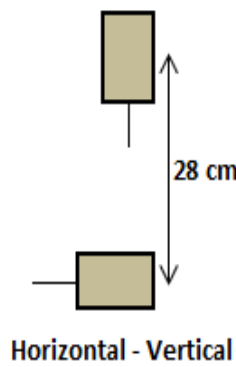


(b)

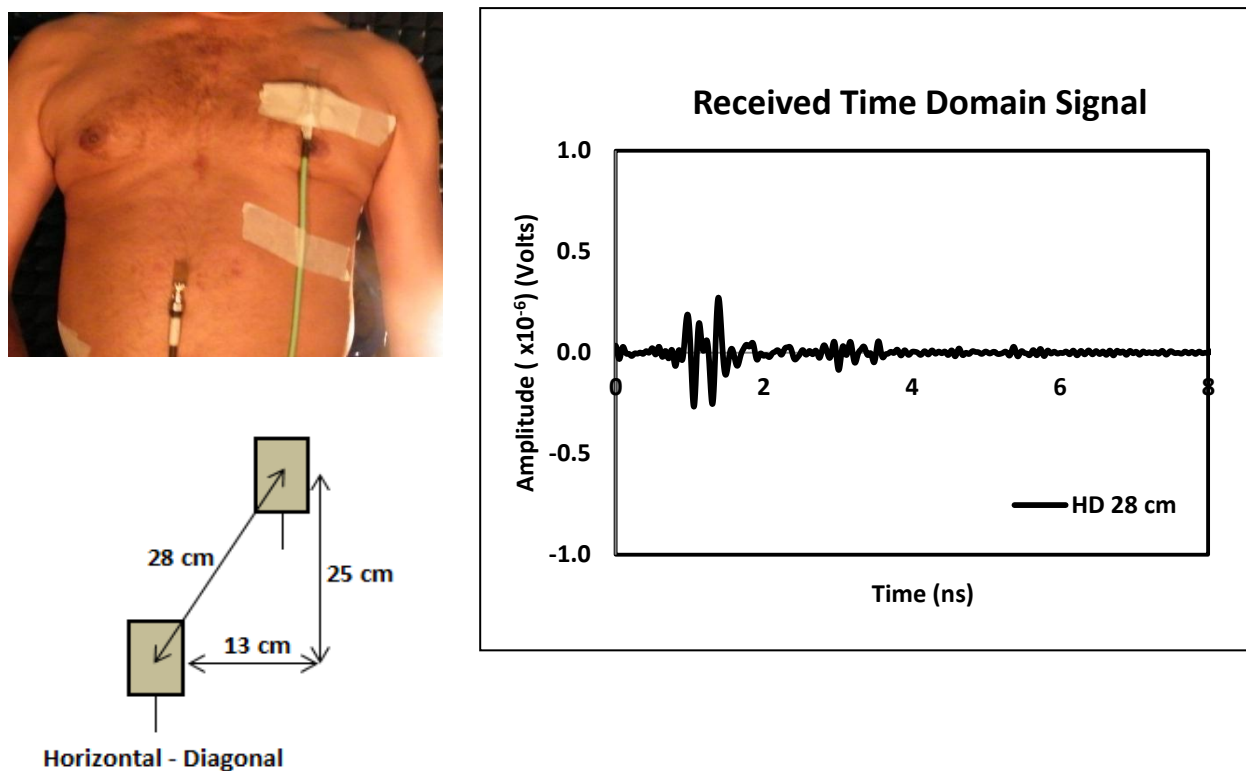
Other Configurations:



(c)



(d)



(e)

Figure 5.9 Received time-domain signals for a pair of transparent UWB tapered slot antennas in different configurations on-body.

From the received time domain signal plots in Figure 5.9, it was noticed that as the horizontal distance between the antennas is increased, the signal becomes weaker; this being depicted by the decrease in signal amplitude. In the same figure also, it can be seen that body tissue does affect the performance of the received signal. In Figure 5.9 (e) the belly fat at the location of the receiver antenna is observed to slightly affect the fidelity of the signal. However, such occurrences can be utilized to identify body tissue structures in medical health applications and monitoring.

In order to determine how well matched or distorted the transmitted signal is when received by the transparent antenna, a correlation detector is employed. The correlation detector as given in equation (5.1) from [7] is used for this. This detector will give the time shape of the radiated pulse. The pattern of this pulse is the normalized correlated coefficient of the electric field with the template as a function of direction given by $\vec{a}(\theta\phi)$. The

transmitted signal is defined in the equation as shown in the red brackets whilst the spacing between the antennas in the blue brackets.

$$= \left[\frac{\int_{-\infty}^{+\infty} (\vec{E}(t, R, \theta, \phi) \cdot \boxed{\vec{a}(\theta, \phi) T(t)} R dt)}{\sqrt{\int_{-\infty}^{+\infty} |\vec{T}(t)|^2 dt} \sqrt{\int_{-\infty}^{+\infty} \vec{E}(t, R, \theta, \phi) \boxed{R^2} dt}} \right]^2 \quad \dots \text{Eqn (5.1)}$$

Template for Tx Signal
Spacing distance between antennas

The correlation obtained for the various antenna configurations and spacing in Figure 5.9 is given by the fidelity factor as shown in Figure. 5.10. The fidelity factor for the same antennas in free space for three different configurations namely, FF, FS and SS at 11cm are given as comparison in Figure 5.11. The antennas on-body are basically in the SS configuration.

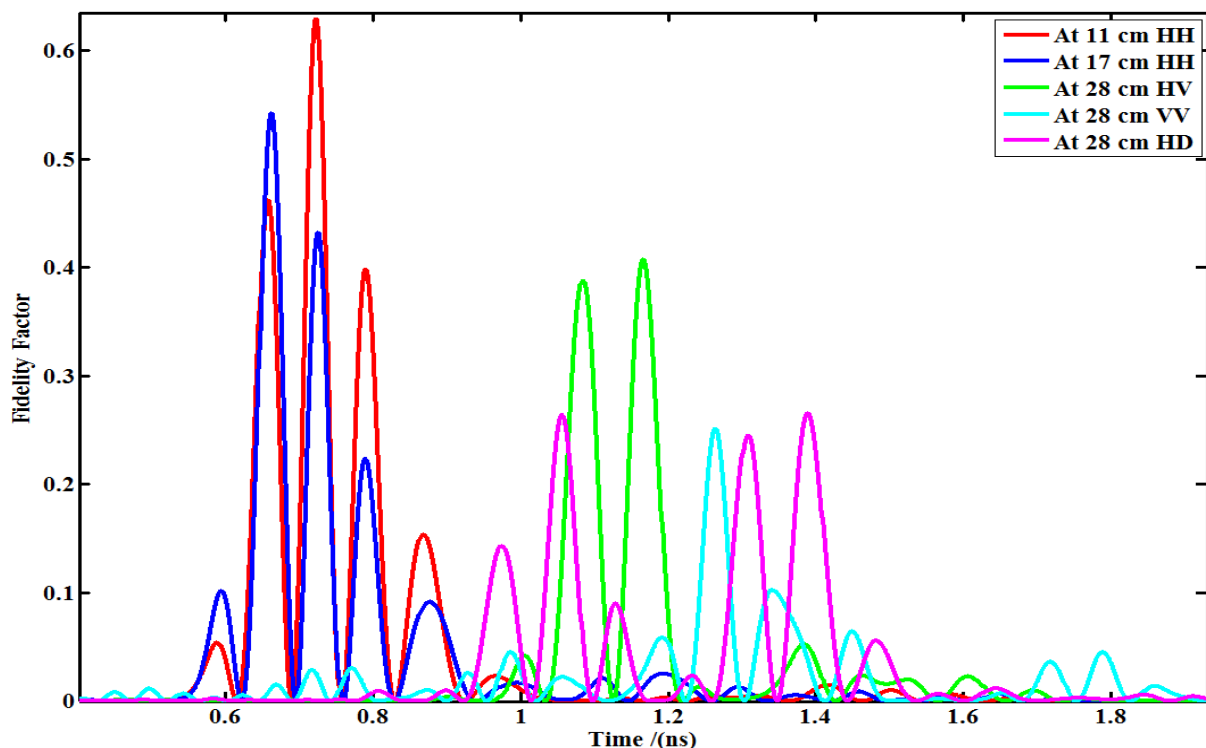


Figure 5.10 Fidelity factor for the antennas on-body.

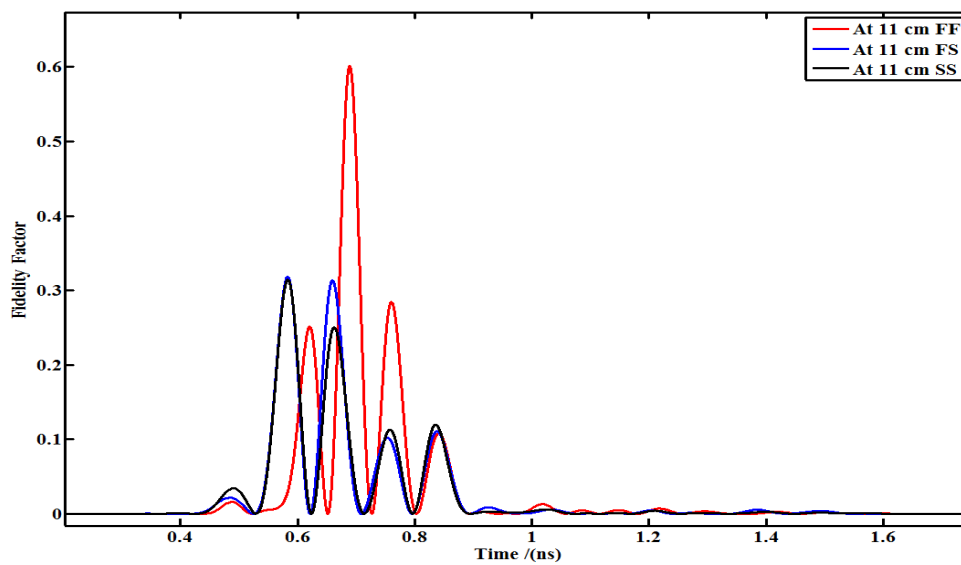


Figure 5.11 Fidelity factor for the antennas in free space in the FF, FS and SS configurations.

From Figure 5.10, there seems to be good correlation for the SS configuration on body at 11 cm and 17 cm. The fidelity factor for the SS configuration at 11 cm spacing for on-body was observed to be better than that of free space, this being depicted in Figure 5.12. The good correlation demonstrated shows that transparent antennas could be effectively used for on-body communications.

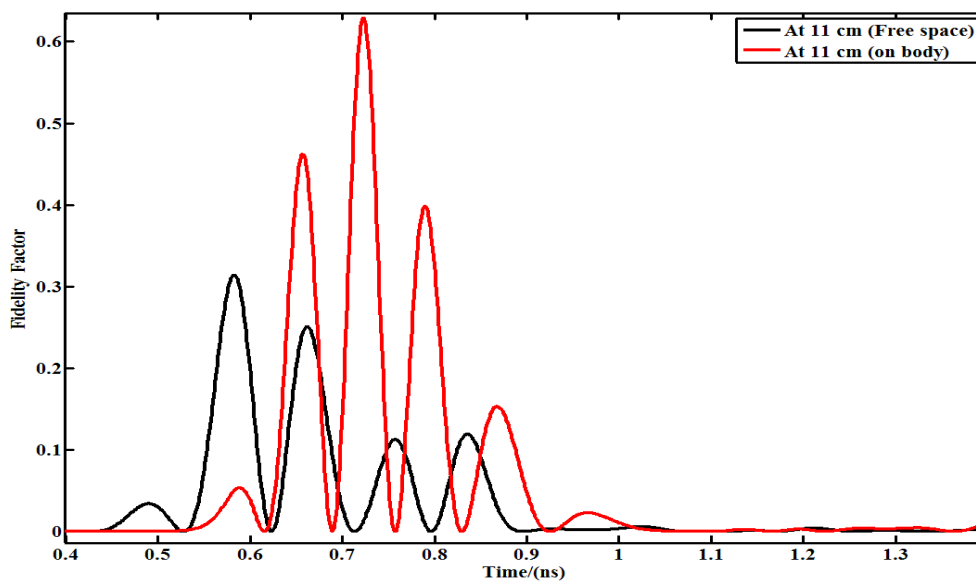


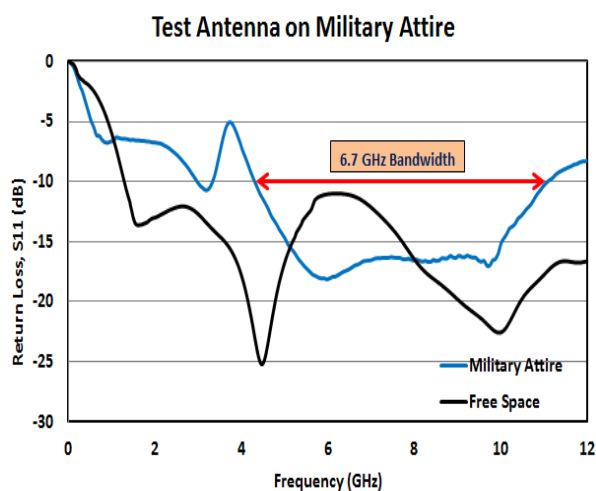
Figure 5.12 Fidelity factor in the SS configuration at 11 cm spacing on body compared to that of free space.

5.3 Transparent UWB Antennas for Wearable Applications

Besides body-centric applications, transparent UWB antennas can also be used as wearable antennas like in defence communications. Figure 5.13 shows the MTA placed discreetly on a military outfit. The return loss shows the attained bandwidth as 6.7 GHz for the MTA. This was because the MTA was not optimized for use on the military outfit but rather free space. The intent here was to show the possibility of the covert use of such transparent UWB antennas to provide a wide frequency range for signal communications. The antenna could be designed to transmit and receive in the military bands if necessary. With the use of Snap-on connectors, these antennas could be easily detached and stored away when the outfits need to be washed.



(a)



(b)

Figure 5.13 (a) Transparent UWB MTA tested on a military outfit (b) measured return loss of the antenna on military attire compared to free space.

5.4 Summary

In this chapter it has been shown how the transparent polymer based UWB antenna such as those made from AgHT material can be used for on-body applications in the health

and medical industry. The additional advantage as the analysis has shown is that, the silver coated polyester (AgHT) antenna is able to deliver an on-body gain that is close to free space gain from 3 to 7 GHz. Health monitoring devices can thus be potentially manufactured in this frequency range to give a stable performance both on-body and off-body. As the PET material is flexible and conformal, it can host a UWB array and be wrapped around the body part if required. Also, the configurations showed in Figure 5.10 can be easily imprinted or inscribed on a large one piece sheet of the AgHT material and used on-body to minimize accessories to hold the antenna in place on the body. It has also been highlighted in this chapter, that this is the first time transparent antenna radiation results on a human subject in an anechoic chamber has been reported for publication.

A brief review of the transparent UWB antenna for wearable applications has also been presented to show how it can provide a solution for current obtrusive and visible wearable antennas.

5.5 References:

- 1) T. Peter, R. Nilavalan, R. DiBari, A. Alomainy, S.W. Cheung and A.R. Tharek, "Analysis of Transparent UWB Antennas for Body-Centric Applications" *Piers*, submitted for publication.
- 2) A. Rahman, A. Alomainy and Y. Hao, "Compact Body-Worn Coplanar Waveguide Fed Antenna for UWB Body-Centric Wireless Communications", *European Conference on Antennas and Propagation (EuCAP 2007)*, November 2007, Edinborough, UK.
- 3) M. Tzyh-Ghuang and T. Chao-Hsiung, "An Ultrawideband Coplanar Waveguide-Fed Tapered Ring Slot Antenna", *IEEE Transactions on Antenna and Propagation*, vol. 54, No. 4, April 2006.
- 4) J. Liang, L. Guo, C.C. Chiau, X. Chen and C.G. Parini, "Study of CPW-fed circular disc monopole antenna for ultra-wideband application" *IEEE Proc- Microw. Antennas Propag.*, vol. 152, no. 6, November 2005.
- 5) A. Katsounaros, Y. Hao, N. Collings and W.A. Crossland, "Optically transparent ultra-wideband antenna", *Electron. Lett.*, vol. 45, Issue 14, pp.722-7232 July 2009.
- 6) Z.N. Chen, A. Cai, T.S.P. See, X. Qing and M.Y.W. Chia, "Small planar UWB antennas in proximity of the human head," *IEEE Transactions on Microwave Theory and Techniques*, vol.54, no.4, pp. 1846- 1857, June 2006.
- 7) J.S. McLean, H. Foltz and R. Sutton, "Pattern descriptors for UWB antennas," *IEEE Transactions on Antennas and Propagation*, vol.53, no.1, pp. 553- 559, Jan. 2005.

CHAPTER 6

Analysis of Transparent UWB Antennas on Glass Structures

6.1 Introduction

This chapter takes a step further to study the effect of introducing glass as a substrate and as a superstrate for a transparent UWB antenna. This study is especially important as the primary application for transparent antennas are glass windows or glass panels whether in cars like Fractal System's Tranztenna [1] or in homes, or high rise buildings like hotels or commercial business centres where AgHT is commercially used as a sunscreen film to conserve energy. Up till now, research material published for transparent UWB antennas, has only used glass as a substrate and Perspex as a superstrate [2]. However, for the transparent antenna to be able to be used on window glass, the effect of glass as a superstrate and also as a substrate on the performance of the antenna needs to be studied. This will further aid in the integration of solar cells or solar films as laminations on the glass.

6.2 Dielectric of the Glass

The dielectric of the glass used in each of the experiments below need to be determined first before it can be used in the simulation. The following approach was used in the determination of the dielectric. From literature on the web, it was found

that soda lime glass had a dielectric constant between 7.2-7.75 [3]. Using 7.2 as an initial value and the approach that is described in the next section it was found that most of the glass pieces available from the glass retailers in the locale had dielectrics ranging from 5.7 to 6.0.

6.2.1 Experimental Determination of Glass Dielectric

A 2.4 GHz patch antenna was first designed in CST using the microstrip patch antenna calculator shown in Figure 6.1 from [4] using an arbitrary dielectric value of 5.9. The patch is then tuned with insets for impedance match in CST and optimized to resonate at 2.4 GHz as shown in Figure 6.2 (a) and (b).

The figure shows a 3D perspective view of a microstrip patch antenna. A yellow rectangular patch is mounted on a grey dielectric substrate of height h . The patch has length L and width W . Below the substrate is a yellow ground plane. Labels include 'patch', 'dielectric (ϵ_r)', and 'ground'. A copyright notice '© emtalk.com' is visible.

Substrate Parameters

Dielectric Constant (ϵ_r):

Dielectric Height (h): mm

Resonant Frequency

f_r : GHz

Physical Parameters

Length (L): mm

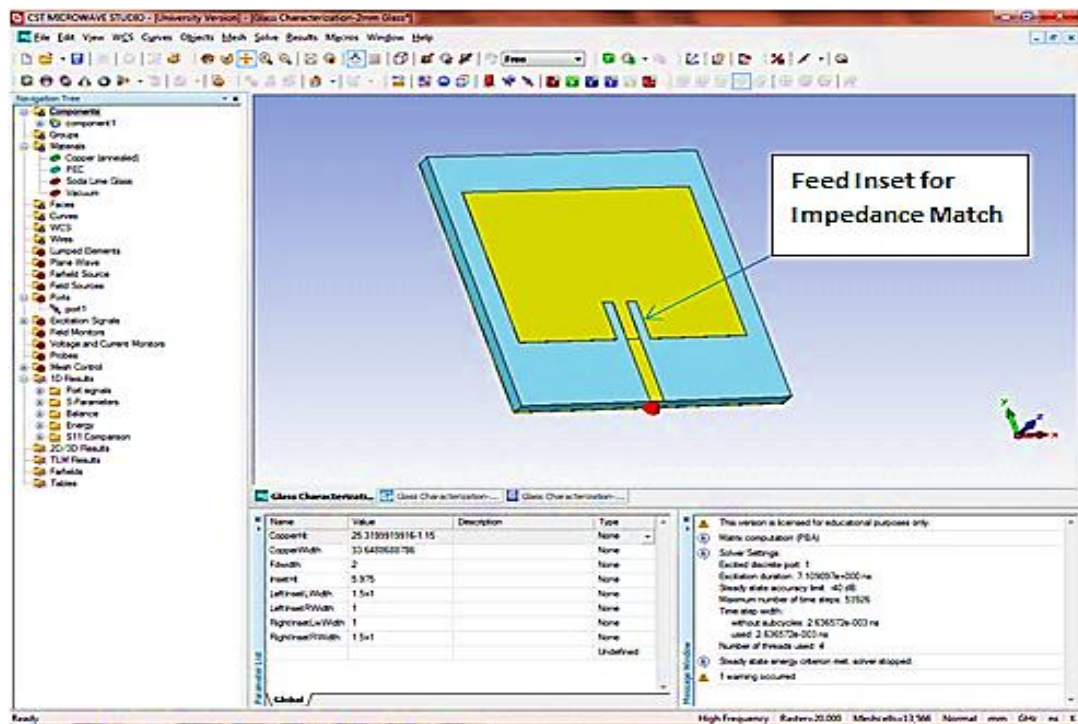
Width (W): mm

Input Impedance (Edge): Ohm

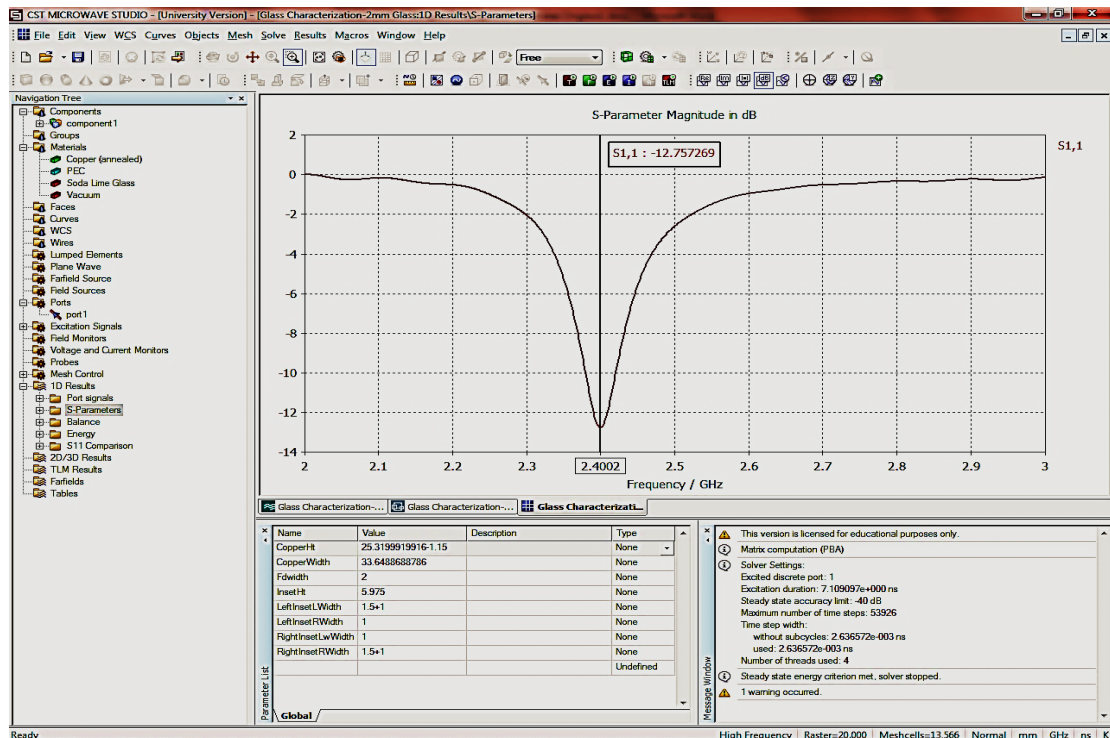
Buttons: Synthesize, Analyze

Figure 6.1 Microstrip patch antenna calculator from emtalk.com.

Chapter 6 – Analysis of Transparent UWB Antennas On-Glass Structures



(a)



(b)

Figure 6.2 (a) Patch antenna after being tuned with feed insets for impedance match and (b) return loss of the patch resonating at 2.4 GHz.

The patch is later fabricated and the return loss at which the patch resonates is observed on a Performance Network Analyzer (PNA). For the 2 mm glass, the fabricated patch resonated at 2.42 GHz as shown in Figure 6.3.

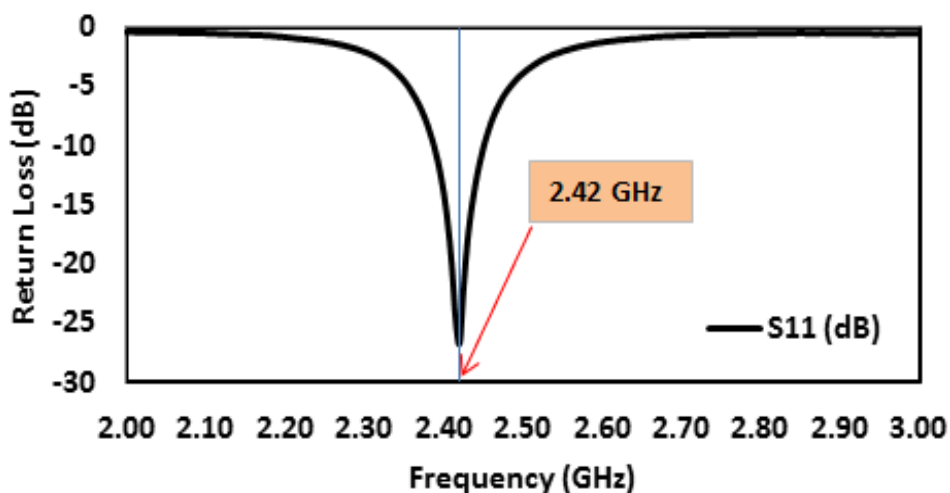


Figure 6.3 Measured value of the fabricated patch on the 2 mm glass for the dielectric value of 5.9.

The dielectric value in CST was then adjusted, in this case reduced, until the patch resonated at 2.42 GHz. The new value of the dielectric was found to be at 5.7. One shortcoming of this approach compared to using a commercial dielectric resonator is that it will not give the loss tangent. However, a tedious way would be to determine the dielectric permittivity for the individual frequencies from say, 1 to 11 GHz to determine the variation in dielectrics and make some compensation for a dispersed fit in CST. For the sake of simplicity, the dielectric constant of the glass is assumed to be of constant fit from 1 to 20 GHz in simulation. This assumption was used in simulation for the various glass thickness used in the research work for this thesis.

6.3 Antennas with Glass Substrate

Antennas with glass as a substrate have been researched on in the past especially for vehicular applications [5]. Due to the higher dielectric of the glass, the antennas

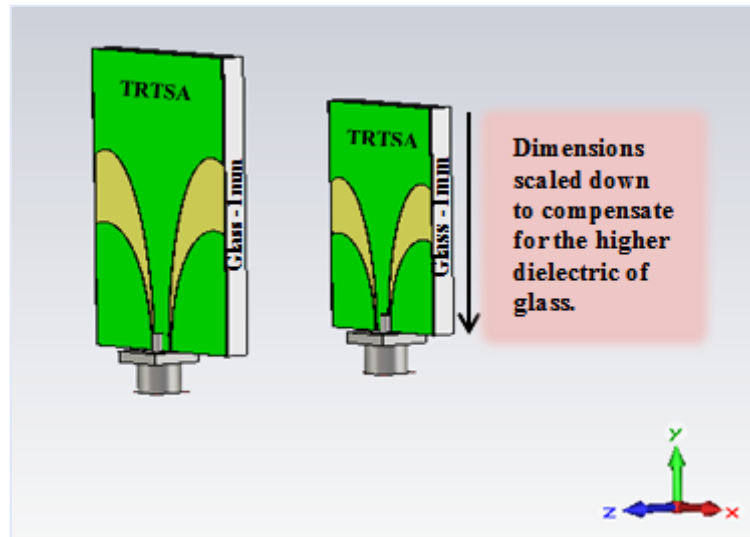
designed for free space have to have their dimensions reoptimized. The antenna will be first decreased in size in correspondence to the dielectric of the glass substrate. Then it will be scaled in height accordingly to compensate for the thickness of the glass material until the optimized dimensions are achieved to have a impedance matched antenna. Some cue is taken from [6-7] to achieve this optimization. For example, when the height of the antenna is increased or decreased, it shifts the operational bandwidth of the antenna lower in frequency or higher in frequency respectively. The two-step approach that is, compensating for the dielectric first and then the thickness, is taken so that the parametric study that will done to achieve the optimization in CST will focus on one parameter at a time.

Different glass thicknesses were studied however, for illustration the study for a 2mm glass is presented here. The dielectric of the glass was first determined by an experimental method as described in section 6.2.1. The 2 mm soda lime glass substrate's dielectric constant was found to be 5.7. Knowing from antenna miniaturization techniques [8-10] that an increase in the dielectric of the substrate would bring about a decrease in antenna size, the antenna was scaled down to obtain the optimized dimensions. The optimum dimensions to scale down the antenna were obtained through parametric study. The optimization was done for a unit thickness 1mm. The height and width of the antenna as well as the ground height played effective roles in obtaining the impedance match for a wide bandwidth. Optimizing the X-Y ratios of the ellipses for the radiators and ground of the TRTSA antenna in the CST aided in fine tuning the impedance matching to obtain a wide bandwidth.

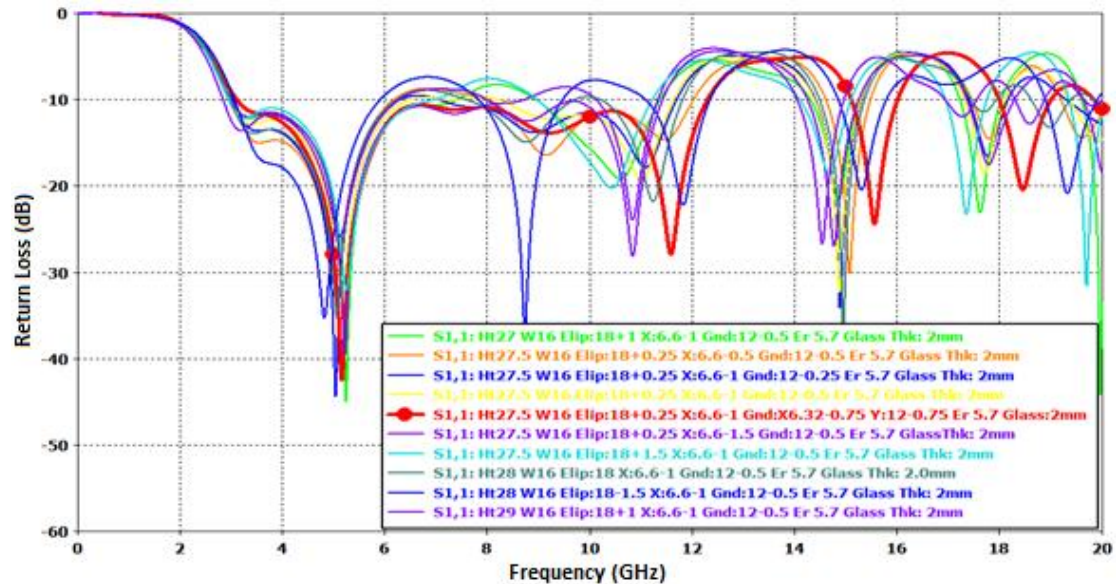
Figure 6.4 (a) depicts the scaling approach for optimizing the dimensions of the TRTSA antenna for the determined dielectric of the 1 mm thick glass while Figure 6.4 (b) shows the parametric study done in simulation for optimization of the dimensions to obtain matched impedance.

Next compensation for the actual thickness of the glass of 2 mm was done by way of another similar parametric study. The height of the antenna was found to play a major role in achieving the impedance match. . The final optimized height and width for the antenna were 27.5 mm and 16 mm respectively with the ground height decreased from 12 mm to 11.5 mm. Hence a free space antenna of 23x16 mm was re-

optimized to 27.5x16 mm when placed on a 2 mm thick glass substrate of dielectric constant, 5.7. The return loss for the optimized antenna size is shown in red in Figure 6.4 (b). The achieved bandwidth in simulation ranged from 3 GHz to 12.2 GHz.



(a)



(b)

Figure 6.4 (a) Scale down of antenna dimensions to compensate for dielectric of glass and (b) parametric study to obtain the optimized dimensions.

Prototypes of the antenna were made and measured for the return loss as well as the gain using the antenna measurement equipment, Star Lab at Hong Kong University. Quick end launchers (QEL) from Gigalane, Korea [11] as shown in Figure 6.5 were used for the mounting. The QELs enabled solder less mounting which made it very convenient for testing and verification of the simulation results. The 50 Ohm QEL SMA connectors can be used for frequencies up to 18 GHz and had a VSWR of 1.25 (max) throughout that range. The QEL came with a maximum board clearance of 2 mm and hence the necessity to use a 2mm or lesser thickness glass for the prototype. Nevertheless, a thicker glass could be used with the normal SMA connector but conductive epoxy is needed to provide contact for the launch pin and also keep it fixed.

Gigalane Quick End Launchers

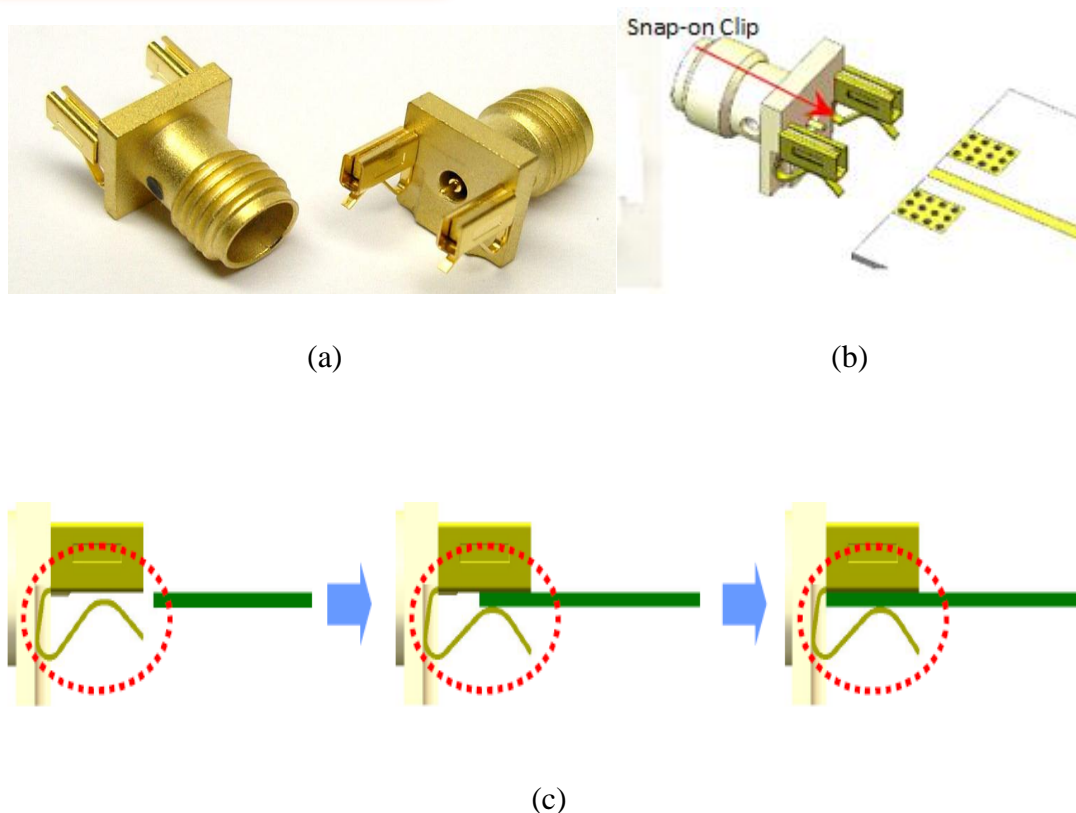


Figure 6.5 (a) Isometric view of the quick end launchers and (b) illustration of the snap on clip that provides tension to hold the connector to a pcb (c) demonstration of ease of mounting onto a pcb [11].

Figure 6.6 shows the simulated and measured return loss of the TRTSA whilst Figure 6.7 and Figure 6.8, the measured gain and efficiency using Star Lab respectively. The shift in the return loss is basically due to fabrication accuracy as it depends very much on a steady hand to trace exactly the design onto the sheet of AgHT film. Also, the absorbency property of the metallized PET, AgHT was not factored in for the simulation as the exact permeability values were not available. The effect of the latter is the prominent resonance dip at the lower frequencies below 3 GHz especially around 1 GHz as can be seen in Figure 6.6 and Figure 6.9. It has to be mentioned that the technique to optimize gain and efficiency through the ‘silver base technique’ was not used here as the silver paint material had expired. Conductive epoxy was directly applied to make the connections and give the QEL leads a tight fit, hence a very low efficiency.

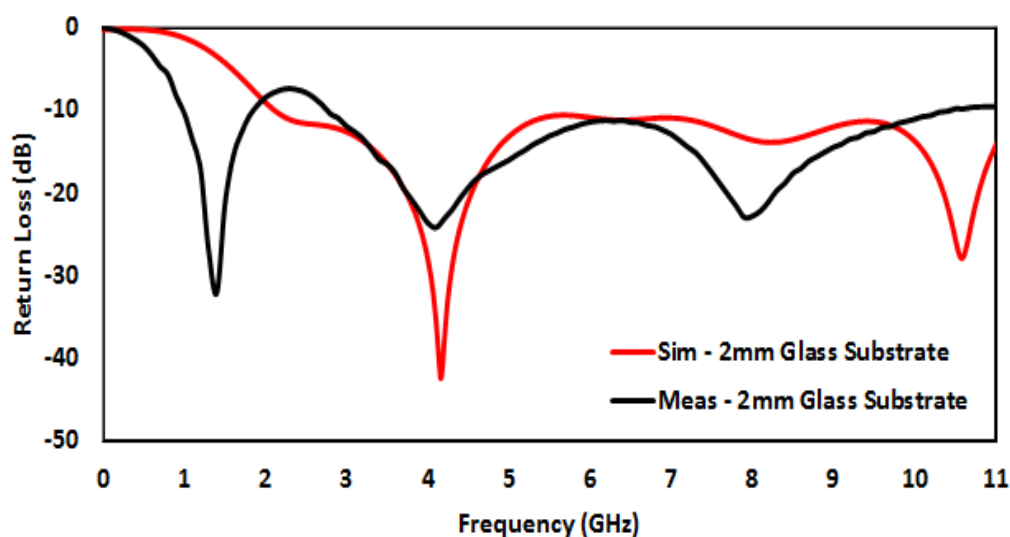


Figure 6.6 Simulated and measured return loss of the TRTSA on a 2 mm glass substrate.

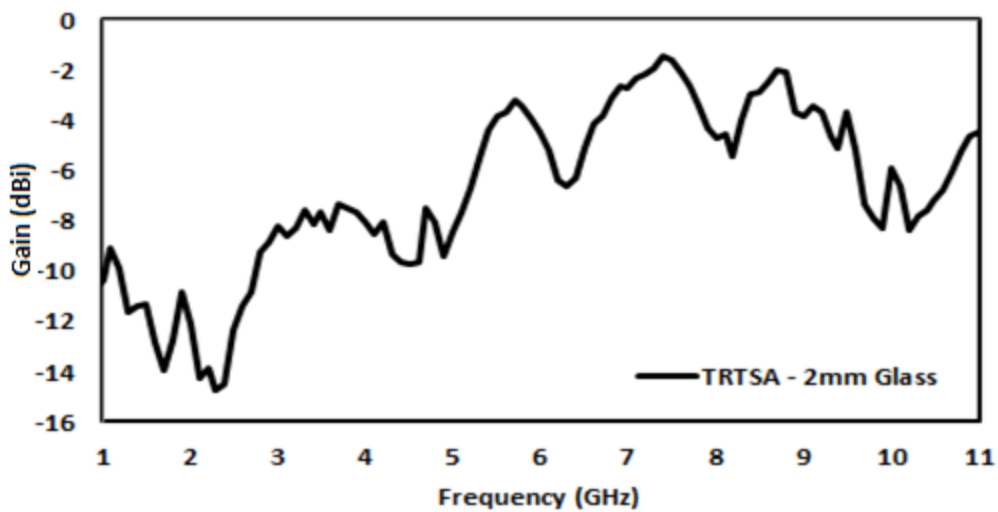


Figure 6.7 Measured gain of the TRTSA on the 2 mm glass substrate.

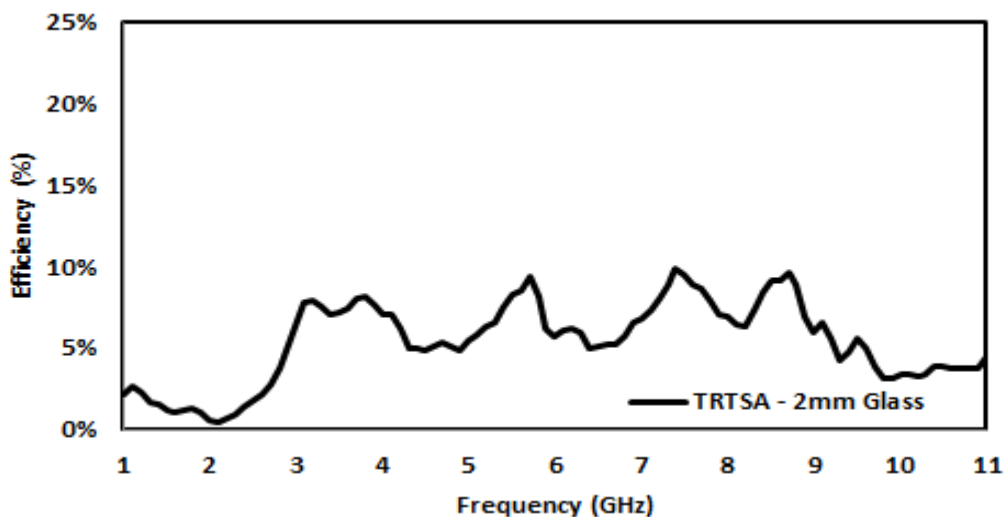


Figure 6.8 Measured efficiency of the TRTSA on the 2 mm glass substrate.

A similar antenna on a 4 mm glass substrate was also designed on CST and fabricated. The simulated and measured return loss of this antenna is shown in Figure 6.9 below. The achieved bandwidth in simulation was from 2.7 – 10.2 GHz. The dielectric of the 4 mm glass determined by experimental method was 5.935 which was slightly higher than the 2 mm glass. The gain and efficiency measured on the Star Lab is shown in Figure 6.10 and Figure 6.11 respectively.

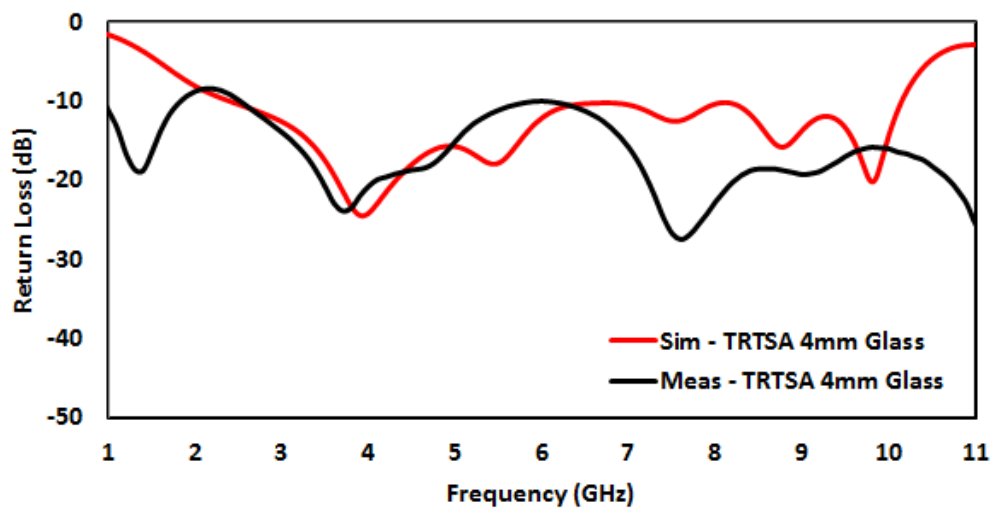


Figure 6.9 Simulated and measured return loss of the antenna on a 4 mm glass substrate.

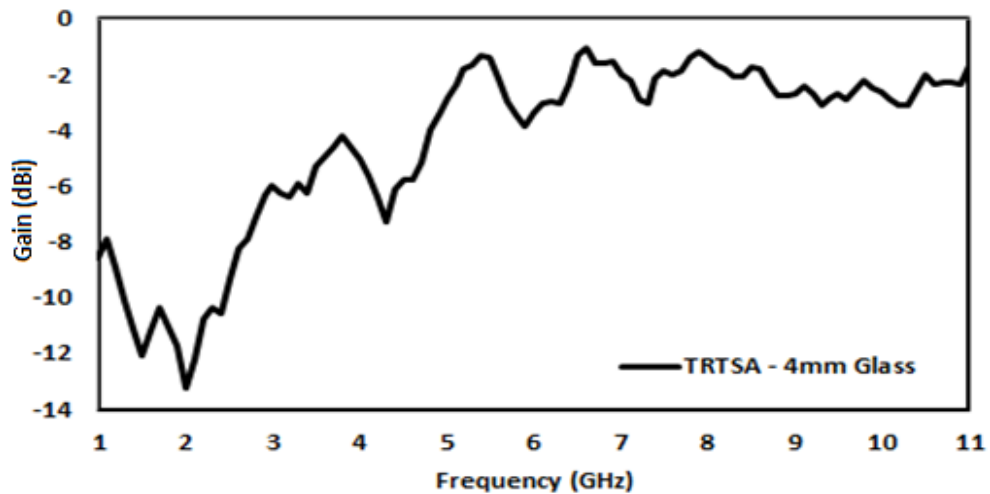


Figure 6.10 Measured gain of the antenna on the 4 mm glass substrate using Star Lab.

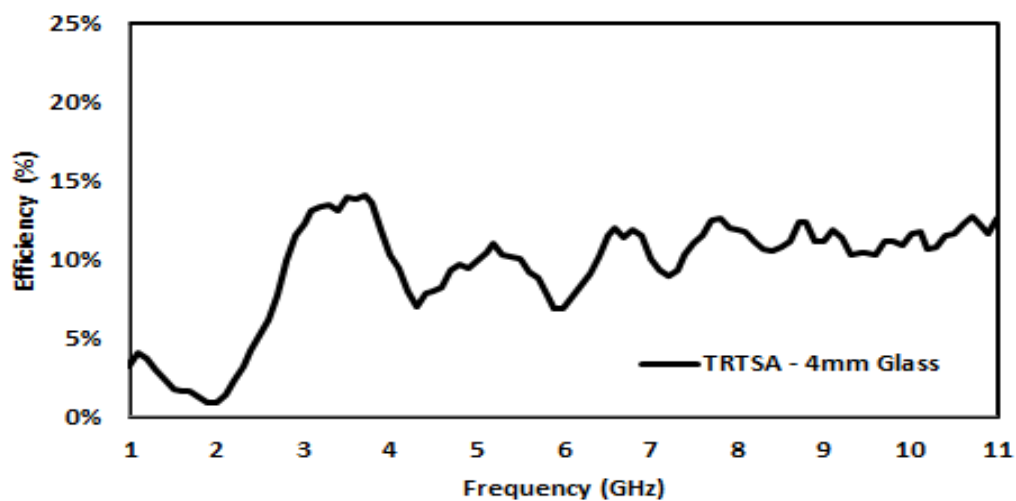


Figure 6.11 Measured efficiency of the antenna on the 4 mm glass substrate using Star Lab.

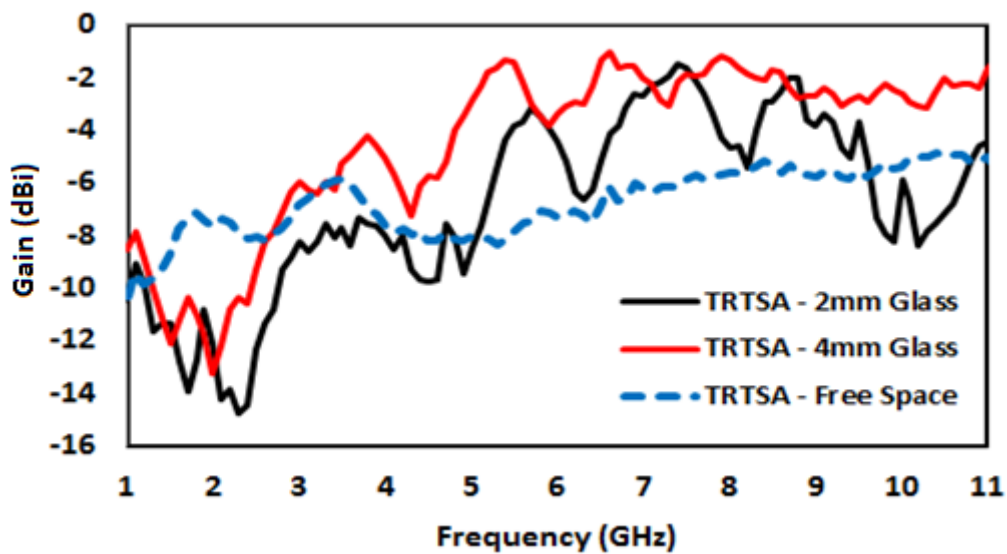


Figure 6.12 Comparison of the measured TRTSA gain: on-glass substrate versus free space.

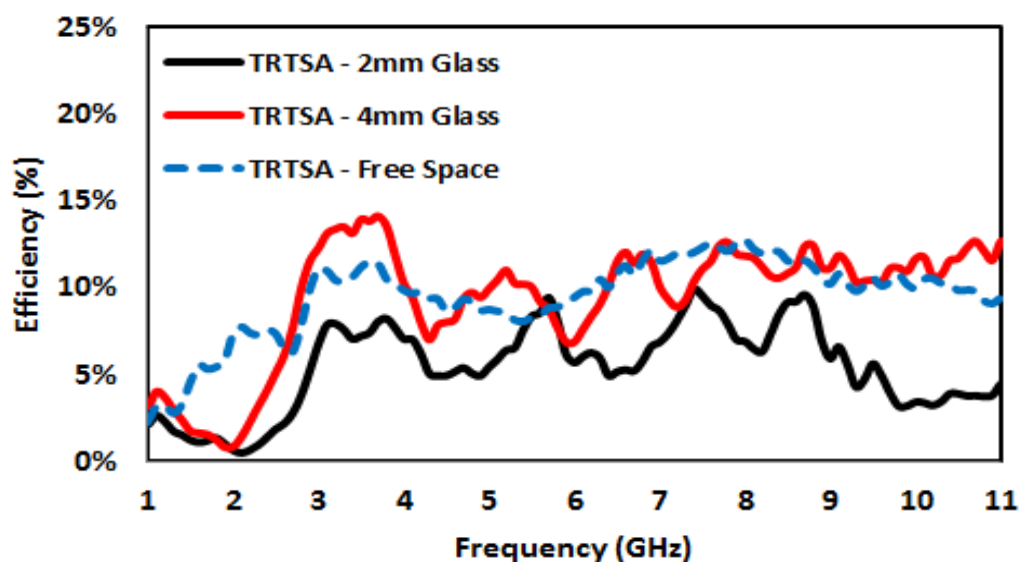


Figure 6.13 Comparison of the measured TRTSA efficiency: on-glass substrate versus free space.

The on-glass gains of the TRTSA when compared to free space gain were higher (Figure 6.12). One can argue that this may be due to the slightly bigger size of the TRTSA when optimized for glass. This may not be so as the larger size MTA in Chapter 4 only registers an average gain of -5 dB for the FCC bandwidth from 3.1 to 10.6 GHz. The glass material does indeed help enhance the gain of the antennas but at the same time slightly attenuates the energy transmitted. This is evident from Figure 6.13 where the measured efficiencies of the TRTSA on the two glasses are on the

whole lesser than that of the TRTSA in free space. The attenuation is basically due to the antenna-glass interactions. The radiated power is reflected at the glass boundaries as well as internally in the glass structures. As already highlighted in Chapter 4, the direct relationship between gain and efficiency is also not observed. However for antennas on glass structures, the Satimo system issue as well as the changing directivity of the antenna affects the efficiency. The directivity is not constant like in free space. It changes possibly due to the thickness of the glass, higher permittivity of the glass or even antenna-glass interactions.

The efficiency for the 2mm glass is a lot lesser due to a cumulative effect. Besides the refraction phenomena, the efficiency of the TRTSA on the 2 mm glass was also affected by the connector. The QEL for the 2mm glass antenna did not provide a very good feed connection unlike that of the free space and the 4mm glass antennas which had cold soldered SMA feed connects, thus additionally affecting the 2 mm glass antenna's efficiency. The QEL's effect is also evident from the low energy conversion of an on-glass CTSA rectenna when compared to its free space performance even though the on-glass dimensions of the antennas are slightly bigger. This is elaborated in more detail in Chapter 7.

6.3.1 UWB Transmission Test

The antennas on the 2 mm and 4 mm glass substrate were tested for video transmission using a UWB audio/visual (A/V) link extender. The A/V link extender transmitter's antenna was swapped with that of the on-glass antennas and the longest transmission range achieved for good wireless video streaming from a laptop onto a distant LCD monitor was noted. The measurement set-up is as shown in Figure 6.14. A free space TRTSA was used for comparison. The transmitter specification gives a maximum range of 30 feet line of sight (LOS) range. The measured ranges for the three TRTSAs are shown in Table 6-1 below. The transmitter transmits at a centre frequency of 7 GHz with a bandwidth of 1.57 GHz. The device has a data transfer rate of up to 220 Mbps via UWB technology. It uses two band groups of the FCC

bandwidth. For the United States (US) it uses the Band Group 1 between 3.168 and 4.752 GHz and for outside the US, Band Groups 3 and 6 between 6.336 and 8.976 GHz. The device used for this work was purchased in Asia.

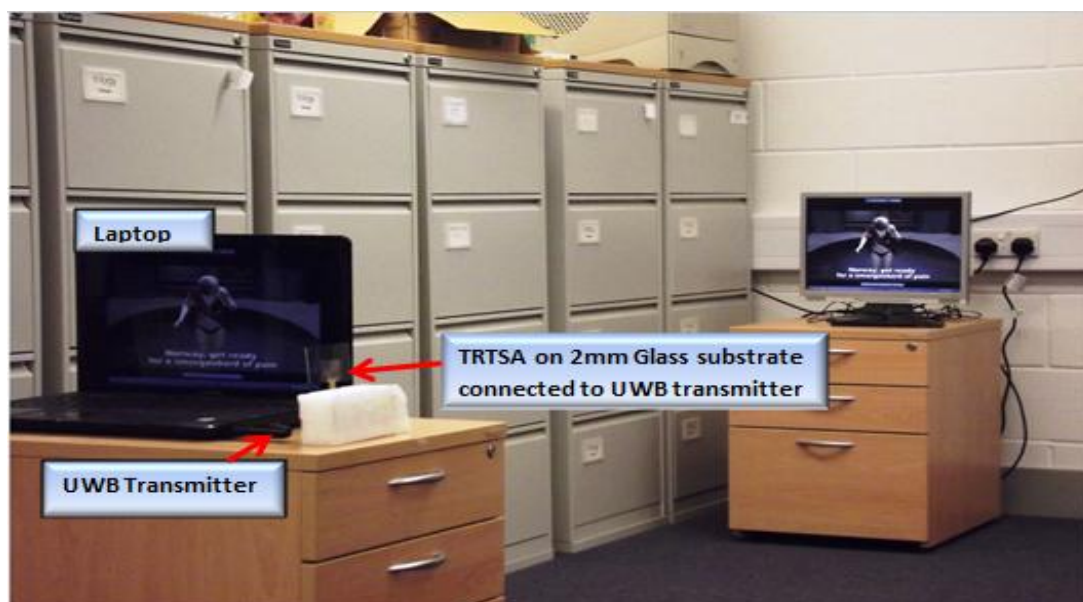


Figure 6.14 Measurement set-up for the UWB video transmission test.

The TRTSA in free space showed good range which was close to the specification of the transmitter's original antenna. However, on the 2mm glass the range in the positive x-axis that is on the side in front of the antenna, dropped drastically to 2.67 m but however improved to 5.0 m in the negative x-axis which is the direction behind the glass substrate as shown in Figure 6.15. Similarly, for the 4 mm glass, a range of 4.39 m and 10.27m was obtained in the front and back respectively. From simulation, the reason for this was found to be because the glass tends to focus and concentrate the radiation energy more in the direction of the free space behind the glass. This is depicted in Figure 6.16. Hence it can be clearly seen, the glass acts as a sort of RF lens 'focusing' the radiation energy on the antenna it is placed on. However, the 'focusing' effect here actually happens by redirecting some of the energy from the front of the antenna to the back of the glass. The thicker the glass, the more the amount of energy redirected and hence longer the LOS transmission ranges of the antenna on the side of the glass.

Table 6-1 Measured video transmission range on a UWB A/V link transmitter.

Antenna Type	Maximum Line of Sight Range (m)
AV Link Transmitter	9.14 m (Specified) 15 m (Measured)
TRTSA – Free Space	9 m
TRTSA – 2 mm Glass Substrate	2.67 m (front)/ 5.0 m (back)
TRTSA – 4 mm Glass Substrate	4.39 m (front)/ 10.28 m (back)

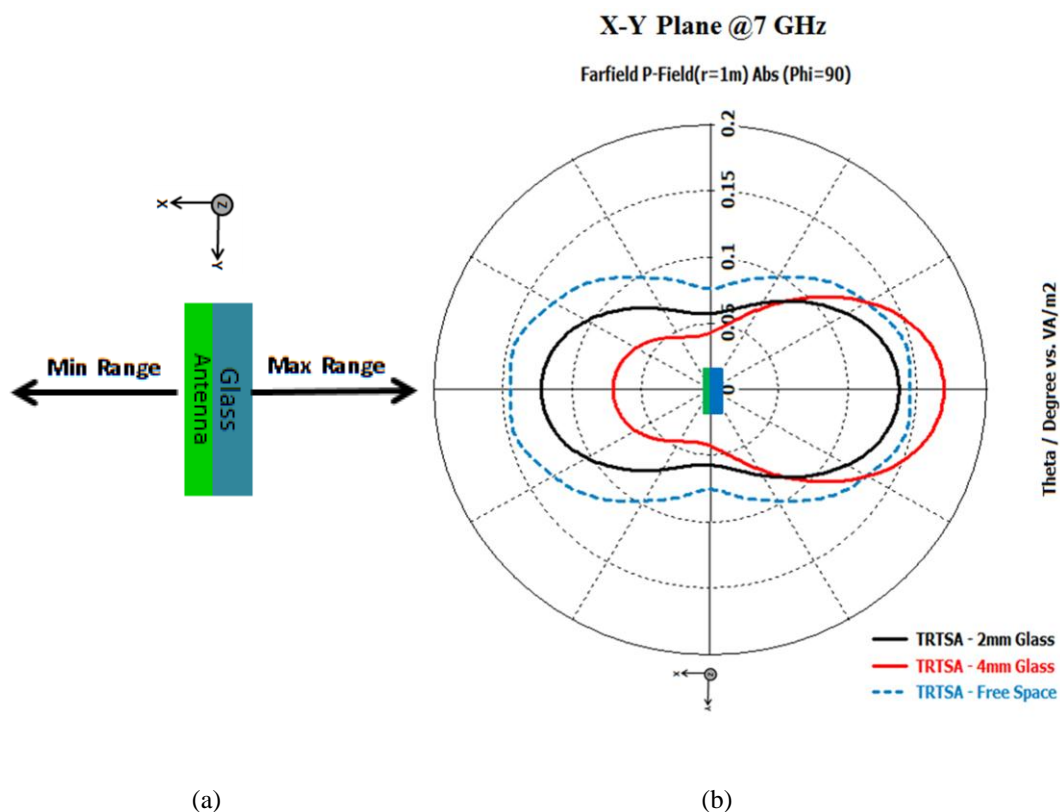


Figure 6.15 (a) Direction of the maximum and minimum transmission ranges of the antennas on the 2 mm and 4 mm glass substrate (b) simulated farfield power pattern showing energy refocused to behind glass at 7 GHz.

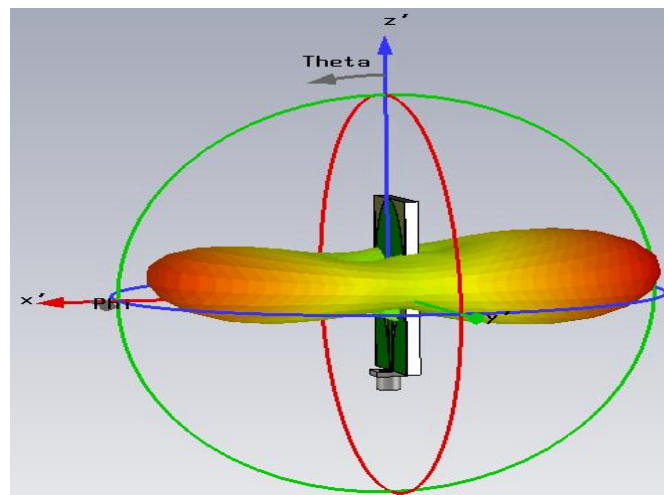


Figure 6.16 3-D Farfield radiation plot at 7 GHz (linear scaling) showing radiation intensity behind glass is greater than in front.

On analysing the measured return losses of the antennas on the 2 mm and 4 mm glass as depicted in Figure 6.17, it was also clear why the antenna on the 4 mm glass had higher transmission ranges than that of the antenna on the 2 mm glass. The return loss of the antenna on the 4 mm glass is higher (-15.86 dB at point B) than that of the antenna on the 2 mm glass (-12.89 dB at point A) at 7 GHz. This means that more energy is radiated by the 4 mm glass substrate antenna. In essence, the 4 mm glass substrate antenna has a higher gain (-2.02 dB) at 7 GHz compared to its 2 mm counterpart's gain (-2.73 dB) and hence the higher ranges of transmission - this being depicted in Figure 6.18.

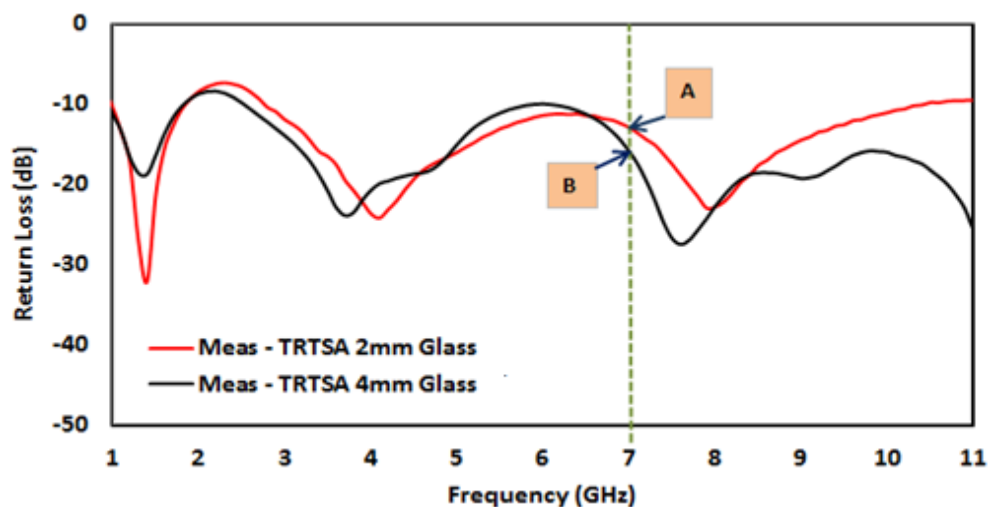


Figure 6.17 Comparison of return loss at 7 GHz.

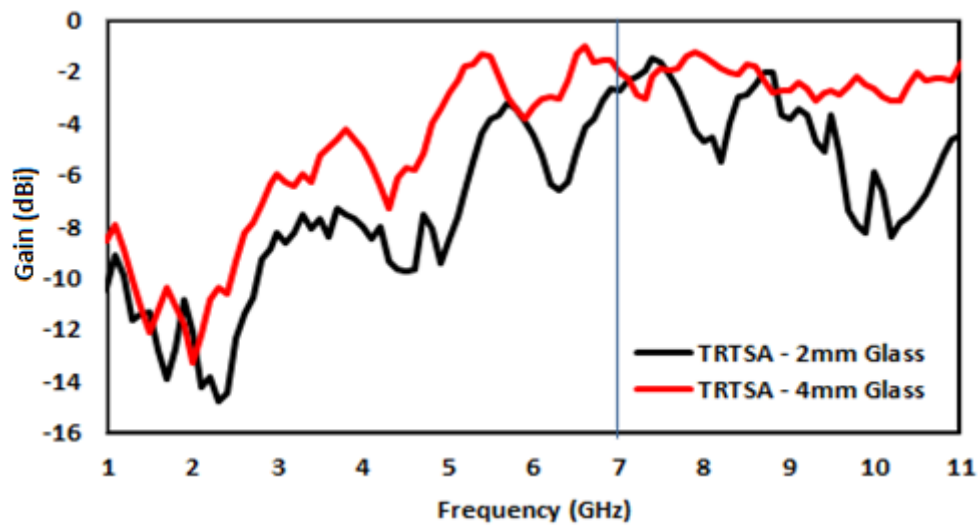


Figure 6.18 Comparison of gain at 7 GHz.

However, when comparing the radiation patterns of the two antennas, we need to compare the energy patterns of the antennas (Figure 6.19) which is the total response of their power patterns in the frequency domain [12]. The maximum gain and hence the direction of maximum transmission is noticed to be in the orientation of the negative x-axis.

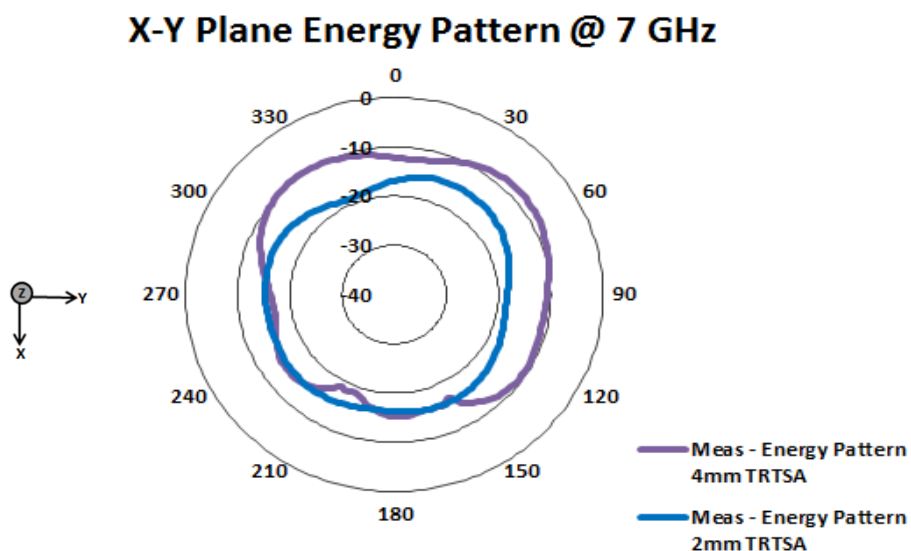


Figure 6.19 Comparison of energy patterns at 7 GHz.

Additionally, it is also possible to improve the transmission range by optimizing the antenna design to have a return loss that exhibits a deep resonance at the desired frequency of transmission of 7 GHz as shown in Figure 6.20. This can be done by parametrically scaling or descaling the structure of the TRTSA in the x and y axis so as to tune the optimum return loss to the desired frequency (Figure 6.21). This solution may involve a compromise on the ultra-wide bandwidth, but this may not be a concern if the application is only for a particular frequency like in the case of the A/V link extender which is designed to operate at 7 GHz to provide a fast video streaming link extender from a PC to a TV.

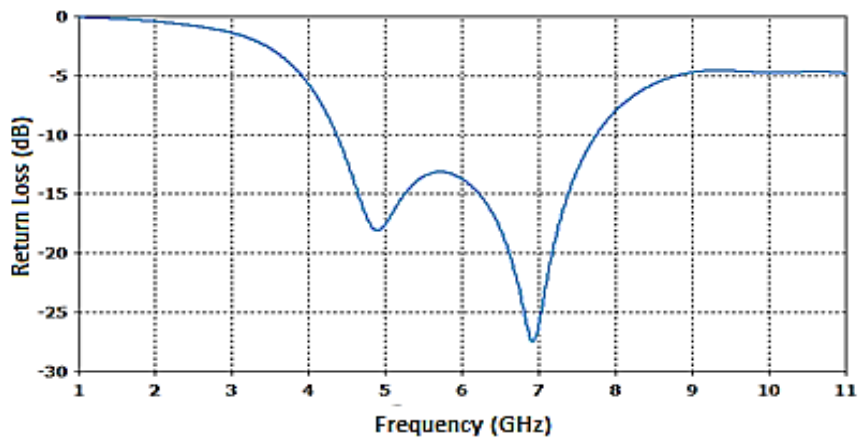


Figure 6.20 Optimizing return loss to peak at 7 GHz through descaling antenna structure by 60% in x-axis and 70% in y-axis in CST.

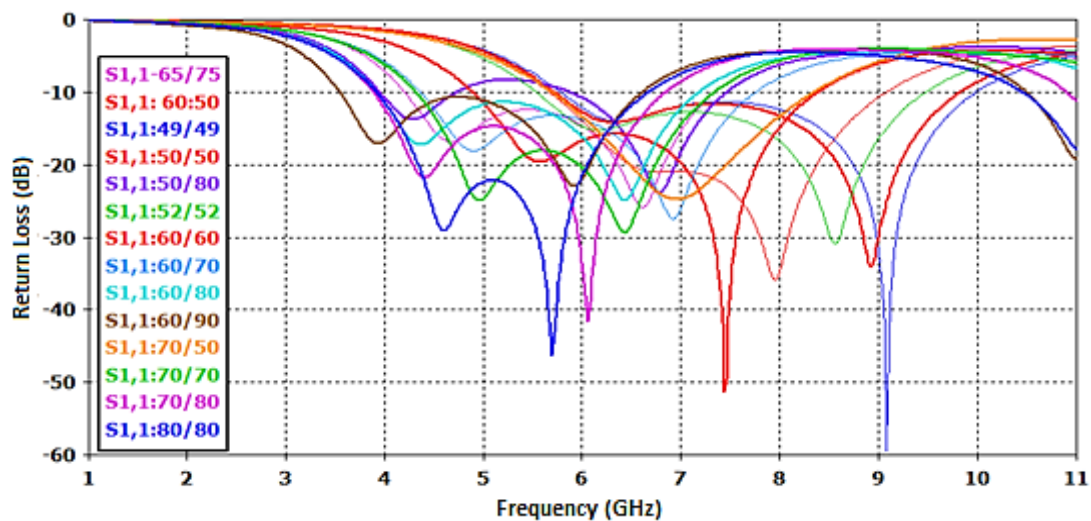


Figure 6.21 Tuning of antenna for optimum return loss response through scaling and descaling of antenna structure in x and y axis in CST.

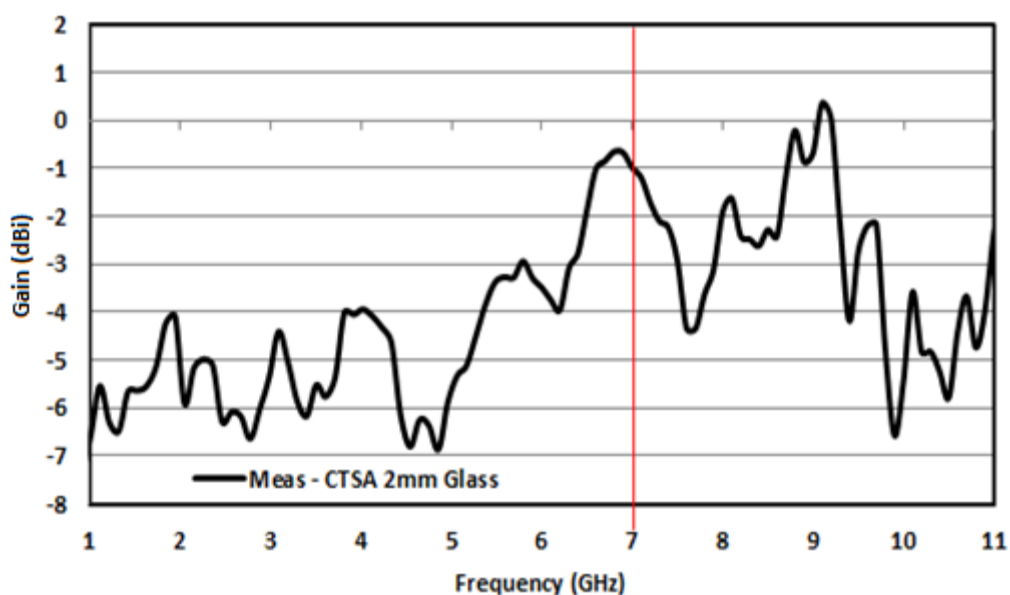
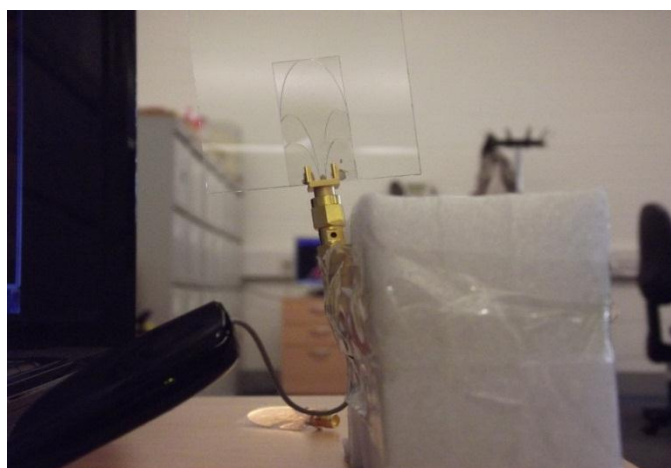


Figure 6.22 Gain optimized for 7 GHz using CTSA geometry (grid lines included for clarity) on 2mm glass substrate.

Alternatively, new geometries can be introduced to maintain the wide bandwidth and yet have a higher optimized gain at the frequency of operation. The novel CTSA of which more is described in Chapter 7 is an example of this geometry technique to improve gain. The CTSA geometry on a 2mm glass substrate showed higher gain at 7 GHz thus enabling the video transmission range to be extended further. The measured gain of the antenna is as shown in Figure 6.22. The measurement set-up is depicted in Figure 6.23 (b) with a close view of the CTSA mounted to the transmitter shown in (a). The new distance that was achieved for the wireless transmission using the A/V Link Extender was 2.74 m in the x-axis and 6.8 m in the opposite axis which is a 2% and 36% improvement respectively in the transmission range than that of the TRTSA on a similar 2mm glass substrate.



(a)



(b)

Figure 6.23 (a) The CTSA mounted on 2 mm glass substrate and connected to the A/V Link Extender's transmitter (b) measurement set-up for the wireless transmission using the CTSA on the 2 mm glass substrate.

6.4 Antennas with Glass Superstrate

Antennas with glass as superstrates have been researched on mainly for vehicular applications. These were mainly for narrow band applications [13-16] and those done on UWB were not with glass superstrates [6, 17]. From these earlier studies, glass has shown to have improved the impedance bandwidth. Laminated glass superstrate was shown to produce surface waves that introduced nulls in the radiation patterns of a narrowband antenna [16]. A transparent solution similar to that in [16] was implemented as a precautionary measure on the UWB antenna for mounting on window glass in the superstrate configuration. In this regard, a non-conducting border of 4 mm was given on the three non-feed sides to eliminate or suppress any surface waves. This is depicted in Figure 6.24.

Since the PET substrate is very thin, the measured return loss, gain, radiation pattern and efficiency obtained for the superstrate configuration were very similar to that of the antenna in the substrate configuration.

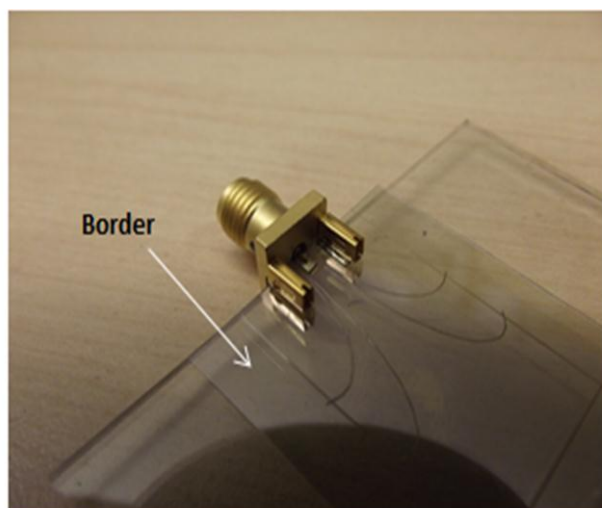


Figure 6.24 Non-conducting AgHT border to suppress surface waves.

6.4.1 Feed Connection for Superstrate Configuration

As the CPW feed of the antenna is sandwiched between the glass and the polymer substrate, connection using an SMA connector is difficult. This was overcome by using a conductive silver ribbon which is normally used in connecting monocrystalline solar cells to form a panel - this is shown in Figure 6.25. This ribbon approach thus facilitates easier transmitter and receiver cable connection to the antenna. There was no impact on the performance of the antenna since the measured results were already observed to be similar for both substrate and superstrate configurations.

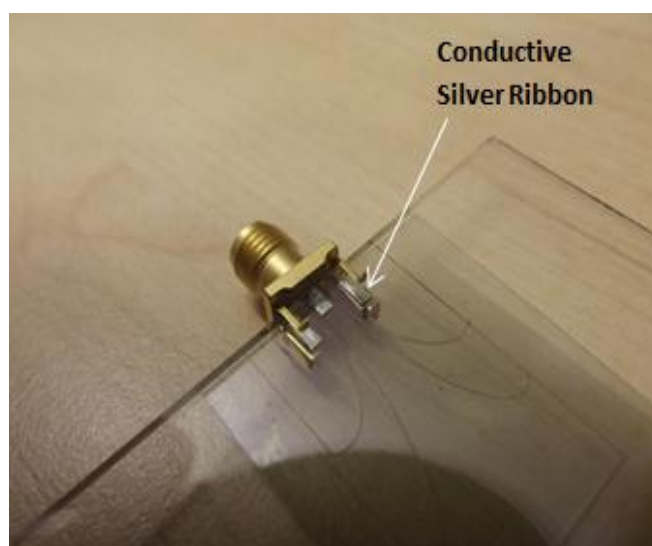


Figure 6.25 Ribbon feed contact for antenna on glass superstrate.

6.5 Antennas Sandwiched Between Glass

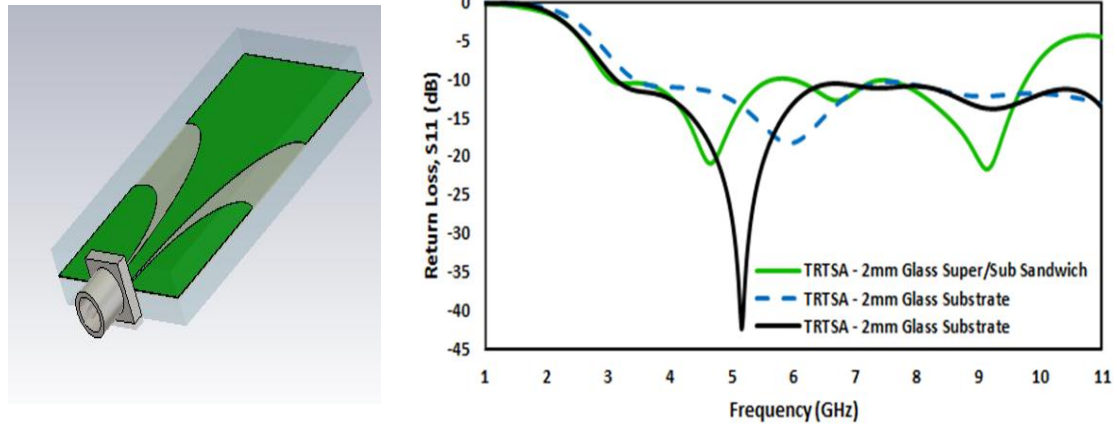


Figure 6.26 Simulated return loss of the TRTSA on a 2 mm glass substrate with a 2 mm glass superstrate.

The return loss of the TRTSA sandwiched between a 2 mm glass superstrate and substrate in comparison to that of the TRTSA in free space and on a 2mm glass substrate in simulation is given in Figure 6.26. The design has been optimized to achieve a bandwidth of 7.5 GHz from 2.5 GHz to 10 GHz. The concept is discussed in more detail in Chapter 7 where experimental measurement of a prototype using a CTSA with a 2 mm glass superstrate laminated on a 1.8 mm glass substrate that forms part of an a-Si solar panel is presented as part of this thesis research to develop an innovative green UWB antenna.

Similar simulated comparisons in gain, efficiency and radiation pattern for the three configurations are depicted in Figures 6.27 – 6.29.

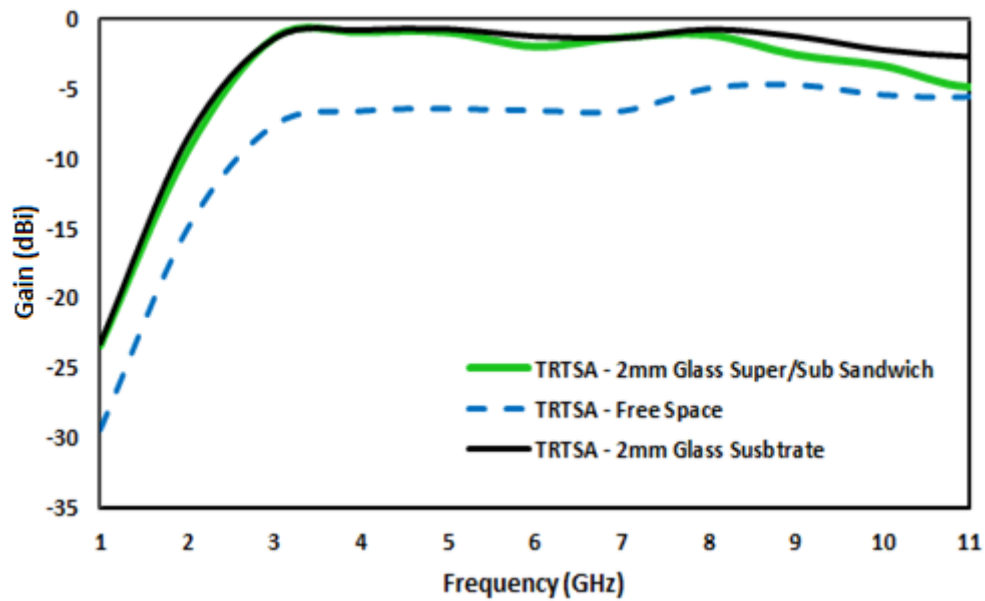


Figure. 6.27 Simulated gain of the TRTSA sandwiched between 2 mm glass superstrate and substrate compared to the TRTSA in free space and on a 2 mm glass substrate.

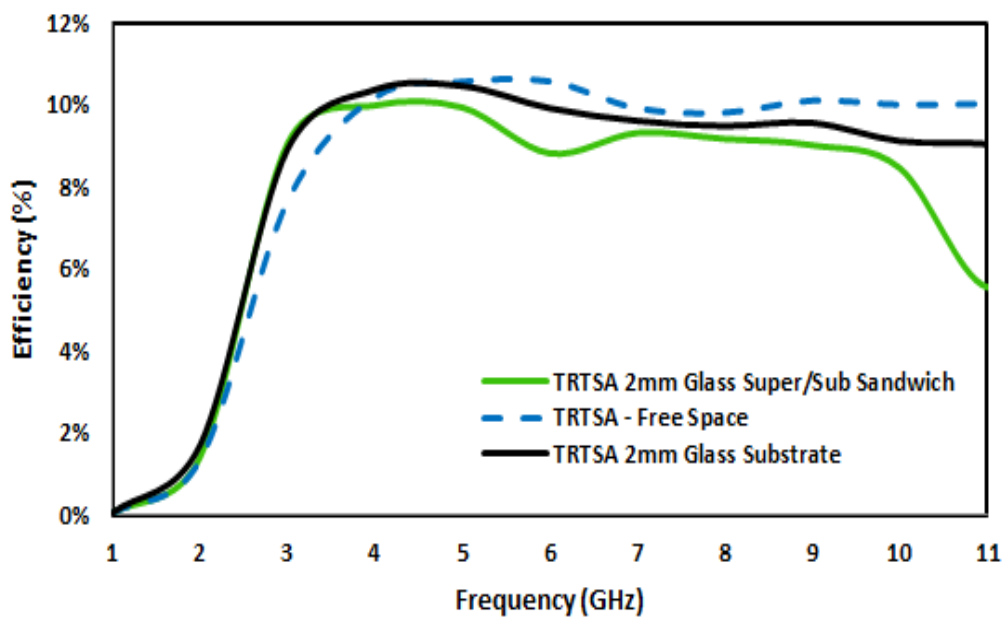


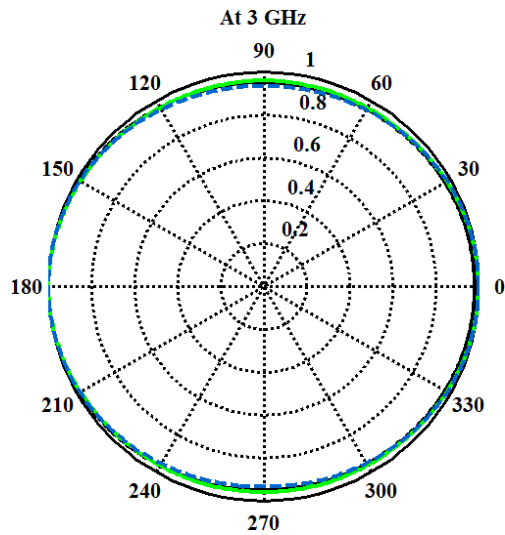
Figure 6.28 Simulated efficiency of the TRTSA sandwiched between 2 mm glass superstrate and substrate compared to the TRTSA in free space and on a 2 mm glass substrate.

From Figure 6.27 and Figure 6.28, it can be noticed from the simulation results that the glass structures whether in the substrate or superstrate/substrate

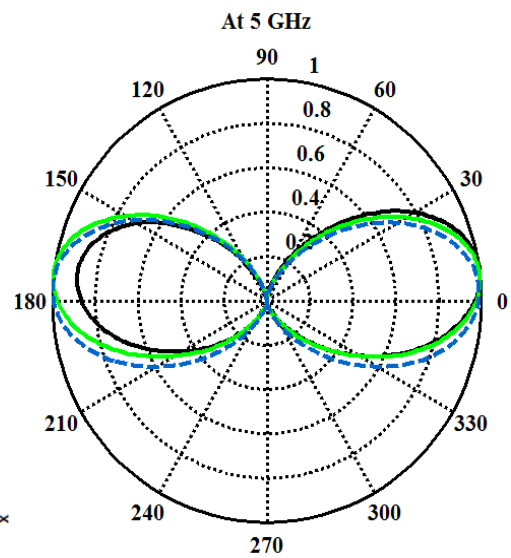
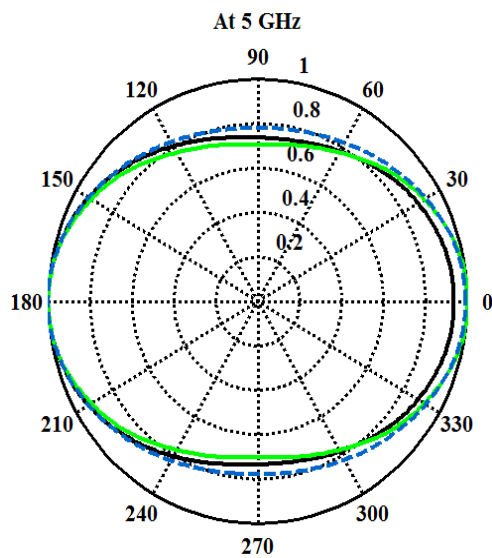
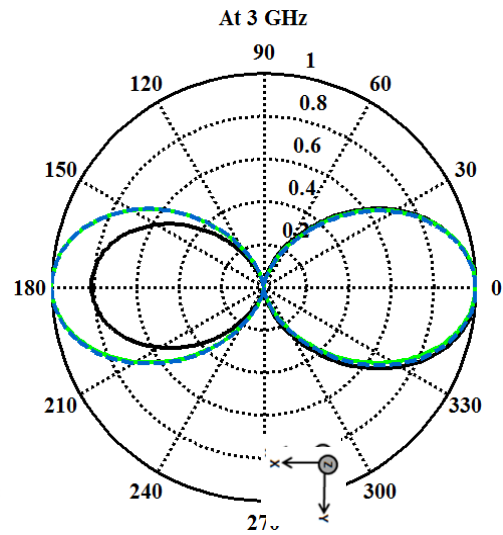
sandwich configuration both increase the gain but however exhibit efficiency drop. Here the direct relationship between gain and efficiency is not observed solely because of the changing directivity; Satimo's system issue is excluded since these are simulated and not measured results. As pointed out for Figure 6.13 earlier, the directivity changes possibly due to the thickness of the glass, higher permittivity of the glass or even antenna-glass interactions. Thicker substrates are known to give better antenna performance or gain [18] and radiation efficiency of TCOs on glass substrates have been shown to drop with increase in permittivity of the glass substrate [18]. The latter is true for the higher frequencies but not for the lower frequencies below 4 GHz as seen in the Figure 6.28. Basing on the return losses in Figure 6.26, this may be due to a matching issue of the free space TRTSA; the latter antenna has a poorer return loss response than that of the other two antennas at the lower frequencies between 2 to 4 GHz. This contention is justified by the fact that in practical applications, the cut-off for the attenuation is seen from 2.4 GHz and above [19].

From comparison of the radiation patterns in Figure 6.29, it is noticed that at lower frequencies, like 3 GHz, the radiation power patterns are Omni-directional and become directional at the higher frequencies. For the sandwich configuration, the glass on both sides balances the effect giving almost similar patterns on either side of the glass. However, for the single glass configuration, that is, the antenna on the 2mm glass substrate, the radiation power field is seen to become directional with increase in frequency (Figure 6.30). Some of the energy from the front of the antenna is redirected or refocused to the back of the glass. This lens effect could be taken advantage of as shown earlier in section 6.3.1 to extend the transmission range of UWB applications.

X-Y Plane



X-Z Plane



- TRTSA 2mm Glass Super/Sub Sandwich
- - - TRTSA - Free Space
- TRTSA 2mm Glass Substrate

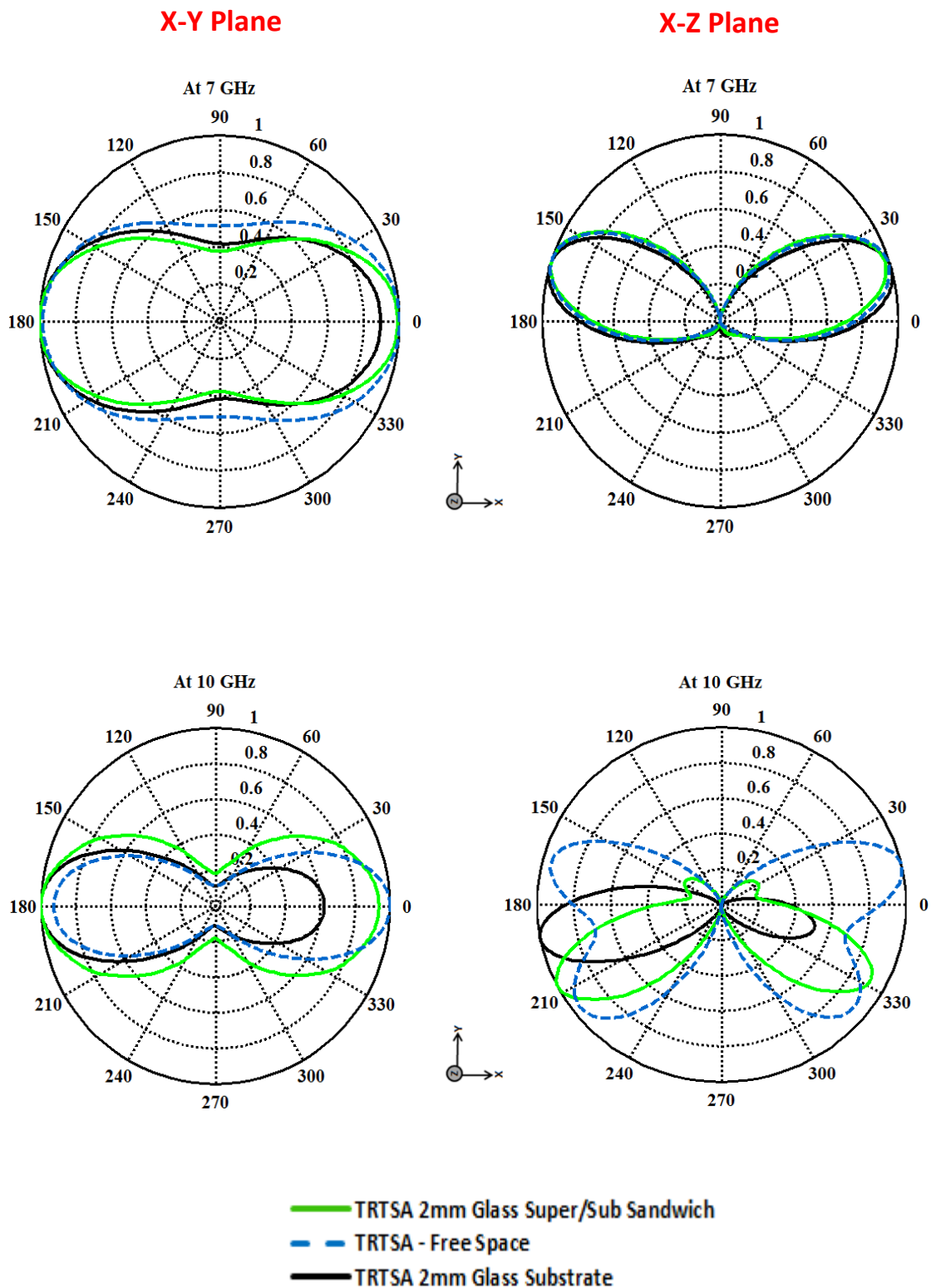


Figure 6.29 Simulated radiation power patterns (linear scaling) of the antennas for 3 GHz, 5 GHz, 7 GHz and 10 GHz.

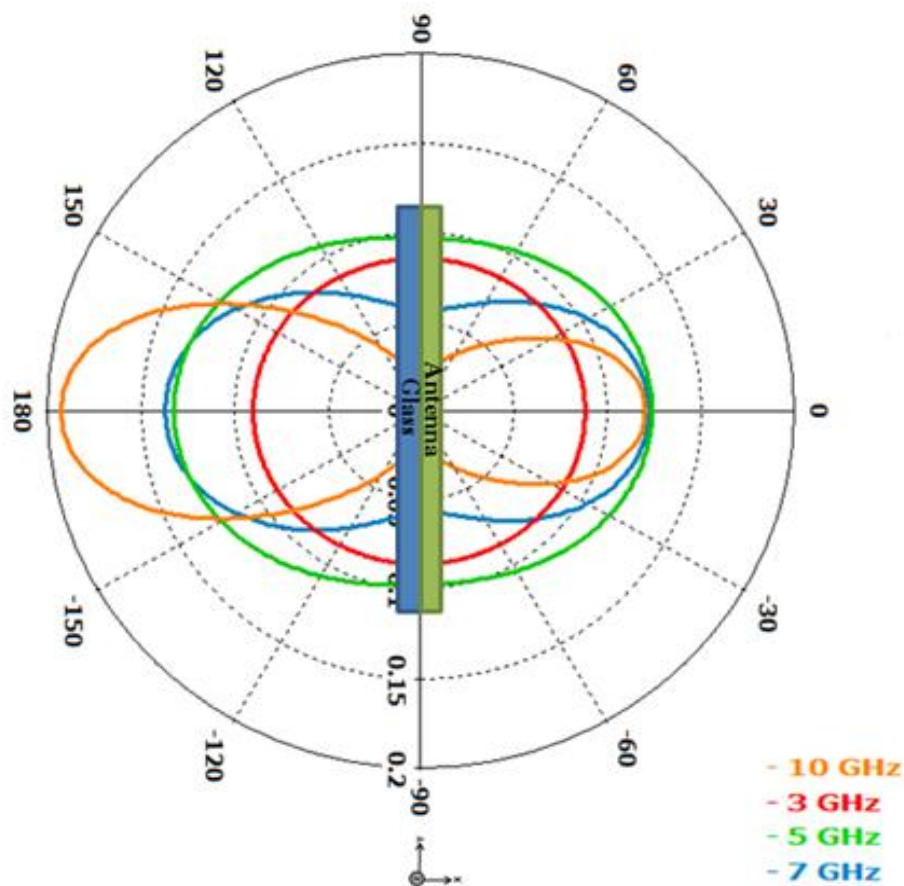


Figure 6.30 Simulated narrowing and refocusing of the microwave beams at 3 , 5 , 7 and 10 GHz through the 2mm glass substrate of the TRTSA.

6.6 Summary

This chapter has shown the impact of glass as substrate and also as superstrate on the performance of a transparent UWB antenna. From experimental study conducted, no significant difference in the performance of the antenna whether on a glass substrate or a glass superstrate was observed. This was probably because of the AgHT material being very thin in thickness. It was also shown in simulation how a TRTSA can be configured or tuned to be optimum at a particular frequency for best

LOS range performance through the scaling or descaling of the antenna structure. The performance application of on-glass antennas for video transmission was also demonstrated, and how tuning the antenna's return loss response to peak at the operation frequency of the antenna can aid in extending the video transmission range. It has also been shown both in simulation and through experimental verification using a UWB A/V link extender how glass acts as a RF/microwave lens redirecting radiation energy of an antenna in a particular direction. The lens effect causes the Omni-directional radiation pattern to become directional thus aiding the improvement of transmission range. The lens effect can thus be taken advantage of to extend LOS transmission distances for UWB applications. However, it has to be highlighted that this also goes hand-in-hand with gain improvement at the frequency of operation of the application. In regard to this too, energy response, an idea first mooted by Dau-Chyrh et al [12] for UWB antennas was used to explain more clearly the reason for the difference in the video transmission performance of the 2mm and 4mm glass substrate TRTSA.

6.7 References:

- 1) Fractal Antenna Systems. [Online]. Available: <http://www.fractenna.com>.
- 2) A. Katsounaros, Y. Hao, N. Collings and W.A. Crossland, "Optically transparent antenna for Ultra Wide-Band applications," *3rd European Conference on Antennas and Propagation, EuCAP 2009*, pp.1918-1921, March 23-27, 2009.
- 3) Permittivity of Glass. [Online]. Available: www.cidraprecisionservices.com/pm/materials/soda-lime.html
- 4) Patch Antenna Calculator. [Online]. Available: <http://www.emtalk.com/mpacalc.php>
- 5) B.A Austin and R.K. Najm, "Conformal on-glass vehicle antennas at VHF," *Eighth International Conference on Antennas and Propagation, 1993*, vol.2, pp. 900-903, 1993.
- 6) M.A. Peyrot-Solis, G.M. Galvan-Tejada and H. Jardon-Aguilar, "State of the art in ultra-wideband antennas," *2nd International Conference on Electrical and Electronics Engineering, 2005*, pp. 101- 105, Sept. 7-9, 2005.
- 7) E. Kaivanto, "Printed UWB antenna for portable devices," *IEEE Antennas and Propagation Society International Symposium, 2008*, pp.1-4, July 5-11, 2008.
- 8) L. Guo, "Study and Miniaturization of Antennas for Ultra Wideband Communications System," PhD Thesis, Sch. of Elec. Eng. & Computer Science, QMUL, Sept. 2009.
- 9) J. Huang, "A Review of Antenna Miniaturization Techniques for Wireless Applications" *trs-new.jpl.nasa.gov*, Oct. Issue, 2001.
- 10) J. Volakis, C.C. Chen and K. Fujimoto, *Small Antennas: Miniaturization Techniques & Applications*, McGraw-Hill Professional; edition 1, Aug 2010.
- 11) Gigalane, Korea. [Online]. Available: <http://www.gigalane.com>
- 12) D.C. Chang, C.H. Liao and P. Hsu, "Could the antenna pattern be in energy instead of in power?," *IEEE International Workshop on Antenna Technology, (iWAT) 2009*, pp.1-4, March 2-4, 2009.
- 13) D. Singh, P. Gardner and P.S. Hall, "Frequency doubling active transponder in car windscreen," *Electronics Letters*, vol. 33, No. 21 pp. 1799-1800, Oct 1997.

- 14) D. Singh, P. Gardner and P.S. Hall, "An active antenna transponder in a car windscreen," *IEE Colloquium on Low Cost Antenna Technology (Ref. No. 1998/206)*, pp. 8/1-8/5, Feb 24, 1998.
- 15) R. Mittra, Y. Li and K. Yoo, "A comparative study of directivity enhancement of microstrip patch antennas with using three different superstrates," *Microwave and Optical Technology Letters*, vol. 52, pp. 327–331, 2010.
- 16) P. Lowes, S.R. Day, E. Korolkiewicz and A. Sambell, "Performance of microstrip patch antenna with electrically thick laminated glass superstrate," *Electronics Letters*, vol.30, no.23, pp. 1903-1905, Nov 10, 1994.
- 17) B. Biscontini and P. Russer, "A Novel Planar Multilayered Ultra Wide Band (UWB) Cylindrical Reflector Antenna," *Asia-Pacific Microwave Conference, APMC 2007*, pp.1-4, Dec. 11-14, 2007.
- 18) T. Yasin, R. Baktur and C. Furse, "A study on the efficiency of transparent patch antennas designed from conductive oxide films," *IEEE International Symposium on Antennas and Propagation (APSURSI), 2011*, pp. 3085-3087, July 3-8, 2011.
- 19) J. Hartley, "Making safe waves in hazardous areas", White Paper, Extronics. [Online]. Available: <http://www.extronics.com>

Chapter 7

Development of a Novel Antenna for Integration of Solar Panels and RF Energy Harvesting

7.1 Introduction

In this chapter a novel transparent UWB Cone Top Tapered Slot Antenna (CTSA) is developed for green applications notably for Solar and RF Energy Harvesting. The development is described in the later parts of this chapter. A brief introduction to green antennas is however presented first to understand the background, progress, research development in this area, and how the newly developed antenna can be used for both solar and RF energy harvesting.

“Green antennas” are basically antennas that harvest or use renewable energy to drive or power the communications system associated with them. In this regard, antennas that collect the sun rays as in [1], or integrate solar cells on their radiating elements [2-3], or are incorporated onto solar panels [4-5] can be regarded as green antennas. These antennas basically harvest or use the solar power harnessed to power their transmitter or receiver. A good example of this is the TG35 radio antenna (Figure 7.1) [6] which has a solar pack incorporated onto the box on which the antenna is plugged into. The solar pack recharges an in-built battery that powers the radio antenna.

The term “Green antennas” can be widened by dotted lines in a manner of speaking to include energy harvesting that is not associated with renewable energy. In this sense, antennas used to scavenge radio frequencies and microwaves [7-13] and convert them

through a rectifying circuit into DC electricity can also be called green antennas. The rectifying circuits can be an external circuit or one that is integrated. These types of green antennas are specifically referred to as “Rectennas” or rectifying antennas. The DC electricity can then be used back to power the active components of the transmitter or receiver connected to the antenna. So in effect, the system has become self-reliant without drawing power from a mains source thus contributing to energy savings indirectly.



Figure 7.1 The TG35 self-powered radio antenna uses a solar pack to harvest energy to power it [6].

In a similar manner, antennas that enable power saving through improved gain [14] can also be loosely categorized as green antennas since in essence anything that contributes to reduction of energy usage indirectly helps to reduce the carbon footprint.

The transparent antennas or specifically, UWB antenna in the purview of this thesis, can easily take on any of the above types of green antenna configurations as can be seen in the sections later on in this chapter. Due to the transparent feature of the TCO film on which they are designed and fabricated, they can easily incorporate solar films as laminates in the form of superstrates or substrates to harness the sun’s energy while the conductive area of the TCO can simultaneously be used as a radiating antenna and a receiver for electromagnetic signals. As receiver it can also be turned into a scavenger for RF and microwaves from the air for conversion into DC power.

7.2 Non-Optically Transparent Green Antennas

7.2.1 Solar Ray Collector Green Antenna

The green antenna proposed by Lim et al [1] is basically a solar ray collector. The entire metallic portion of the antenna and its ground are used as light-reflecting surfaces for a solar-cell system. The antenna comprises of a suspended plate antenna (SPA) array built on a non-planar ground that provides a focusing effect of the solar light onto solar cells. Each of the SPA element is excited to operate in a microwave band. The SPA elements are arranged in an array on the non-planar ground in such way or configuration as to focus the light that falls on them onto the solar cells. The focusing effect increases the intensity of the light falling on the solar cells thus increasing the voltage output of the solar-cell system. The paper claims that an increase as much as 80% in voltage output is possible with the SPA approach. The harvested power is to be used on wireless systems that require self-sustained power. Figure 7.2 depicts the configuration set-up of this concept of a green antenna.

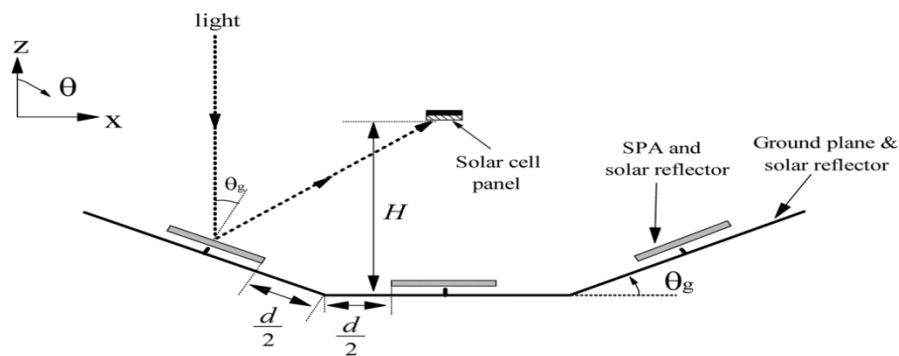
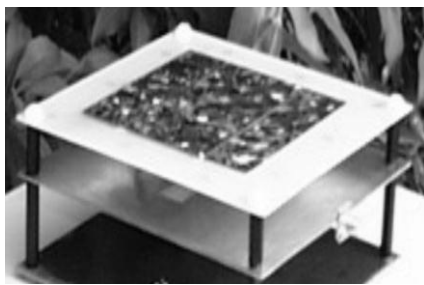


Figure 7.2 The solar ray collector [1].

7.2.2 Solar-cell Integrated Antennas

These types of antennas as portrayed in [2-3], incorporate solar cells on the surface of the antennas. The antenna demonstrated in [2] however, integrates both the solar cell and antenna that is, the electrically conductive parts or contacts of the solar cell element is simultaneously used as an antenna to radiate or receive electromagnetic waves. Here, the

metallic ground of the solar cell is made to act as the radiating patch. The ‘patch’ is fed by way of a feed line through aperture coupling on its reverse side. The patch is separated from the solar cell through an air gap or a substrate (foam being a good alternative) with similar dielectric properties. Figure 7.3 depicts the layout and prototype of the antenna. The DC connects are through vias to the solar cell and are designed as $\lambda/4$ transformers which are shorted with capacitance at their ends. This creates a high impedance at the input of the DC lines making them virtually invisible to the RF current thus preventing the DC circuitry influence on the antenna properties.



Prototype

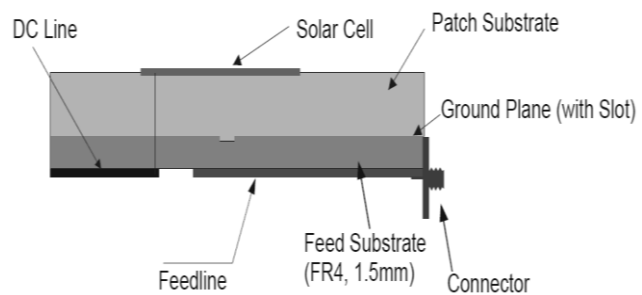


Figure 7.3 Prototype and layout of the aperture coupled antenna with solar cell [2].

Henze et al [3] , proposed a GPS patch antenna for vehicular applications integrating photovoltaic cells. This is a modified version of the antenna topology in [2] but tailored to be used on the roofs of cars or vehicles. The DC decoupling from the RF signal path is achieved in a similar manner as in [2] by using the aperture coupled antenna topology, the designed antenna is able to isolate the DC current from the RF line. The working principle and the antenna design is illustrated in Figure 7.4. The authors of [2] and [3] who are from the same research group have called their design approach as the Solar Planar Antenna (SOLPLANT) which uses the conductive parts of the solar cell to simultaneously work as antenna.

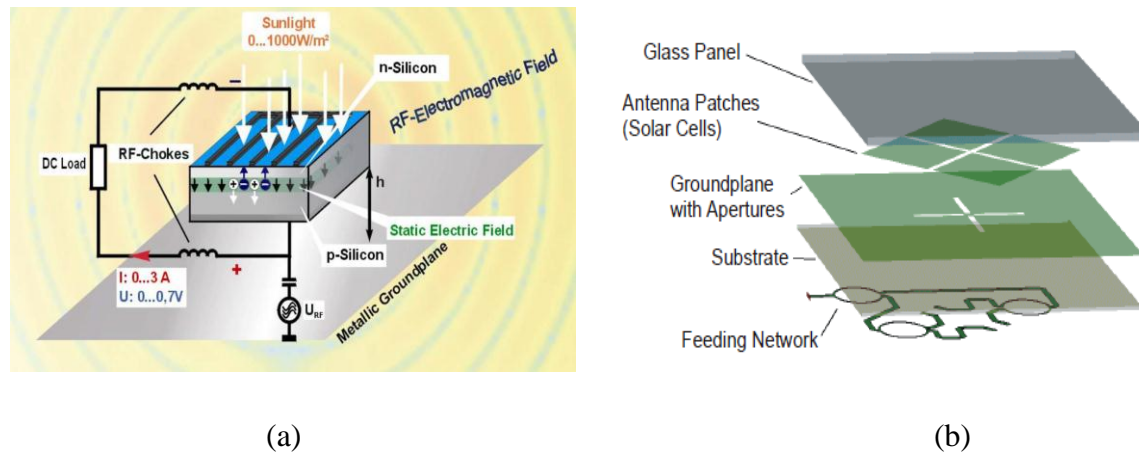


Figure 7.4 (a) Basic working principle of the Solar Planar Antenna (b) the antenna design layout [3].

7.2.3 Antenna Incorporated Onto Solar Cells/Panels

One of the easiest ways of having an antenna's transceiver system powered by a solar cell is to place the system's antenna right on top of the solar cell or panel. This approach has been taken by [4] and [5]. The concept in [4] is a reversal of that in [2-3] that is, the solar cell is now used as the ground plane for the antenna. The semiconductor properties of the silicon of the solar cell degraded the gain of the antenna slightly but it was still in acceptable levels. The antenna performance was stable and not affected by variations in light intensity which is typical of countries in northern latitudes. The exploded layout of the antenna is shown in Figure 7.5.

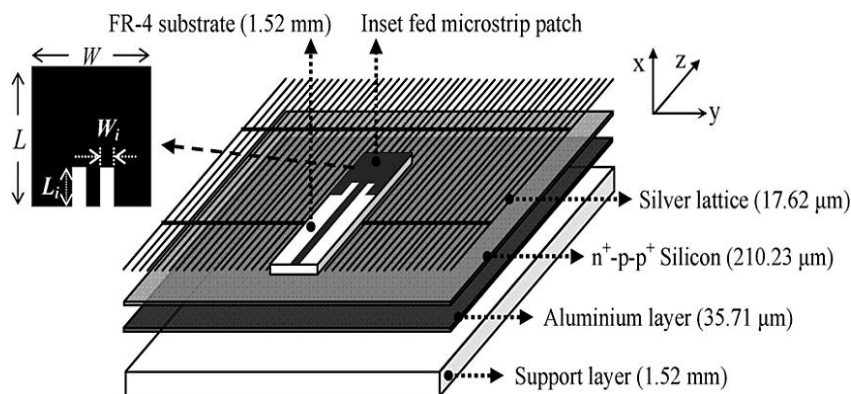


Figure 7.5 Layout of the solar antenna geometry [4].

The antenna in [5] is of a similar concept except that a mesh antenna is used instead of a microstrip patch to be incorporated onto the solar cells to achieve a solar antenna. The authors proposed to integrate meshed patch antennas directly onto the solar cells of a small satellite to save as much surface area of the solar cells which would not be possible if antennas like the microstrip patch was used. In this regard, the antenna was claimed to have an optical transparency of 93% in lieu of its meshed geometry which aided the proper functionality of the solar cells. An isometric view of the mesh solar antenna for satellite is shown in Figure 7.6.

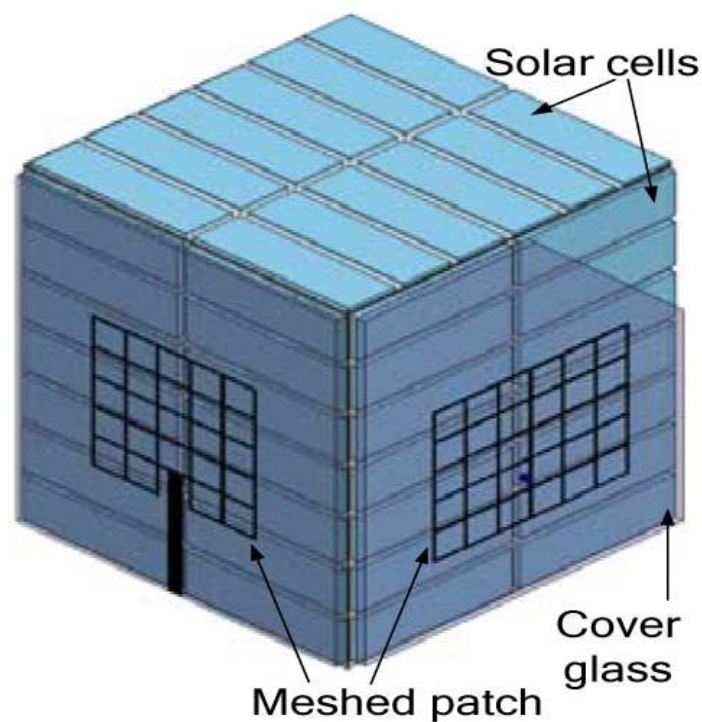


Figure 7.6 Isometric view of a small satellite with mesh antennas integrated onto solar panels [5].

7.2.4 Rectennas

A rectenna is a rectifying antenna or a special type of antenna that is used to directly convert microwave energy into DC electricity. This idea was initially mooted by Tesla a century ago. Brown then researched, demonstrated and patented it [7-8]. It was Brown who first proposed the term rectenna as it consisted of a rectifying antenna combined with a

rectifying circuit to convert radio or microwave power to DC power. Since then, there have been numerous applications such as providing DC power from space by receiving a microwave beam via a geostationary solar powered satellite and converting it into DC [9], RFID tags [10] and health monitoring [11], wireless power transmission in distributed wireless sensor networks [12] and most recently in mobile phones by Nokia to provide standby power. The Nokia system scavenges TV, radio waves and waves from other mobile systems, and converts them to useful current that can charge the phone's battery [13].

Works on both narrowband and wideband rectennas have been published in recent years, the latter type being limited only by the bandwidth capability of the rectifier circuit. Here, three types of rectennas are presented namely, a narrowband, broadband and a rectenna with an integrated rectifier circuit to demonstrate how, over the years, research into developing more capable rectennas have progressed, and how these features are exploited in developing a transparent green rectenna in this chapter.

7.2.4.1 Narrowband Rectenna

An aperture coupled microstrip antenna using E-pHEMT technology is described in [14] to harvest RF and microwave energy. The E-pHEMT was used to improve the efficiency of the rectenna. An air gap was used as a substrate in this work because of its low permittivity. The low permittivity of air was taken advantage of to help improve gain. An efficiency of 85.4 % was obtained at 11.5 dBm (14.12 mW) at a frequency of 900 MHz. The authors emphasized that because of the high efficiency for a low input power, the power to be transmitted may be reduced or the operating range may be increased. The power saving aspect of the antenna on its own itself makes the antenna a green antenna without even having to consider the role of the antenna as a power harvester. Figure 7.7 shows the rectenna with a blow-up of the E-pHEMT in use on the left.

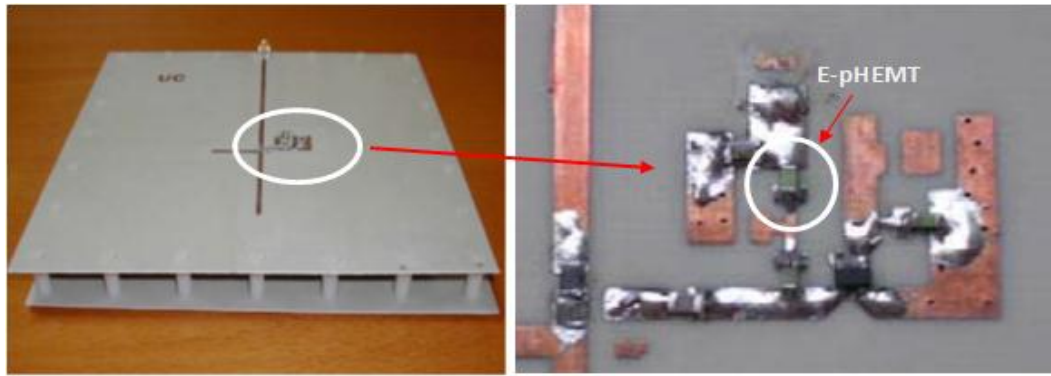


Figure 7.7 The 900 MHz E-pHEMT rectenna [14].

7.2.4.2 Ultra Wideband Rectenna

Bouchouicha et al [15], presented a broadband rectenna in 2010 using a frequency independent antenna operating between 1 to 3 GHz and incorporated to a rectifier that did not have a matching circuit. The frequency independent spiral antenna was designed as an Omni-directional broadband antenna to enable recovery of all available signals within the operating frequencies to maximize the DC power harvested. To avoid losses in the matching circuit the antenna was connected directly to the rectifier. The antenna was fabricated on a FR4 substrate of 0.8 mm thickness, relative permittivity of 4.4 and $\tan \delta$ of 0.02. The optimum load resistance value to increase the DC power was determined to be about 100Ω for the operating range of 1 to 3 GHz. In order to obtain maximal power transfer, the antenna impedance had to be matched to the optimal diode impedance across all frequencies. This was made possible through the use of the frequency independent spiral antenna which allowed a constant 100Ω impedance to be presented to the diode across all frequencies in the operating range. The prototype of the rectenna is depicted in Figure 7.8. The physical size of the prototype could have been reduced by incorporating the rectifier circuit on the reverse side of the antenna rather than in front. This would make it more planar and less obtrusive. Although much effort was made, it was reported that the rectenna was not very efficient due to mismatch still occurring between the antenna and the rectifier resulting in a very low DC power even though a voltage doubler RF/DC converter configuration design was used.

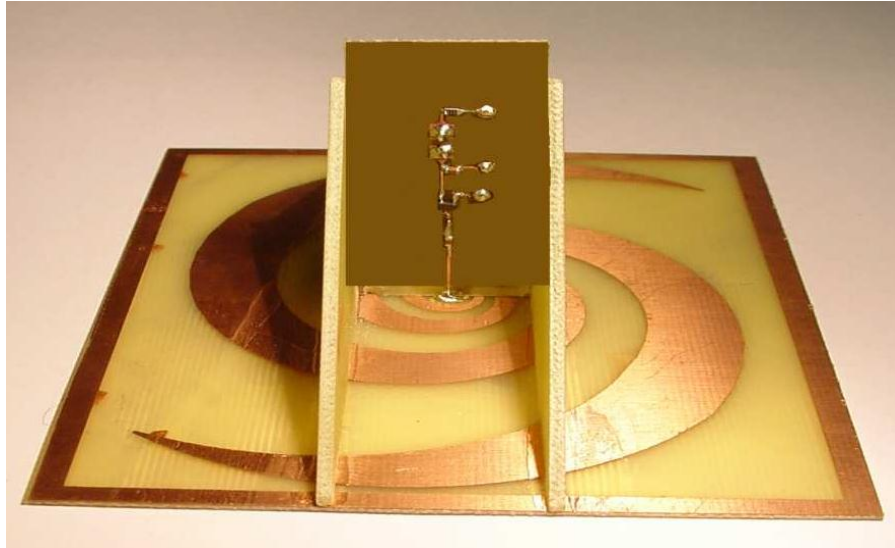


Figure 7.8 Frequency independent spiral rectenna prototype [15].

7.2.4.3 Integrated Rectenna

The integrated rectenna in [16] consists of a printed monopole antenna and a band-pass short stub filter as shown in Figure 7.9. The rectifying circuit with stub filter is fabricated on the ground plane which is widened to acquire broadband characteristics. The broadband stub band-pass filter is used to suppress the second harmonics generated from the diode. The rectenna was fabricated using a photolithographic process. The antenna was designed as a H-shaped monopole antenna to operate in the 2.45 GHz WLAN frequency. A peak RF to DC conversion of 66% was reported using a load resistor of 270Ω at 2.45 GHz. A conversion efficiency of 50% was able to be maintained from 2 to 3 GHz. The whole rectenna had a physical size of $34 \times 46 \text{ mm}^2$ making it by far the largest rectenna amongst the three reported in this section. The integrated concept does away a separate rectifying circuit thus making it ideal for window glass applications. However, with TCOs like AgHT films having no ground planes, such a concept would only be suitable for standalone rectennas and not window glass applications.

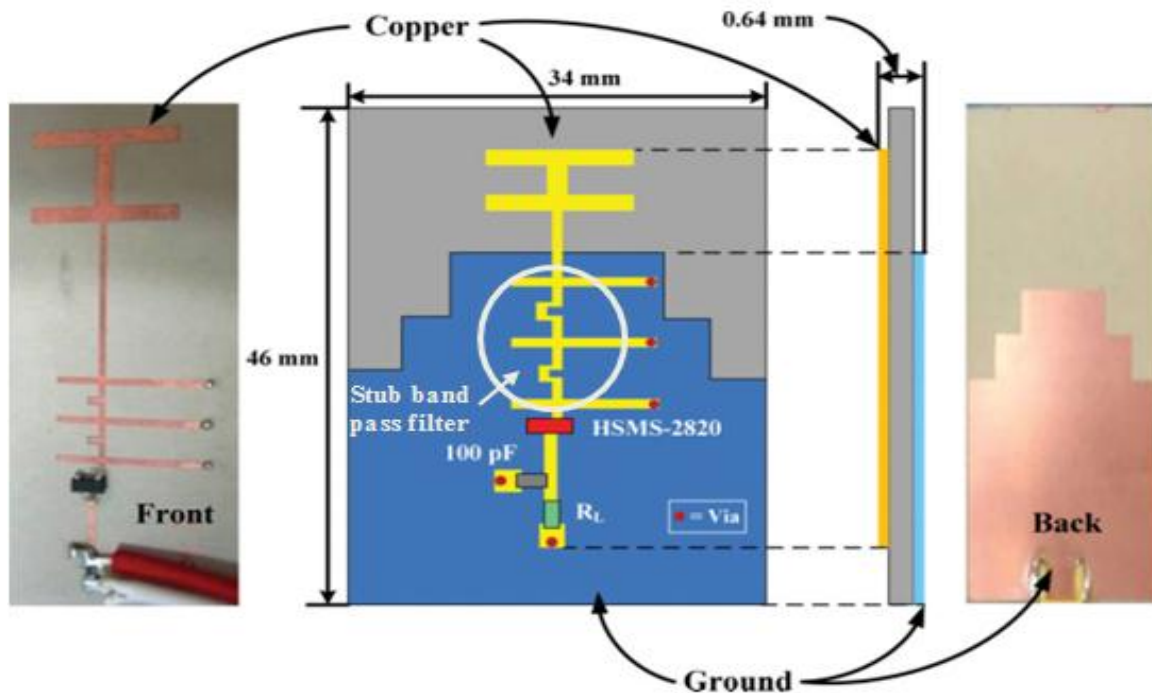


Figure 7.9 Geometry of the integrated rectenna with a broadband stub band-pass filter [16].

7.2.5 Power Saving Antennas

A semi-planar antenna was demonstrated to provide improved gain through introduction of higher dielectric constant materials into the embossed portions of a circular patch UWB antenna in [17]. The improved gain is not consistent over all frequency bands but over certain frequency bands. These improved gains can be exploited to reduce the transceiver's power for applications operating over the frequencies where the gains are seen. In this regard, the antennas can be seen to reduce the demand on power from mains source thus indirectly contributing to reduction in carbon footprint making them virtually green antennas. Figure 7.10 shows the simulated gain increments for different dielectrics introduced in a 73 mm diameter embossed circular patch (also known as semi-planar (SP) antenna) compared to a planar (P) version of it. A higher dielectric constant of 2.08 produces a higher gain compared to a dielectric constant of 1 (example, air). The dielectric constant of 1 represents a hollow emboss in the case presented. A layout of the antenna is presented in Figure 7.11.

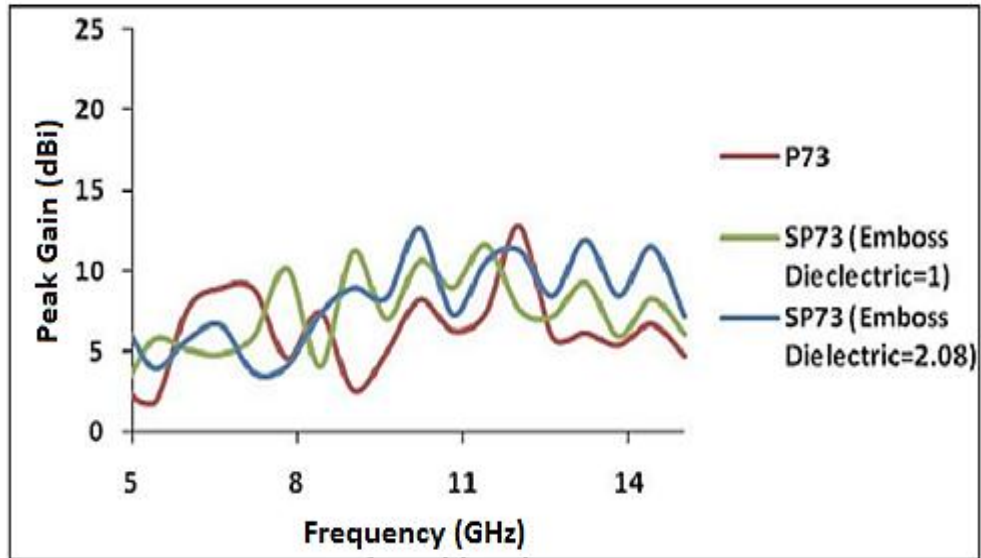


Figure 7.10 Simulated gain of SP73 antenna with different dielectrics in emboss versus P73 [17].

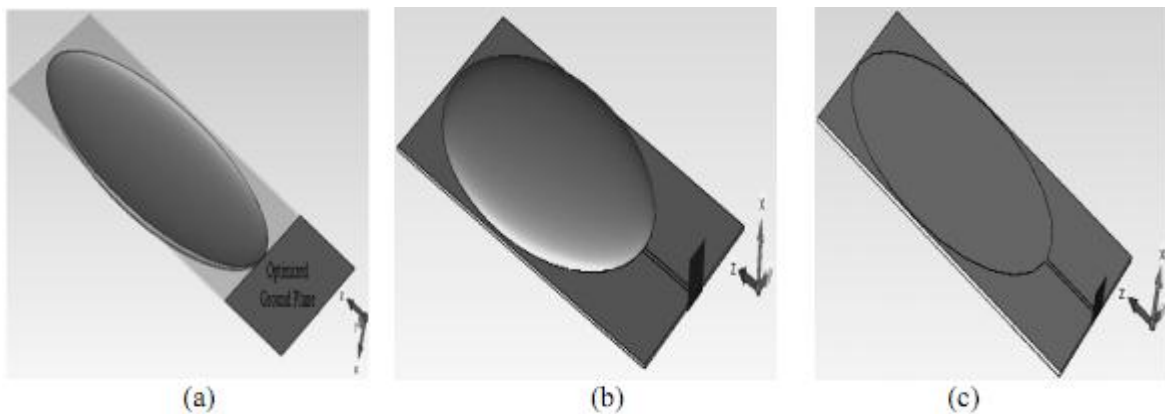


Figure 7.11 (a) Ground plane-SP73 (b) embossed antenna-SP73 (c) planar antenna-P73 [17].

7.3 Transparent Green UWB Antennas

When a transparent antenna is integrated onto a glass structure especially, as a superstrate laminate on a glass substrate that forms part of a solar cell (Figure 7.12) [18], the antenna’s performance would be greatly affected. In fact, the antenna becomes directional as the metallic rear contact of the solar cell acts as a reflector. Hence the UWB characteristic of

the antenna is affected as the antenna becomes directional with the bandwidth being greatly affected. As the transparent UWB antennas were meant to be used on glass to take advantage of their Omni-directional characteristic to receive and transmit on both sides of the glass that is, outside as well as inside the building, it became necessary to develop a UWB antenna that was capable of maintaining its Omni-directional characteristic. It was in this regard, the CTSA was developed. The next section describes in more detail the developed antenna and its performance in free space and when integrated on an amorphous silicon solar panel for solar energy harvesting.

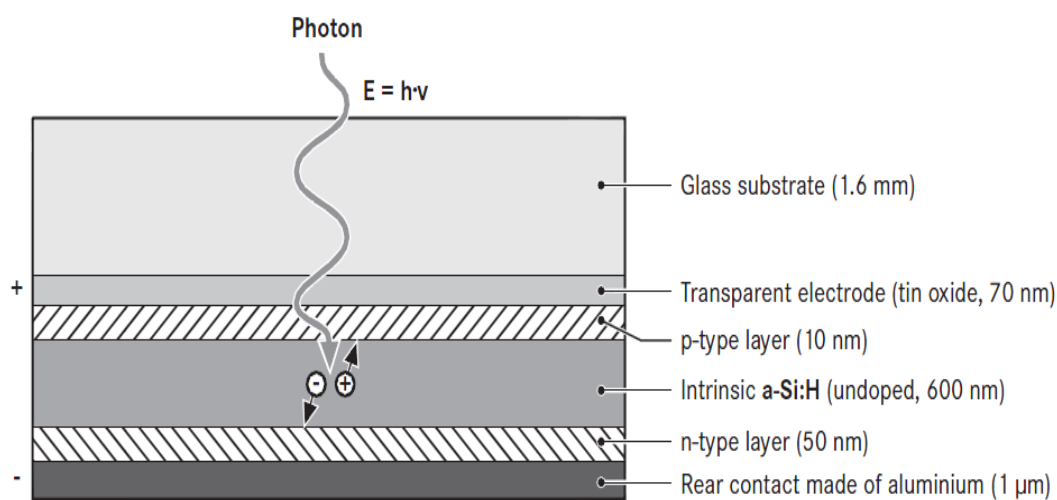


Figure 7.12 Layered structure of the amorphous silicon solar cell [18].

7.3.1 Transparent CTSA for Integration onto Solar Panels

The developed antenna's prototype, geometry and dimension are as shown in Figure 7.13. It is a CPW fed CTSA inscribed on a thin TCO film, AgHT-4. The overall size of the antenna is $17 \times 33.5 \text{ mm}^2$. The feed gap is 0.1mm, and the feed line is designed to slowly taper and merge into the radiator.

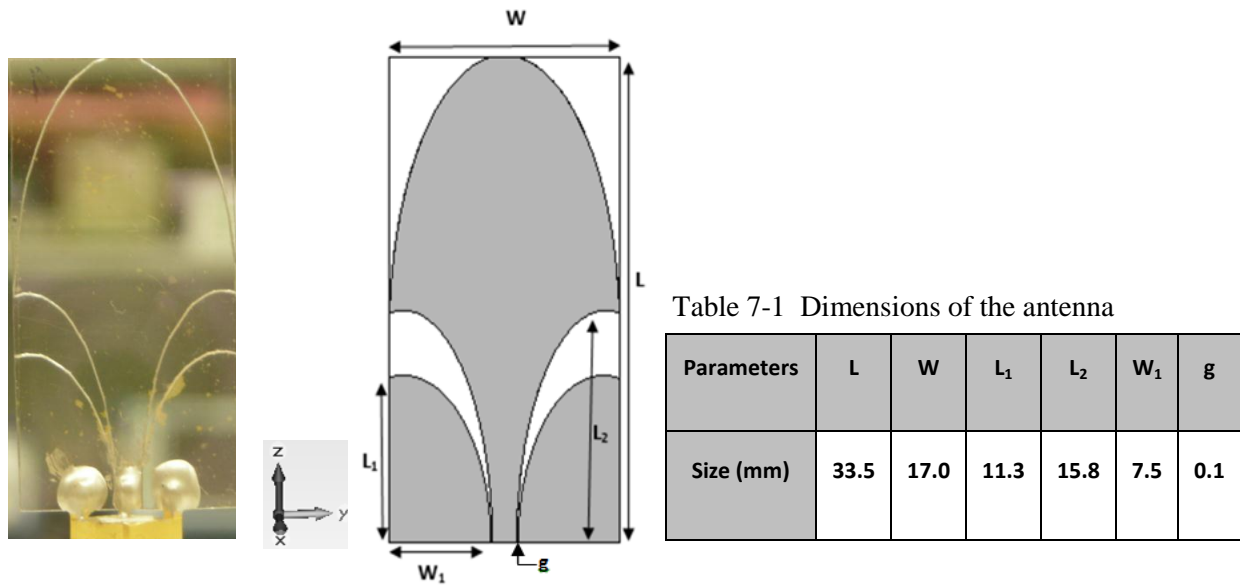


Figure 7.13 Prototype, geometry and dimensions of the CTSA in free space.

7.3.1.1 Simulated and Measured Results for the CTSA in Free Space

The simulated and measured results of the CTSA in free space are given in Figures 7.14 to 7.16.

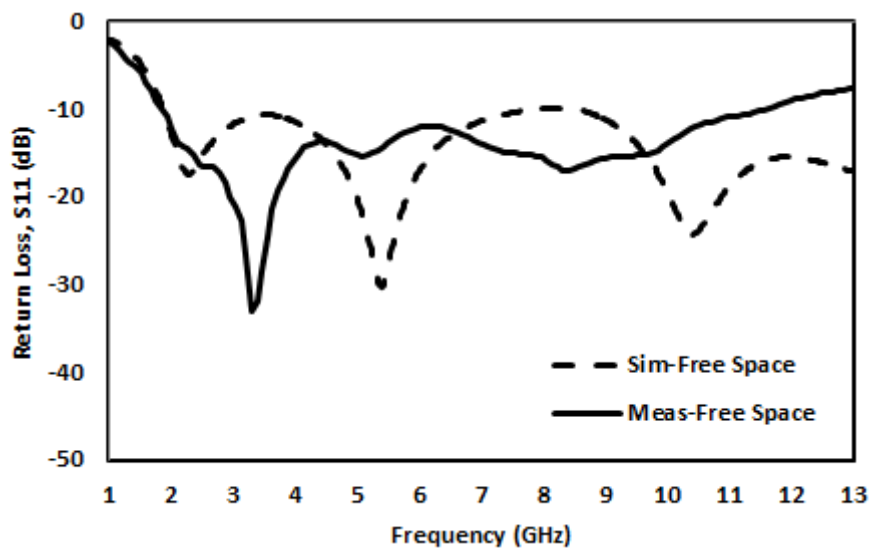


Figure 7.14 Simulated and measured return loss of the CTSA in free space .

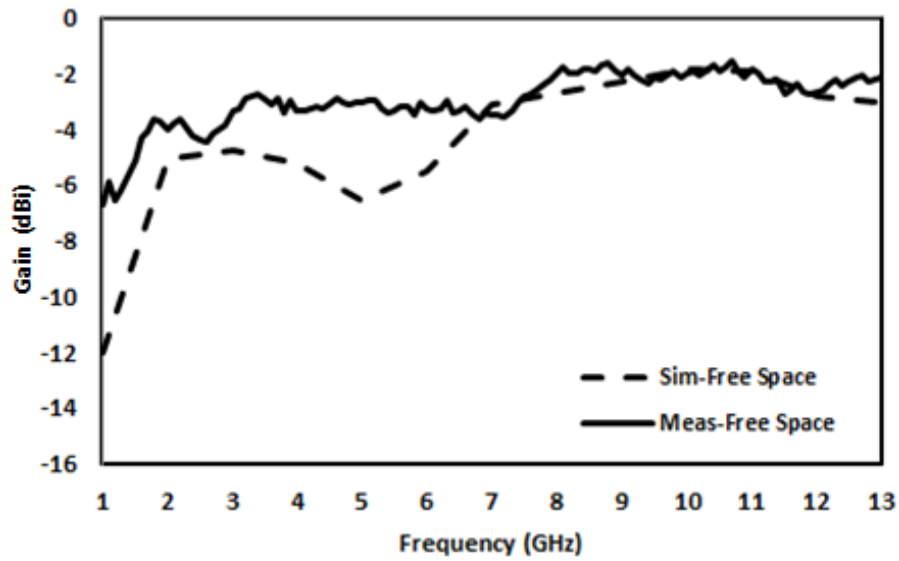
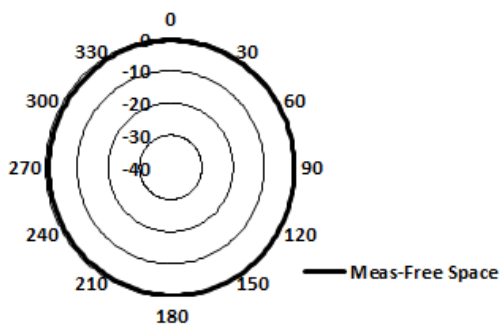
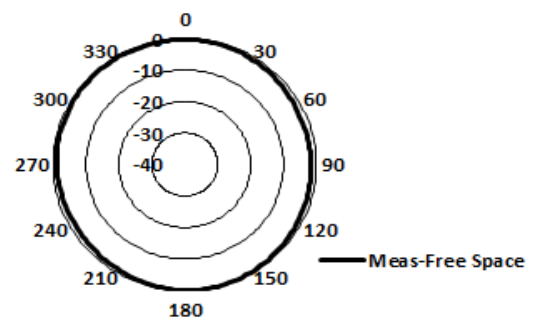


Figure 7.15 Simulated and measured gain of the CTSA in free space.

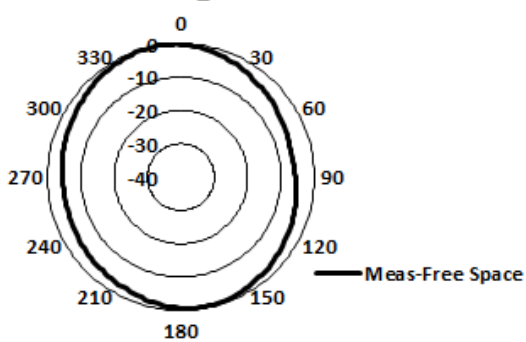
X-Y Plane @ 3 GHz



X-Y Plane @ 5 GHz



X-Y Plane @ 7 GHz



X-Y Plane @ 10 GHz

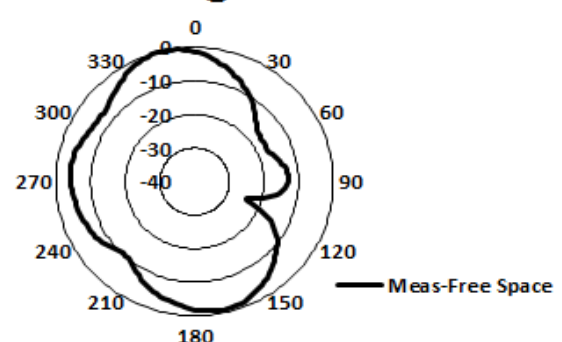


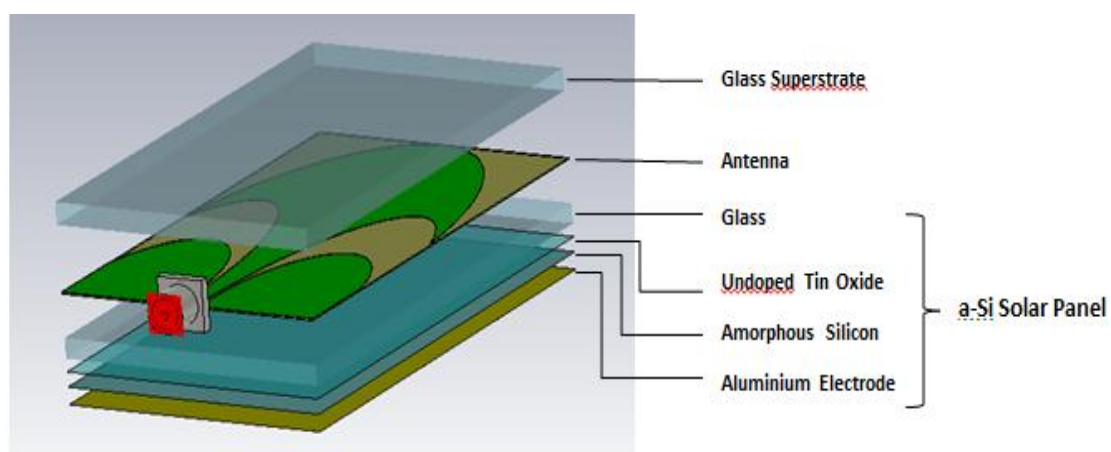
Figure 7.16 Measured radiation pattern of the CTSA in free space.

The CTSA had a free space average gain of -3 dB for the FCC bandwidth from 3.1 to 10.6 GHz. The antenna was optimized in dimensions for integration between an a-Si solar panel as substrate and a 2mm glass superstrate. This was done in a two-stage process. It was first optimized for lamination onto the a-Si solar panel. Once this was done, the antenna was then optimized with a glass superstrate mounted on top of the antenna. The solar panel's glass was 1.8 mm thick with a dielectric of 5.7. The glass superstrate was 2 mm thick and had an experimentally determined dielectric of 5.7 also. The a-Si solar portion was modelled as in Figure 7.17 (a). The thicknesses of the individual layers were constructed to be as similar as to that of Figure 7.12. The p-type and n-type layers were not included in the modelling. Figure 17 (b) shows an exploded view of the final model of the integrated structure of the antenna sandwiched between the 2 mm glass superstrate and a-Si solar panel that was used for the CST simulation.

Glass Substrate	1.8 mm
Tin Oxide	700 nm
Amorphous Silicon	600 nm
Aluminium Electrode	0.1 um

a-Si Solar Cell Structure

(a)



(b)

Figure 7.17 (a) CST model of the a-Si solar cell (b) exploded view of the structure of the CTSA placed between a glass superstrate and an a-Si solar panel.

7.3.1.2 Simulated and Measured Results for the CTSA on Solar Panel

The simulated and measured results of the CTSA with the solar panel as a substrate are as shown in Figures 7.18 to 7.20.

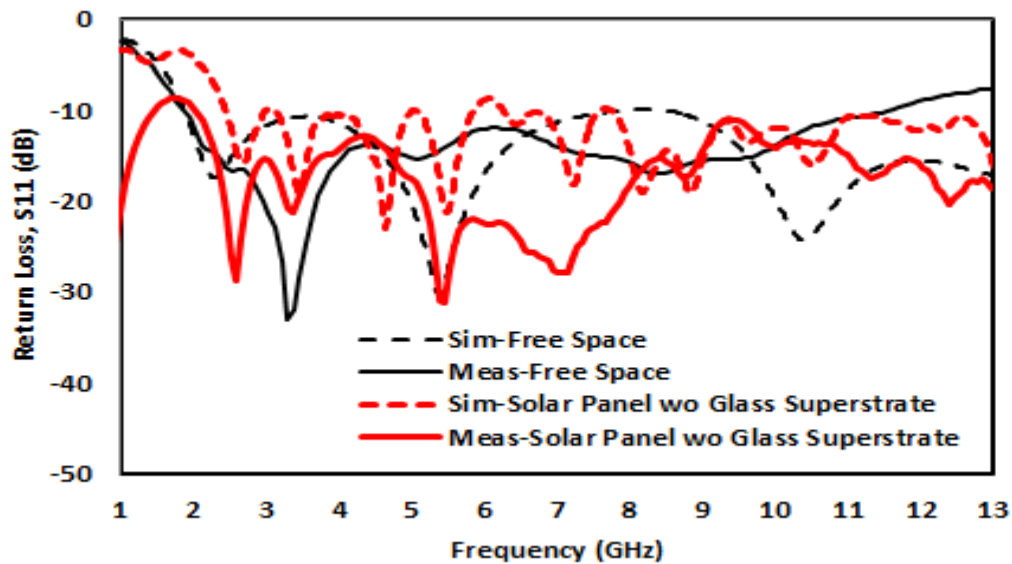


Figure 7.18 Simulated and measured return loss of the CTSA on the a-Si solar panel without a superstrate.

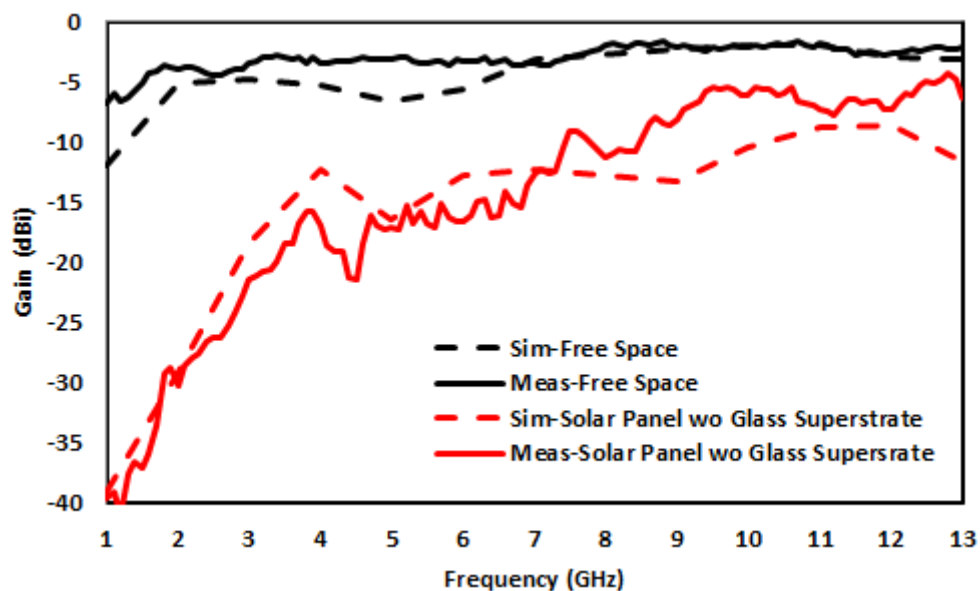


Figure 7.19 Simulated and measured gain of the CTSA on the a-Si solar panel without a superstrate. Free space results included for comparison.

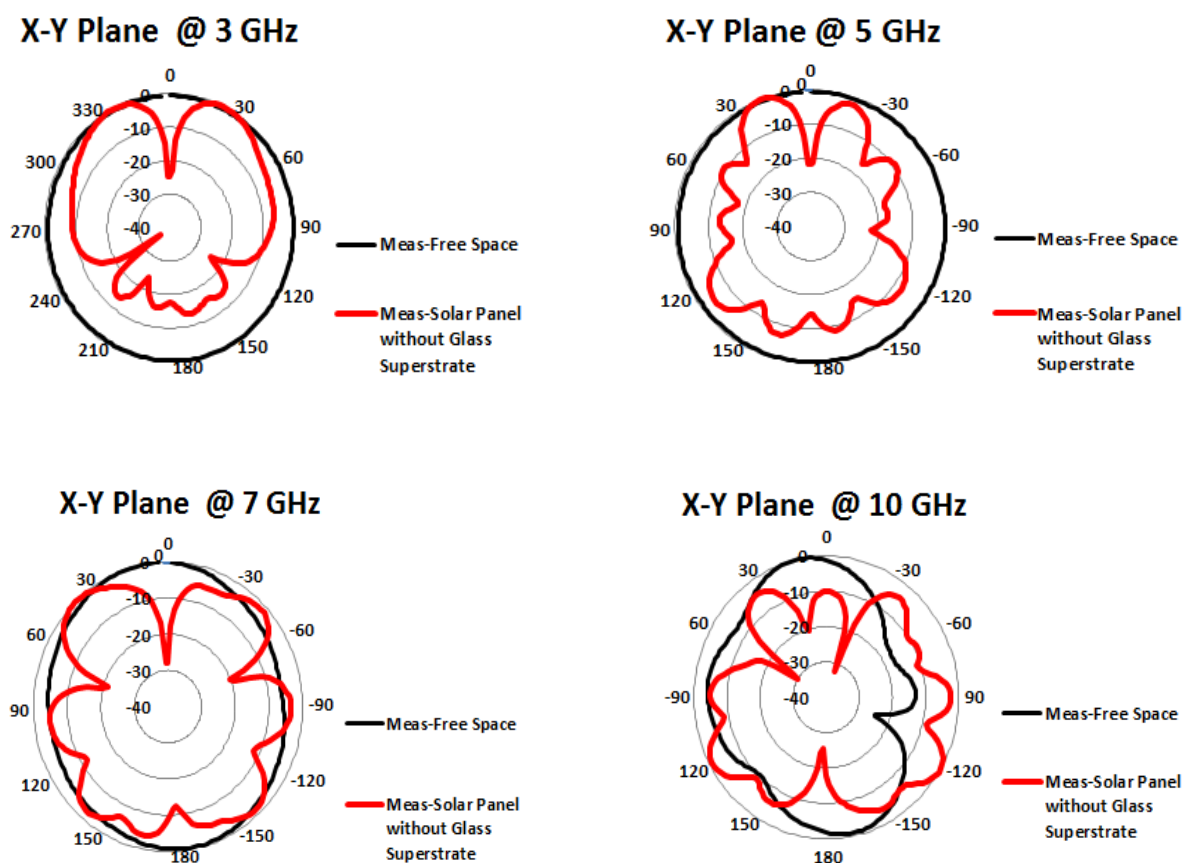


Figure 7.20 Measured radiation pattern of the CTSA on the a-Si solar panel substrate.

The measured radiation pattern in the azimuth or x-y plane for the CTSA on the a-Si solar panel substrate was directional at 3 GHz but had a quasi-omni directional pattern at the higher frequencies of 5, 7 and 10 GHz as shown in Figure 7.20.

7.3.1.3 Simulated and Measured Results for the CTSA on Solar Panel with a 2mm Glass Superstrate

Similarly, the simulated and measured results for the CTSA design on a-Si solar panel with a 2mm glass superstrate are shown in Figures 7.22 to 7.25. The 3-D simulated radiation patterns are also included to give a three dimensional visual illustration of the expected outcome in measurement. The simulated radiation pattern in the azimuth plane is Omni-directional at 3 and 5 GHz but becomes quasi Omni-directional at 7 and 10 GHz. Figure 7.21 shows the CTSA on the a-Si solar panel with the glass superstrate under measurement in the Star Lab.

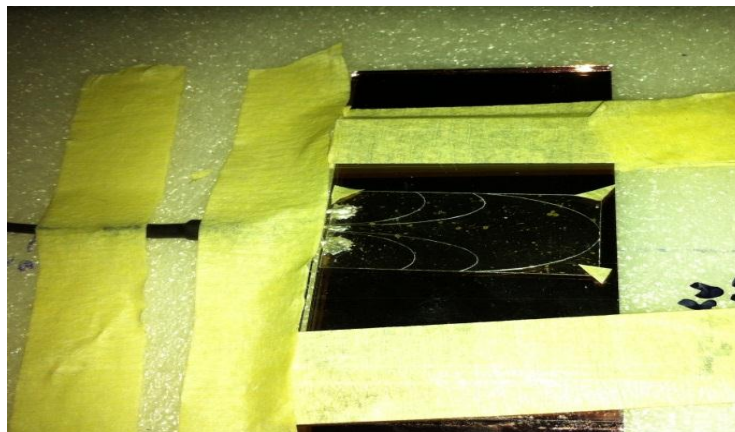


Figure 7.21 The CTSA with a 2 mm glass superstrate on an a-Si solar panel undergoing measurement on the Star Lab.

The connection for the measurement was done with a cable feed through a contact method rather than soldering with a conductive epoxy as the epoxy was not available at the measurement lab in HKU. This possibly led to improper contact and resulted in a not very smooth gain curve and inaccurate results. In this regard it has to be mentioned that the measured return loss as given in Figure 7.22 may also not be accurate since it was difficult to calibrate the cable with an open wire feed. The open wire feed cable could also have additionally contributed to the gain and radiation pattern measurement inaccuracy through impedance mismatch.

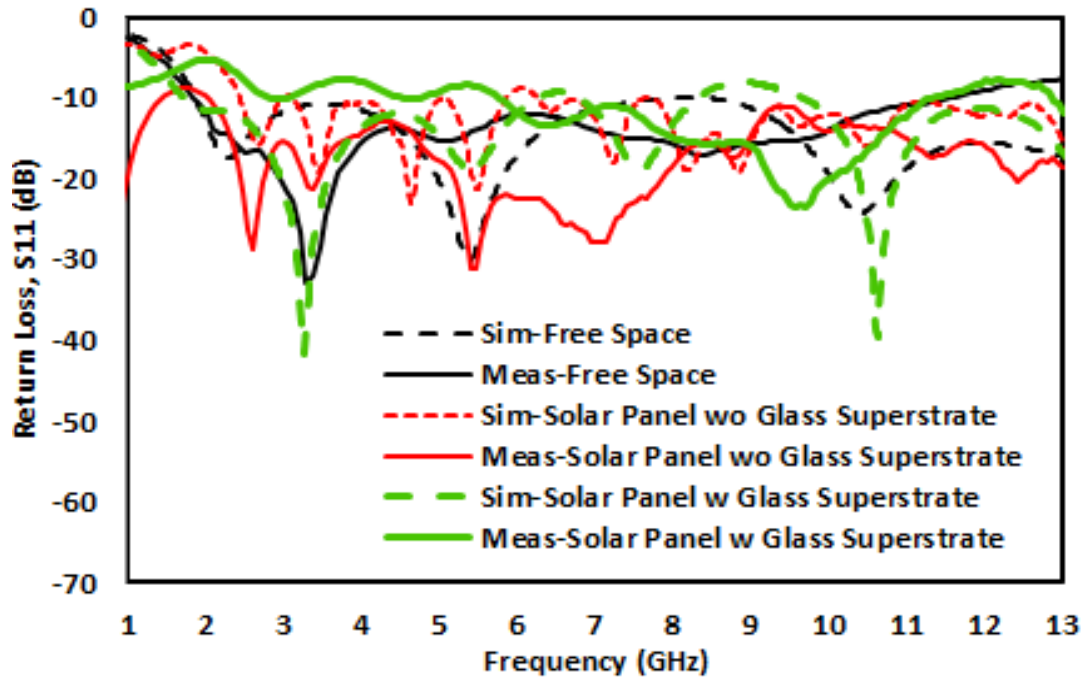


Figure 7.22 Simulated and measured return loss of the CTSA on the a-Si solar panel with a 2 mm glass superstrate. Free space and without glass superstrate results given for comparison.

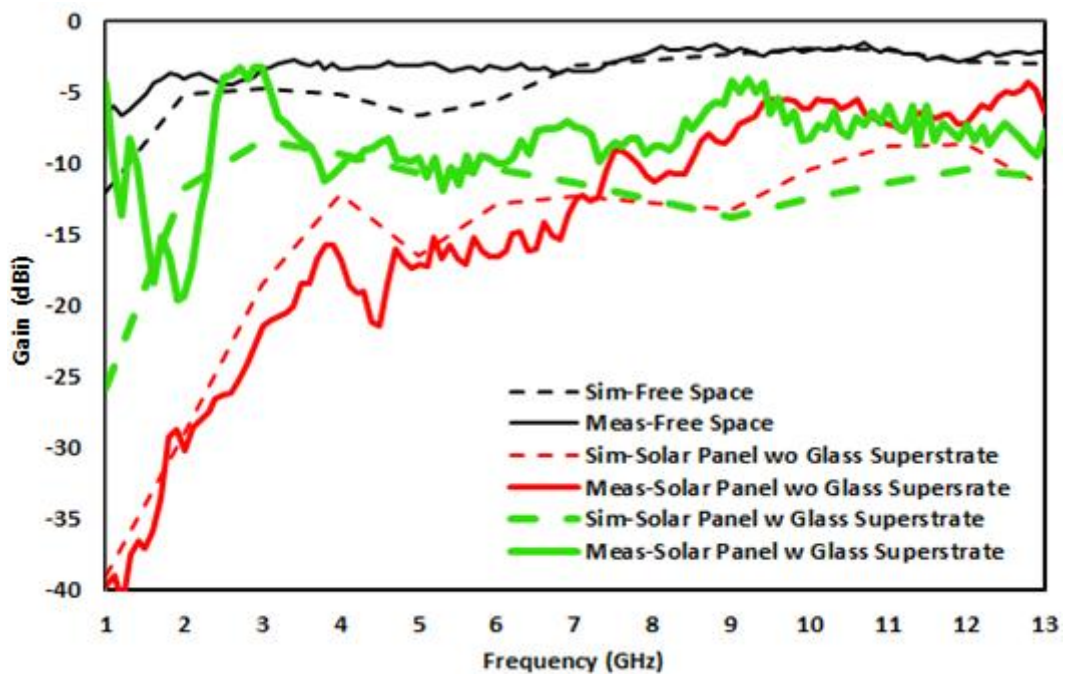


Figure 7.23 Simulated and measured gain of the CTSA on the a-Si solar panel with a 2mm glass superstrate. Free space and without glass superstrate results given for comparison.

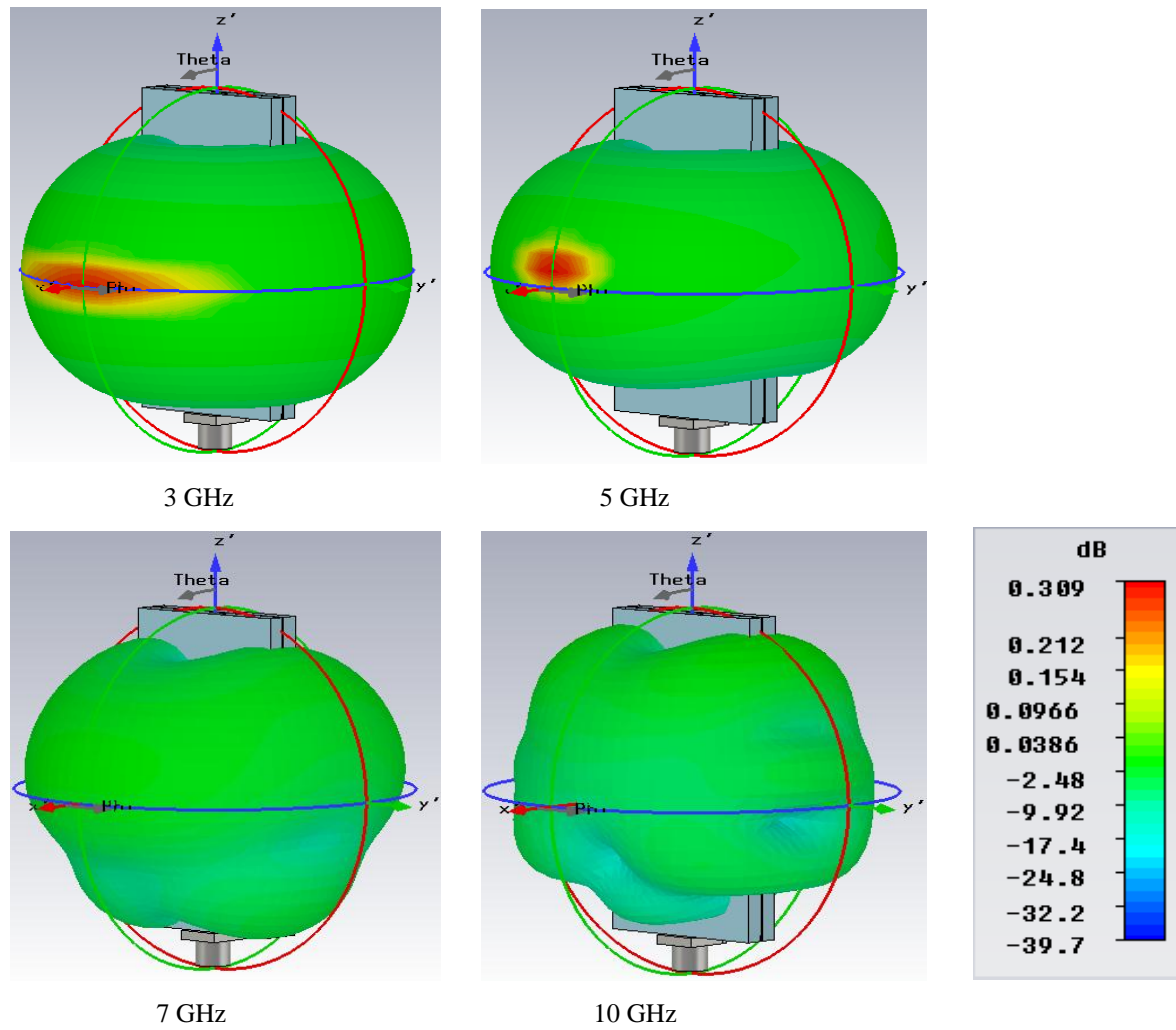
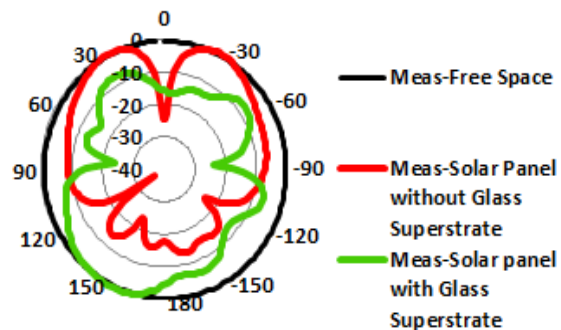
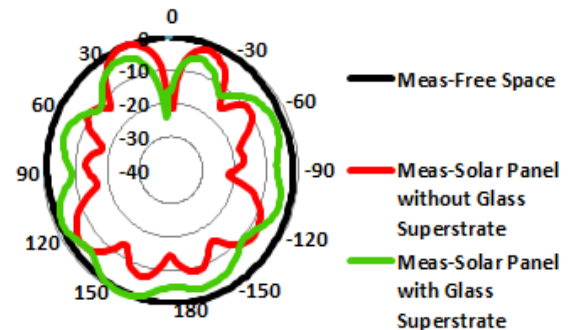


Figure 7.24 Simulated 3-D radiation patterns for the CTSA on a-Si solar panel with a 2 mm glass superstrate.

X-Y Plane @ 3 GHz



X-Y Plane @ 5 GHz



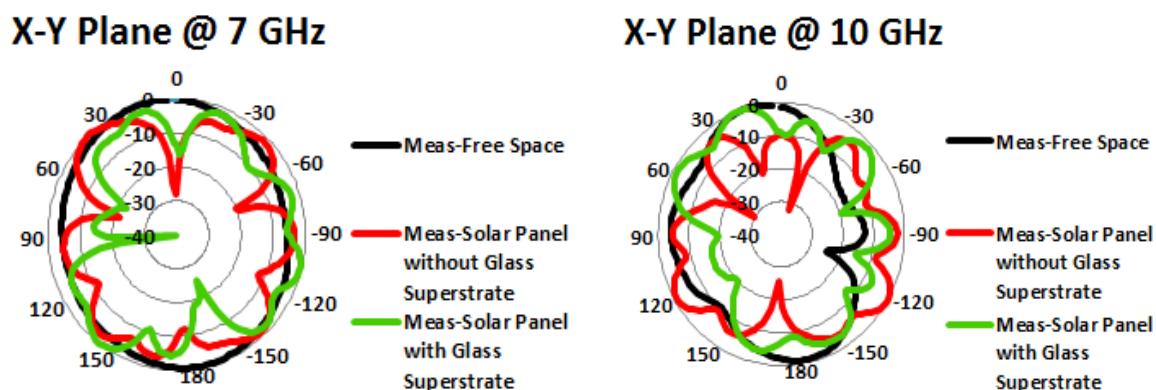


Figure 7.25 Measured radiation patterns for the CTSA on a-Si solar panel with a 2 mm glass superstrate. Free space and without glass superstrate results given for comparison.

For the CTSA sandwiched between the glass superstrate and a-Si solar panel, the measured radiation patterns were quasi-omni directional for all the four different frequencies of 3, 5, 7 and 10 GHz (Figure 7.25). Besides, the optimization, the thinness of the a-Si layer aided in allowing the CTSA to radiate in a quasi-omni directional pattern. The finding is also encouraging as this shows that if the photovoltaic portion of the solar cell can be made very thin it could improve the omni-directionality of the radiation pattern of the UWB antenna. The glass superstrate structure also helped improve the gain. And as mentioned earlier, this results could have been better if a better feed contact was made by soldering the cables with conductive epoxy.

7.3.2 Transparent CTSA Rectenna for RF/Microwave Harvesting

Transparent antennas can easily be incorporated with a rectifying circuit (or rectifier) to scavenge for RF and microwaves to convert them into DC power. The additional advantage is that they can be laminated on glass buildings without being obtrusive, and at the same time take advantage of the large square footage or glass area available to increase the size of the antenna and indirectly the gain to improve the performance of the transparent rectenna. In this regard, large narrow band antennas with bandwidths extending into the lower frequencies to tap television and cellular phone waves, or UWB arrays to improve the gain and performance of the antennas may be designed. Transparent UWB rectennas have an

additional advantage as they allow scavenging of these waves from both outside and inside of the building in lieu of their Omni-directional radiation pattern.

7.3.2.1 Rectenna in Free Space

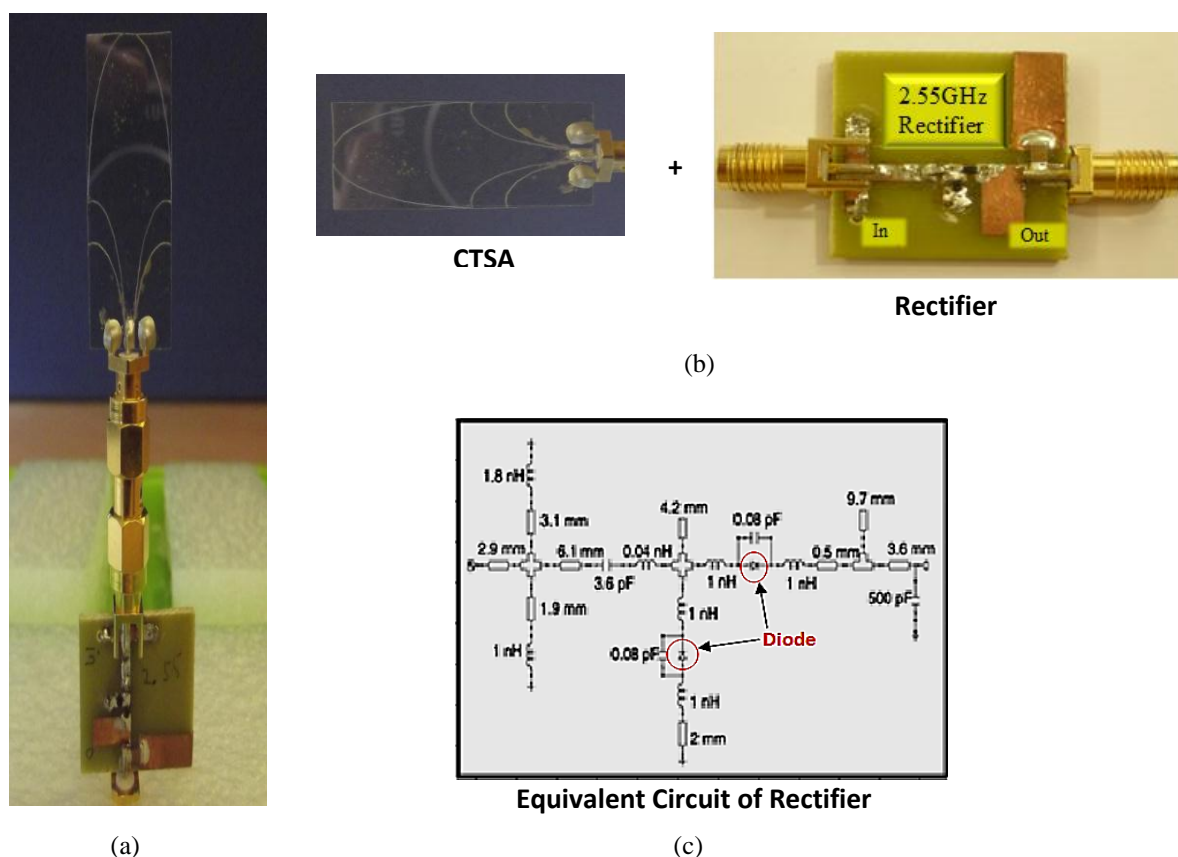


Figure 7.26 (a) The 2.55 GHz rectenna (b) rectenna components (CTSA + rectifier) (c) equivalent circuit of rectifier.

The same CTSA described earlier is presented by the author in [19] as a rectenna to harvest energy. The operational frequencies of the rectenna basically depend on the rectifier's capability whether it is narrowband or wideband. In the paper [19], an available rectifier circuit in the laboratory was used to demonstrate the ability of the CTSA as a rectenna. The rectifier (Figure 7.26) was designed to work at a frequency of 2.55 GHz. The detector circuit of the rectifier was configured as a voltage doubler that is, the output voltage would be doubled. A verification of the operating frequency was then done by connecting the rectifier or detector circuit to a Network Analyser to check the S11 response. This was to test whether the detector circuit was operating at 2.55 GHz [20]. A frequency sweep measurement of the

input return loss was done with the applied RF power to the input set at -30 dBm and the output of the detector circuit terminated in a 50 Ω load. The input return loss showed a minimum at 2.55 GHz and this is shown in Figure 7.23. This is the frequency where the voltage sensitivity is maximum and should be the frequency at which the circuit's transfer characteristic is optimized. This was verified by doing a signal power sweep from 2.5 to 2.6 GHz using a signal generator connected to the input of the rectifier and the voltage across the 50 Ω load resistor recorded. The results of the measurement are tabulated in Table 7-2. The optimum output of 25.6 mV was noticed at 2.55 GHz. However, it should be pointed out that this zero bias diode rectifier at the load of 50 Ω has a 10dB operating bandwidth from 2.49-2.58 GHz. Hence when the rectifier circuit is integrated with an antenna it is able to tap RF and microwave signals in this operating range and convert the electromagnetic energy received to DC.

Table 7-2 Output voltage of rectifier versus frequency for -30 dBm input power.

Frequency (GHz)	2.50	2.51	2.52	2.53	2.54	2.55	2.56	2.57	2.58	2.59	2.60
Voltage (mV)	14.8	16.5	17.8	19.6	23.6	25.6	22.4	20.9	18.2	14.4	10.5

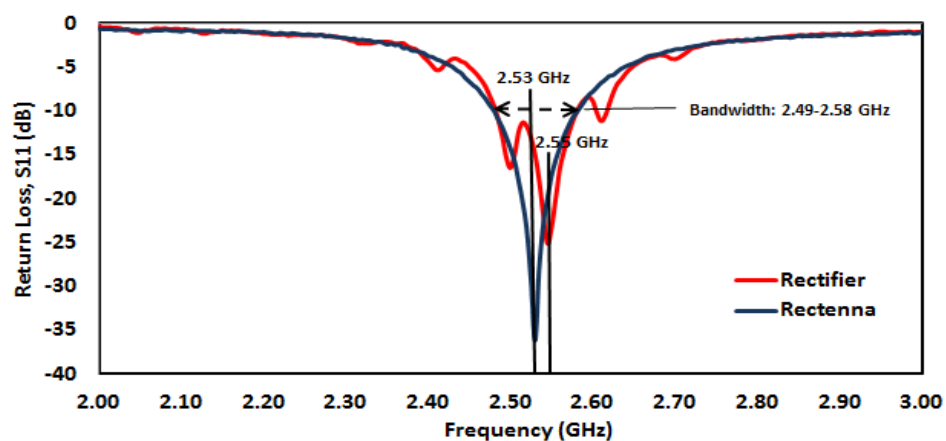


Figure. 7.27 Peak return loss response of the rectifier circuit.

The CTSA was then connected to the rectifier, and the return loss of the rectenna measured. It peaked at 2.53 GHz and this is also depicted in Figure 7.27. This is the operating frequency of the rectenna system for a 50 Ω load. A transmit horn antenna which

has an average gain of 9.8 dB for the range 2.5 to 2.6 GHz was next connected to a signal generator. The CTSA rectenna was then set-up at the receiver end 5cm away to receive the signal. To determine the frequency at which the rectenna system would be operating at an optimum, a frequency sweep ranging from 2.5 to 2.6 GHz was also done, with the voltage across a 50 Ω load noted. The optimum output was found to be at 2.53 GHz as shown in Table 7-3. This confirmed the system’s optimum operating frequency at a 50 Ω load to be 2.53 GHz. The optimum operating frequency however, changes if the load is increased. For a 100 Ω load, the optimum operating frequency shifted to 2.51 GHz. This is also depicted in Table 7-3. The reason for this is the matching; the antenna’s impedance is matched to the optimal diode impedance at different frequencies for different loads [15]. Hence maximal power transfer occurs at the frequency at which the matching occurs for a particular load.

Table 7-3 Output voltage of rectenna system versus frequency for -30 dBm input power

50Ω	Frequency (GHz)	2.50	2.51	2.52	2.53	2.54	2.55	2.56	2.57	2.58	2.59	2.60
	Voltage (mV)	7.1	8.4	8.8	9.4	9.2	9.2	9.1	8.6	7.5	7.4	7.2
100Ω	Frequency (GHz)	2.50	2.51	2.52	2.53	2.54	2.55	2.56	2.57	2.58	2.59	2.60
	Voltage (mV)	17.8	18	17	16.7	15.3	16	16.4	17	16	15.4	14.2

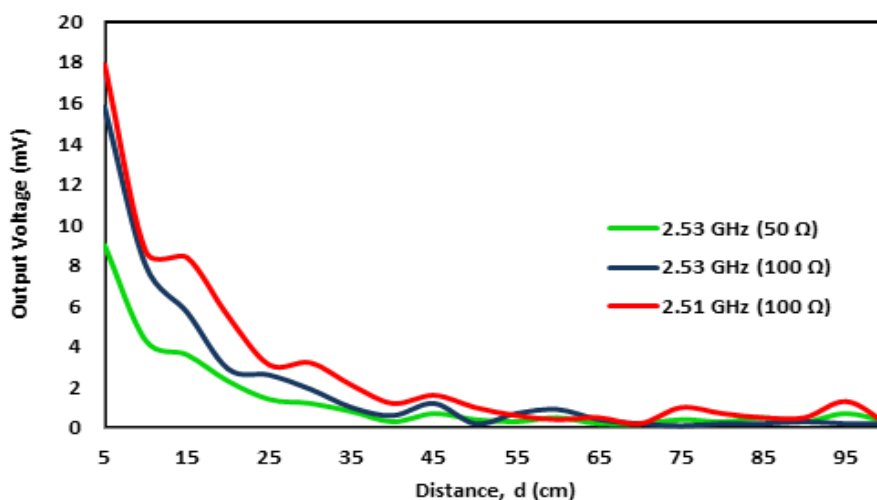


Figure 7.28 Comparison of output voltage versus distance, d with different loads at 2.53 GHz and 2.51 GHz operating frequency for input power of 10 dBm for the rectenna in free space.

In Figure 7.28, the output voltages at 2.53 GHz for a 50 Ω load baseline and at 2.53 GHz and 2.51GHz for a 100 Ω load, along a span of 100 cm are compared to show the impact of the load on the optimum operating frequency.

7.3.2.1.1 Rectenna Measurement Set-up

The measurement set-up for the rectenna performance is as shown in Figure 7.29 with a diagrammatic representation of it depicted on its right.. P_T is the transmitted power, G_T is the transmitting horn antenna gain, d the path distance, AUT the antenna under test, and P_{AC} and P_{DC} the ac and dc power output respectively.

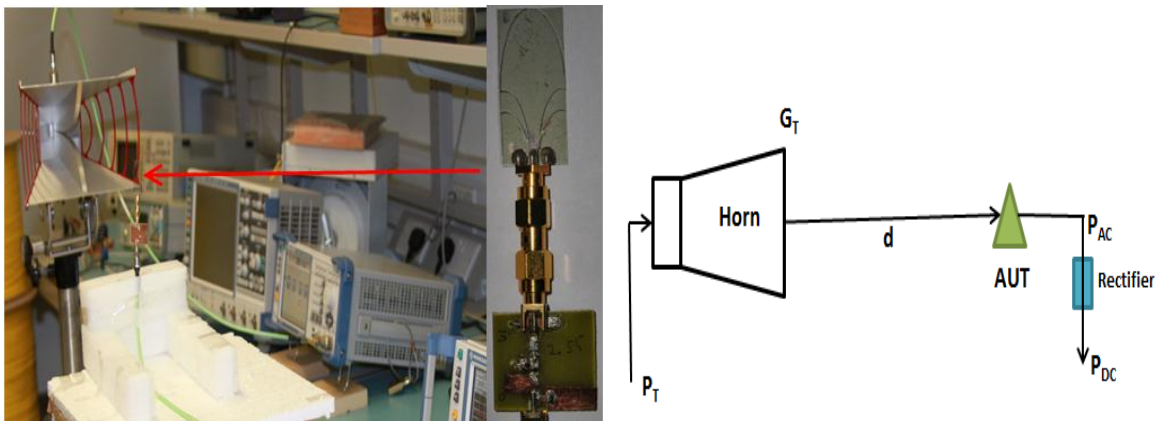


Figure 7.29 Measurement set-up for the CSTA rectenna (left) with diagrammatic representation (right).

7.3.2.1.2 Rectenna Efficiency

The rectenna's efficiency is given by,

$$\text{Rectenna efficiency, } \eta_{\text{rectenna}} = \eta_{\text{rectifier}} \times \eta_{\text{antenna}} \quad \dots \text{Eqn (7.1)}$$

By knowing the P_T, G_T and measuring d and P_{dc} and calculating P_{ac} from equations (7.2 to 7.4) given below, we are able to determine the rectenna efficiency.

$$P_{ac} = \frac{P_T \cdot G_T}{4\pi d^2} \times A_{eff} \quad \dots \text{Eqn (7.2)}$$

$$= \frac{P_T \cdot G_T}{4\pi d^2} \times \frac{G_R \times \lambda^2}{4\pi} \quad \dots \text{Eqn (7.3)}$$

Knowing P_{ac} from equation (7.3) we can compute the dc power output, P_{dc} from,

$$P_{dc} = P_{ac} \times \eta_{rectifier} \quad \dots \text{Eqn (7.4)}$$

Hence,

$$\text{rectifier efficiency, } \eta_{rectifier} = P_{dc}/P_{ac}.$$

Knowing the rectifier's efficiency, we are able to determine the rectenna's efficiency from equation (7.1) given earlier.

The CTSA rectenna system's efficiency was determined by taking the output power of the rectenna system for varying power inputs from -30 dBm to -0 dBm at frequencies of 2.51 GHz and 2.53 GHz at different loads of 50 Ω and 100 Ω . The measured efficiencies of the antenna at these two frequencies were 18%. The output power of the rectenna for different input power levels is shown in Figure 7.30 and its efficiency in Figure 7.31.

The system's efficiency improves with load as shown in Figure 7.31 but at the different operating frequencies as earlier shown in Figure 7.28. From Figure 7.28, the system's voltage output is also noticed to attenuate over distance and this is mainly due to path loss. It has to be mentioned at this stage that this measurement was done in a Lab environment and as such the environment somewhat contributed to fluctuations in the received power and correspondingly the voltage outputs; that is why at certain distances the output voltage seemed to be slightly higher or lower than the previous. However, the general trend is a gradual reduction in signal strength and hence the received RF power that is converted by the rectenna over distance. Also, there seems to be less differentiation in the voltage output for the two different power inputs for "d" above 35 cm. This was because the measurements were done using a 0.1 mV resolution multi-meter which was the only available multi-meter in the lab.

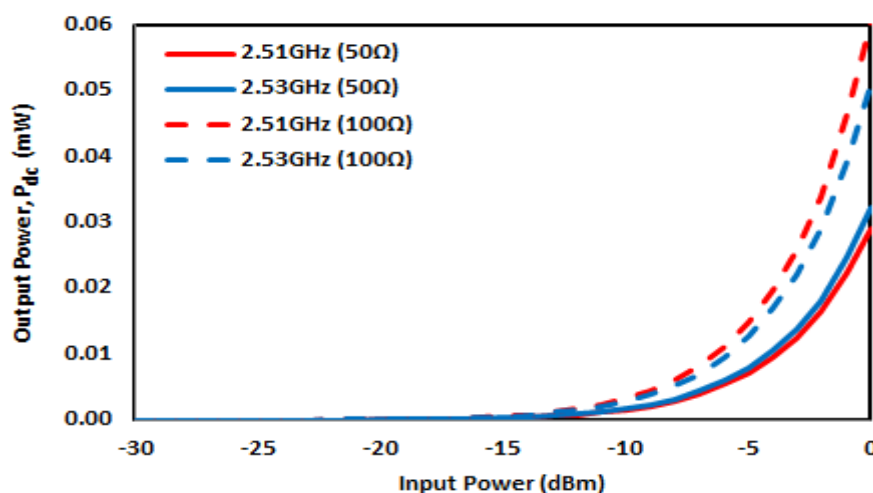


Figure 7.30 Output power of CTSA rectenna versus input power on a 50 Ω and 100 Ω load at 2.51 GHz and 2.53 GHz.

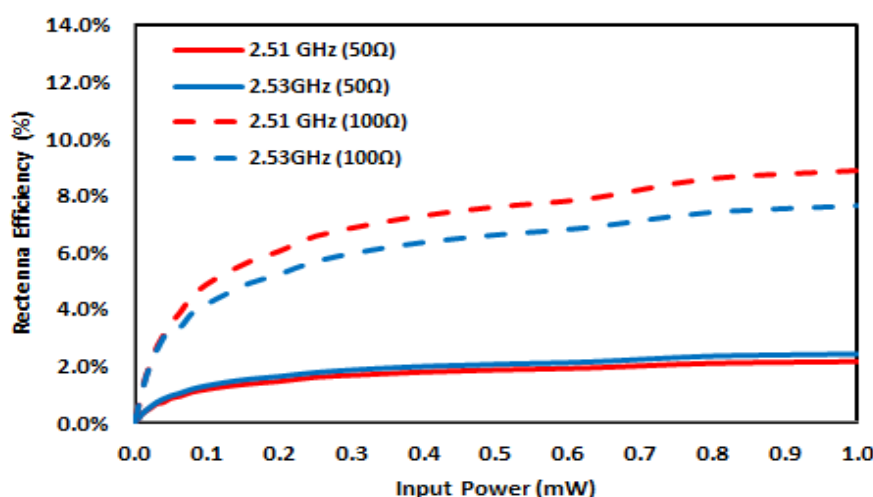


Figure 7.31 Rectenna system efficiency at 2.51 and 2.53 GHz at 50 Ω and 100 Ω load.

The efficiency of the transparent rectenna demonstrated in Figure 7.31 is notably low but is however comparable to thin film solar panels currently available in industry for example, like those manufactured by Solyndra [21]. However, this could be improved via arrays and also larger antennas or redesigning the geometry to have better gain at the frequency of operation. The example presented here is for a rectenna in free space. The same design on glass will take on a slightly larger or smaller size depending on the dielectric and thickness of the glass. A higher dielectric could further improve the gain however, a higher

thickness could possibly degrade the efficiency of the system. Nevertheless, the dimensions of the antenna design should be optimized to achieve the maximum gain possible.

7.3.2.2 Rectenna on Glass

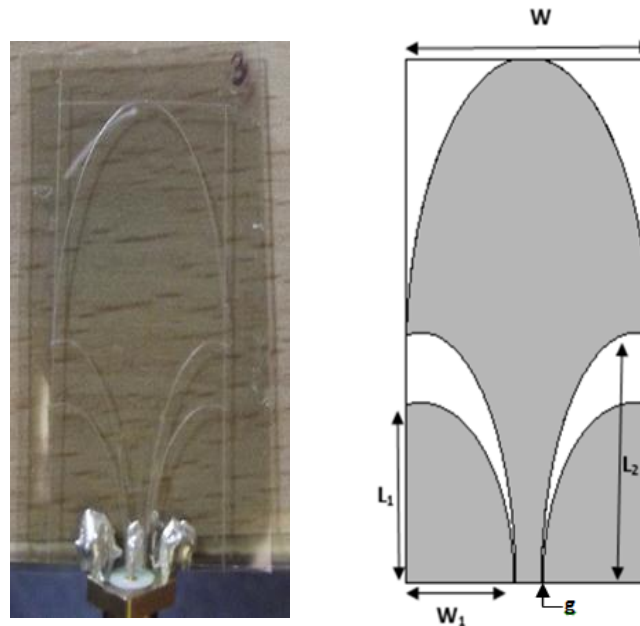


Table 7-4 Dimensions of the antenna geometry on a 2 mm glass with $\epsilon_r = 5.7$

Parameters	L	W	L ₁	L ₂	W ₁	g
Size (mm)	35.1	17.5	10.6	15.8	7.82	0.23

Figure 7.32 Prototype of CTSA on a 2mm glass substrate with geometry and dimensions.

The CTSA optimized for use on a 2mm thick glass with dielectric of 5.7 is shown in Figure 7.32 with the optimized dimensions given in Table 7-4. Overall, the planar area of the antenna on-glass was only 0.8 % bigger than that of free space. The simulated and measured return loss, and measured gain are shown in Figure 7.33 and Figure 7.34 respectively.

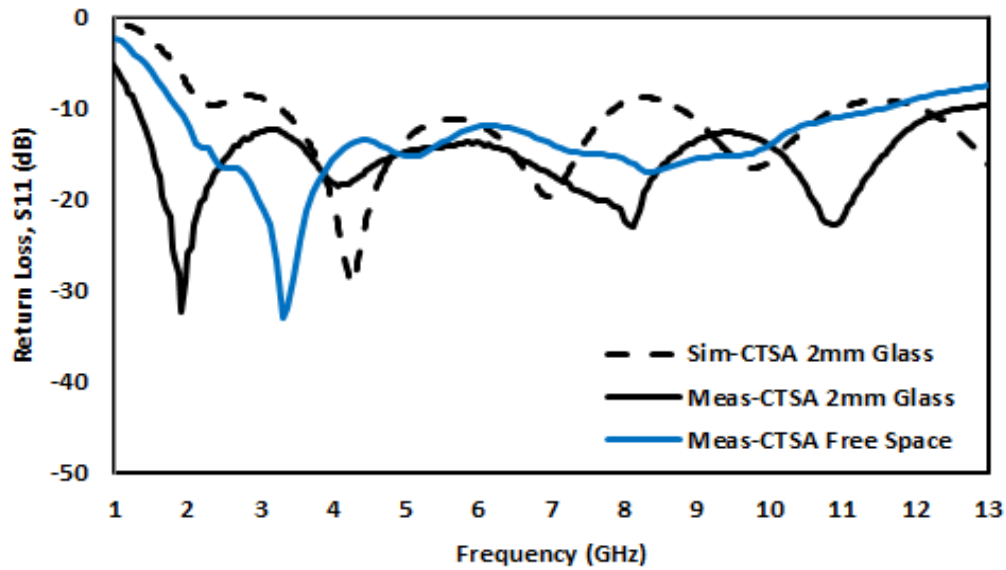


Figure 7.33 Simulated and measured return loss of the CTSA on a 2 mm glass substrate with the measured free space return loss given for comparison.

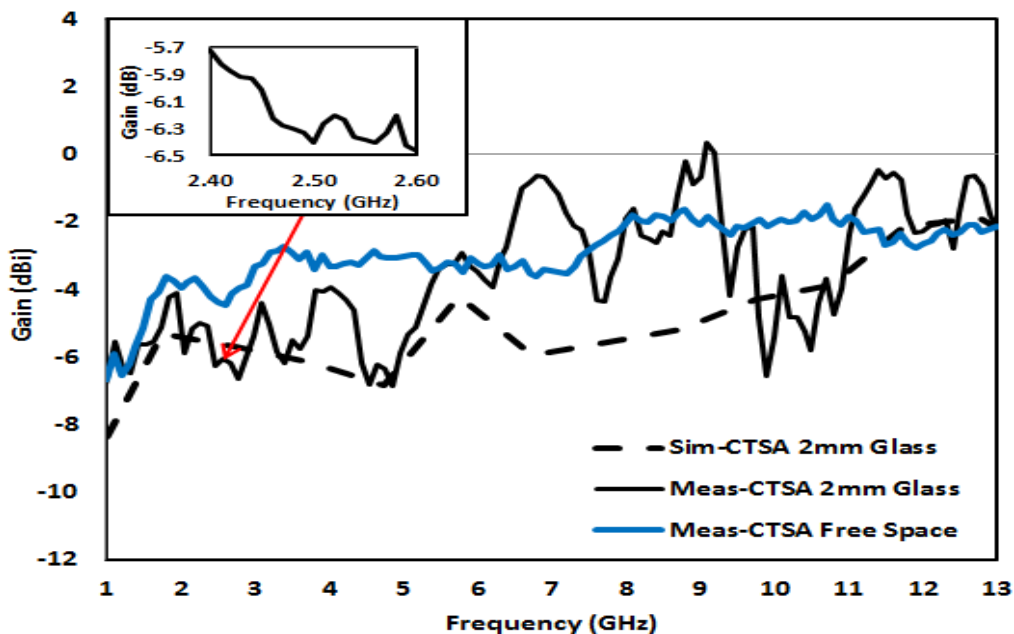
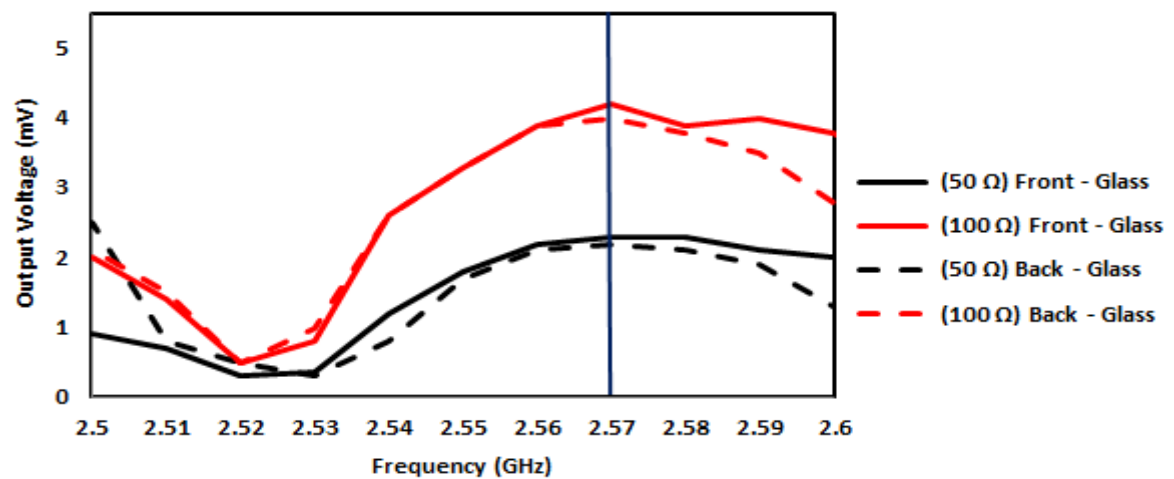


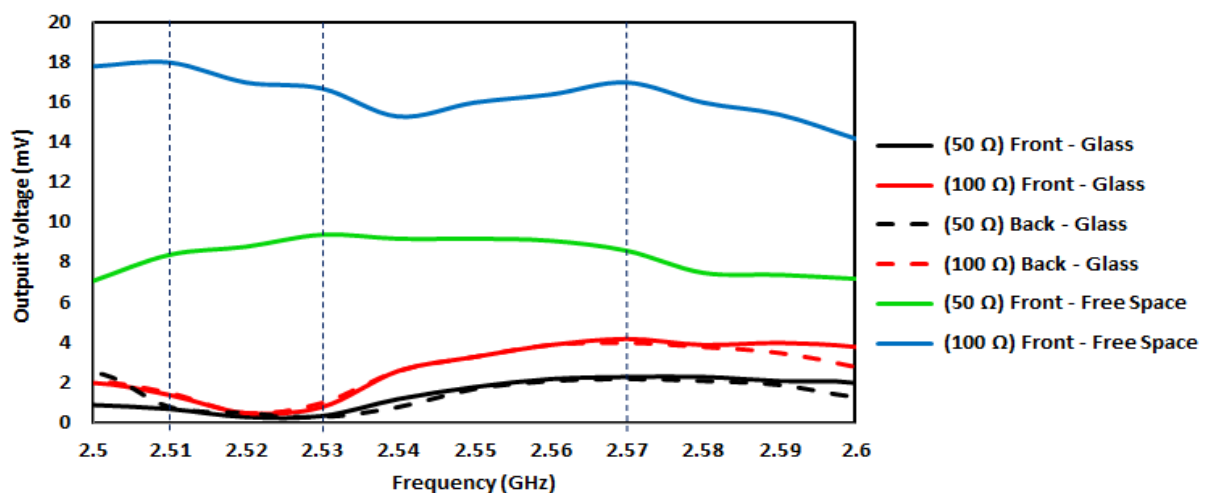
Figure 7.34 Measured gain of the CTSA antenna on a 2 mm glass with inset showing a close-up view from 2.4 GHz to 2.6 GHz. The measured free space gain is given for comparison.

The optimum operating frequency for the CTSA with the glass substrate was found to be at 2.57 GHz for a frequency sweep done at a signal input power of 10 dBm. This is depicted in Figure 7.35. The gain at 2.57 GHz from Figure 7.34 was found to be -6.34 dB which was a drop of 1.84 dB from its free space gain of -4.5 dB [19]. This drop could be

addressed by optimizing the design to have a higher gain at 2.57 GHz in a similar manner to that done to improve the gain at 7 GHz to extend the video transmission range. In this manner, the voltage output could be improved at 2.57 GHz. From, Figure 7.35 also, it can be noticed that the optimum operating frequency did not vary with load unlike that in free space. It was however found to be the same for both the 50 Ω and 100 Ω loads at 2.57 GHz. Besides this, the lens effect of the glass substrate too did not have any significant effect on the amount of energy harvested and converted to DC. Except for a few occasional spikes, the measured output voltage for both orientations that is in the directions in front of the antenna and at the back of the glass was almost similar.

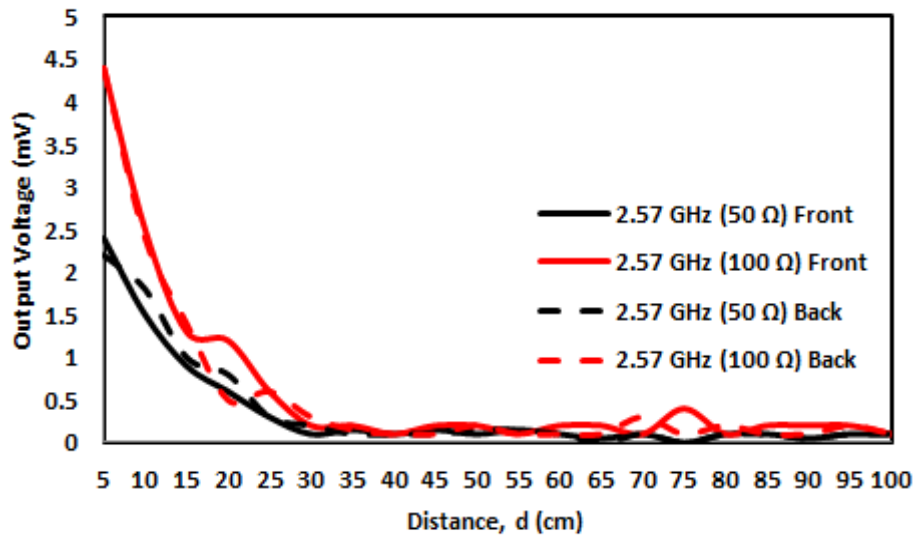


(a)

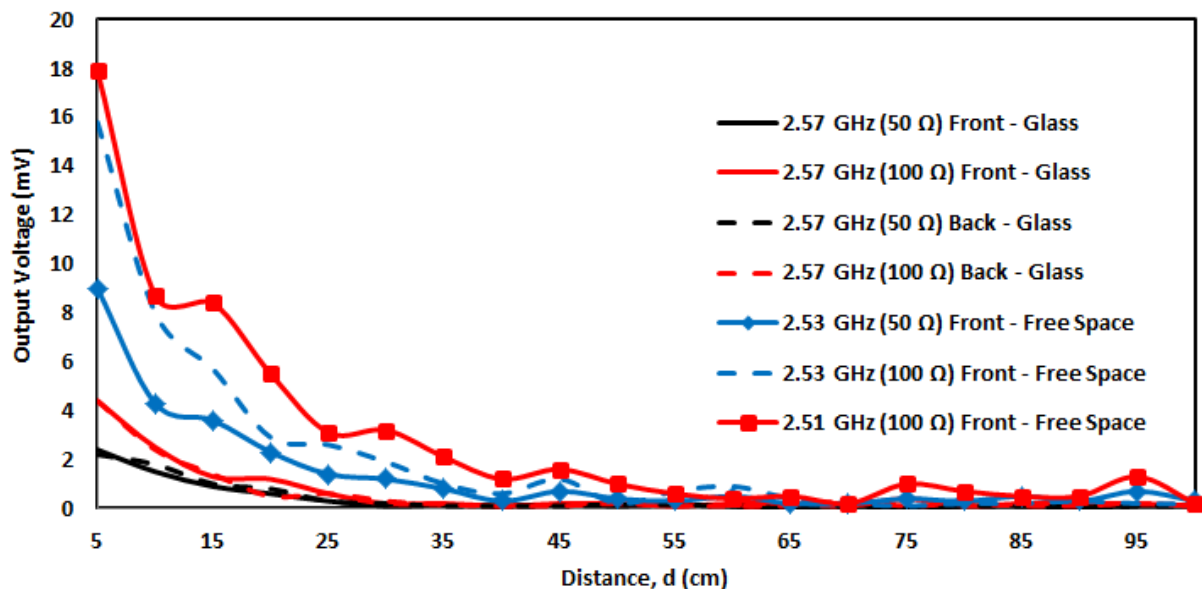


(b)

Figure 7.35 (a) Output voltage optimum at 2.57 GHz for both 50 Ω and 100 Ω load at 10 dBm on the 2 mm glass substrate (b) the output voltage for the rectenna in free space shown in comparison.



(a)



(b)

Figure 7.36 (a) Output voltages versus distance for a 10 dBm signal input on a 2mm glass substrate (b) the free space output voltage versus distance shown in comparison.

Similar trend was also noticed in the output voltage taken over distance, d as depicted in Figure 7.36. The output voltages in both directions were almost the same. As such, the only way to improve the efficiency of the rectenna on glass was to improve the operating frequency gain of the antenna. Free space path loss is also shown here again to be a critical factor that affects the voltage output and consequently, the amount of energy harvested from

the RF signal input. As such, the energy that can be harvested depends very much on the signal strength of the incident RF or microwave signal hitting the glass panels or windows on which such transparent antennas are mounted.

Voltage output can be improved using wideband rectifiers to collect signals arriving at different frequencies and consolidating the rectified voltages. Also, as explained earlier, the antenna design could be optimized through geometry or otherwise, to have higher gain at the desired operating frequencies. In this thesis, the study was done using a commercially existing material with a maximum conductivity of 250,000 S/m and a 75 % optical transparency. Although performance of the rectenna can be improved with higher conductive films but this comes at the expense of their optical transparency. Higher conductivity materials exhibit less transparency and hence reduce the amount of light falling on a solar cell that may be incorporated behind the antenna. For rectenna applications, this may not be much of an issue as it is more related to RF power rather than transparency. However, such highly conductive rectennas may find use in limited glass applications where a tinted glass to reduce glare or minimize visibility from outside the building is a priority.

7.4 Summary

Various types of green antennas whether proper, or indirectly associated have been described in this chapter. Further, it has also been shown how a novel transparent UWB green antenna was developed to harvest both solar as well as RF energy by integrating a solar cell as a laminate on the back of its polymer substrate and connecting it to a rectifier to operate as a transducer to produce DC electricity whether in free space or on glass. The antenna could be used separately for either solar or RF or together depending on the necessity and requirement. Either way, it could provide transmission and reception both sides of the glass. The capabilities, potentials and performance of this ‘green’ UWB antenna have been demonstrated and shown with experimental data earlier in the chapter. It has also been explained how the performance of the transparent energy harvesting can be improved especially in reference to the rectenna. In regard to the solar cell integrated transparent antenna, improvement in the performance of the antenna does not impact the performance of

the solar cell. It is the capability and efficiency of the solar cell that plays a key role in such a green antenna system.

Further development of this novel solar cell integrated transparent antenna is being undertaken as a continuation of this thesis study under a green technology project funded by the University of Technology Malaysia. The project involves the development of transparent photovoltaic films to be integrated with the transparent antenna to provide a green communication system as well as harness solar energy to promote green buildings.

7.5 References:

- 1) E.H. Lim, K.W. Leung, C.C. Su and H.Y. Wong, "Green Antenna for Solar Energy Collection," *IEEE Antennas and Wireless Propagation Letters*, vol. 9, pp. 689-692, 2010.
- 2) C. Bendel, J. Kirchhof and N. Henze, "Application of photovoltaic solar cells in planar antenna structures," *Proceedings of 3rd World Conference on Photovoltaic Energy Conversion, 2003*, vol. 1, pp.220-223, May 18, 2003.
- 3) N. Henze, A. Giere, H. Fruchting and P. Hofmann, "GPS patch antenna with photovoltaic solar cells for vehicular applications," *IEEE 58th Vehicular Technology Conference, 2003*. VTC 2003-Fall, vol.1, pp. 50- 54, Oct. 6-9, 2003.
- 4) S.V. Shynu, M.J.R. Ons, P. McEvoy, M.J. Ammann, S.J. McCormack and B. Norton, "Integration of Microstrip Patch Antenna With Polycrystalline Silicon Solar Cell," *IEEE Transactions on Antennas and Propagation*, vol.57, no.12, pp.3969-3972, Dec. 2009.
- 5) T.W. Turpin and R. Baktur, "Meshed Patch Antennas Integrated on Solar Cells," *IEEE Antennas and Wireless Propagation Letters*, vol.8, pp.693-696, 2009.
- 6) Degen TG35 Radio Antenna. [Online]. Available: <http://www.uk-radiocommunicationequipment.info/active-antenna>.
- 7) W.C. Brown, "The History of Power transmission by Radio Waves," *IEEE Transactions on Microwave Theory and Techniques*, vol.32, no.9, pp. 1230- 1242, Sep 1984.
- 8) W.C. Brown, U.S. Patent 3 434 678, Mar. 25, 1969
- 9) W.C. Brown, "Status of the Microwave Power Transmission Components for the Solar Power Satellite," *IEEE Trans. Microwave Theory Tech*, vol. MTT-29, no.12, pp 1319-1327, Dec. 1981.
- 10) B. Strassner and K. Chang, "Passive 5.8 GHz Radio Frequency Identification Tag for Monitoring Oil Drill Pipe", *IEEE Trans. Microwave Theory Tech*, vol. 51, no. 2, pp. 356-363, Feb. 2003.
- 11) V. Sakamuri and J. Frolik, "Design of a 2.4 GHz interrogator for a rectenna-based sensor system," *IEEE 12th Annual Wireless and Microwave Technology Conference (WAMICON), 2011*, pp.1-4, 18-19 April 2011.

- 12) K.M.Z. Shams and M. Ali, "Wireless power transmission to a buried sensor in concrete", *IEEE Sensor*, J 7, pp. 1573-1577, 2007.
- 13) D.G. Rowe, "Nokia developing phone that recharges itself without mains electricity", www.guardian.co.uk, Wed., June 10, 2009.
- 14) C. Gómez, J. A. García, A. M. Sanchez, and A. T. Puente, "A high efficiency rectenna element using E-pHEMT technology," in *Proceedings of Gallium Arsenide Applications Symposium 2004*, pp. 315-318, October, 2004,.
- 15) D. Bouchouicha, F. Dupont, M. Latrach, L. Ventura, "Ambient RF energy harvesting," *International Conference on Renewable Energies and Power Quality*, Spain, pp. 1-5, March, 2010.
- 16) T.U. Hong, K.M. Oh, H.W. Lee, H. Nam, T.S. Yun, D.S. Lee, H.I. Hwang and J.C. Lee, "Novel broadband rectenna using printed monopole antenna and harmonic-suppressed stub filter." *Microwave and Optical Technology Letters*, vol. 52 pp. 1194–1197, 2010.
- 17) T. Peter, R. Nilavalan, H.F. AbuTarboush, S.W. Cheung and Y.F. Weng, "Investigative Study on the Development of a Green UWB Antenna", *International Symposium on Antennas and Propagation in 2010 (ISAP 2010)*.
- 18) Manufacturing Solar Cells with Amorphous Silicon. [Online]. Available: http://www.stiftung-solarenergie.de/fileport.php?file=v2_de...7
- 19) T. Peter, S. Reza, R. Nilavalan, S.W. Cheung and A. Vilches, "A Novel Transparent UWB Antenna for Energy Harvesting," *IEEE Transaction on Antennas and Propagation*, submitted for publication.
- 20) Hewlett Packard – 2.45 GHz Detector Demonstration Board (Assembly and Operating Instruction).
- 21) Most Efficient Solar Panels. [Online]. Available: <http://sroeco.com/solar/most-efficient-solar-panels>.

CHAPTER 8

Conclusion and Future Work

8.1 Conclusions

This thesis has mainly focused on three research areas namely, the study of the characteristics of the transparent conductive polymer, AgHT and its property for use in the design of transparent antennas; development of transparent UWB antennas with good gain and efficiency for UWB wireless applications and integration of such antennas with solar panels or films for energy harvesting to operate as green antennas.

8.1.1 Characteristics and Properties of AGHT

In studying, the characteristics and property of the AgHT material, it was found the material exhibited absorbency property besides being flexible and conformable. The PET substrate of AgHT was basically impermeable to absorption of water but however demonstrated RF and microwave absorbency when metallized by virtue of the silver coating on it; inherent characteristic of the material that could aid or give an antenna designed on it stealth features. It was also explained why AgHT had an advantage over ITO in that the latter could not be manufactured on PET at such low resistivity of $4 \Omega\text{-m}$ as it becomes brittle causing disconnects in the metallic layer affecting conductivity when bent. Also, the AgHT material is commercially available as a sun shielding material for window glass applications thus keeping the cost of designing and fabricating antennas on them very low.

8.1.2 Development of Transparent AgHT UWB Antennas and Its Features

Development of the transparent UWB antenna was highlighted in great depth in Chapter 4. It was shown in this chapter how antenna developed on the AgHT material can have their gain and efficiency improved through a novel technique of introducing a silver base at the feed location. In the same chapter, mutual coupling, sensitivity to proximity and RAM properties were analysed and discussed. It was also shown how AgHT antennas could be used to reduce mutual coupling while maintaining good gain in composite arrays for MIMO applications. In Chapter 5, a potential use of UWB antennas for on-body applications was analysed and presented. The AgHT UWB antenna was shown to provide stable performance off-body as well as on-body. Justification for the development of transparent antennas is eventually highlighted in Chapter 6 where an analysis of on-glass UWB antennas is done and presented. The use of transparent antennas for wireless video streaming was demonstrated both in free space and on glass. It was explained how transmission in a specific operation frequency can be improved by increasing the radiation energy in the direction of the transmission by designing the UWB antenna to show strong resonance in the frequency band of operation. Also, it was shown when glass is used as a substrate or superstrate on the UWB antenna they exhibit a ‘lens effect’ redirecting the radiation energy from one broadside axis of the antenna to the other, and when sandwiched between glass maintain the Omni-directionality of the radiation pattern but with some attenuation. It has been demonstrated with experimental video transmission results how this lens effect can help improve LOS transmission range in UWB applications.

8.1.3 Transparent Green UWB Antennas for Energy Harvesting

Next, the integration of UWB antennas with solar panels or films or its direct use with a rectifying circuit as rectenna was presented in Chapter 7. It was demonstrated in this chapter how it was possible to develop an Omni-directional transparent AgHT UWB antenna even though integrated onto an opaque metal based silicon solar cell. Radiation pattern results to attest to this fact were presented. The knowledge gathered through the analysis of the transparent antenna on glass

structures enabled to design and develop the CTSA for integration on to an amorphous silicon solar panel and deliver an Omni-directional radiation pattern which was necessary for window glass applications to provide wireless transmission and reception on both sides of the glass on buildings. This initial prototype delivered a quasi-Omni-directional pattern. The improvement through test and development to achieve a good Omni-directional radiation and a high gain and efficiency would be left to future works. It was further demonstrated how transparent conductive antennas besides being capable of providing wireless transmission and reception is also capable of directly harnessing RF and microwaves and converting them into DC electrical energy. Hence it has shown how UWB antennas on transparent conductive materials like AgHT could be utilized to provide an integrated wireless communications and power harvesting solutions for green homes and buildings a concept that has been adapted for further research by the University Technology Malaysia in their Green Building Project. This is explained further under future works.

Finally, in summary, it can be said that the objectives spelled out on page 6 in Chapter 1 has been achieved in general through the development of transparent UWB antennas that can be used for wearable, body-centric, energy harvesting and wireless applications with the expected gains and efficiencies both in free space and on glass.

8.2 Future Work

8.2.1 Energy Saver for Green Technology Building in Wireless Communication System

Fig 8.1 depicts the concept of a 3-in-1 Green Technology Building system consisting of a sun screen, a wireless communication system and a solar energy harvester. Such a system has been the basis of a research project that has been embarked on by the University Technology Malaysia in collaboration with Hong Kong University and the author as a representative of Brunel University.

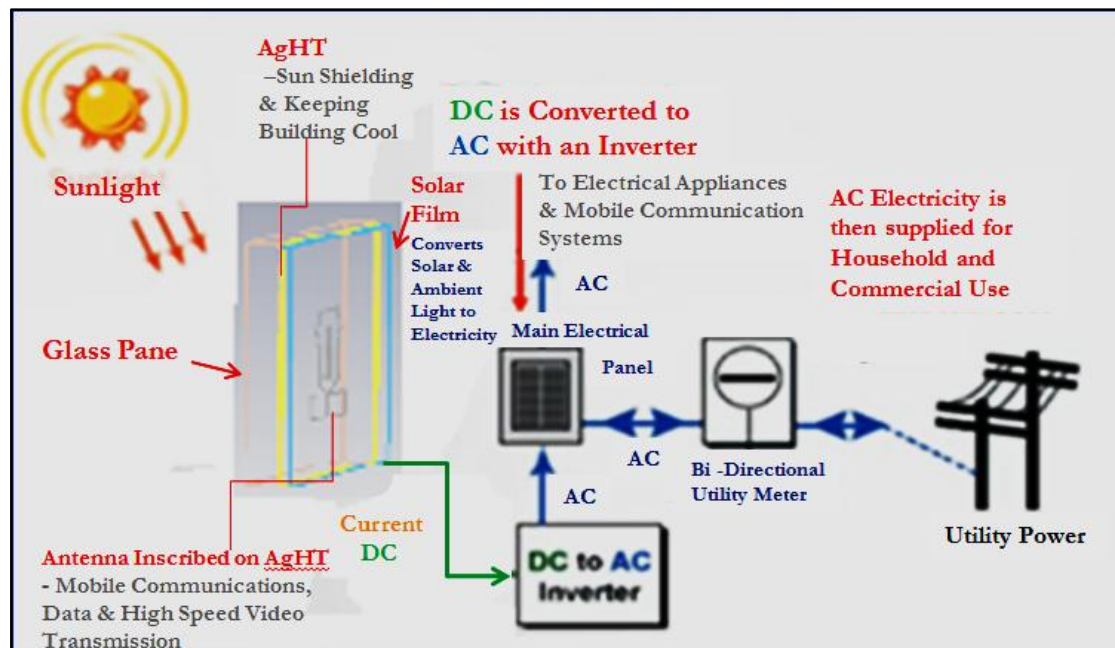


Figure 8.1 Putting solar energy to use: Drive communications system & harvest energy to power building

The proposed project known as “Energy Saver for Green Technology Building in Wireless Communication System” incorporates wireless communications and energy harvesting into the building aspect by using the AgHT film to also provide shielding from Infra-red and other harmful rays to keep the building cool and conserve energy. The EMC/RFI shielding film lets useful light in to brighten the building and keeps it cool whilst the antennas inscribed on the conductive layer of the film provides wireless communication; a second layer of transparent film with photovoltaic cells providing the final and essential element for harvesting solar energy to provide backup power or complementary power to meet the requirements of the building as well as drive the wireless systems. The project envisages the employment of improved photovoltaic materials that would allow the second layer to function also in dim lighting so that it can work after sunset, tapping the building’s lighting itself. The building’s lighting will then be able to be harvested back to continually provide power to save energy. Any extra power generated through this film photovoltaic system can then be off loaded into the national power grid. The green technology advancement-cum-consumer application research undertaken here is the first of its kind, and successful implementation of the concept could have global implications in terms of

power saving as well as providing buildings' the necessary communication network via discreet antennas that can be designed for narrow band mobile communications, Wi-Fi, or ultra wideband for fast data and video transmission.

8.2.2 Satellite Dish Integrated Solar Energy Harvester

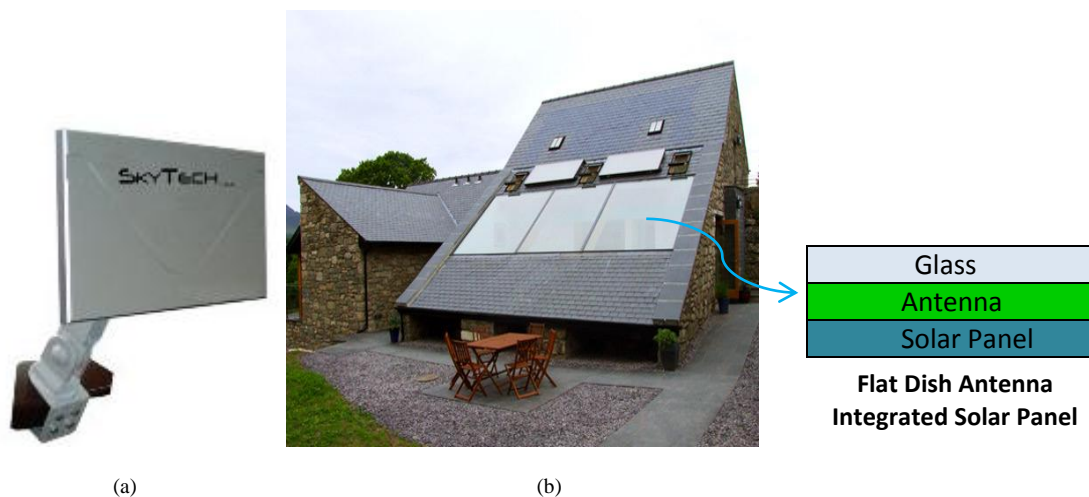


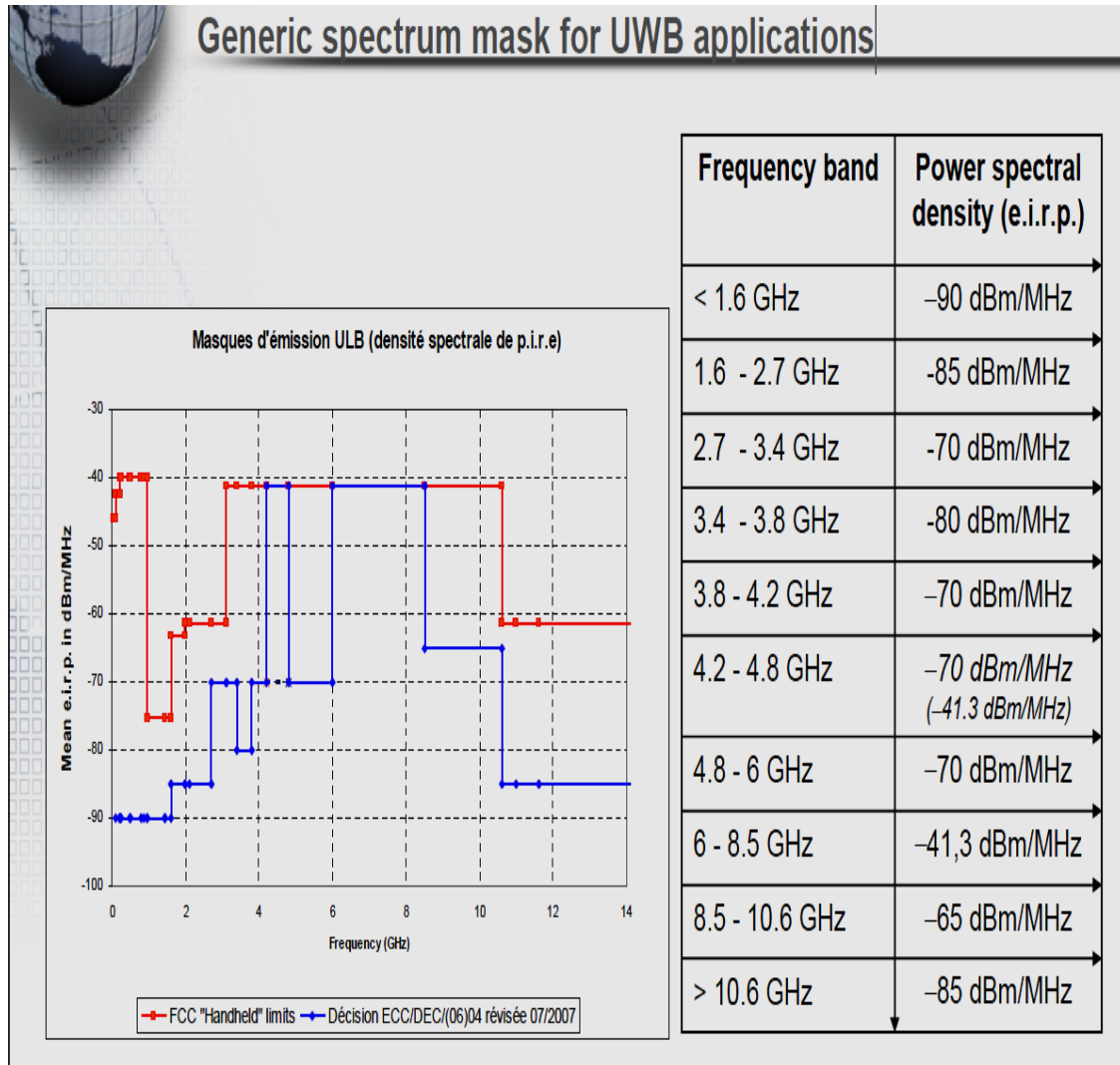
Figure 8.2 (a) SkyTech Flat KU Dish Antenna (b) Picture of a solar panel and the proposed flat dish integrated solar panel for future work.

Figure 8.2 (a) depicts a Flat KU Dish Antenna from SkyTech. Such flat dish satellite antennas can be integrated on to solar panels to provide an integrated solution that can enhance the aesthetics of the building or homes. This integration can be achieved by making the flat dish antenna using TCOs sandwiched between a glass layer and the solar panel on the roofs of buildings as shown in Figure 8.2 (b). Of course the antenna needs to be placed on the solar panel at the location of maximum reception of the satellite signals.

As the operating frequencies of the Direct Broadcast Satellites (DBS) for TV in most countries fall in the Ku band (10.7 to 14.5 GHz) as per International Telecommunication Union's (ITU) allocation, this would mean the antenna has to be designed as a wide band antenna operating between 10.7 GHz to 14.5 GHz. The flat dish antenna shown in Figure 8.2 (a) is stated to have an efficiency of 85% compared that to that of the dish antenna which is less than 70%. However, using transparent

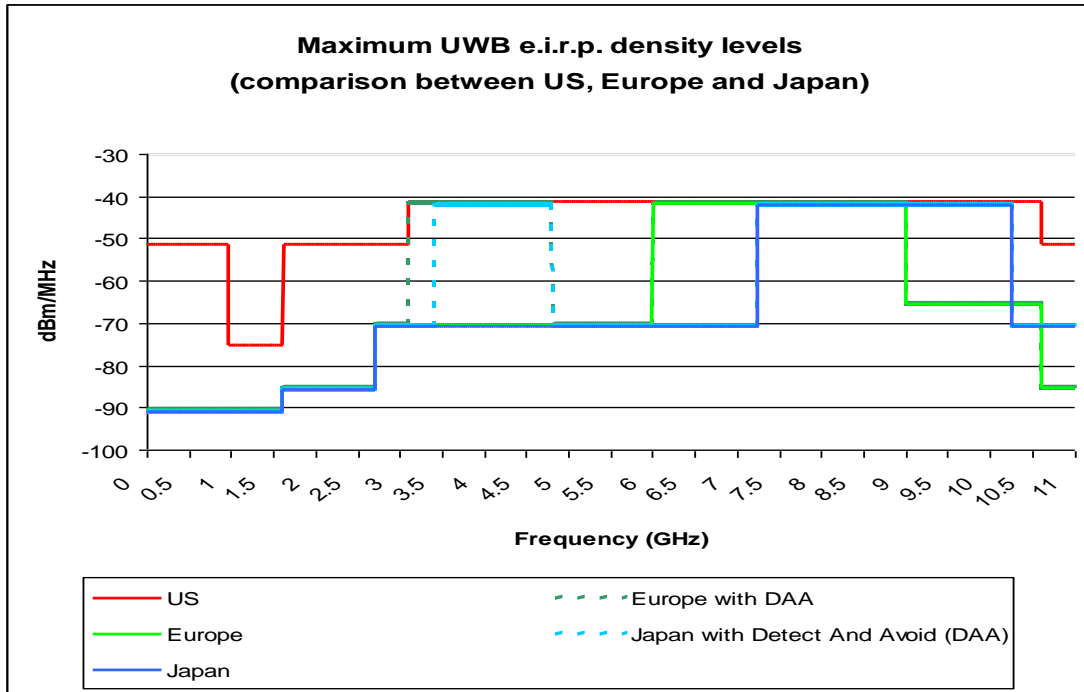
materials will greatly reduce this efficiency. This poses a great challenge namely, to improve the gain of the antenna and at the same time the efficiency which may be slightly affected by the glass superstrate. Nonetheless, arrays could be implemented to improve the directivity and gain which would directly translate into improved efficiency.

Appendix A.1 UWB Spectrum for EU

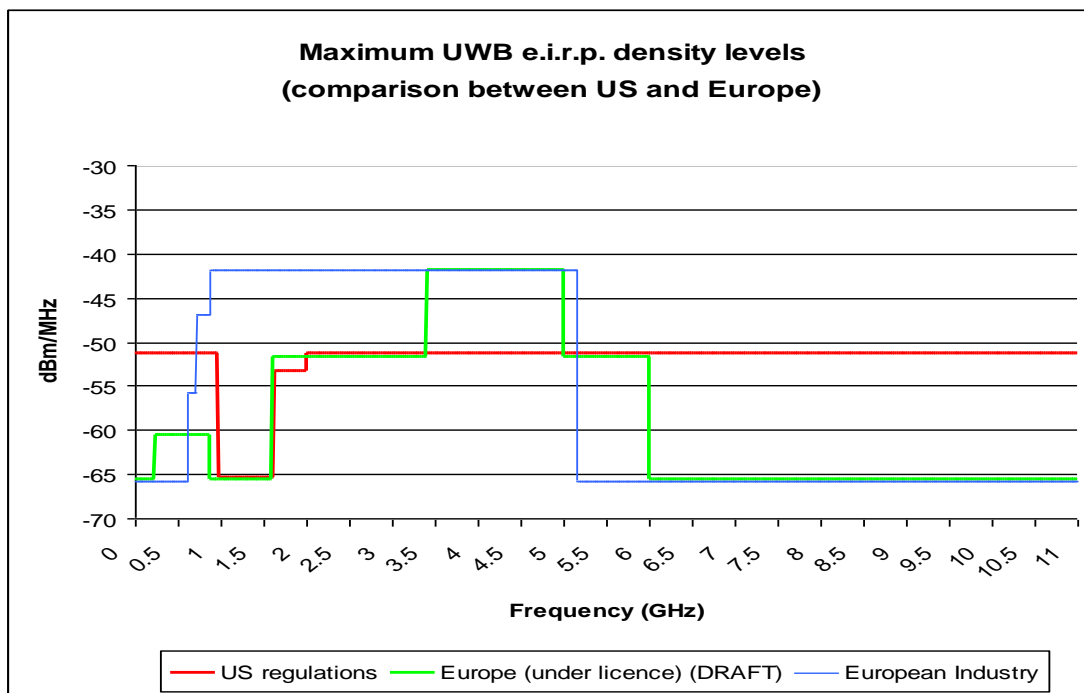


Appendix A.2 UWB Spectrum for EU

Communication and Location Tracking



GPR/WPR



Appendix B.1 Properties of PET

Properties of PET (Mylar)

Physical Properties				
Properties	Typical Value	Units	Test Method	
Tensile Strength (MD)	28,000	psi	ASTM-D882	
Tensile Strength (TD)	34,000	psi	ASTM-D882	
Strength Elongation MD	15,000	psi	ASTM-D882	
Strength F-5 TD	14,000	psi	ASTM-D882	
Modulus MD	710,000	psi	ASTM-D882	
Modulus TD	740,000	psi	ASTM-D882	
Elongation MD	115	%	ASTM-D882	
Elongation TD	92	%	ASTM-D882	
Surface Roughness	38	nm	Optical Profilometer	
Density	1.39	g/cc	ASTM-D1505	
Viscosity	0.56	dL/g	ASTM-D4603	
Yield	21,000	in ² /lb	n/a	

Electrical Properties				
Properties	Typical Value	Units	Test Method	
Dielectric Strength	AC, 20° C, .00092"	7,000	volts/mil	ASTM-D149-64
Dielectric Constant	25° C, 1kHz	3.2	n/a	ASTM-D150-81
Dissipation Factor	25° C, 1kHz	0.005	n/a	ASTM-D150-65
Volume Resistivity	25° C	1.00E+19	ohm-cm	ASTM-D257-78
Corona Threshold		V-AC	V-AC	ASTM-D2275-80

Thermal Properties			
Properties	Typical Value	Units	Test Method
Melting Point	254	° C	n/a
Dimensional Stability	n/a	n/a	n/a
at 105° C MD	0.6	%	n/a
at 105° C TD	0.3	%	n/a
at 150° C MD	1.8	%	n/a
at 150° C TD	1.0	%	n/a
Specific Heat	0.28	cal/g/° C	n/a
Thermal Expansion	1.7 x 10 ⁻⁵	in/in/° C	ASTM-D696
UL94 Flame Class	94VTM-2	n/a	Slow to self extinguishing

Appendix B.2 Tan δ and Q Factor

Dielectric Loss and Q Factor

Loss Tangent $\tan \delta = \frac{\epsilon_r''}{\epsilon_r'}$

Q Factor

$$Q = \frac{1}{\tan \delta} = \frac{\text{energy_stored}}{\text{energy_dissipated}}$$

ϵ_r' = real part of the complex dielectric constant, ϵ_r'' = imaginary part of the complex dielectric constant

From *Principles of Electronic Materials and Devices, Third Edition*, S.O. Kasap (© McGraw-Hill, 2005)

Appendix B.3 Malaysian Flagship Project

FLAGSHIP CONCEPT PAPER

Program Leader : Prof. Dr. Tharek Abd. Rahman
Research Alliance : Infocomm
Niche Area : ICT
Program Tittle : Energy Saver for Green Technology Building in
Wireless Communication System
Duration : 3 Years
Proposed Budget for Program: RM 990,000

1. EXECUTIVE SUMMARY

Since 2004, tremendous efforts have been put into incorporating solar cells onto antennas in the communications field to harvest solar energy for backup power especially with regard to antennas employed for satellites. Subsequent research until now, has been focusing using solar panels that were mounted onto metallic antenna radiators and connected to the antenna circuitry; the thickness of the solar panels gradually getting thinner with progress in advance techniques for fabricating thinner and more efficient solar cells. However, as focus changed over the last few years to look for Green alternatives to the depleting fossil fuels and reducing carbon footprints, researchers and architects were trying to incorporate solar panels onto glass panels of buildings to harvest energy to complement and provide back-up power as well as offload the excess into the nation's power grid. However, such approaches affected the aesthetic values of the buildings' architecture as well as involved additional structures. These structures were usually of steel and other building materials that were needed to support the solar panels to create a pleasing structure that was big and with the right exposure in terms of direction to harness enough of the sun. This method not only alleviated building cost but also blocked the natural light from falling through the glass panels into the building to brighten it. This thus reduced the brightness of the building calling for additional lighting to light up the building which is most often the case in "Building Integrated Photovoltaic (BIPV)" technology. Such an approach is counterproductive if the energy harvested just replaces the amount of power that was lost due to the installation of the solar panels.

The proposed green technology research project however, incorporates the communications as well as the building aspect into one whilst providing shielding from Infra-red and other harmful rays with commercially available conductive shielding film material. The EMC/RFI shielding film lets useful light in to brighten the building and

Appendix B.3 Malaysian Flagship Project

keeps it cool whilst the antennas inscribed on the conductive layer of the film provide wireless communications; a second layer of transparent film with photovoltaic cells providing the final and essential element for harvesting solar energy to provide backup power or complementary power to meet the requirements of the building as well as drive the wireless systems. The project envisages the employment of improved photovoltaic materials that would allow the second layer to function also in dim lighting so that it can work after sunset, tapping the building's lighting itself. The building's lighting will then be able to be harvested back to continually provide power to save energy. Any extra power generated through this film photovoltaic system can then be off loaded into the national power grid. The green technology advancement-cum-consumer application research proposed to be undertaken here is the first of its kind, and successful implementation of the concept could have global implications in terms of power saving as well as providing buildings' the necessary communication network via discreet antennas that can be designed for narrow band mobile communications, Wi-Fi, or ultra wideband for fast data and video transmission.

2. Background and Rationale of Concept Paper

The concept outlined in this project is the use of the conductive AgHT coating on a polymer substrate (PET) to act as a radiating surface for the transmission and reception of electromagnetic energy for wireless communication. The concept makes use of the transparency of the AgHT material itself to allow light whether natural (e.g. solar) or unnatural (lighting systems) to fall onto a second layer of transparent or semi-transparent material (either polymer embedded with spherical photovoltaic cells or translucent panels) to be converted to electrical energy. This energy being thus a green power source to complement the power and energy needs of the building as well as the national power grid into which any extra power can be offloaded.

The background and concept rationality for this project has to be addressed categorically with regard to i) wireless communication, ii) solar integration for energy harvesting and power savings for green technology advancement and iii) extension to consumer application especially to reduce energy consumption in homes.

Appendix C.1 How PET is Made

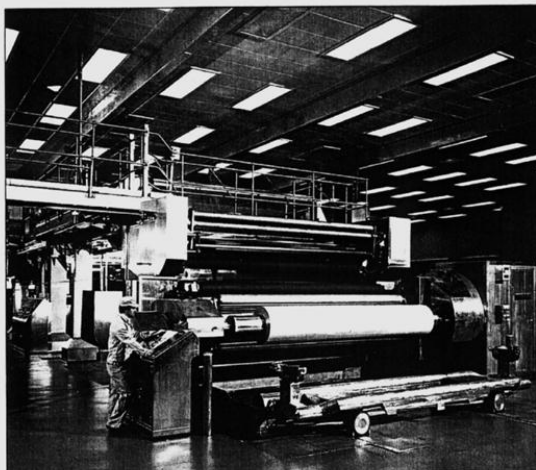
ORIENTATED PET FILM

Next, the cast film travels through a forward draw unit where it is heated at about 90°C and stretched to roughly three times its original length. This drawing process causes some of the molecular chains to straighten or align themselves in the direction of the draw.

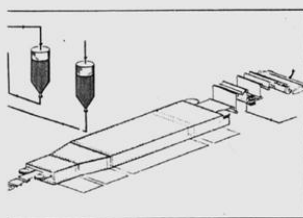
The drawn film is then fed into two sets of continuous chains which grip it on each side and carry the film into special ovens where it is heated to again about 90°C and stretched out to three times its original width. As a result, some of the polymer chains align themselves in a sideways or transverse direction. The film is now biaxially orientated. It is then passed through a heat setting region and exposed to a temperature of 220-240°C.

Heat setting in this way, makes the molecular chains pack together in a regular, more crystalline, arrangement. The end product is a very strong, tough, clear, dimensionally stable and chemically resistant film.

After cooling, the film is trimmed and wound up to create a mill roll which can then be cut into the widths and lengths required by customers.

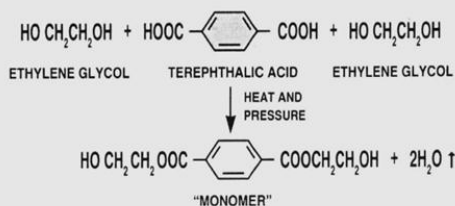


Melinex Film production at Dumfries, Scotland.



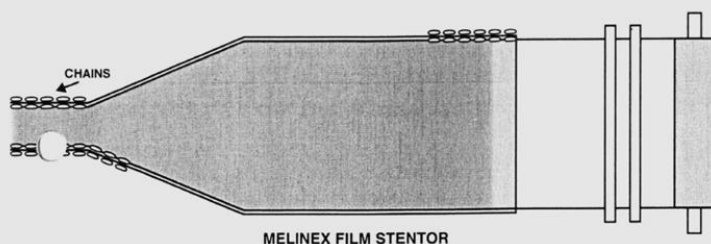
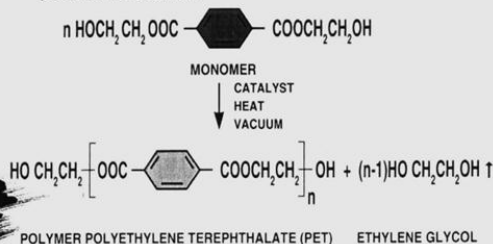
DIRECT ESTERIFICATION

This reaction takes place in the direct esterification vessel and produces the monomer.



POLYMERISATION:

This reaction takes place in the polymer autoclave and produces the polymer.



Appendix C.2 Barrier Film for PET



PRELIMINARY DATA SHEET

PET Moisture Barrier Film

PRODUCT DESCRIPTION

- 25 micron moisture barrier film, MVTR < 0.1 g/m² * day
- Optically clear, visible light transmission > 88%
- Max width = 59 inches

MATERIAL PROPERTIES

ITEM	STANDARD	MEASURED VALUE	UNIT	CONDITIONS	REMARKS
THICKNESS	ISO 4593	25 0.001	micron inches	standard	Typical Values
VLТ	ASTM D 1003	89	%	standard	Typical Values
HAZE	ASTM D 1003	5.5	%	standard	Typical Values
YELLOW INDEX	ASTM D1925	< 3.0	YI (2°Std Obs/Illum C)	standard	Typical Values
YIELD	--	31 42	m ² /Kg K in ² /lb	standard	Typical Values
TENSILE STRENGTH	ASTM D 882	MD TD 22,000 27,800 151.7 191.7	psi Mpa	standard	Typical Values
ELONGATION	ASTM D 882	MD TD 135 95	%	standard	Typical Values
HEAT SHRINK	IPC -TM-650 Method 3.7.1	MD TD 1.5 -0.25	%	150 C 30 min.	Typical Values
MOISTURE PERMEABILITY	ASTM F 1249	0.05 - 0.03	g / m ² * day	38 C 90%RH	Typical Values
OXYGEN PERMEABILITY	ASTM D 3985	TBD	cc / m ² * day	30 C 70%RH	Typical Values

NOTE: Typical value is a reference number based on current evaluation results. These are preliminary values and are subject to change.

SOLUTIA

Solutia Inc., St. Louis, Missouri, USA. All rights reserved. Flexvue™ and Flexvue Logo™ are trademarks of Solutia Inc. All technical information set forth herein is based upon tests which Solutia believes to be reliable. However, Solutia does not guarantee accuracy or completeness. The buyer should conduct tests of this product before use to determine suitability for the proposed application. Suggestions made concerning uses or applications are only the opinion of Solutia and Solutia makes no warranty of the results to be obtained. Solutia MAKES NO REPRESENTATION OR WARRANTY OF ANY KIND, EXPRESS OR IMPLIED, WITH RESPECT TO THE MATERIAL. THERE ARE NO WARRANTIES, EXPRESS OR IMPLIED, OF MERCHANTABILITY, WORKMANSHIP OR FITNESS FOR A PARTICULAR PURPOSE. The responsibility of Solutia for claims arising out of breach of warranty, negligence, strict liability or otherwise is limited to the purchase price of the material. Solutia shall have no other liability for any incidental, consequential, or punitive damages. Nothing herein is to be taken as a license to operate under, or a recommendation to infringe upon, any patents.

Appendix C.3 ECCOSORB FGMU-125

EB-322

ECCOSORB® FGM-U-125

THIN, FLEXIBLE, BROADBAND, MICROWAVE ABSORBER

Description:

Eccosorb FGM-U-125 is thin, flexible, broadband urethane absorber. It is effective in reducing specular reflections as well as surface currents in cavity resonance applications. The main advantages of the polyurethane version are its ease of bonding to various substrates and the availability of a self-adhesive version. Further they offer high mechanical strength and excellent abrasion resistance. Will withstand temperatures from -40°C to 120°C.

Application:

Eccosorb FGM-U-125 is used to line cavities in which antennas operate. It may be applied to surfaces to improve radar performance, reduce radar cross section or backscattering. Eccosorb FGM-U-125 is effective in reducing specular reflections as well as surface currents due to the high magnetic loss properties. When bonded to a metal surface Eccosorb FGM-U-125 will significantly reduce the reflectivity of metal objects or structures due to the flow of microwave currents on that surface. It can be applied to antenna elements, microwave dishes, the inner or outer surfaces of waveguides for isolation, attenuation or modification of radiating patterns. Applications include power amplifiers, oscillators, down/up converters and LNB's. It is also utilized to modify antenna patterns, cover antenna feed supports, line antenna caps to reduce reflections and improve the isolation of sensitive RF devices.

Physical Properties:

Colour	brown
Dimensions (mm)	305 x 305
Nominal thickness (mm)	3.3
Weight (kg/m ²)	10.6
Hardness (Shore A)	91

Emerson & Cuming Microwave Products N.V.
Bell Telephonedaan 2B – B-2440 Geel – Belgium
Tel: +32 14 56 25 00 – Fax +32 14 56 25 01
sales@eu.eccosorb.com - www.eccosorb.eu



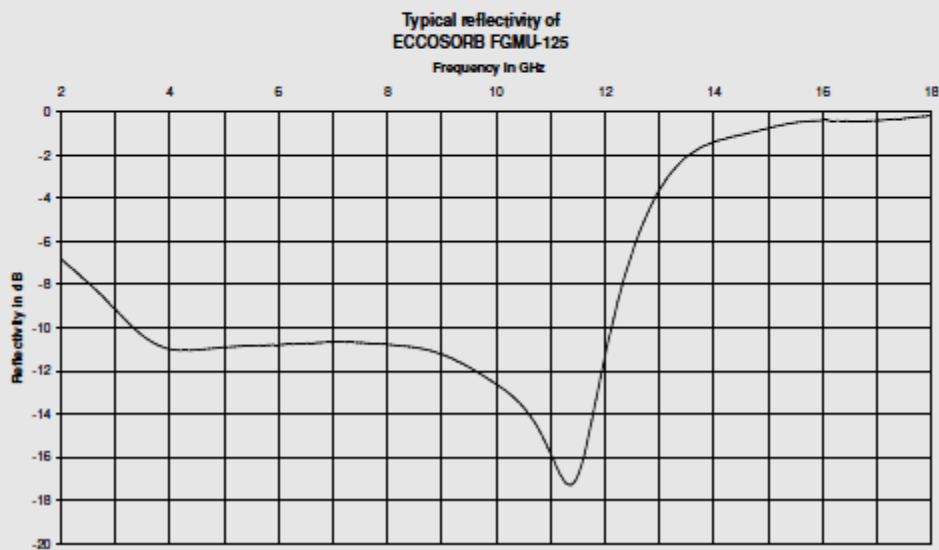
Appendix C.3 ECCOSORB FGMU-125

EB-322

ECCOSORB® FGM-U-125

THIN, FLEXIBLE, BROADBAND, MICROWAVE ABSORBER

Electromagnetic Properties:



Availability:

Eccosorb FGM-U-125 is available in sheets of 305 mm x 305 mm, with a nominal thickness of 3.3mm. The product is also available in other sizes, customer specified configurations and thicknesses upon request.

Instructions for use:

Eccosorb FGM-U-125 is designed to function directly in front of a metallic surface.

If this is not the case, a metallic foil should first be bonded to the object.

As it is a homogeneous material, there is no distinction between its front and back face.

To obtain a strong bond of the absorber to the object, the metallic surface should be first thoroughly cleaned with a degreasing solvent.

Epoxy and acrylic adhesives are recommended or use the self-adhesive version.

Recommended is to use the self-adhesive version on smaller parts only as the weight of a full sheet will not be supported by the self-adhesive tape.

Eccosorb FGM-U-125 can be readily cut with a sharp knife and template.

It is a flexible material and will conform to mild curvatures.

Safety Considerations: It is recommended to consult the EMERSON & CUMING MICROWAVE PRODUCTS product literature, including material safety data sheets, prior to use EMERSON & CUMING MICROWAVE PRODUCTS products. These may be obtained from your local sales office.
WARRANTY: Values shown are based on testing of laboratory test specimens and represent data that falls within the normal range of properties of the material. These values are not intended for use in establishing maximum, minimum or ranges of values for specification purposes. Any determination of the suitability of the material or any use contemplated by the user and the manner of such use is the sole responsibility of the user who must ensure that the material as subsequently processed meets the needs of the particular product or use. We hope the information given here will be helpful. It is based on data and knowledge considered to be true and accurate and is offered for the user's consideration, investigation and verification but we do not warrant the results to be obtained. Please read all statements, recommendations or suggestions in conjunction with our conditions of sale INCLUDING THOSE LIMITING WARRANTIES AND REMEDIES which apply to all goods supplied by us. We assume no responsibility for the use of these statements, recommendations or suggestions nor do we intend them as a recommendation for any use which would infringe any patent or copyright.
2011.04 - V012

Emerson & Cuming Microwave Products N.V., Bell Telephoneaan 23, 9-3440 Geel, Belgium.

ECCOSORB, ECCOSTOOL, ECCOSWELD, ECCOLINS, ECCOFAD are registered trademarks of EMERSON & CUMING MICROWAVE PRODUCTS NV

